Study of convective heat transfer phenomena for turbulent pulsating flows in pipes

Marco Simonetti

To cite this version:

Marco Simonetti. Study of convective heat transfer phenomena for turbulent pulsating flows in pipes. Other. Université d'Orléans, 2017. English. NNT : 2017ORLE2057 . tel-01985040

HAL Id: tel-01985040
https://theses.hal.science/tel-01985040

Submitted on 17 Jan 2019

UNIVERSITÉ D'ORLÉANS

ÉCOLE DOCTORALE
ENERGIE, MATERIAUX, SCIENCES DE LA TERRE ET DE L'UNIVERS

LABORATOIRE PRISME

THESIS presented by:

Marco SIMONETTI

defended on: **15 – December – 2017**

for the degree of: **PhD from the University of Orléans**
Specialty: Energetics

Study of convective heat transfer phenomena for turbulent pulsating flows in pipes

THESIS supervised by:

Pascal HIGELIN	Professor, PRISME - University of Orléans

THESIS co-supervised by:

Christian CAILLOL	Associate Professor, PRISME - University of Orléans

REVIEWERS:

Alberto BROATCH	Professor, CMT - Polytechnic University of Valencia
David CHALET	Professor, Ecole Centrale de Nantes

JURY:

Alberto BROATCH	Professor, CMT - Polytechnic University of Valencia
Christian CAILLOL	Associate Professor, PRISME - University of Orléans
Clement DUMAND	PhD, Groupe PSA
David CHALET	Professor, Ecole Centrale de Nantes
Pascal HIGELIN	Professor, PRISME - University of Orléans
Pawel WAWRZYNIAK	Associate Professor, Technical University of Lodz

UNIVERSITÉ D’ORLÉANS

ÉCOLE DOCTORALE
ENERGIE, MATERIAUX, SCIENCES DE LA TERRE ET DE L’UNIVERS

LABORATOIRE PRISME

THÈSE présentée par:

Marco SIMONETTI

soutenue le: **15 – Décembre – 2017**

pour obtenir le grade de: **Docteur de l’Université d’Orléans**
Spécialité: Energétique

Etude du transfert thermique convectif des écoulements turbulents pulsés dans un conduit cylindrique

THÈSE dirigée par:

Pascal HIGELIN	Professeur, PRISME - Université d’Orléans

THÈSE co-encadrée par:

Christian CAILLLOL	Maitre de conférence, PRISME - Université d’Orléans

RAPPORTEURS:

Alberto BROATCH	Professeur, CMT - Universitat Politècnica de València
David CHALET	Professeur, Ecole Centrale de Nantes

JURY:

Alberto BROATCH	Professeur, CMT - Polytechnic University of Valencia
Christian CAILLOL	Maître de Conférence, PRISME – Université de Orléans
Clément DUMAND	Docteur Ingénieur, Groupe PSA
David CHALET	Professeur, Ecole Centrale de Nantes
Pascal HIGELIN	Professeur, PRISME - Université de Orléans
Pawel WAWRZYNIAK	Maître de Conference, Technical University of Lodz

Contents

List of figures

Nomenclature

Roman letters

a	Overheat ratio
A	Flow area
A_{o}	Dimensionless pressure amplitude
$\mathrm{A_s}$	Heat transfer surface area
C	Sound velocity
$\mathrm{c_{cond}}$	Manifold specific heat
$\mathrm{C_f}$	Friction coefficient
$\mathrm{C_t}$	Temperature corrective coefficient
$\mathrm{C_p}$	Pressure corrective coefficient
c_p	Fluid specific heat coefficient at constant pressure
d	Diameter
d_r	Wire diameter
D	Pipe diameter
e	Total internal specific energy
E_{cond}	Conduction energy
E_{conv}	Convection energy
E_{irr}	Thermal radiation energy
$E_{tr,air}$	Energy transferred from air to manifold
$E_{re,air}$	Energy recovered from the air
ΔE_{man}	Internal energy variation of the manifold
f	Pulsation frequency
F	Total drag force
$F_{ht,unst}$	Unsteady heat transfer factor
Gz_T	Graetz number
h	Convective heat transfer coefficient
H	Total enthalpy
k	Turbulent kinetic energy
L	Length scale
$\dot{m}$	Mass flow rate
m_{cond}	Manifold mass
Ma	Mach number
N_{const}	User-defined constant heat transfer factor
N_{unst}	User-defined unsteady heat transfer factor
Nu	Nusselt number
P	Flow pressure
q	Total specific heat transfer rate

q''	Total specific convective heat flux
Q_{conv}	Convective heat transfer
R_{ii}	Autocorrelation function
R	Wire electrical resistance
R_{in}	Internal radius
R_{out}	Outer radius
Re	Reynolds number
Pr	Prandtl number
S	Thermal exchange surface
t	time
T	Temperature
T_b	Bulk temperature
T_g	Fluid temperature
T_0	Flat plate temperature
T_∞	Uniform stream temperature
U_∞	Uniform stream velocity
U_{avg}	Axial velocity amplitude
U_{eff}	Effective velocity
U_m	Time-average axial velocity
U_o	Lagrangian velocity
u	Axial flow velocity
u_τ	Friction velocity
v	Radial flow velocity
V_w	Wire voltage
$\boldsymbol{w}$	State noise
y	Distance from the wall
W	Width of the flat plate
Wo	Womersley number
Z	Flow instantaneous property
Z_b	Bulk component
Z_r	Radius-dependent component
$\bar{Z}$	Time-average component
Z'	Turbulent component
$\tilde{Z}$	Oscillating component

Greek symbols

α	Fluid thermal diffusivity
ρ	Flow density
τ	Skin friction
τ_1, τ_2	Thermocouple response times
μ	Fluid viscosity
λ	Fluid thermal conductivity
λ_{eff}	Effective thermal conductivity
λ_t	Turbulent thermal conductivity
η_{rec}	Recovery efficiency

η_{res}	Restoring efficiency
ν	Kinematic flow viscosity
δ	Cinematic boundary layer thickness
δ_{ij}	Delta of Knorecker
δ_T	Thermal boundary layer thickness
ΔT_{lm}	Logarithmic temperature difference
ε	Kinetic energy dissipation rate
ε_M	Momentum eddy diffusivity
ε_H	Thermal eddy diffusivity
ω	Flow pulsation
ω^+	Dimensionless flow frequency
Λ	Integral length scale
$\mathit{\Sigma}$	Pipe Surface
γ	Ratio of specific heats
$\boldsymbol{\theta}$	Vector of the latent variables
θ_w	Wire temperature
θ_{air}	Air temperature

Abbreviations

BMEP	Break Mean Effective Pressure
CA	Crank angle
CAD	Camshaft degree
CTA	Constant temperature anemometer
EGR	Exhaust gas recirculation
GHTM	Global Heat Transfer Multiplier
HESS	Heat Energy Storage System
HWA	Hot-Wire Anemometer
ICE	Internal Combustion Engine
LDV	Lased Doppler Velocimetry
MFR	Mass Flow Rate
PSD	Power Spectral Density
STD	Standard Deviation
TEG	Thermo-Electric Generator
WER	Waste Energy Recovery

Chapter / Chapitre I

General Introduction

I. General Introduction

I.1 Motivation and concern of the work

Legislation on vehicle emissions continues to become more stringent in an effort to minimize the impact of Internal Combustion Engines 'ICEs' on the environment, forcing engine manufacturers companies to face always more to the challenge of increasing engine efficiency and decreasing pollutant emissions.

ICE efficiency is still improving but it is today limited at best to around 40%, a large part of energy contained in the fuel is lost in coolant, oil, exhaust gas and air around the engine. Bourhis and Leduc [1] evaluated the energy balance for ICEs and estimated that, for a Spark Ignition gasoline engine (operated at 2000 rpm and Brake Mean Effective Pressure 'BMEP' = 0.2 MPa) and for a Diesel engine (operated at 2300 rpm and BMEP = 0.8 MPa) respectively, 39% and 51% of the fuel available energy is lost in the form of heat through oil, water coolant, exhaust gas, intercooler and EGR heat exchanger. Considering the exergetic limits, Waste Energy Recovery (WER) represents a promising way to go further in fuel saving and pollutant emissions control: a waste heat recovery system produces power by using the thermal energy lost in the surroundings from thermal processes without an additional fuel input.

They can be generally classified into direct and indirect energy conversion machines: among the direct machines, the turbine of the turbocharger and the turbocompound systems have been the first to exploit WER in ICE [2]. Although the advantage of an ulterior power output, the presence of the turbine, at the engine exhaust, can lead to an increase in exhaust gas pressure that can worsen, in some cases, the engine global cycle efficiency. Furthermore, because of the low turbine efficiency a total recovery of the exhaust thermal energy is not possible to be achieved, with the use of the turbine only: in a SI engine, for instance, the exhaust gases at the turbine outlet can reach a temperature up to 500°C, making feasible the use of an additional WER technology. Recovering and transforming in electrical energy the wasted thermal energy by thermoelectric generators (TEG) is a technical solution that has been extensively investigated in [3], [4]. The low thermal efficiency of the TEG, which is typically inferior at 4%, remains to be still overcome [5]. Using the thermal energy of the exhaust gases to heat the engine coolants as well as the air of the vehicle's interior, represents a cogeneration solution for WER. Such systems are, for instance, adopted by the Groupe PSA for the vehicles intended for the Norwegian market.

Among the indirect machines, the Stirling engine uses the thermal energy of the exhaust gases as a heat source for the waste thermal energy conversion. Aladayleh and Alahmer [6] have shown that the vehicle fuel consumption can be reduced by about 15%, as well as authors in [7]–[9] have argued that a Stirling engine has many advantages such as high potential efficiency (up to 45%), reversible operation, low maintenance, smooth torque delivery and ability to run at different fuels. Waste heat recovery in ICE, involving a Rankine cycle, also utilizes the enthalpy from the hot exhaust gases as the heat source. In a review on the use of the Rankine cycle for ICE exhaust waste heat recovery, Sprouse and Depcik [10] have reported a potential fuel economy of around 10%.

As previously cited several technologies for WER have been extensively investigated in the past few years, each of these systems extracts the thermal energy still available in the engine exhaust gases and transforms such thermal energy in a mechanical or electrical output. An efficient thermal energy extraction from exhaust gases represents the first important requirement for such systems. For this reason, high efficiency heat transfers should be ideally established between the engine exhaust gases and the WER machines, in order to be able to extract the major quantity of available exhaust energy.

In the case of the design of a heat exchanger in a Rankine machine, for example, whether the thermal convective mechanisms occurring in the flow are well comprehended; instead of increasing the exchange surface to enhance the convective heat transfers, the heat transfer quality could be ameliorated by modifying the cinematic field of the flow, for instance, and by this way the exchanger dimensions could be reduced while keeping constant the total exchanged energy. Here the reasons which may justify a study of the heat transfer phenomena for the engine exhaust-type flow.

Furthermore, besides the WER for the ICE efficiency increase, a particular attention is also being paying in the catalytic converters design and exhaust manifold design to respect emission standards requirements.

A catalytic converter is an emissions control device that converts toxic gases and pollutants in exhaust gas to less toxic pollutants by catalyzing a redox reaction. During the cold start phase, which is the engine operation period until the catalyst and engine reach the starting temperature, the catalytic converter does not work efficiently because it has not reached its activating temperature called ‘light-off’ temperature. According to references, 60% – 80% of the total CO and HC emission is emitted during this period. In order to reduce emission during the cold start phase, various constructive solutions are applied in both engine and exhaust system such as making impact on faster catalytic converter action and increase of entire efficiency on additional exhaust gases processing. In references, this approach is very often called “Catalyst Fast Light-off Techniques (FLTs)”. Among all the techniques, in the few past year, as demonstrated by the work of Petković et al. [11] passive systems are being widely investigated. They include simple constructional alteration on exhaust manifold, which may be used for reducing the heat losses in the atmosphere. Thus, it increases exhaust gas temperature before catalyst and accelerates reaching of its starting temperature.

As argued in the previous lines, similarly to the WER machines also for the optimal design of an engine exhaust a good management of the heat transfer phenomena represents an important requirement, as it is furthermore demonstrated by the work of Host et al. [12].

Heat transfers in the engine manifolds, either intake or exhaust, occur under pulsating conditions. The unsteadiness of the flow, due to the pulses coming from the cylinder ports, increases the difficulty of the phenomena analysis. While during one engine cycle, a mass of exhaust gases leaves the combustion chamber in order to be ejected out from the engine, as well a fresh mixture of air and fuel enters the cylinder, suggesting that within an engine cycle the physical mechanisms of the flow are completely non-stationary; observing the flow in a time period wider the engine cycle period, it could be noted that coherent patterns in the flow properties occur cyclically in time, i.e. they are cycle-stationary.

The term ‘pulsating’ or ‘pulsatile’ is used for the class of cycle-stationary flows in which the oscillations occur around a time-average value different from zero.

Although for a stationary flow the Reynolds number characterizes the laminar or turbulent behavior of the bulk flow, the amplitude and the frequency of the superimposed oscillations play a dominant role in the structures of the pulsating flow. Over the past decades, widespread studies have been dedicated to pulsating flows, and their associated heat transfer process, in a wide range of experimental configurations. However, some available results are contradictory and the main questions are still open: *does pulsation enhance or else degrade heat transfers compared to a steady flow? Which are the main heat transfer mechanisms?* (Further details, about the state of art of the previous studies, are reported in the next chapter).

In view of all previously claimed, the main objective of this thesis is thus to attempt to answer and to go further to the previous questions, by an experimental and analytical approach, in the comprehension of the convective heat transfer phenomena for turbulent pulsating pipe flows.

A better comprehension of such phenomena, could be exploited to better design the future ICEs and the WER technologies, as well as it could be the basis for the development of more precise numerical models to predict convective heat transfers in such kind of industrial applications.

The work presented in this thesis has been totally funded by the Groupe PSA in the framework of the ‘OpenLab Energetics’, with the PRISME laboratory of the University of Orleans.

I.2 Thesis outline

This manuscript reports the main works and results found in this three years thesis. To avoid to be pedantic the fundamental of thermodynamics are considered to be acquired for the readers. Only some principles useful for the correct comprehension of the work will be revised in the next chapter.

The manuscript is organized as follows: Chapter 2 (page 7) presents the theoretical background on fluid mechanics and heat transfers necessary to the analysis and understanding of the experimental results. Starting from the laminar boundary layer theory, the turbulent pulsating pipe flow principles are revised and discussed to evidence the limits of the available models for the convective heat transfer prediction. An analysis of the previous works, ranging from pulse combustor tail pipe applications to internal combustion engine applications, is also conducted to point out the recent advancements on the comprehension of the heat transfer phenomena. In this manner it has been possible to finally define the thesis strategy to fulfill the main previous cited purpose.

In the Chapter 3 (page 59) the experimental apparatus designed to reproduce a turbulent pulsating pipe flow, representative of an engine exhaust-type flow, is presented. The experimental procedure to characterize the convective heat transfers as well the measurements techniques have been detailed.

A particular attention is paid in the presentation of the instantaneous measurement techniques for the flow velocity and temperature. Such techniques have been experimentally validated and the results have been included in the manuscript. Then a characterization of flow field under stationary flow conditions has been conducted, as well as the acoustic characterization of the test rig.

In the remaining chapters 4 and 5 (respectively at page 107 and 137), with a 1D and a 2D assumption, the experimental results have been presented, analyzed and discussed. The main mechanisms playing an important role in the convective exchange of thermal energy have been discussed. Such particular analytical approach has permitted to highlight the major mechanism which contribute to the heat transfer enhancement, as well as a secondary radial phenomenon impacting the convective thermal transport. Although such thesis has been based on an experimental approach, as it will be possible to observe in the following lines, in addition to the analytical development of the energy balance equation used for the experimental data analysis, a CFD modelling phase has been conducted: using a commercial CFD software, the turbulent pulsating pipe flow has been modeled with a 2D assumption. Actually to be clear for the reader, due to some constraints on the possibility to measure, in a detailed enough way, all the flow properties, the main purpose of such 2D CFD modelling phase has been to furnish further elements required for the comprehension of the convective heat transfer phenomena.

Finally, in the 6 and last chapter (page 184) a summary of the main findings of this thesis has been presented, in order to lead the reader to the conclusions and the perspectives of the study.

Chapter / Chapitre II

Convective heat transfers for pulsating flows

Abstract

Convective heat transfers, or simply, convection, is the study of heat transport processes effected by the flow of fluids. In this chapter the principles of convective heat transfer are reviewed in order to establish a common language for the more specific issues addressed in later chapters. For the sake of brevity and to avoid a pedantic speech the governing balance equations of mass, momentum and energy are considered acquired for the reader and they are not demonstrated.

Starting from the boundary layer theory, the main problem of the convective heat transfers prediction has been presented: the definition of the Nusselt number has been introduced. Paying a particular attention on the simplification hypotheses, the form of a time-average Nusselt number correlation for a boundary layer flow has been demonstrated.

Focusing on the particular case of a laminar and turbulent stationary pipe flows the energy governing equations have been analyzed and discussed in order to validate the assumption of the boundary layer hypotheses adopted in the previous turbulent steady analysis.

In this manner, it has been possible to go further and introduce the flow pulsation to the energy governing equation, in order to be able to finally lead to the formulation of the heat transfer problem for a pulsating turbulent pipe flow.

In the second part of this chapter the state of art of the previous studies has been reviewed: it has been observed that although widespread studies have been allocated to pulsating flows and their associated heat transfer problems over the past decades, some available results are contradictory and the main question is still open: Does pulsation enhance or else degrade heat transfer compared to steady flow.

In particular, we have focused our attention on the convective heat transfers for pulse combustor tail pipes, laminar or turbulent pipe flows and internal combustion engines.

Also an experimental investigation on the potential of a Heat Energy Storage System has been presented in such chapter: the main purpose is to evidence the flow operating conditions occurring in the engine manifold, as well as the inaccuracy of the literature model to predict convective heat transfers for such applications.

Considering all these aforementioned elements, in the last part of the chapter the thesis strategy has been defined; as well as the potential contribution which such work could bring to the physical comprehension of convective heat transfer phenomena for turbulent pulsating pipe flow. In the same manner also the contribution, which this work may have for the Groupe PSA, has been claimed.

II. Convective Heat Transfers for Pulsating Flows

II.1 Introduction

Convective heat transfer, or simply, convection, is the study of heat transport processes affected by the flow of fluids. Convective heat transfer has grown to the status of a contemporary science because of our need to understand and predict how a fluid flow acts as a ‘‘carrier’’ or ‘‘conveyor belt’’ for energy and matter; it is clearly a field at the interface between two older fields: heat transfer and fluid mechanics. For this reason, the study of any convective heat transfer problem must rest on a solid understanding of basic heat transfer and fluid mechanics principles.

The objective of this chapter is to review these principles in order to establish a common language for the more specific issues addressed in later chapters. For the sake of brevity and to avoid a pedantic speech the governing equations of mass, momentum and energy balance are considered acquired for the reader and they will only reminded in specific cases, nevertheless they will not be demonstrated.

After having reviewed the fundamentals of the convective heat transfers in the first part of this chapter, a re-examination of the previous experimental studies has been reported in the second part of the chapter. Several experimental configurations, such as pulse combustor tail pipes, laminar of turbulent pipe and internal combustion engines have been reviewed, to be able to conclude finally to the thesis strategy and contribution to the phenomena comprehension.

II.2 Theoretical background

II.2.1 Laminar & Turbulent boundary layer flows theory

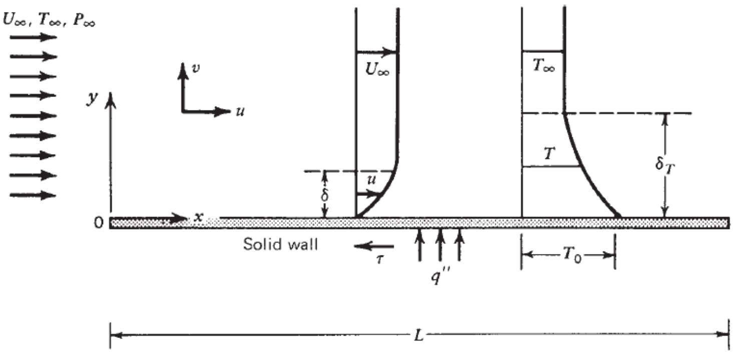

Figure 1: Velocity and temperature boundary layers near a plate parallel to a uniform flow.

Considering the fundamental questions that arise in connection with heat transfer from a solid object to a fluid stream in external flow, for example, for a flat plate of temperature T_0 suspended in a uniform stream of velocity U_∞ and temperature T_∞, as shown Figure 1, we want to know:

1. the net force exerted by the stream on the plate;
2. the resistance to the transfer of heat from the plate to the stream.

We must answer question 1 in order to predict the total drag force exerted by the stream on the heat exchanger surface. From a simple force balance around the duct through which the stream flows, we learn that the drag force felt by the solid surface translates into the pressure drop, hence, the pumping power required to keep the stream flowing. Question 2 must be answered in order to predict the heat transfer rate between solid and fluid.

Referring to the Figure 1, we are interesting to calculate the total drag force

$$F = \int_0^L \tau W dx \qquad \text{II - 1}$$

and the total heat transfer rate

$$q = \int_0^L q'' W dx \qquad \text{II - 2}$$

Symbols τ and q'' stand respectively for skin friction

$$\tau = \mu \left.\frac{\partial u}{\partial y}\right|_{y=0} \qquad \text{II - 3}$$

and the total heat flux

$$q'' = h(T_0 - T_\infty) \qquad \text{II - 4}$$

and 'W' represents the width of the flat plate in the direction perpendicular to the plane.

Equations II - 3 and II - 4 serve as definitions for the concepts of viscosity μ and heat transfer coefficient h.

In this treatment, we accept empirically (i.e., as a matter of repeated physical observation) that the fluid layer situated at $y = 0^+$ is, in fact, stuck to the solid wall. This is the no-slip hypothesis, on which the bulk of convective heat transfer research is based.

The no-slip condition implies that since the $0 < y < 0^+$ fluid layer is motionless, the transfer of heat from the wall to the fluid is first by pure conduction. Therefore, in place of eq. II - 4, we can write the statement for pure conduction through the fluid layer immediately adjacent to the wall:

$$q'' = -\lambda \left.\frac{\partial T}{\partial y}\right|_{y=0} \qquad \text{II - 5}$$

Where λ represents the thermal conductivity of the fluid, contrarily to h, it is only a property of the fluid and not of the flow.

Combining equations II - 4 and II - 5 we can calculate the convective heat transfer coefficient when the temperature distribution in the fluid near the wall is known:

$$h = \frac{-\lambda \left.\frac{\partial T}{\partial y}\right|_{y=0}}{T_0 - T_\infty} \qquad \text{II - 6}$$

To summarize the questions of friction and thermal resistance, boil down to carrying out the calculations dictated by eqs. II - 1 and II - 2. However, eqs. II - 3 and II - 5 demonstrate that to be able to calculate F and q, we must first determine the flow and temperature fields in the vicinity of the solid wall. Thus, it is the demand for F and q that leads to the mathematical problem of solving for the flow (u, v) and temperature (T) in the fluid space outlined in Figure 1.With the assumption of incompressible flow, constant fluid properties and stationary laminar flow, the complete 2D mathematical statement of this problem consists of the following four equations:

$$\frac{\partial u}{\partial x}+\frac{\partial v}{\partial y}=0 \qquad \text{II - 7}$$

$$u\frac{\partial u}{\partial x}+v\frac{\partial u}{\partial y}=-\frac{1}{\rho}\frac{\partial P}{\partial x}+\nu\left(\frac{\partial^2 u}{\partial x_2}+\frac{\partial^2 u}{\partial y_2}\right) \qquad \text{II - 8}$$

$$u\frac{\partial v}{\partial x}+v\frac{\partial v}{\partial y}=-\frac{1}{\rho}\frac{\partial P}{\partial y}+\nu\left(\frac{\partial^2 v}{\partial x_2}+\frac{\partial^2 v}{\partial y_2}\right) \qquad \text{II - 9}$$

$$u\frac{\partial T}{\partial x}+v\frac{\partial T}{\partial y}=+\alpha\left(\frac{\partial^2 T}{\partial x_2}+\frac{\partial^2 T}{\partial y_2}\right) \qquad \text{II - 10}$$

Where $\nu=\mu/\rho$ is the kinematic viscosity of the flow and $\alpha=\frac{\lambda}{\rho c_p}$ is the thermal diffusivity of the flow. The four unknowns (u, v, P, T) are subjected to the following boundary conditions:

$$\text{At the solid wall}\begin{cases}u=0 & \text{i. No slip}\\ v=0 & \text{ii. Impermeability}\\ T=T_0 & \text{iii. Wall temperature}\end{cases}$$

$$\text{Infinitely far from the solid}\begin{cases}u=U_\infty & \text{iv. Uniform flow}\\ v=0 & \text{v. Uniform flow}\\ T=T_\infty & \text{vi. Uniform temperature}\end{cases} \qquad \text{II - 11}$$

The nonlinear partial differential problem stated as eqs. II - 7 ÷ II - 11 has served as one of the central stimuli in the development of the field of applied mathematics during the past 200 years. The most remarkable feature of this problem is that despite all this time and effort, it has not been solved. It is this feature that makes the boundary layer idea so special: referring to Figure 1 and the complete problem statement II - 7 ÷ II - 11, we have the freedom to think that the velocity change from u = 0 to u = U_∞ and the temperature change from T = T_0 to T = T_∞ occur in a space situated relatively close to the solid wall.

A revolutionary hypothesis has been taken by Prandtl in thinking of the region close to the wall (the boundary layer) as a region distinct from the immense domain, in which the unsolvable mathematical problem II - 7 ÷ II - 11 was formulated by his contemporaries. Prandtl's decision is equivalent to carving out of the entire flow field only that region that is truly relevant to answering the questions formulated in the preceding section. Outside the boundary layer, he imagines a free stream, that is, a flow region not affected by the obstruction and heating effect introduced by the solid object. The free stream is characterized by the boundary conditions in equation II - 11.

Such kind of hypothesis allows to simplify the problem stated in eqs. II - 7 ÷ II - 11: let δ be the order of magnitude of the distance in which u changes from 0 at the wall to roughly U_∞ in the free stream. Thus, in the space of height δ and length L in Figure 1, we identify the following scales for changes in x, y, and u:

$$x \sim L, \quad y \sim \delta, \quad u \sim U_\infty \qquad \text{II - 12}$$

In the δ × L region, then, the longitudinal momentum equation II - 8 accounts for the competition between three types of forces:

$$\begin{array}{ccccc} \multicolumn{2}{c}{\text{Inertia}} & \text{Pressure} & \multicolumn{2}{c}{\text{Friction}} \\ U_\infty \dfrac{U_\infty}{L} & v\dfrac{U_\infty}{\delta} & \dfrac{P}{\rho L} & \nu\dfrac{U_\infty}{L^2} & \nu\dfrac{U_\infty}{\delta^2} \end{array} \qquad \text{II - 13}$$

Since the mass continuity equation II - 7 requires that $\frac{U_\infty}{L} \sim \frac{v}{\delta}$ we learn that the inertia terms in the previous equation are both of order $\frac{U_\infty^2}{L}$; hence, neither can be neglected at the expense of the other. Next, if the boundary layer region could be supposed to be slender, such that

$$\delta \ll L \qquad \text{II - 14}$$

then the last scale in eq. II - 13 is the scale most representative of the friction force in that region leading to the following simplified equations:

$$u\frac{\partial u}{\partial x} + v\frac{\partial u}{\partial y} = -\frac{1}{\rho}\frac{\partial P}{\partial x} + \nu\frac{\partial^2 u}{\partial y_2} \qquad \text{II - 15}$$

$$u\frac{\partial v}{\partial x} + v\frac{\partial v}{\partial y} = -\frac{1}{\rho}\frac{\partial P}{\partial y} + \nu\frac{\partial^2 v}{\partial y_2} \qquad \text{II - 16}$$

Assuming several hypotheses on the pressure field, which we not detail (particular could be found at page 36 of [13]), the pressure could be supposed to vary chiefly in the longitudinal direction; in other words, at any *x*, the pressure inside the boundary layer region is practically the same as the pressure immediately outside it,

$$\frac{\partial P}{\partial x} = \frac{dP_\infty}{dx} \qquad \text{II - 17}$$

Making this last substitution in the x momentum equation II - 15 we finally obtain:

$$u\frac{\partial u}{\partial x} + v\frac{\partial u}{\partial y} = -\frac{1}{\rho}\frac{dP_\infty}{dx} + \nu\frac{\partial^2 u}{\partial y_2} \qquad \text{II - 18}$$

The boundary layer equation for energy follows from eq. II - 10 where we neglect the term accounting for thermal diffusion in the x direction,

$$u\frac{\partial T}{\partial x} + v\frac{\partial T}{\partial y} = +\alpha\frac{\partial^2 T}{\partial y_2} \qquad \text{II - 19}$$

With this statement, we finish rewriting the original flow and heat transfer problem (eqs. II - 7 ÷ II - 11) in the language of boundary layer theory. Only three equations have to be solved for three unknowns (u, v, T). In addition, the disappearance of the $\frac{\partial^2}{\partial x_2}$ diffusion terms from the momentum and energy equations makes this new problem solvable in a variety of ways such as the integral or scale analysis methods. The first one, through some hypothesis integrates the governing equations in the boundary layer to find a precise solution, the second one compares the order of magnitude of each term in the equations to find the most important and simplify the problem. Since, our purpose is to qualitatively analyze the problem in the following lines we are going to detail the *scale analysis* method.

As previously supposed, let δ be the thickness of the region in which u varies from 0 at the wall to U_∞ in the free stream, and, let δ_T be the thickness of another slender region super imposed on the first in which T varies from T_0 at the wall to T_∞ in the free stream. Keeping up with tradition, we refer to δ and δ_T as the velocity boundary layer thickness and the thermal boundary layer thickness, respectively.

In scaling terms, the flow friction question II - 3 becomes

$$\tau \sim \mu \frac{U_\infty}{\delta} \qquad \text{II - 20}$$

Thus, to estimate the wall frictional shear stress, we must evaluate the extent δ of this imaginary slender wall region. Assuming a fully developed hypothesis for the cinematic field, according to $\frac{dP_\infty}{dx} = 0$ the boundary layer momentum equation implies that:

$$U_\infty \frac{U_\infty}{L}, v \frac{U_\infty}{\delta} \sim \frac{U_\infty}{\delta^2} \qquad \text{II - 21}$$

Referring once again to the mass continuity scaling $\frac{U_\infty}{L} \sim \frac{v}{\delta}$ we conclude that the two inertia terms are of the same order of magnitude. Therefore, eq. II - 21 requires that

$$\delta \sim \left(\frac{vL}{U_\infty}\right)^{1/2} \qquad \text{II - 22}$$

Introducing the Reynolds number $Re_L = \frac{U_\infty L}{v}$, based on the longitudinal dimension of the boundary layer region, which is representative of the weight of the inertia force on the viscous one we lead to the following statement:

$$\frac{\delta}{L} \sim (Re_L)^{-1/2} \qquad \text{II - 23}$$

Previous equation is a test of whether a given external flow situation lends itself to boundary layer analysis, as Re_L can easily be calculated beforehand, and even when $Re_L^{1/2} \gg 1$ it can be used to assess the limitations of the boundary layer analysis.

The heat transfer question II - 19 is answered by focusing on the thermal boundary layer of thickness δ_T,

$$h \sim \frac{\lambda}{\Delta T} \qquad \text{II - 24}$$

Where $\Delta T = T_0 - T_\infty$. The boundary layer energy equation II - 19 states that there is always a balance between conduction from the wall into the stream and convection (enthalpy flow) parallel to the wall:

$$convection \sim conduction$$

$$u\frac{\Delta T}{L}, v\frac{\Delta T}{\delta_T} \sim \frac{\alpha \Delta T}{\delta_T^2} \qquad \text{II - 25}$$

The δ_T scale could be determined as following; for a flow with a Prantdl number inferior to one, it could be assumed a thick thermal boundary layer $\delta_T \gg \delta$ (details for the reader page 40 of [13]). With this assumption, and according to $\frac{U_\infty}{L} \sim \frac{v}{\delta}$ the left side of equation II - 25 is of order

$$v\frac{\Delta T}{\delta_T} \sim U_\infty \frac{\Delta T}{L}\frac{\delta}{\delta_T} \qquad \text{II - 26}$$

In which $\frac{\delta}{\delta_T} \ll 1$, it means that the term $v\frac{\Delta T}{\delta_T}$ is $\frac{\delta}{\delta_T}$ times smaller than the $u\frac{\Delta T}{L}$, suggesting that the entire left side of the equation II - 25 is dominated by the scale $U_\infty \frac{\Delta T}{L}$. Finally rewriting the equation II - 25 we obtain:

$$\frac{\delta_T}{L} \sim Pr^{-1/2} Re_L^{-1/2} \qquad \text{II - 27}$$

Then the convective heat transfer coefficient is:

$$h \sim \frac{\lambda}{L} Pr^{1/2} Re_L^{1/2} \qquad \text{II - 28}$$

Or, expressed as a Nusselt number:

$$Nu = \frac{hL}{\lambda} \qquad \text{II - 29}$$

Where L is a characteristic length of the geometry, in this case is the axial length of the flat plat.

$$Nu \sim Pr^{1/2} Re_L^{1/2} \qquad \text{II - 30}$$

The previous equation is very important, it states the heat transfer problem: the Nusselt number, which is the ratio between the convection and the conduction heat exchanges, is proportional to the product of the Prandtl and Reynolds number. It means that the convective heat transfers are dependent from the fluid properties (Prantdl number) and from the flow properties such as the cinematic field. Some exact solutions, as in chapter 2.4 of [13], are available in literature, otherwise, several correlations have been fitted to experimental results. An exhaustive reviews of such correlation is available in [14].

For a turbulent boundary layer flow, characterized by a Reynolds number higher than 3.5E^5 suggesting that the inertia forces are widely higher than the viscous stress, the heat transfer problem approach remains unchanged: to know the convective heat transfer between the flow and a solid wall equation II - 5 has to be computed by knowing the temperature profile to calculate the convective heat transfer coefficient in II - 6.

To account for the turbulent behavior of the flow in the governing equation, the concept of the *Reynolds decomposition and averaging* of the instantaneous local flow properties has been applied. Leaving the details for the reader in ref. [15], we can affirmed that because of the turbulent motions associated with the turbulent eddies are approximately random and because of the local instantaneous governing equations cannot be solved for all the length scale of the flow due to computational power limits, statistical concepts could be applied to overcome the cited problems.

Confronted with this difficulty, historically Reynolds [16] was the first that thought that some of the complications of instantaneous turbulent flow could be removed if one considers not the instantaneous behavior, but the time-mean behavior averaged over a long enough period. In terms of mean velocities, pressure, and temperature, the time-averaged flow field is a simpler one, a field without fluctuations (eddies). The time-averaged flow behavior is not a simpler flow (because only the real turbulent flow exists); rather, it is a simpler way to think about turbulent flows.

The derivation of the conservation laws for time-averaged flow begins with the transformation according to each of the flow property could be decomposed as following:

$$Z = \bar{Z} + Z' \qquad \text{II - 31}$$

Where $\bar{Z}$ is the time-average component and Z' represents the turbulent instantaneous fluctuations.

The time-average component is obtained by averaging the quantity Z over a large enough period as following:

$$\bar{Z} = \frac{1}{period}\int_0^{period} Zdt \qquad \text{II - 32}$$

Combining the eqs. II - 31, II - 32 we recognize, by definition that the fluctuating component averages to zero over time:

$$\frac{1}{period}\int_0^{period} Z'dt = 0 \qquad \text{II - 33}$$

From the previous equations, a special kind of algebra emerges about the properties of the time-averaging operators as the linearity and the independency from other operators such as the derivation.

Combining the equation II - 18, II - 19 and the Reynolds decomposition, applying the time-averaging as in equation II - 32 and neglecting inferior scale terms we obtain for the boundary layer the equations of momentum and energy:

$$\bar{u}\frac{\partial \bar{u}}{\partial x} + \bar{v}\frac{\partial \bar{u}}{\partial y} = -\frac{1}{\rho}\frac{d\bar{P}_\infty}{dx} + \frac{1}{\rho}\frac{\partial}{\partial y}\left(\mu\frac{\partial \bar{u}}{\partial y} - \rho\overline{u'v'}\right) \qquad \text{II - 34}$$

$$\bar{u}\frac{\partial \bar{T}}{\partial x} + \bar{v}\frac{\partial \bar{T}}{\partial y} = \frac{1}{\rho c_p}\frac{\partial}{\partial y}\left(\lambda\frac{\partial \bar{T}}{\partial y} - \rho c_p\overline{v'T'}\right) \qquad \text{II - 35}$$

Comparing eqs. II - 18, II - 19 and II - 34, II - 35 we note the apparition of the two terms $\rho\overline{u'v'}$ and $\rho c_p\overline{v'T'}$ because of the turbulent behaviour of the flow, and, they represents the eddy shear stress and the eddy heat flux due to the turbulence. Such terms appear into the time-average equations to account for the information lost that it should exist because of the time-averaging process, in other terms, they represent the time-average contribution of the turbulence on the momentum and energy balance equations.

Turbulence modelling challenge through the past years has been to search for additional information to close the problem in eqs. II - 34, II - 35, or rather to found a way to model turbulence term and then be able to solve balance equations. This empirical activity consists of scrutinizing the available body of experimental data in order to identify possible trends that might lead to generally applicable expressions for the additional terms.

Focusing on the heat transfer part of the turbulent boundary layer problem, we use the time-averaged energy equation II - 35: making the assumption that sufficiently close to the solid wall the left-hand side of eq. II - 35 becomes negligible, the energy equation reduces to the statement that sufficiently close to the wall the apparent heat flux q'' does not depend on y:

$$\alpha\left(\frac{\partial \bar{T}}{\partial y} - \overline{v'T'}\right)\bigg|_0 = -\frac{q''}{\rho c_p} \qquad 0 - 36$$

As expressed by the previous equation, conductive heat transfer in the last slice of the flow, which is in no-slip condition at the wall, is increased by the turbulent term $\overline{v'T'}$.

Without detailing all the mathematical steps, the scale analysis applied to the eq. II - 35 allows to lead to a Nusselt correlation form (pages 338-341 in [13]) similar to the laminar case in eq. II - 30. We report the time-average Nusselt correlation for a flat plate flow for a $Pr \geq 0.5$:

$$\overline{Nu_L} = 0.037 Re_L^{4/5} Pr^{1/3} \qquad 0 - 37$$

It is important to remind that an important acquired hypothesis, which allows to lead to the previous equation, consists always into consider the flow cinematically and thermally fully-developed, in order to neglect the axial gradient of the flow properties. As for the laminar flow case, also for the turbulent flow several experimental correlations for the time-average Nusselt number are available in literature, furthermore, some of these account for some secondary effects such as the fluid properties variation due to temperature change.

Anyway, because of reviewing all the available correlations in literature does not represent the main purpose of this part of the chapter, they are not detailed.

II.2.2 Turbulent pipe flows

The time-averaged analysis of friction and heat transfer in turbulent pipe flow involves many of the assumptions made in the presentation of the turbulent boundary layer problem (Chapter II.2.1). To avoid repetition, only the differences are reported.

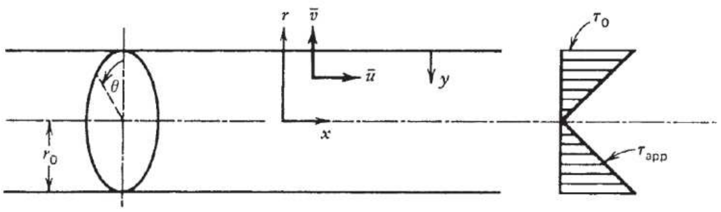

Figure 2: Distribution of apparent shear stress in fully developed turbulent flow in a pipe

Consider turbulent flow through the round tube sketched in Figure 2. The time-averaged equations for mass, momentum, and energy are respectively:

$$\frac{\partial \bar{u}}{\partial x} + \frac{1}{r}\frac{\partial (r\bar{v})}{\partial r} = 0 \qquad \text{II - 38}$$

$$\bar{u}\frac{\partial \bar{u}}{\partial x} + \bar{v}\frac{\partial \bar{u}}{\partial r} = -\frac{1}{\rho}\frac{d\bar{P}_\infty}{dx} + \frac{1}{r}\frac{\partial}{\partial r}\left(r(\nu + \varepsilon_M)\frac{\partial \bar{u}}{\partial r}\right) \qquad \text{II - 39}$$

$$\bar{u}\frac{\partial \bar{T}}{\partial x} + \bar{v}\frac{\partial \bar{T}}{\partial r} = \frac{1}{r}\frac{\partial}{\partial r}\left(r(\alpha + \varepsilon_H)\frac{\partial \bar{T}}{\partial r}\right) \qquad \text{II - 40}$$

Where ε_M and ε_H are two empirical functions known as momentum eddy diffusivity and thermal eddy diffusivity, note that they are flow parameters and not fluid properties.

Previous equations have already been simplified based on the boundary layer arguments of the type employed in Chapter II.2.1, as well as the hypothesis of fully developed field has been assumed. It has been experimentally observed that the flow becomes hydrodynamically and thermally fully developed after a relatively short distance from the entrance to the tube $\frac{X_T}{D} \cong 10$, in the laminar case such distance is higher, anyway, some experimental correlations exist to validate the fully developed hypothesis.

It could be observed that the equations II - 38 ÷ II - 40 have a similar form in comparison to the boundary layer case (eqs. II - 34, II - 35); the thermal and friction problem could be treated in the same manner. By a scale analysis is possible to lead to a Nusselt number formula (Colburn [17] correlation for a pipe with smooth internal surface and a $2E^4 < Re_D < E^6$):

$$Nu_D = \frac{hD}{\lambda} = 0.023 Re_D^{4/5} Pr^{1/3} \qquad \text{II - 41}$$

In such case the geometric length scale, which was 'L' in the case of the flat plate, is the pipe diameter 'D'. There are many formulas that in one way or another improve on the accuracy with which eq. II - 41 predicts actual measurements. The most popular formula is a correlation of Dittus and Boelter:

$$Nu_D = \frac{hD}{\lambda} = 0.023 Re_D^{4/5} Pr^{n} \qquad \text{II - 42}$$

Which was developed for $0.7 \leq Pr \leq 120$, $2500 \leq Re_D \leq 1.24E^5$, and $L/D > 60$. The Prandtl number exponent is $n = 0.4$ when the fluid is being heated ($T_0 > T_b$), and $n = 0.3$ when the fluid is being cooled ($T_0 < T_b$). All the physical properties needed for the calculation of Nu_D, Re_D, and Pr have to be evaluated at the bulk temperature T_b.

Correction of the previous correlation to account for temperature effect on the fluid properties, such as the Gnielinski correlation, could be found at page 379 of [13].

From what has been presented in the previous lines, it could be concluded that as well for a boundary layer flow also for a turbulent steady flow, assuming the hypothesis of fully developed flow, the governing equations could be simplified, and the convective heat transfers could be predicted by a Nusselt number correlation with a time-averaged assumption. Several correlation accounting for turbulence phenomena are available in literature for different flows and geometries such as flat plate or pipe flows.

In the following paragraph the flow pulsation will be introduced in the in the definition of the governing equations, in order to treat the heat transfer problem for a turbulent pulsating pipe flow.

The main purpose is to verify if the hypotheses assumed for a turbulent boundary or pipe steady flow could be still kept in consideration, as well as they will be revised in order to figure out their limits.

II.2.3 Pulsating & Turbulent pipe flows

A pulsating flow, either in laminar or turbulent conditions, is a particular flow which belongs to the cycle-stationary category flows. In practice, although such class of flows are non-stationary in time, they could be decomposed in a time-average component plus a coherent pattern which is cyclically repeated in time, allowing to be able to extract some coherent phenomena of the flow physics.

In details, as proposed by Reynolds et al. [18], in the specific case of a turbulent pulsating flow each of the flow properties may be decomposed in three different terms, as expressed in the following equation:

$$Z = \bar{Z} + \tilde{Z} + Z' \qquad \text{II - 43}$$

Where $\bar{Z}$ represents the time-average component, $\tilde{Z}$ is the oscillating term of the coherent cycle-stationary pattern and Z' corresponds to the turbulent fluctuations term.

Time-averaging determines $\bar{Z}$ and the phase-average (< >), i.e. the average over a large ensemble of points having the same phase with respect to a reference oscillator, leads to:

$$< Z >= \bar{Z} + \tilde{Z} = \lim_{N\to\infty} \frac{1}{N} \sum_{n=0}^{N} Z(t + n\tau) \qquad \text{II - 44}$$

Actually, the phase-averaging process rejects the background turbulence and extracts only the organized motions from the total instantaneous profile. For the sake of brevity some useful mathematical properties that follow from the basic definitions of the time and phase averages are not reported, they are detailed in the reference [18].

The 2D instantaneous local governing equations for an incompressible pipe flow, without assuming the boundary layer hypotheses (radial spatial gradient are not a-priori neglected), are:

$$\frac{\partial u}{\partial x} + \frac{1}{r}\frac{\partial (rv)}{\partial r} = 0 \qquad \text{II - 45}$$

$$\rho\left(\frac{\partial v}{\partial t} + u\frac{\partial v}{\partial x} + v\frac{\partial v}{\partial r}\right) = -\frac{\partial p}{\partial r} + \mu\left(\frac{\partial^2 v}{\partial r^2} + \frac{1}{r}\frac{\partial v}{\partial r} - \frac{v}{r^2} + \frac{\partial^2 v}{\partial x^2}\right) \qquad \text{II - 46}$$

$$\rho\left(\frac{\partial u}{\partial t} + u\frac{\partial u}{\partial x} + v\frac{\partial u}{\partial r}\right) = -\frac{\partial p}{\partial x} + \mu\left(\frac{\partial^2 u}{\partial r^2} + \frac{1}{r}\frac{\partial u}{\partial r} + \frac{\partial^2 u}{\partial x^2}\right) \qquad \text{II - 47}$$

$$\rho c_p\left(\frac{\partial T}{\partial t} + u\frac{\partial T}{\partial x} + v\frac{\partial T}{\partial r}\right) = \lambda\left(\frac{1}{r}\frac{\partial}{\partial r}\left(r\frac{\partial T}{\partial r}\right) + \frac{\partial^2 T}{\partial x^2}\right) \qquad \text{II - 48}$$

Considering the triple-decomposition in equation II - 43, the previous governing equations, and the possibility to apply both the time- and space- averaging increases the simplification levels of the heat transfer problem.

If studied with a phase-average assumption the variation of the flow properties within the averaged pulsation cycle could be found by solving the governing equations in which the time-dependent terms still exist. Differently, with a time-average assumption, according which the governing equation are averaged over a period enough large compared to the pulsation period, the governing equations are furtherly simplified, and only the large scale phenomena are solved.

Introducing the equation II - 43 in eqs. II - 45 ÷ II - 48 and phase-averaging the resulting equation, leads to the 2D local phase-averaged governing equations, following reported:

$$\rho\left(\frac{\partial v}{\partial t}+u\frac{\partial v}{\partial x}+v\frac{\partial v}{\partial r}+\frac{\partial < u'v' >}{\partial x}+\frac{\partial < v'v' >}{\partial r}\right) = -\frac{\partial p}{\partial r}+\mu\left(\frac{\partial^2 v}{\partial r^2}+\frac{1}{r}\frac{\partial v}{\partial r}-\frac{v}{r^2}+\frac{\partial^2 v}{\partial x^2}\right) \qquad \text{II - 49}$$

$$\rho\left(\frac{\partial u}{\partial t}+u\frac{\partial u}{\partial x}+v\frac{\partial u}{\partial r}+\frac{\partial < u'u' >}{\partial x}+\frac{\partial < u'v' >}{\partial r}\right) = -\frac{\partial p}{\partial x}+\mu\left(\frac{\partial^2 u}{\partial r^2}+\frac{1}{r}\frac{\partial u}{\partial r}+\frac{\partial^2 u}{\partial x^2}\right) \qquad \text{II - 50}$$

$$\rho c_p\left(\frac{\partial T}{\partial t}+u\frac{\partial T}{\partial x}+v\frac{\partial T}{\partial r}+\frac{\partial < u'T' >}{\partial x}+\frac{\partial < v'T' >}{\partial r}\right) = \lambda\left(\frac{1}{r}\frac{\partial}{\partial r}\left(r\frac{\partial T}{\partial r}\right)+\frac{\partial^2 T}{\partial x^2}\right) \qquad \text{II - 51}$$

For a simplification of the notation in the eqs. II - 49 ÷ II - 51 the unknowns u, v, T, p correspond to the phase-average term of the instantaneous quantities as in equation II - 44.

To know the heat transfer coefficient, function of the time and space, the energy balance equation should be solved, and then the equation II - 5 should be applied.

Nowadays the equations II - 49 ÷ II - 51 are considered as Unsteady-Reynolds Averaged Navies-Stokes equations, the turbulent terms appearing in the governing equations although are theoretically different to the steady case (eqs. II - 39, II - 40), they are modeled in the same manner.

Nevertheless, some questions are still unanswered to be able to apply them in a pulsating case: Does the pulsation impact the turbulent behavior of the flow? Otherwise, could the simplification hypotheses, assumed in the boundary layer theory, be assumed also for a pulsating flow?

An exhaustive review of the presents state of art on the pulsatile flow theory for laminar, transitional and turbulent flow regimes is available in [19], [20]. Authors conclude that several aspect of the turbulent pulsating flow such as the development length required to obtain the fully developed turbulent flow, the characteristic turbulent bursting frequency, the interaction between the pulsation and the turbulence structures within the Stokes layer have still to be clarified.

Focusing on the heat transfer problem of equation II - 51, it could be affirmed that it represents the following scales comparison:

$$time - variation \sim convection + turbulence \sim conduction$$

$$\frac{\Delta T}{period} \quad \sim \quad u\frac{\Delta T}{L}, v\frac{\Delta T}{\delta_T} + u'\frac{T'}{L}, v'\frac{T'}{\delta_T} \quad \sim \quad \frac{\alpha \Delta T}{\delta_T^2}, \frac{\alpha \Delta T}{L^2} \qquad \text{II - 52}$$

In addition to convection and conduction also the time-variation and the turbulence scales have to be considered to impact the heat transfers: if, for example, the pulsation frequency is high enough that the $period \gg L/\bar{u}$, the time-variation term in the left side of eq. II - 51 may have the same order of magnitude of the axial energy advection and thus should not be neglected. In a similar manner, the radial convection scale term could not be a priori neglected.

To simplify the problem resolution the equation II - 51 could be integrated over a period enough large in comparison to the pulsation period, in order to erase the time-dependent term in the phase-average energy balance equation. It leads to:

$$\rho c_p\left(\bar{u}\frac{\partial \bar{T}}{\partial x}+\bar{v}\frac{\partial \bar{T}}{\partial r}+\frac{\partial \overline{\tilde{u}\tilde{T}}}{\partial x}+\frac{\partial \overline{\tilde{v}\tilde{T}}}{\partial r}+\frac{\partial \overline{<u'T'>}}{\partial x}+\frac{\partial \overline{<v'T'>}}{\partial r}\right) = \lambda\left(\frac{1}{r}\frac{\partial}{\partial r}\left(r\frac{\partial \bar{T}}{\partial r}\right)+\frac{\partial^2 \bar{T}}{\partial x^2}\right) \qquad \text{II - 53}$$

Comparing the eqs. II - 40 and II - 53 it could be noted that in addition to the turbulent terms which cannot be a-priori considered equal to the steady case, the time-average effects of the flow pulsation are represented by the terms $\frac{\partial \overline{\tilde{u}\tilde{T}}}{\partial x}, \frac{\partial \overline{\tilde{v}\tilde{T}}}{\partial r}$. They represents the time-averaged contribution of the cross-product of the oscillating components of the air velocity and temperature.

The prediction of such terms could not be done a-priori and an analytical solution doesn't exist, furthermore, since these terms cannot be neglected, the Nusselt number correlation form for the steady turbulent pipe flow remains not-adapted for a pulsating case.

As proposed by Kearney et al. [21] a Buckingham Π analysis shows that the local time-average Nusselt number in a low-speed, wall-bounded laminar flow may depend on as many as seven dimensionless groups:

$$\overline{Nu} = f\left(\frac{\Delta < u >}{\bar{u}}, \frac{U_0}{\omega D}, \frac{c}{\omega D}, Wo, Gz_T, Re, Pr\right) \qquad \text{II - 54}$$

Additional parameters arise because of the flow pulsation:

- The Womersley number $Wo = \sqrt{\frac{\rho\omega D^2}{\mu}}$, which is a ratio of the channel height to the Stokes boundary-layer thickness. It is a dimensionless expression of the pulsatile flow frequency in relation to viscous effects.
- The amplitude ratio $\frac{\Delta<u>}{\bar{u}}$, which is a measure of the amplitude of the velocity waveform, as mentioned earlier in this study.
- The parameter $\frac{U_0}{\omega D}$, which represents the relative magnitudes of the Lagrangian and convective accelerations and dictates the importance of ''acoustic streaming''. This term has been investigated in the works of Jackson et al. [22]: U_0 represents the Lagrangian velocity generated from the acoustic streaming which is generally calculated from the acoustic theory for a plane wave propagation.
- The grouping $\frac{c}{\omega D}$ which is a measure of the wavelength of the applied pressure oscillation to the relevant streamwise length scale (c is the velocity of sound).

A parametric study of the impact of each of the term in eq. II - 54 on the time-average Nusselt number is not available in the literature, as the bibliography studies survey in the following paragraph demonstrates.

II.3 State of arts

In the previous paragraph the fundamentals of the heat transfer problem have been analyzed for a pulsating turbulent pipe flow. Starting from the easy flat plate case, the hypotheses which lead to a Nusselt correlation have been discussed. The pulsating effects on the governing equations have been pointed out by introducing the triple decomposition of equation II - 43, being oble to evidence the limits of the stationary case assumption.

In the following lines the previous works on study of the heat transfer problem for pulsating flows are revised and discussed, to finally show, in the last paragraph of this chapter, the thesis strategy and contribution which it can have to the comprehension of the convective heat transfer phenomena for turbulent pulsating flows.

Widespread studies have been allocated to pulsating flows and their associated heat transfer problems over the past decades, however, some available results are contradictory and the main question is still open: Does pulsation enhance or else degrade heat transfer compared to steady flow.

Martinelli et al. [23] initiated their works on heat transfers already in 1943, they conducted the experiments for a pulsating turbulent flow in a vertical tube under uniform wall temperature boundary condition. The results showed that heat transfer reduced for pulsatile flow compared to steady flow at Reynolds numbers greater than 4500 and increased at Reynolds number less than 4500.

In the following years, such interest did not lose its intensity, several researchers studied pulsating flows in many experimental configurations such as pulse combustor tail pipes, turbulent or laminar pulsating pipe flows, heat exchangers and ICEs. This variety of the experimental configurations has led to contradictory results, most of the previous investigators considered a small number of the operating variables, usually confining their studies to a relatively narrow domain. In the following paragraphs these studies and their contribution to the understanding of the heat transfer phenomena will be detailed and discussed.

II.3.1 Heat transfers in pulse combustor tail pipes

The need for highly efficient combustion systems has led to active research in pulse combustion, furthermore, a high rate of convective heat transfer in the tail pipe has always represented another commonly advantage of such technology.

Dec et al. [24], [25] studied the influence of pulsation frequency, amplitude and mean flow rate on the heat transfers for a pulse combustor tail pipe, depicted in the following figure:

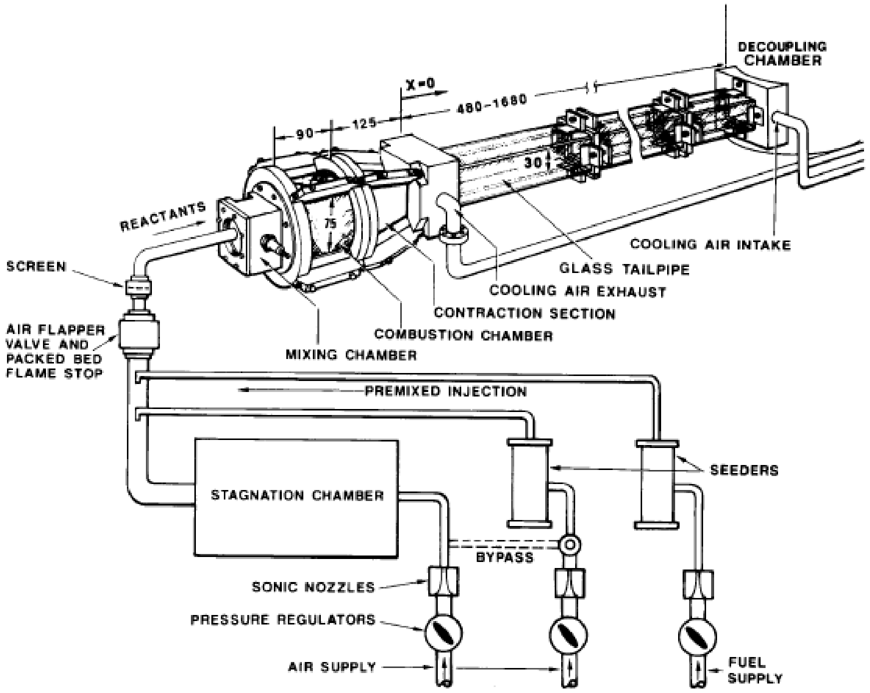

Figure 3: Schematic of the pulse combustor facility – Dec et al.

This combustor consists of an axisymmetric injection or "mixing" chamber, and square cross-section combustion chamber, contraction section, and tail pipe. Acoustic termination for the tail pipe was provided by a large-volume (0.031 m^3) decoupling chamber.

The tail pipe consisted of a coaxial square Pyrex tube arrangement, as shown in the Figure 3. In this arrangement, the inner tube, which was 30 mm square with a wall thickness of 4.75 ram, formed the resonance tube for the pulse combustor and carried the combustion products. The outer tube was 51 mm square, which provided a 5.75 mm wide channel between the tubes on all four sides. Cooling air flowed through this square annular space between the inner and outer tubes, entering at the decoupler end of the tail pipe and exiting at the contraction section end.

The tail pipe was constructed in a modular fashion, allowing its length to be varied in 200 mm increments from 680 to 1680 mm, to obtain operating frequencies from 101 to 54 Hz respectively.

Combustor frequencies, and then pulsation frequencies, were varied by changing the natural resonance frequency through variations in the tail pipe length, and subsequent adjustment of the timing of the energy release rate. The timing of the energy release rate for this premixed system is controlled by the mixing rate of the reactants with the hot products and the chemical reaction rate. By adjusting these two processes, the energy release was optimally timed for each natural resonance frequency, providing a maximum pulsation amplitude. Pulsation amplitudes were then decreased from this maximum by detuning the timing of the energy release through the addition of various amounts of nitrogen diluent to the reactants.

Pulsation frequency was varied from 67 to 100 Hz, for a Reynolds number based on the time average velocity varying between 3100 and 4750.

It is worth to cite the advanced diagnostics which were used to measure instantaneous radial profile of air velocity and temperature. Pressure transducers, laser Doppler velocimetry (LDV), and thermocouples were the diagnostics used in the study. Pressure transducers were used to determine the combustor frequency and to measure the combustion chamber pressure. The root mean square about the mean of the combustion chamber pressure (P_{rms}) was used as a measure of pulsation amplitude. LDV was used to measure a typical oscillating gas velocity in the tail pipe. Further, spatially and temporally resolved gas temperature measurements were made using TLAF. Axially resolved measurements were made using two movable test sections, which were 200 mm long. One test section had an access port that allowed a thermocouple to be inserted into the exhaust gas at the axial center of the test section. The second test section was equipped with a thin-film thermocouple, vacuum deposited on the exhaust gas side surface of the inner tube, to measure wall temperature and wall heat flux. A second thermocouple was imbedded in the wall directly opposite the junction of the thin film thermocouple.

Time-resolved velocities [26] and temperatures [27] were analysed to describe the heat transfer enhancement mechanism. A characteristic phase-average temperature and heat flux measurement from this study is showed in Figure 4 while the velocity and pressure profiles are showed in Figure 5:

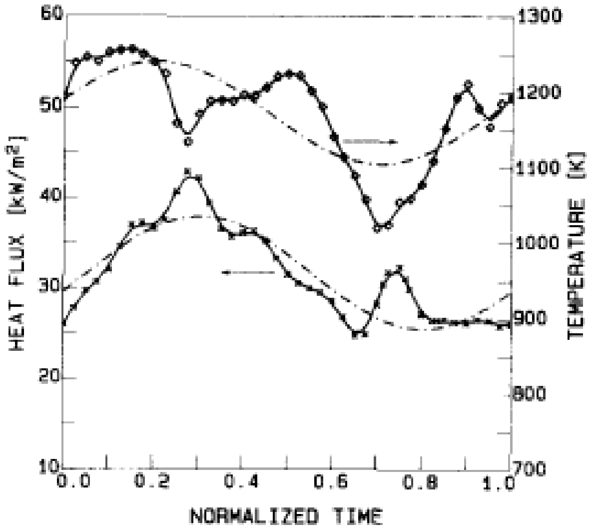

Figure 4: Tail pipe centerline temperature & wall heat flux oscillations

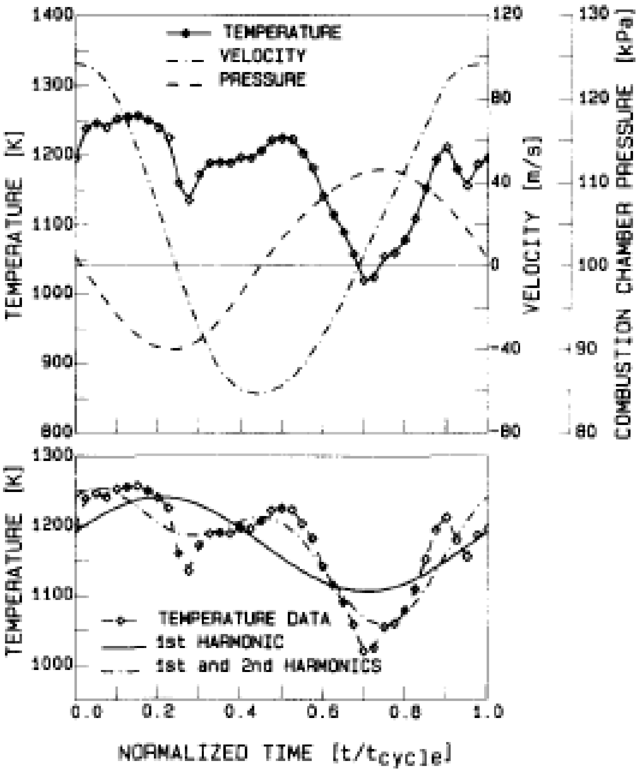

Figure 5: Gas Temperature & Velocity at the tail pipe centerline and the combustion chamber pressure

Results, in the previous figures, show that two features are present in this temperature field, although the detailed structure varies with operating condition authors said. First, there is a fundamental oscillation at the combustor frequency, which is 90 degrees out-of-phase with the velocity and 180 degrees out-of-phase with the pressure. Second, superimposed on this oscillation are two dips (temporal locations of 0.25 and 0.7) in the temperature which slightly phase-lag the zero-velocity crossings. Such dips correspond to a peak in the heat flux. Such phenomenon has been observed for all the pulsation frequencies once the flow reversal appears. Time-resolved Nusselt numbers were then calculated from time-resolved gas temperatures and time-resolved heat flux data. The Nusselt number was found to be nearly constant over most of the cycle with large increases twice each cycle, at times of flow reversal.

Although further results show that there are variations in the nature of the thermal boundary layer, the thermal boundary layer is well developed throughout all the cycle. Thus, the hypothesis that the increased heat transfer results from the thermal boundary layer being periodically broken down by the flow oscillations were not valid.

Several mechanisms responsible for the heat transfer enhancement in reversing, oscillating turbulent flows were presented and discussed from the authors. Among those the acoustic streaming, the entrance effects and the turbulence intensity increase were revised. According to the authors as well for the acoustic streaming, which corresponds to the apparition of a secondary time-average velocity component having the form of large longitudinal recirculation cells, as well for the entrance effects, their influences were smalls and not important in the observed Nusselt number enhancement.

Contrarily, authors supposed that the turbulence intensity may be the main mechanism for momentum transport in this oscillating flow: time-averages of the wall shear stress was found to increase with pulsation magnitude, but to have no variation with frequency. Finally, authors claimed that the increased turbulence intensity undoubtedly contributed to the Nusselt number enhancement; however, there must be another contributor, which increased the heat transfer with frequency, but did not affect the wall shear stress. The results suggested that a combination of increased shear-layer generated turbulence, and, strong convection at the zero-velocity crossings by transverse flows were the best explanation for the mechanisms causing the observed heat transfer enhancement during flow reversal. However, the fluid mechanics responsible for the additional convective transport during the flow reversal were not fully understood.

Although, the results of Dec et al. are very interesting since show a phase- and time- average analysis of the heat transfer problem, it is worth to underline that the different nature of the pulse combustor pulsating flow makes such result hardly comparable with a pulsating pipe flow of engine exhaust. Contrarily to a pulse combustor flow, which is always in a resonance state i.e. it is excited with a frequency equal to the resonance frequency of the system, the pulsating flow of an engine exhaust is mostly excited by a frequency different from the resonance. As consequence, some phenomena, as for example the flow reversals which have been observed to be a heat transfer enhancement mechanism, don’t always occur in an engine exhaust-type pulsating flow.

Although in a different experimental flow condition, heat transfer enhancement due to the transversal convection increase during flow reversal was also observed in the boundary layer of a pulsating channel flow by Kearney et al. [21]. In their works the authors investigated the time-resolved thermal boundary layer structure and surface heat flux in a pulsatile, laminar channel flow. Pulsations were imparted to the flow by four co-rotating vanes located in the settling chamber, upstream of the flow- conditioning honeycomb and screens. The vanes rotated in phase and modulated the settling chamber pressure by providing a blockage that varied the flow area between an almost fully open position and roughly 8 percent of the total settling chamber cross section. Nominal forcing frequencies of 2.5 and 5 Hz were used so that the wavelength of the travelling pressure wave was much longer than the length of the wind tunnel test section.

It could be already noted that the pulsation creation and the flow operating conditions in this case are different from Dec et al. [24], [25]: the flow is not in resonance state. For instance, the operating conditions recreated by Kearney et al. are more similar to an engine exhaust-type pulsating flow then in the studies of Dec et al. The only difference is that in a channel configuration, the flow is not considered to be axial-symmetric; anyway, adopting the Taylor hypothesis as in the paragraph II.2.1, the boundary structures since concentrated near the wall should not be quite different from a pipe flow case.

Providing a pulsatile, developing channel flow whose relative velocity oscillation amplitude could be varied to provide non-reversing, partially reversed, and completely reversed flow, represents an interesting characteristic of this study. Furthermore, through two different techniques, pure-rotational CARS and cold-wire anemometry, phase-averaged temperature were acquired and the thermal impact of flow reversal was systematically investigated. Results, in Figure 6, showed that the cycle-resolved impact of flow reversal was a dramatic thickening of the thermal boundary layer, which appeared to be caused by a vertical ejection of fluid from the near-wall region and by a limited degree of turbulent transition. During the reversed-flow portion of the cycle, a cyclic heat-transfer minimum was attained. Following reversal, the wall heat transfer recovered as the accelerated boundary-layer flow swept the channel clear of high-enthalpy fluid. All of the pulsatile flows, according to the authors, exhibited an enhancement relative to accepted Nusselt number data for a developing, laminar channel flow. Their results showed that enhancement can be achieved with low-amplitude velocity variations which will produce lower noise levels and require less energy input relative to acoustically resonant schemes that were used previously to produce large bulk flow reversals.

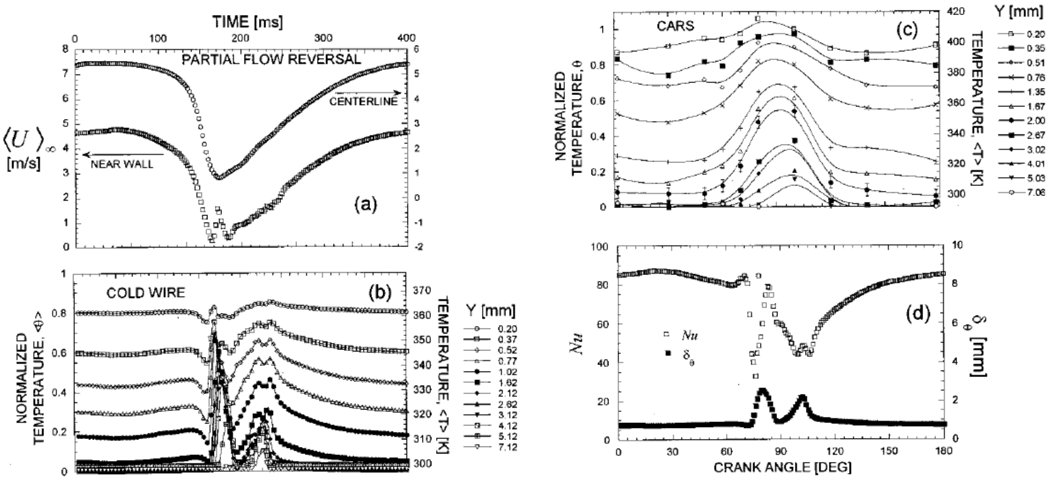

Figure 6: Time-resolved boundary-layer temperature and heat flux data from a partially reversed flow

Such recirculation coherent structures were also observed in a recent study of Xu et al. [28]: a valveless Helmholtz pulse combustor with an elbow tailpipe was designed and heat transfers were investigated. The pulsating flow in the elbow tailpipe was numerically simulated by Fluent, a frequency of 29.83 Hz was imposed to the flow for a time-average mass flow rate of 3.4 g/s. While the results of the numerical simulation agree with the experimental data, phase-average velocity and temperature radial profile were found to be relatively flat away from the wall upstream the inlet of the elbow section. Overshoots in temperature and velocities profiles in the boundary layer were observed to lead to a decrease in thermal boundary layer thickness and to an enlargement of the temperature difference between internal and external elbow wall surface. Mass-Averaged temperature dropped sharply and appeared two extreme points when the direction of the mass-averaged velocity oscillation changed. During flow reversal dean vortexes at the elbow section appeared, however, the shapes of the vortex were various, and the positions of the vortex core were different in a cycle. Dean vortex forming, shedding and reforming process at inlet and exit of the elbow section in a cycle was affirmed to be beneficial to the heat transfer enhancement.

In the same application, Zhai et al. [29] studied the impact of the flow pulsation on the time-average convective heat transfers. They proposed a Nusselt correlation for the pulsating flow, based on the addition of two independent physical properties. The mean Reynolds number of the experimental cases ranges from about 2500 to 8400. The velocity oscillation amplitudes range from about 1.3 to 17.7 m/s, and the frequencies range from about 25 to 55 Hz.

Authors started to apply the quasi-steady theory to compare experimental data with predictions. Such theory assumes the flow at an instantaneous moment follows the rule of stable heat transfer state, i.e. the flow is stabilized at the instantaneous rate. The assumption is reliable in low frequency oscillation, for it requires the flow to stabilize in the time limit much less than a cycle. The convective time scale is the ratio of the shear layer thickness and the velocity of the flow. The acoustic time scale is the ratio of the tailpipe's length and the sound speed. The convective time scale may be equal to or faster than the acoustic time scale by one order of magnitude. Physically, when the acoustic time is slower than the convective time, the hydrodynamics are driven by the acoustics but do not affect it. It is because the influence of the hydrodynamics averages out over the long time scale of the acoustics.

Applying the quasi-steady theory to the Dittus-Boelter Nusselt number correlation (II - 42) and assuming an instantaneous pulsating velocity $U = U_m + U_{avg}\cos(2\pi t)$ the following formula could be found:

$$Nu = 0.023Pr^{1/3}Re^{0.8}\int_0^1 \left(1+\frac{U_{avg}}{U_m}\cos(2\pi t)\right)^{0.8} dt \qquad \text{II - 55}$$

The time-average Nu number obtained in the experiments (Figure 7) apparently 2 to 5 times as much as the Nu number obtained in the quasi-steady theory. It seems that only taking the pulsating amplitude into account for pulsating is irrational, and frequency is also a key influential factor affecting heat transfer of pulsating flow, authors claimed. Except for velocity, amplitude and frequency are also key factors affecting heat transfer, and the criterion number under the quasi-steady theory cannot convey the pulsating heat transfer characteristics accurately under experiment conditions, the authors claimed.

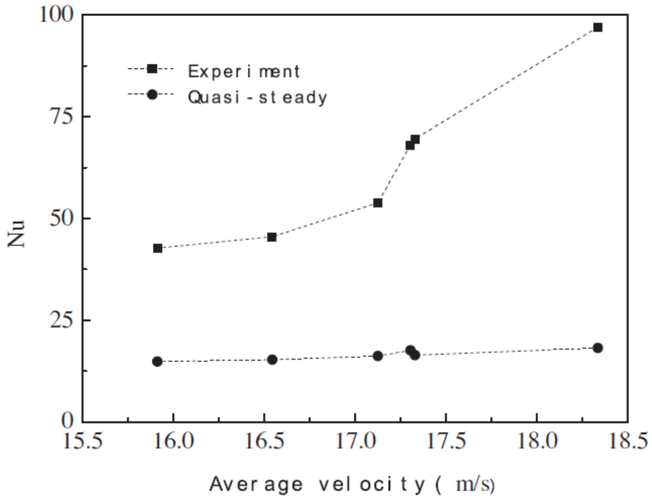

Figure 7: Variation of Nu with $\overline{U}$ – Exp. Vs Quasi-steady predictions

The Buckingham Π theorem in eq. II - 54 was further applied to the experimental results fitting. The following correlation for a time-average Nusselt number was proposed:

$$Nu = 0.0524\overline{Re}^{\frac{3}{4}}\left(1 + 68.52\frac{U_0 f D}{\overline{U}^2}\right)^{3/4} \qquad \text{II - 56}$$

The constants in the correlation are determined by least-squares fitting of experimental data. Where U_0 is the velocity amplitude. It could be observed that, as well as the Reynolds number is always used in the correlation to account for the turbulent or laminar state of the flow, also the pulsation frequency f, and the velocity waveform scale $U_0/\overline{U}$ are included in the correlation to account for pulsation effects. Results, in Figure 8 , showed a 20% of a maximum error between experiments and predictions.

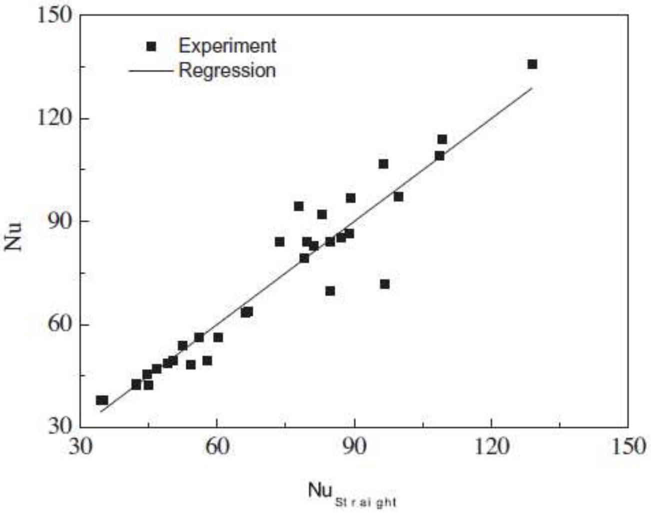

Figure 8: Time-average Nusselt number compared between experiments and calculation for a straight pipe

II.3.2 Heat transfers in laminar & turbulent pipe flows

Several experimental and numerical studies were also conducted on turbulent and laminar pulsating pipe flows. In the following lines a particular attention will be paid on the experimental configurations in which the heat transfer problem has been investigated and in the main results.

In a recent study Patel et al. [30] investigated on the heat transfer characteristics of pulsating turbulent air flow in pipe under different conditions of Reynolds number, pulsation frequency and pulsator location. An experimental set up was designed, depicted in Figure 9 basically consists of three parts; the air supply unit with necessary adoption and measuring devices, the test section and the pulsating mechanism. The air supply unit and its accessories consist of a blower, flow control valves, orifice meter. The proposed pulsating mechanism consists of the variable speed rotating butterfly valve connected to motor with the help of belt-pulley to create flow pulsations. The whole mechanism is kept in front of the pipe outlet which repetitively opens and closes the flow through butterfly valve and thus imparts pulsations to the air.

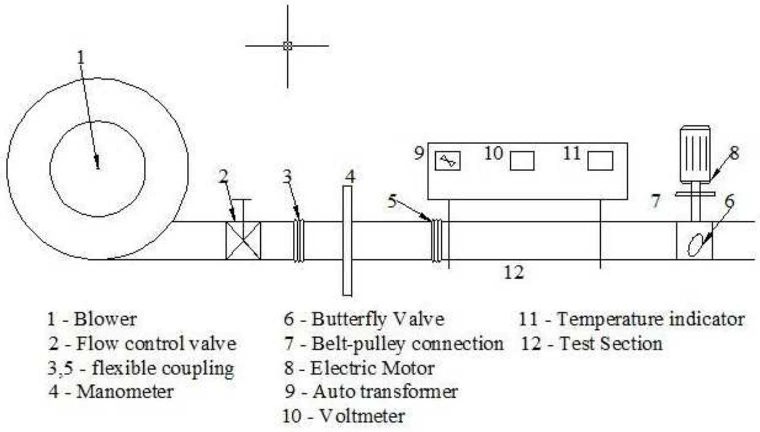

Figure 9: Experimental apparatus – Patel et al.

The test section is a copper tube of 25 mm inner diameter, 28 mm outer diameter. The pipe wall temperatures are measured by 4 k-type thermocouples distributed along the tube surface from outside. The bulk air temperatures at inlet and outlet of the test section are measured by two k-type thermocouples. An electric heater of 0.4 m total length is a nickel chromium wire which has a resistivity of 15.5 Ω/m, it has been divided into two equal lengths to heat up the test section tube. Experiments in pulsating flow were executed while the pipe wall is heated with different heat input and the pulsation mechanism was located downstream and upstream of the test section. The mass flow rate of air was adjusted and held unvaried while varying the pulsation frequency from 0.0 up to 3.33 Hz. The investigation covered different values of time-average Reynolds numbers in the range of 7000 < Re < 16500. Axial heat loss by conduction from both ends of the tested tube was eliminated by a two Teflon washers located between the test section flanges. The heat loss in radial direction through insulation was checked and found to be about 2% of heat input that can be ignored. The time-average convective heat transfer was calculated as follow:

$$Q_{conv} = \dot{m}c_p\Delta T \qquad \text{II - 57}$$

The previous equation states that Q_{conv} could be considered equal to the difference of the time-average air enthalpy across the test-section ports. Results show that the average heat transfer coefficient increases with increasing the pulsation frequency and Reynolds number. The maximum enhancement obtained in heat transfer coefficient is 44.4% at downstream and 17.68% at upstream when pulsation frequency is 3.3 Hz. The Nusselt number increases with increasing the pulsation frequency and Reynolds number. The maximum enhancement obtained in Nusselt number is 43% at downstream and 11.2% at upstream when pulsation frequency is 3.3 Hz. With increase in heat input the enhancement in average heat transfer coefficient and Nusselt number were observed for pulsation mechanism at upstream and downstream position. Enhancement in mean heat transfer coefficient and mean Nusselt number is more prominent in case of downstream position in caparison to upstream position and no-pulsation case.

In a study on a pulsating turbulent water stream, Zohir [31] also pointed out that the heat transfer coefficient was strongly affected by pulsation frequency and amplitude and by the Reynolds number.

An experimental apparatus was established for the investigation of the heat transfer characteristics of the turbulent pulsating water flow through a concentric tube heat exchanger where a coiled wire inserts around the outer surface of the inner tube. A schematic diagram of the experimental apparatus is shown in Figure 10. It consists of a test section, a pulsated mechanism, hot water closed loop, and cold water closed loop. A full set of instruments for measuring and control of temperature and flow rate of all fluids are installed at all important points in the circuit. The test section is a horizontal concentric tube heat exchanges, it consists of a horizontal water-to-water concentric tubes heat exchanger with counter flow of water, a coiled wire (coated metal) to act as turbulators, pulsating mechanism, and temperatures measuring devices. The pulsated mechanism was constructed of an electric motor, a variable speed transmission and a reciprocating piston.

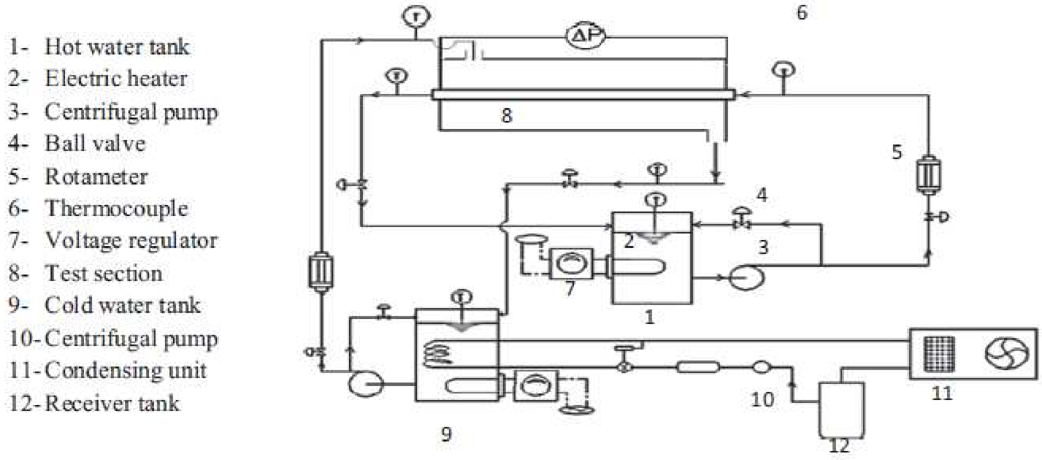

Fig. 1. Experimental apparatus.

Figure 10: Experimental apparatus – Zohir et al.

The pulsation was imposed to the cold water by the reciprocating piston mechanism. The pulsating flow is carried out for different piston stroke lengths and different operating Reynolds number ranged from 3856 to 11,568. To minimize the heat losses in the system, the hot water is fed through the inner pipe, with cooling water in the outer annulus of the heat exchanger. The outer surface of the heat exchanger was well insulated to minimize convective heat loss to the surroundings. The inlet hot water temperature was kept at about 65 °C and the inlet cold water temperature was about 25 °C. The heat transfer through the inner tube and annulus of tube-in-tube heat exchanger was determined from inlet and outlet temperature measurements and mass flow rate using the equation II - 57.

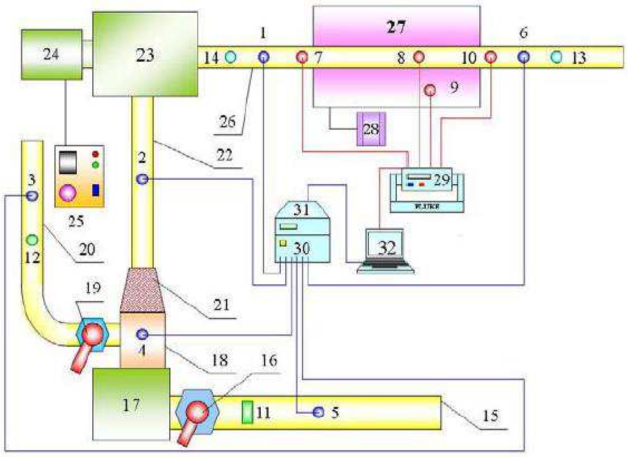

1-6. pressure transducers; 7-10. thermocouples; 11. anemometer; 12. pitot; 13, 14. manometer; 15. draft tube; 16, 19. flow- rate control valve; 17. air blower; 18. T-junction; 20. branch channel; 21. porous medium stack; 22. calming section; 23. pulsation generator; 24. electromotor; 25. speed controller; 26. test section; 27. heat exchanger; 28. transformer; 29. temperature data acquisition instrument; 30, 31. pressure signal acquisition systems; 32. computer

Fig.1 Schematic diagram of experimental system

Figure 11: Experimental apparatus – Hua et al.

Hua et al. [32] studied heat transfer in turbulent pulsating pipe flows in the test-rig of Figure 11. A device for producing pulsatile air flow named vane-type pulsating flow generator was imposed to make the air flow from pump be in pulsating state. The thermal boundary condition in this paper was a constant wall temperature by means of employing constant temperature water in tank outside tubes. Time-average Reynolds number varied from 6×10^4 to 12×10^4 and pulsation frequency ranged from 0 to 100 Hz. New dimensionless amplitude definition, which is based on the ratio of inlet pressure amplitude to outlet pressure amplitude was introduced from the authors, it was obtained for description of pulsation amplitude characteristics. The relationships between Nusselt number and the factors including Reynolds number Re, Womersley number W and non-dimensional pulsation amplitude A_o were analyzed. Based on the experimental data, the correlation in equation II - 58 of time-averaged Nusselt number with dimensionless parameters of Re, A_o and W is obtained for pulsating turbulent air flow inside a circular pipe in the study domain for 10 Hz < f < 100 Hz, 16 m/s < $\overline{U}$ < 40 m/s:

$$Nu = 0.0127Re^{0.8454}Wo^{-0.025}A_0^{0.048} \qquad \text{II - 58}$$

Where Wo is the Womersley number as in eq. II - 54. A close agreement between experimental data and correlated values from the equation is presented in the Figure 12.

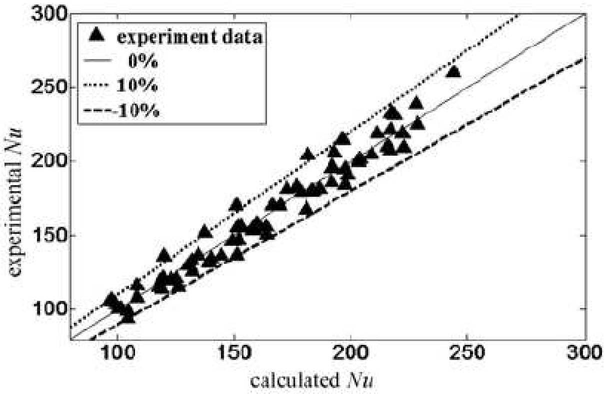

Figure 12: Time-average Nusselt comparison between experimental data and a fitting correlation

It could be observed that the correlation form proposed in II - 58 widely differs from the correlation proposed by Zhai et al. [29] in II - 56, while the pulsation frequency is accounted for in both the correlations, the pressure amplitude terms in II - 58 doesn't exist in II - 56. Actually such pressure amplitude term is not even contemplated from the Buckingham Π theorem in equation II - 54, suggesting that the correlation proposed Hua et al. [32] should be valid only in the study domain in which it has been found.

Habib et al. [33] studied the heat transfers in laminar pulsating pipe flows, where the Reynolds number and the pulsation frequency were ranged from 780 to 1987, and from 1 to 29.5 Hz respectively: an experimental facility (Figure 13) has been designed and constructed for this purpose. Dry air is forced to pass through a test-section which consists mainly of a main tube heated using an electric heater, of which the surface temperatures have been measured by 14 type K thermocouples concentrated at the beginning of the pipe to measure the entrance effect on heat transfers.

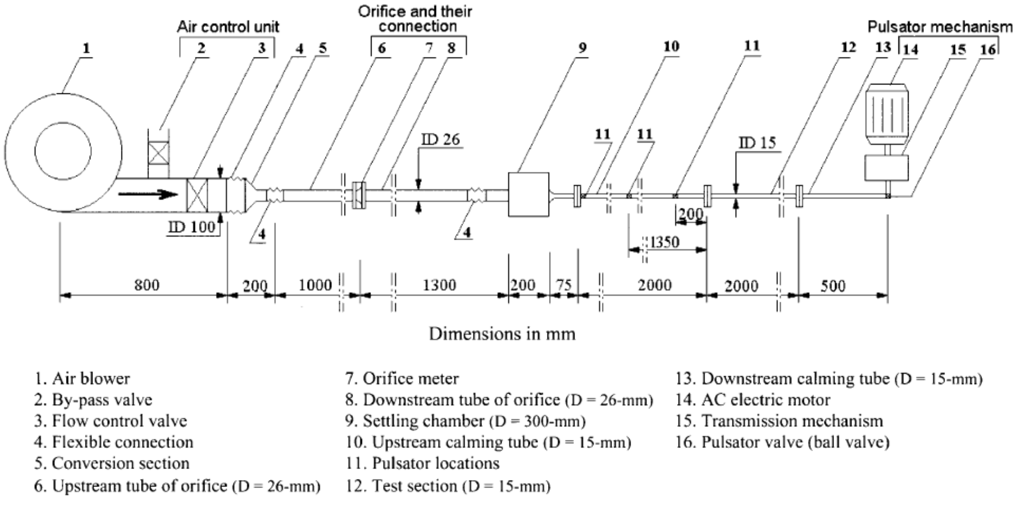

Figure 13: Experimental apparatus – Laminar, Habib et al.

The pulsation mechanism was constructed of three main parts, an AC electric motor, a variable speed transmission and a rotating ball valve of 15 mm of inner diameter to create the pulsations. The pulsator, as in Figure 13, as located downstream the test-section. Also in this study, convective heat power was computed according the equation II - 57, and then a relative Nusselt number has been defined as:

$$\overline{Nu}_{rel} = \frac{\overline{Nu}_{puls}}{\overline{Nu}_{steady}} \qquad \text{II - 59}$$

Where $\overline{Nu}_{puls}$ the time-average Nusselt for the pulsating is flow and $\overline{Nu}_{steady}$ is the time-average Nusselt for the counterpart steady flow with the same time-average Reynolds number. The results showed that the pulsation frequency affected heat transfers stronger than the Reynolds number. Compared to a steady flow, both an enhancement and a reduction of heat transfers, corresponding to different pulsation frequency range, were observed. An enhancement in heat transfer coefficient of up 30% was obtained at pulsation frequency range of 1 - 4.1 Hz and an enhancement of up to 9% obtained at pulsation frequency range of 18 - 22 Hz. While a reduction of heat transfers has been observed in the remaining range of frequency up to a maximum value of 40% at 14 Hz for all the investigated Reynolds number.

In turbulent conditions (for Reynolds numbers range of 5000 – 29000), in a further study, Habib et al. [34] also found an increase or a decrease of heat transfer in function of the pulsation frequency. A different experimental apparatus, showed in Figure 14, was proposed.

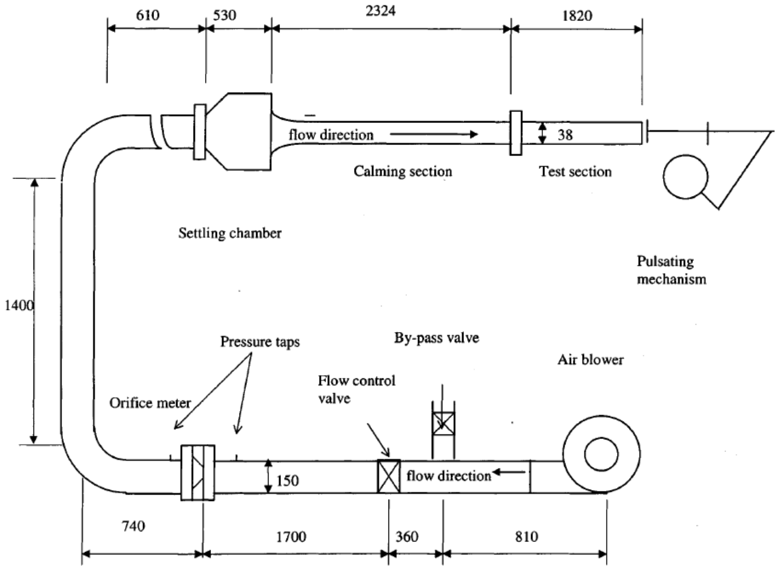

Figure 14: Experimental apparatus – Turbulent, Habib et al.

While the test-section was always a main tube heated from an electric resistance, the pulsating mechanism located downstream at the exit of the pipe and is a four bar slider crank mechanism, driven by a variable voltage D.C. motor. The slider is connected to a flexible disc in form of a piston which moves back and forth in order to create the pulsation. The displacement amplitude is equivalent to the stroke of the piston which can be, three different amplitudes were considered in the present work to investigate the influence of the pulsation amplitude on the heat transfer characteristics. The pulsation frequency corresponds to the rotational speed of the motor. Also the computation of the convective heat transfer was the same of the laminar study.

Turbulent bursting, mode was identified as a possible explanation of the observed heat transfer modification. The turbulent bursting was studied by Kline at Stanford University [35], he was one of the pioneering teams that have carried out studies on the detailed structure of near-wall turbulence by visualization of flows, from 1956 onward. These studies showed that the viscous sublayer adjacent to the wall, which had thitherto been incorrectly called the "laminar" sublayer, is actually made up of high- and low-velocity streaks. These streaks alternate in the spanwise direction *z*; they are sinuous and their spacing in the direction is remarkably quasi-regular. The earliest visual observations revealed that the low-velocity streaks "become detached" and oscillate before being ejected far from the wall in the form of a sudden eruption, dispersed over "small scales". Eighty percent of turbulence production takes place during these relatively short periods, covering around 10 inner units. This phenomenon, overall, was called "bursting" by the community of wall-turbulence researchers at that time. With the works of Rapamaprian et al. [36], [37], experimental data on phase and amplitude and energy spectrum were used to study the effect of the imposed oscillation on the turbulence structure at these interactive frequencies of oscillation. Authors inferred that turbulent shear flows respond very differently from laminar shear flows to imposed unsteadiness. A turbulent Stokes number relevant for characterizing the unsteady turbulent shear flows was identified and used to classify such flows in 5 different flow regimes according to at high frequency there is an accordance between the pulsation frequency and the event frequency of such turbulent structures (further details are available in [36]).

In the same way, the experimental studies of Said et al. [38] and of Nishandar et al. [39] confirmed that the heat transfer coefficient was either increased or decreased in function of the pulsation frequency in turbulent conditions. The experimental data of Said et al. [38] were analysed, as in Figure 15, according the regimes classification of Rapamaprian et al. [36], [37]: as can be seen, data fall into the preferred range of the bursting frequencies (segment B and C). It is also observed that the pulsation frequencies at which overall heat transfer enhancement occurs are very close to the mean bursting frequency line, suggesting that the changes in the mean bursting frequency are imposed by the pulsation frequency. Therefore, authors said, based on this model the critical frequencies at which resonance interaction should likely occur are in the neighborhood of 2 and 3 Hz, as the results confirm.

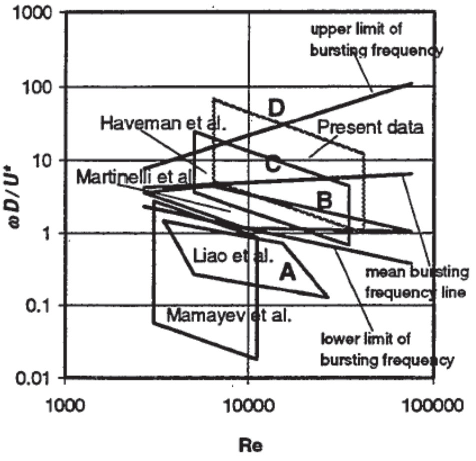

Figure 15: Classification of the study domain by the time-average Reynolds number and the turbulent Stokes number

Also in the work of Monschandreou et al. [40], both an enhancement and a degradation of heat transfers was observed: the results indicated that, in a range of moderate values of the frequency, the effect of the pulsation was to increase the bulk temperature of the fluid and the Nusselt number, but the effect was reversed outside this range.

Elshafei et al. studied numerically [41] and experimentally [42] the heat transfers for a fully developed pulsating turbulent flow, over a range of $10^4 \leq \mathrm{Re} \leq 4\times10^4$ and $0 \leq f \leq 70$ Hz.

The experimental apparatus is depicted in Figure 16, also in this study the test section was heated by an electric wire resistance as well as the pulsating mechanism was constructed of three main parts; an AC electric variable speed motor (13), a variable speed transmission mechanism 11, 12, and a rotating butterfly valve (14) of 15.5 mm inner diameter. Also in this study the convective heat transfers were computed according the equation II - 57.

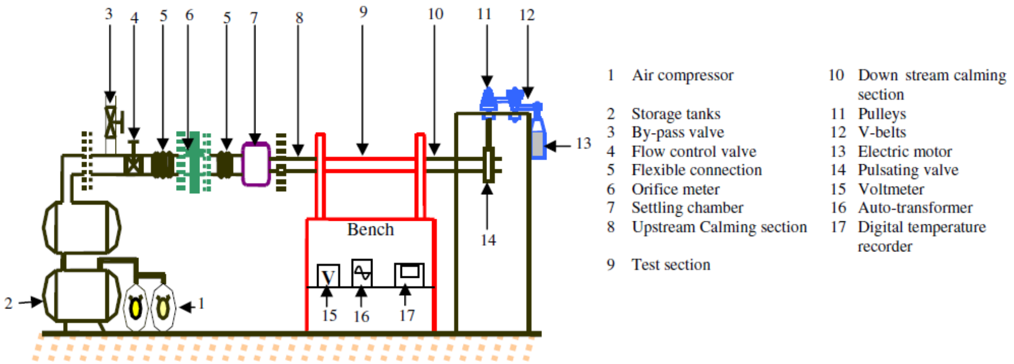

Figure 16: Experimental apparatus – Elshafei et al.

Experimental results show that the heat transfer coefficient may be increased or decreased, depending on the value of frequency and Reynolds number. Higher values of the local heat transfer coefficient occurred in the entrance of the tested tube. The maximum enhancement in gm of about 9% is observed at Re = 37,100, f = 13.3 Hz and ω^+ of about 0.5 where the interaction between the bursting and pulsation frequencies is expected. The maximum reduction of about 12% was detected for Re = 13,350, f = 42.5 Hz and ω^+ of about 4.4. Where $\omega^+ = \frac{\frac{2\pi}{T}\nu}{u_\tau^2}$ is a dimensionless frequency and u_τ is the friction velocity.

In a further numerical study [41], the pulsating flow in the experimental apparatus was modelled with the CFD software Fluent 6.1 2003. Among the available turbulent models, those based on Eddy viscosity are widely applied to the turbulent kinetic energy – turbulent energy dissipation rate (k-ε). Two additional equations for the standard k-ε turbulence model: the turbulence kinetic energy, k, and the dissipation rate, ε, are determined using the following transport equations, respectively. The solution domain of the considered 2D, axisymmetric pipe flow is geometrically quite simple, which is a rectangle on the x-r plane, enclosed by the inlet, outlet, symmetry and wall boundaries. On walls no-slip condition are assumed for the momentum equations. The inlet velocity values have been derived from given Reynolds numbers. For pulsating cases, the inlet velocity is varied with time. The outlet boundary condition is called "outflow", which implies zero-gradient condition at the outlet. At the pipe wall a uniform heat flux is imposed for the heated section and q" = 0 for the adiabatic wall.

Results showed that at all values of pulsation frequency, the variations in the local time-averaged Nusselt number exhibit similar trends to the steady flows. The local time-averaged Nusselt number either increases or decreases than steady flow values depending on the frequency and Reynolds number. Frequency has little effect on the values of mean time-averaged Nusselt number especially at higher values of pulsation frequency. The presence of any pulsation frequency has a notable effect on the heat transfer coefficient in comparison with that of steady flow, even at a very small value of pulsation frequency. However, the change of the value of pulsation frequency has relativity small effect on the heat transfer rates. No increase in the time-averaged Nusselt number for frequency $f \leq 39.34$ Hz. For $f \geq 42.5$ Hz, little increase in time averaged-Nusselt number is detected at $\mathrm{Re} \approx 22.5 \times 10^3$.

Also Wang et al. [43] developed a two-dimensional model to simulate convection heat transfer in pulsating turbulent flow, with large velocity oscillating amplitudes, in a pipe at constant wall temperature. The simulation, performed with the Fluent CFD software were based on the same turbulent model (k-ε) of Elshafei et al. [41].

At the inlet, a parallel uniform flow was assumed as boundary condition, the velocity was considered to be sinusoidally oscillatory around a periodically time-averaged value of the mean velocity. To model the temperature pulsation that could appear in some cases, for example as in the flow in pulse combustor, the temperature condition at the inlet also was pulsated. Here the same wave pattern and the phase angle as those of the inlet velocity were used for the inlet temperature while the no-slip condition at the wall and a constant wall temperature were imposed. At the exit, the velocity and temperature were assumed to be fully developed with zero velocity gradient and zero-temperature gradient in the axial direction of the pipe because the pipe is long enough.

Results in terms of a relative Nusselt number, as in II - 59, calculated according equation II - 6, showed that heat transfer was enhanced by both larger amplitude of velocity oscillation and flow reversal (as in the works of Dec et al. [24], [25]) and highlighted the existence of an optimum Womersley number at which heat transfer is maximally enhanced.

II.3.3 Pulsating flow an active method for the heat transfer enhancement

The way to improve heat transfer performance is referred to as heat transfer enhancement (or augmentation or intensification). Nowadays, a significant number of thermal engineering researchers are seeking for new enhancing heat transfer methods between surfaces and the surrounding fluid. Due to this fact, such methods are widely classified as active or passive methods of enhancing heat transfer. Those which require external power to maintain the enhancement mechanism are named active methods. Examples of active enhancement methods are well stirring the fluid or vibrating the surface. On the other hand, the passive enhancement methods are those which do not require external power to sustain the enhancements characteristics. Examples of passive enhancing methods are: treated surfaces, rough surfaces, extended surfaces, swirl flow devices, coiled tubes, additives for fluids, and many others. Because widely accepted that flow pulsations could enhance heat transfers in comparison to the steady case, in recent works, flow pulsation was investigated also as an active method to enhance heat transfers in industrial applications such as heat exchangers in which the flow develops mainly in stationary conditions. An exhaustive review of the recent advances in heat transfer enhancements could be found in [44].

Kharvani et al. [45] investigated the potential to increase heat transfers by using a rotating ball valve as a pulse generator mounted downstream/upstream of a spiral-coil tube. Reynolds number was ranged from 6220 to 16300, while the pulsation frequency was varied from 0 to 20 Hz. It was observed that, although the overall average heat transfer coefficient was strongly affected by Reynolds number, it was enhanced up to 26% for pulsating flow compared to steady flow. Ghaedamini et al. [46] investigated the potential to increase heat transfers with wavy walled micro-channels. Although such geometries demonstrated their capability of inducing chaotic advection, an important pressure drop penalty was observed for highly modulated channels. To overcome this issue, a pulsatile flow was introduced, leading to a strong enhancement of heat transfers for channels with slightly modulated walls corresponding to a reasonable pressure drop penalty. This increase was attributed to a chaotic advection phenomenon near a characteristic frequency of excitation. In [47], Wantha experimentally studied the enhancement of heat transfer in finned tube heat exchangers by using a pulsating air flow. The influence of velocity amplitude, pulsation frequency, Reynolds number and blockage ratio of heat exchangers were investigated. The results showed that the pulsation frequency and velocity amplitude play major roles in heat transfers. An empirical correlation, based on a Colburn j-factor, was deduced from the experimental results.

II.3.4 Heat transfers in Internal Combustion Engines

Growing awareness of environmental issues pushes governments to impose stricter emission standards to the Internal Combustion Engine, forcing engine manufacturers companies to face the challenge to increase engine efficiency and to decrease engine pollution. ICE efficiency is still improving but it is today limited at best to around 40%, a large part of energy contained in the fuel is lost in coolant, oil, exhaust gas and air around the engine.

Although the first works on this subject are more than 10 years old, the study of heat transfers in automotive exhaust systems has only recently attracted the importance it deserves due to its key role in the design of modern exhaust after-treatment systems [48] or in the design of the Waste Heat Recovery, machines. Considering, moreover, that engine manufacturers are always more interested in decreasing experimental phases, within the conception life cycle of an engine, to reduce time and costs; a better predictable modeling of heat transfer phenomena for pulsating pipe flow represents thus an import requirement.

The prediction of the heat transfer exchanged between a fluid and a solid wall in all the engineering applications represents nowadays an important challenge. In the case of an engine manifold, for instance, the heat transfer problem, if approached with a 1D assumption and assuming the laminar hypothesis, could have the following form:

$$\rho c_p\left(\frac{\partial T}{\partial t}+\frac{\partial(uT)}{\partial x}\right)= \lambda\frac{\partial^2 T}{\partial x^2}+q \qquad \text{II - 60}$$

Where u represents the bulk axial instantaneous air velocity, T the bulk temperature of air, ρ the fluid density, c_p the specific heat at constant pressure and q the local specific convective heat transfer exchanged through the perimeter of a pipe length ∂x.

The modelling of the term q in eq. II - 60 represents nowadays the aforementioned main challenge.

As the works in [48]–[50] show, several attempts have been made into the prediction of heat transfers in such conditions, the main problem is that, as previously showed, available heat transfers models don't account for pulsating effects. The typical flow conditions in automotive exhaust systems produce Re numbers in the range of $10^3 – 5 \times 10^4$. Among the numerous heat transfer coefficient correlations, which are useful to calculate the term q in eq. II - 61, for the fully developed flow in a straight channel, we mention the Sieder-Tate relation which correlates the Nu number with Re and Pr [15]:

$$Nu = 0.027Re^{0.8}Pr^{1/3} \qquad \text{II - 61}$$

The correlation proposed by Gnielinski [16] takes additionally into account the effect of wall roughness by means of the friction factor f. As the flow enters the pipe, the thin thermal boundary layer gives higher local Nu numbers, and it takes an order of 15 to 30 diameters for the Nu to approach the asymptotic value of the fully developed flow [17].

For low Re numbers, Reynolds et al. correlated their analytical results as [18]:

$$\frac{Nu(x)}{Nu_\infty} = 1 + 0.2\left(1 + 7E^4Re^{-\frac{3}{2}}\right)\left(\frac{x}{d_1}\right)^{-1} \qquad \text{II - 62}$$

The turbulent boundary layer also decreases in thickness in the vicinity of a bend. This tends to enhance the heat transfer between the pipe wall and the exhaust gas. The following relation to account for pipe bend effects is recommended in Ref. [20]:

$$\frac{Nu_{bend-pipe}}{Nu_{straight-pipe}} = 1 + \frac{21 d_1}{Re^{0.14} d_{bend}} \qquad \text{II - 63}$$

However, the highly unsteady, pulsating nature of the flow in the exhaust manifold has been suggested as an explanation for the increased heat transfer rates observed in exhaust systems and as previous affirmed such effects have not been yet accounted for.

In the case of the engine manufacturer company ‘Groupe PSA’, empirical compensations of heat transfers for pulsating effects are used, anyway, since such models are deduced a-posteriori from the experiments, they are not predictive and cannot be used to study new concepts.

To investigate the potential of new technologies, among all the CFD tools the widely used by the engine manufacturer companies is GT-Power of the GT-Suite software.

GT-Power is used to predict engine performance quantities such as power, torque, airflow, volumetric efficiency, fuel consumption, turbocharger performance and matching, and pumping losses, to name just a few. Beyond basic performance predictions, GT-Power includes physical models for extending the predictions to include cylinder and tailpipe-out emissions, intake and exhaust system acoustic characteristics (level and quality), in-cylinder and pipe/manifold structure temperature, measured cylinder pressure analysis, and control system modeling.

The flow model involves the solution of the Navier-Stokes equations, namely the conservation of continuity, momentum and energy equations. These equations are solved in one dimension, which means that all quantities are averages across the flow direction. There are two choices of time integration methods, which affect the solution variables and limits on time steps. The time integration methods include an explicit and an implicit integrator. The primary solution variables in the explicit method are mass flow, density and internal energy. The primary solution variables in the implicit method are mass flow, pressure and total enthalpy.

Without reporting the continuity and the mass conservations equations (details page 2 of [51]) we focus on the energy balance equation, shown below:

Explicit solver

$$\frac{d(me)}{dt} = -p\frac{dV}{dt} + \sum_{boundaries} (\dot{m}H) - hA_s(T - T_{wall}) \qquad \text{II - 64}$$

Implicit solver

$$\frac{d(\rho HV)}{dt} = +V\frac{dp}{dt} + \sum_{boundaries} (\dot{m}H) - hA_s(T - T_{wall}) \qquad \text{II - 65}$$

where:

- $\dot{m}$ boundary mass flux into volume, $\dot{m} = \rho A u$
- m mass of the volume
- V volume
- p pressure
- ρ density

- A flow area
- $A_s$heat transfer surface area
- e total internal energy (internal energy plus kinetic energy) per unit mass
- H total enthalpy, $H = e + \frac{p}{\rho}$
- h heat transfer coefficient
- T_{wall} wall temperature
- u velocity at the boundary
- D equivalent diameter
- dp pressure differential acting across dx

As observed in eqs. II - 64 and II - 65, the energy governing equation is differently written in function of the equation solver.

In eq. II - 64 the primary solution variables in the explicit method are mass flow rate, density, and internal energy. The values of mass flow, density and internal energy at the new time are calculated based on the conservation equations. In the explicit method, the right hand side of the equations is calculated using values from the previous time step. This yields the derivative of the primary variables and allows the value at the new time to be calculated by integration of that derivative over the time step. To ensure numerical stability, the time step must be restricted to satisfy the Courant condition, while for the implicit solver (eq. II - 65) the primary solution variables in the implicit method are mass flow, pressure, and total enthalpy. The implicit method solves the values of all sub-volumes at the new time simultaneously, by iteratively solving a non-linear system of algebraic equations. This approach is useful for fluid systems where high frequency pressure fluctuations are not of interest (i.e. cooling systems) and typical simulation durations are higher, so that large time steps may be taken, authors affirmed.

The convective heat transfer modeling role is played by the term $hA_s\left(T_{fluid} - T_{wall}\right)$ in both eqs. II - 64 and II - 65, where the heat transfer coefficient $'h'$ is calculated at every time step from the fluid velocity the thermo-physical properties and the wall surface roughness.

The heat transfer coefficient of smooth pipes is calculated using the Colburn analogy for turbulent, laminar and transitional flow, as follows:

$$h_g = \frac{1}{2} C_f \rho U_{eff} c_p Pr^{-2/3} \qquad \text{II - 66}$$

where:

- C_f is the friction coefficient of smooth pipe
- ρ density
- U_{eff} the effective velocity outside boundary layer
- c_p specific heat
- Pr Prandtl number

As mentioned in the paragraph II.2.2 the Colburn correlation has been experimentally computed for a fully developed turbulent pipe flow, in GT -Power corrections for rectangular cross-section, for a high surface roughness are furtherly applied. Anyway, the approach used in such software suppose a quasi-steady theory: the Colburn theory is applied at each instant of the cycle assuming that the flow behaviors as it is in internal and external equilibrium. As previous claimed in function of the unsteady state of the flow such assumption could not be applied.

To account the unsteady state of the flow, an ad-hoc 'Global Heat Transfer Multiplier - GHTM' is multiplied to the convective heat transfer coefficient; such correction is available only for the explicit solver. GHTM has the following form:

$$GHTM = N_{const}\left(1 + N_{unst}F_{ht,unst}\right) \qquad \text{II - 67}$$

Where: N_{const} and N_{unst} are user-defined constant terms independent from the time and the unsteady state of the flow, while, $F_{ht,unst}$ is an unsteady heat transfer factor which variates in time. Unlikely, due to confidential limits, further details about $F_{ht,unst}$ is calculated are not available.

In the following figures, the heat transfer coefficient predicted from the GT-Suite unsteady model for a pulsating pipe flow with and without unsteady correction is shown in the figure above:

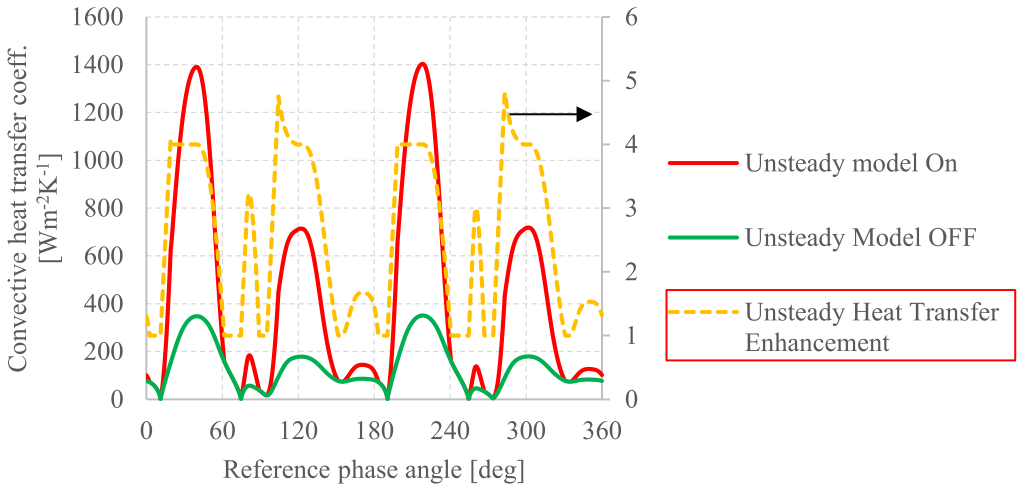

Figure 17: GT-Suite Unsteady model prediction of the phase-average Convective Heat Transfer coefficient for pulsating flows in pipes

As observed, $GHTM$ (with $N_{const} = 1$ and $N_{unst} = 1$) varies from 1 to a value up to around 5. With such correction the time-average convective heat transfer coefficient has been observed to be seven times higher than the other one calculated without unsteady model correction.

II.3.4.1 Investigation of heat energy storage systems for internal combustion engine applications

As previous affirmed, prediction of heat transfers in internal combustion engine applications is nowadays not so easy, the limits of the actual predictive models make the results useless; consequently, to investigate on innovative concepts to increase engine efficiency and decrease engine pollutant emissions, an experimental approach is still necessary.

During the thesis project the potential of various designs of Heat Energy Storage System (HESS) have been studied to temporally recover thermal energy from hot gases and to restore heat to a cold gas for a

WER application in a conventional ICE. The thermal behavior of the HESS, in terms of its potential to recover and restore energy, and, the modification of flow conditions, in terms of pressure losses, are analyzed and detailed in the following lines. Finally a comparison between the convective heat transfer coefficient calculated from experiments and from the predictive available models is presented to evidence the inaccuracy of the actuals model for heat transfers prediction. (A paper and an oral presentation have been realized in the occasion of the World Automotive Conference FISITA2016 in South Korea.)

Heat Energy Storage System design

In order to evaluate the capacity of the HESS to temporally recover the thermal energy contained in a hot gas and then to restore it into a cold gas, both the hot and cold fluids are forced to pass through the HESS. The HESS have been designed as empty cylinders with several rows of crossbars perpendicular to the cylinder axis (Figure 20). The rows of crossbars are not aligned between each other in order to create flow breakpoints and consequently to distribute the axial kinetic energy and then enhance the convective heat transfers.

HESS	t_k [mm]	d_s [mm]	n_r	Crossbars mass [g]
1	0.4	0.3	10	34.6
2	1	0.7	10	35.2
3	0.7	1	10	25.0
4	0.3	1	10	12.9
5	0.3	1.5	10	9.0
6	0.3	2.5	10	5.5
7	0.3	2.5	5	2.6

Table 1: HESS geometric properties

Geometrical characteristics of the tested HESS correspond to crossbars thicknesses 't_k' varying from 0.3 mm to 1 mm and to distances 'd_s' between crossbars ranging from 0.3 mm to 2.5 mm. Depending on the HESS, the number of row of bars 'n_r' is equal to 10 or 5. The external and internal diameters of each HESS are, respectively, 19 mm and 17 mm. The HESS are made with a 3D printing process and are made of stainless steel 304L. Table 1 shows the geometric characteristics of the HESS:

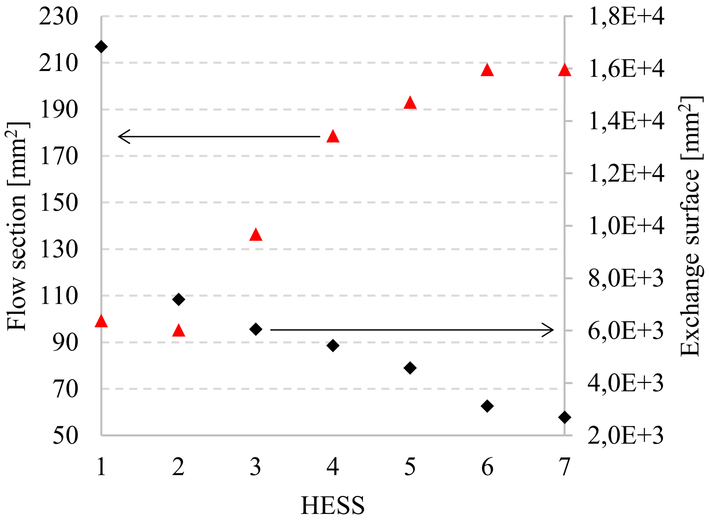

Figure 18: Geometrical characteristics of the HESS

The different flow sections, total mass of the crossbars and heat exchange surfaces (Figure 18) are the result of the geometric characteristics variation of the HESS. These parameters will influence the pressure losses and the potential to recover and restore thermal energy.

Experimental setup and diagnostic

In order to reproduce the thermodynamic gas conditions at the engine exhaust, a conventional SI engine has been used to test the HESS. The test rig is showed in Figure 19: the gasoline mono-cylinder engine (2) has been adapted to generate and receive a flow of compressed air. The cylinder volume displacement is 0.4L and the geometric compression ratio is 10.5. The compressed air flows into the cylinder through the charging valve (5). The charging valve timing and its lift law are managed independently thanks to a camless system. Via an independent exhaust manifold, the charging valve is directly connected to a terminal of the external manifold (6). The other terminal of the HESS manifold is connected to a tank with a 30 litres volume (7). The HESS is placed inside the manifold. The tank is designed to resist at a maximum pressure of 30 bars. Tank pressure is controlled thanks to two electro-pneumatic control valves (10 and 11). Valve 10 allows controlling the tank pressure by flowing into the tank a compressed air flow generated by a pneumatic compressor (8). Valve 11 is used to flow out of the tank the excess air to keep tank pressure constant. Valve 12 is a completely open/close evacuation air valve used to restore ambient pressure inside the tank. Valve 14 is a reverse-acting bursting disc, placed in order to avoid a pressure higher than 30 bars. The incoming or outgoing mass flows from the tank are measured by two Coriolis Effect mass flow meters with a maximum combined standard uncertainty of ±0.2% for the entire measure range.

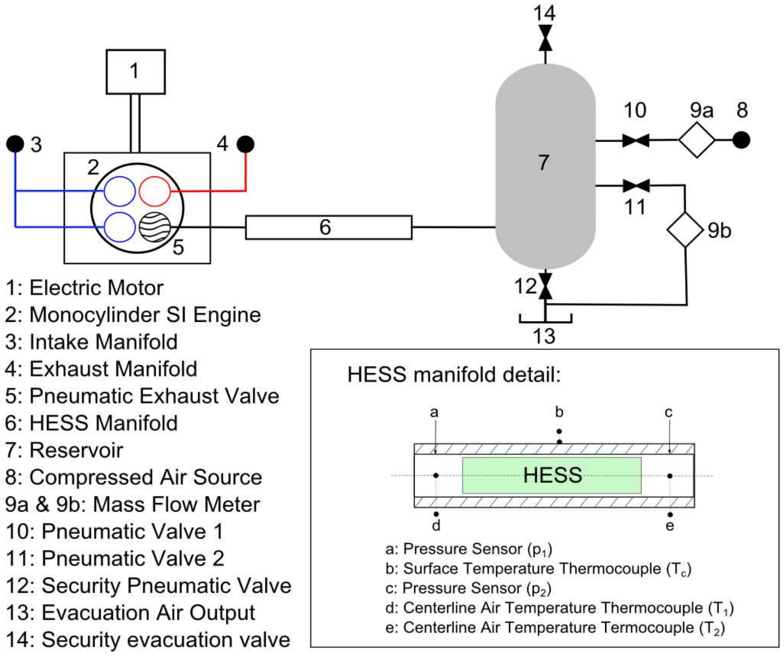

Figure 19: Mono-cylinder engine apparatus

Figure 20: HESS design

Cylinder pressure ‘p_{cyl}’, exhaust and intake pressures are measured with pressure transducers commonly used in ICE research. Air pressures ‘p_1’upstream and ‘p_2’ downstream the HESS (HESS manifold detail in Figure 20) are measured with 0-30 bar PSA pressure transducers. Tank pressure ‘p_t’ is measured with a Kistler 0-50 bar type 4005B pressure transducer. The intake and exhaust cylinder air temperatures, air reservoir temperature ‘T_t’, gas temperatures ‘T_1 and T_2’ upstream and downstream the HESS are measured with 1.5 mm type K thermocouples. External wall temperature of the HESS manifold ‘T_c’ is measured with a 0.5 mm type K thermocouple attached to the external surface. Temperature measurements have an accuracy of around 1.1°C, according to the thermocouple type K standards. Rapid pressure signal acquisition is performed with an equivalent frequency of 10 measures for 1 crank angle ‘CA’. Temperatures are acquired with a frequency of 10Hz.

Experimental procedures

In order to characterize the pressure losses, several cold air mass flow rates flow through the HESS and the pressure drop is measured. The air mass flow is generated by a compressor and is forced to flow from the tank, through the HESS, to the engine cylinder. Tank pressure is kept constant at the absolute pressure of 10 bars thanks to the control valve 10. Engine rotation speed is maintained constant at 2000 rpm. In order to have a positive pressure gradient between the tank and the cylinder, the throttle valve is partially closed, reaching an intake pressure of about 0.4 bar, and the charging valve is opened after the firing Top Dead Center (fTDC). The opening of the charging valve occurs at 360 CA, and the closing timing is ranged from 410 to 470 CA with a step of 10 CA (0 CA corresponds to the start of the admission stroke). In order to precisely know the fluid properties, the working fluid is air (fuel is not injected) which flow rate is measured with the flow meter 9a. Air pressures upstream and downstream the HESS are acquired and averaged over 100 engine cycles. Temperatures and mass flow rate are measured and time-averaged over a period of 30 seconds. Pressure losses are defined as the maximum of the difference between the averaged air pressures upstream and downstream the HESS within the engine cycle.

The second experimental procedure corresponds to a dual phase cycle designed to evaluate the ability to recover and to restore thermal energy of each HESS. For each test, before starting the dual phase cycle, stationary thermal initial conditions are reproduced, corresponding to temperatures of the cooling water and the lubricant oil between 82°C and 85°C, and to an exterior wall temperature of the HESS manifold of about 35°C. The first cycle phase, called ‘recovery phase’, corresponds to the thermal energy storage into the HESS. A hot flow, generated by the engine compression stroke, has a maximum temperature of 180°C and is forced to pass through the HESS to the tank. The HESS recovers a part of the air thermal energy through the convective heat transfer and its internal energy is increased. During the recovery phase, the engine speed is maintained constant at 2000 rpm and the throttle valve is completely open. No combustion occurs, the working fluid is only air. The charging valve is opened before the fTDC at 323 CA for a duration of 50 CA. The instantaneous pressure inside the cylinder, during the charging valve opening, is always higher than the tank pressure so as the hot air always flows through the HESS. The evacuation valve 12 and the control valves 10 and 11 are closed in order to store all the air into the tank. Although air pressure inside the tank increases, the air temperature inside the tank remains constant because of the high thermal capacity of the tank. When the tank pressure reaches 10 bars, the ‘recovery phase’ finishes. Since the total mass of air stored in the tank as well as the air temperature at the inlet of the HESS manifold remain constant for each test, it can be deduced that the total energy that passes through the manifold is kept constant.

The second phase, called ‘restore phase’, corresponds to the restoration of the previous recovered thermal energy to a cold gas which flows in an opposite direction inside the HESS. In order to flow a cold air from the tank to the engine, the charging valve opening is retarded after the fTDC, during the expansion stroke, at 400 CA for a duration of 50 CA. The throttle valve is partially closed so as to have an intake absolute pressure of 0.67 bar. Engine speed is maintained at 2000 rpm. The control valve ‘10’ operates to keep constant the tank pressure at 10 bars. During the opening of the charging valve, the tank pressure is always higher than the cylinder pressure, allowing cold air to flow from the tank to the engine through the HESS. A part of the energy, stored by the HESS, is restored to the cold air and the HESS outlet air temperature is increased. The second cycle phase finishes when the external wall surface temperature of the HESS manifold reaches the initial temperature condition.

Results & Discussion

- Pressure losses

The flow field in the HESS manifold can be described as a pulsating flow, in which a coherent pattern is repeated cyclically with a frequency related to the engine speed. The Coriolis flow meters are not able to measure rapid mass flow rate (MFR) variations related to these flow properties. However, plotting the maximum of the instantaneous pressure drop versus the time averaged air mass flow rate, as in Figure 21, allows showing a coherent trend of the increase of pressure losses with respect to an increase of the mass flow rate. Only for the HESS 6 and 7, the measured pressure drop is constant.

To explain this trend, shows the ratio of the air pressure, upstream and downstream the HESS, for three MFRs corresponding to the minimum, mean and maximum width of the charging valve lift law, which are respectively CA410, CA440 and CA470.

Figure 23 shows that, for HESS 1, an increase of the width of the charging valve lift law leads to a decrease of the pressure ratio. It is the same characteristic behavior as that of a convergent nozzle, in which the mass flow rate is a parabolic function of the pressure ratio ‘p_r’. Mass flow rate increases with the decrease of the pressure ratio until a maximum value corresponding to p_r=0.428 for air at 25°C. Moreover, the condition of sound velocity at the exit section is reached and for a further decrease of the pressure ratio the mass flow rate remains constant. In these HESS cases, an increase of the width of the charging valve lift law leads to an increase of the averaged mass flow rate, then it can be considered that the time-average MFR is representative for the characterization of the pressure losses. For the CA470 case, at the point A in Figure 23, it can be observed that the tangent of the curve is horizontal. It can be conclude that the minimum pressure ratio has been reached at this point and that the air velocity inside the HESS may be close to the sound velocity. Figure 24 shows that, for HESS 6, the minimum pressure ratio remains constant at 0.9 when the charging valve is completely open. It means that, for each valve lift law case, the instantaneous mass flow rate can be considered constant. Consequently, the time-average MFR is not representative of the pressure losses in these conditions. HESS 7 shows similar results.

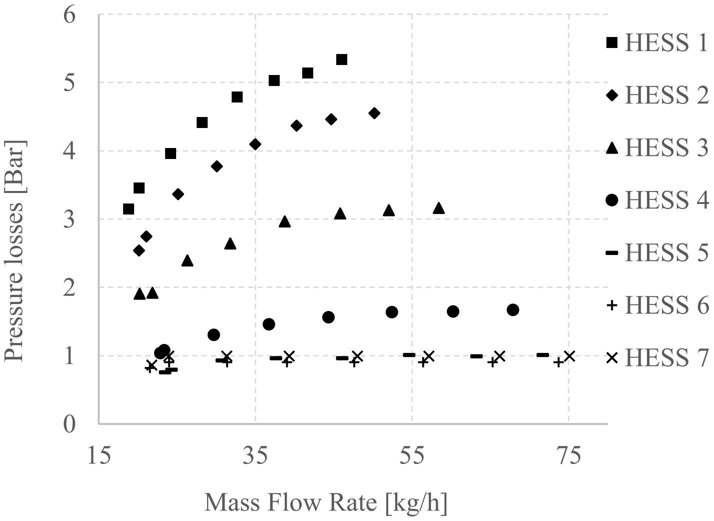

Figure 21: HESS Pressure losses in function of the MFR

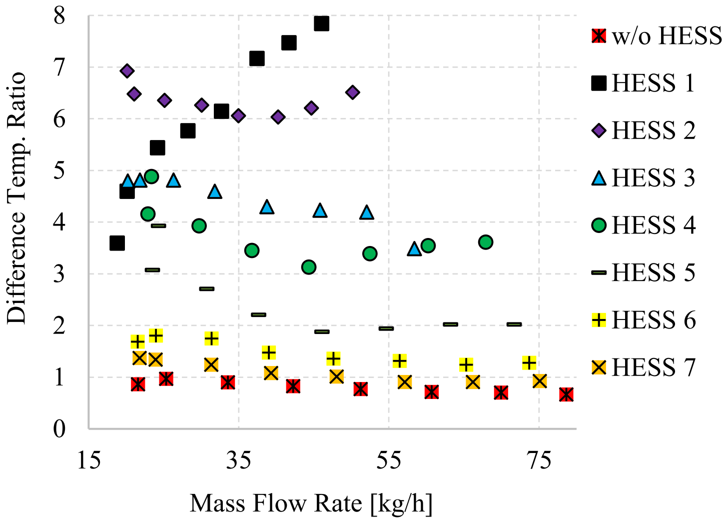

Figure 22: Difference Temperature Ratio

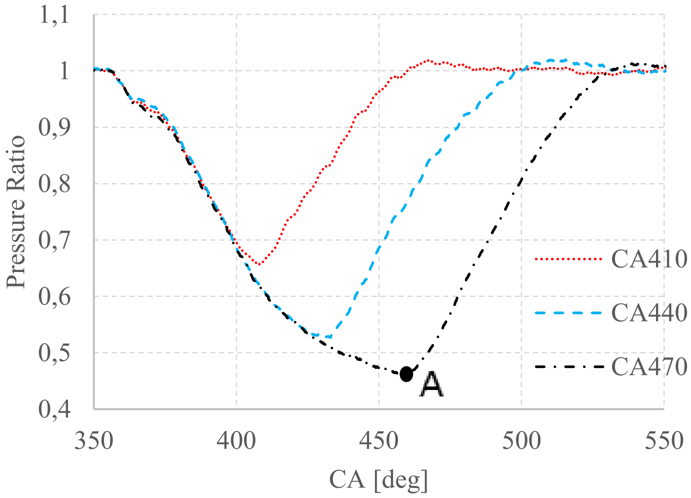

Figure 23: Phase-average Output/Input Pressures ratio HESS 1

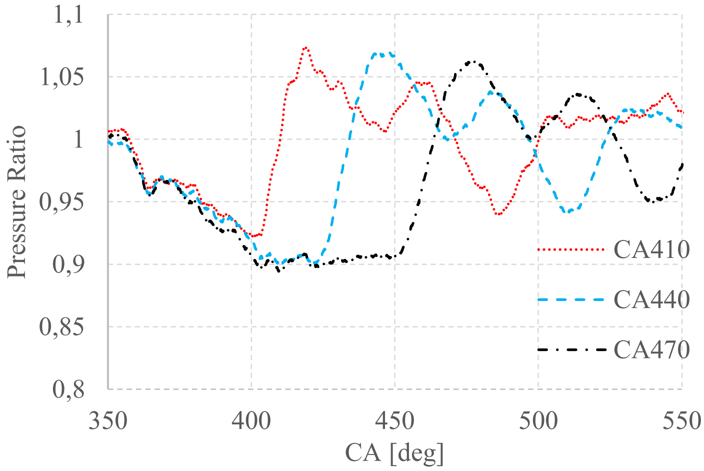

Figure 24: Phase-average Output/Input Pressures ratio HESS 6

As a consequence of the high velocities inside the HESS, a potential air warming, due to the dissipation of the pressure losses in heat because of the internal viscous forces, has to be considered in the air energy balance. In order to confirm the assumption of internal heat generation, the temperature difference ratio $dT_{ef} = \frac{T_2-T_1}{T_2-T_c}$, for the same experimental points as in Figure 21, is plotted on Figure 22. A value of dT_{ef} greater than one is representative of an air temperature, at the outlet of the manifold, higher than the wall temperature. Three possible reasons can explain this result:

1. Heat transfer by conduction occurs between the engine, at a constant temperature of around 82°C, and the manifold, at a temperature of around 20°C. A temperature gradient inside the manifold is then generated. As a consequence, the measured temperature of the external manifold wall, which is used as a reference, may be not representative of the manifold mean temperature.
2. Air can be heated due to the internal viscous forces because of the high velocity reached inside the HESS.
3. Thermocouple measurement can be disturbed by the engine radiation.

Figure 22 shows that for the case without HESS, in which only the physical phenomena that correspond to the assumptions 1 and 3, dT_{ef} is always lower than one. It can be conclude that the predominant source of air warming is the air viscous friction.

- HESS thermal response
  - Phenomena of Recovery and Restoration of Thermal Energy

Figure 25 shows the energy transferred from the hot air to the HESS $'E_{tr,air}'$ and the energy restored by the HESS to the cold air $'E_{re,air}'$ versus the variation of the manifold internal energy 'ΔE_{man}' for the dual phase cycle. Each term is computed as in the following equations:

$$E_{tr,air} = E_{re,air} = \int_{t_{start}}^{t} \dot{m} c_p (T_{inlet} - T_{outlet}) dt \qquad \text{II - 68}$$

$$\Delta E_{man} = m_{cond} c_{cond} \int_{t_{start}}^{t} T_c dt \qquad \text{II - 69}$$

Where $\dot{m}$ is the air MFR, c_p is the air specific thermal capacity at constant pressure expressed in function of the mean air temperature $(T_{inlet} + T_{outlet})/2$, $m_{cond} = 0.4kg$ is the manifold mass and $c_{cond} = 390\,J/kgK$ is the specific thermal capacity of the steel 304L.

The variation of the internal energy of the manifold is calculated under the assumption of a homogeneous temperature field.

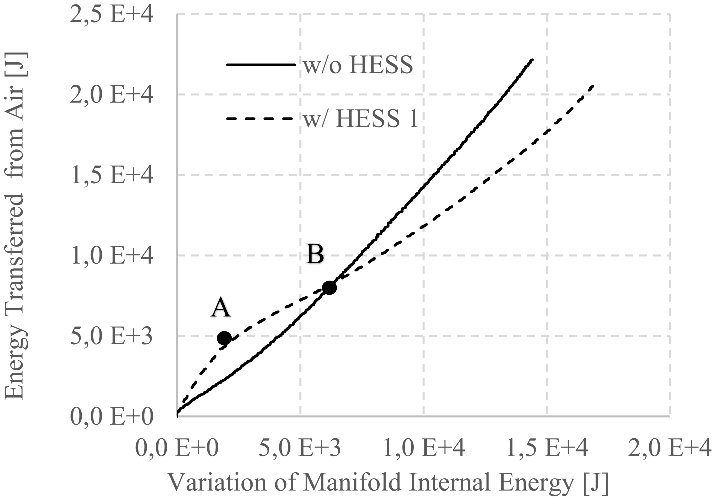

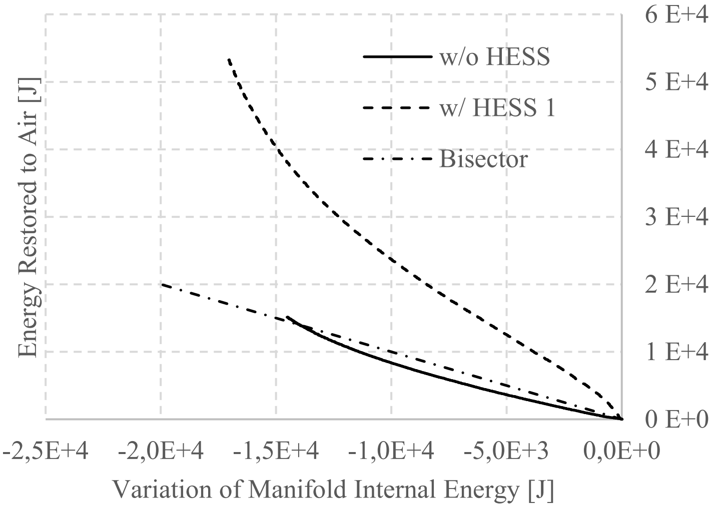

Figure 25: a (top), 'Recovery phase'; b (bottom), 'Restore phase'

In Figure 25a the results for the 'recovery phase' are shown. The initial condition of the recovery phase corresponds to zero energy transferred from the air. The energy balance for the two cases are expressed in the following equations:

$$E_{tr,air} = \Delta E_{man} + E_{conv} + E_{cond} + E_{irr}; \qquad \textit{case without HESS} \qquad \text{II - 70}$$

$$E_{tr,air} = \Delta E_{man} + \Delta E_{HESS} + E_{conv} + E_{cond} + E_{irr}; \qquad \textit{case with HESS} \qquad \text{II - 71}$$

Where E_{conv} represents the energy exchanged by natural convection between the manifold and the surrounding air, E_{cond} is the energy exchanged by conduction from the extremities of the manifold to the connected bodies, E_{irr} is the energy exchanged by radiation between the manifold and the surrounding surfaces and ΔE_{HESS} is the variation of the HESS internal energy.

At the instant of point 'A', in Figure 25a, for a same variation of the manifold internal energy, the energy transferred from the air is higher in the case with the HESS 1 than in the reference case. According to the assumptions of homogeneous temperature, same variation of the manifold internal energy and same initial conditions, the manifold has reached the same temperature in both cases compared on Figure 25.

The terms $E_{conv}, E_{cond}, E_{irr}$ in eqs. II - 70 and II - 71 can then be considered equals and the energy recovered by the HESS can be derived from the two equations. From point 'B', less energy is transferred from the air to the HESS 1 in comparison with the reference case. At this point the HESS has reached its maximum recoverable energy amount and the convective heat transfer is decreased. Owing to its low thermal inertia, resulting from a thermal capacity around twenty times less than that of the manifold, the HESS requires 6.1 seconds less than the empty manifold to recover 5 kJ from the air.

Figure 25b the 'recovery phase' is shown. The bisector represents the ideal case in which the internal energy of the manifold is totally restored into the cold flow. The results show that, in the reference case (solid line), energy of the manifold is not fully restored and is partially dissipated to the surrounding. Only for the final period of the reference case, the results show that there is an additional contribution to the energy restored. This contribution results from the heat transfer by conduction between the engine and the manifold. Results also show that the energy restored to air, in the HESS case, is always above the bisector because of the restored energy contribution which comes from the HESS. Another benefit of the HESS is that 10 kJ are restored into the cold flow in 40 seconds less than in the reference case.

- Restoration/Recovery Energy Efficiency of the HESS

It has been shown that the thermal inertia of the HESS is low compared to than that of the manifold. It is then possible to define a time period 't_{eff}' during which it can be assumed that the energy transferred to air by the HESS (both during the recovery phase that during the restoration phase) is predominant, compared to the energy transferred by the manifold, in the air energy balance equation. As a consequence, the difference of the energy transferred from and to the air, between the HESS and the reference case, corresponds to the energy contribution coming from the HESS. Thereby, during this time period, the air energy balance is used to define the efficiency of the HESS.

During the recovery phase, $t_{eff,}$ is defined as the time when the difference of the energy transferred to air, between the HESS and the reference case, reaches its maximum. The same time period is adopted for the restore phase and the resulting value for t_{eff} is 11.8 seconds.

The energy efficiencies for the recovery phase (η_{rec}) and for the restore phase (η_{res}) are expressed as in the following equations:

$$\eta_{rec} = \frac{E_{rec}}{E_{input}}; \qquad where\ E_{input} = \int_{t_{start}}^{t_{start}+t_{eff}} \dot{m} C_p T_{input} dt \qquad \text{II - 72}$$

$$\eta_{res} = \frac{E_{res}}{E_{rec}} \qquad \text{II - 73}$$

η_{res} is the ratio of the energy transferred from the air (eq. II - 72) to the air energy which enters the manifold. The energy entering the manifold, expressed as E_{input}, has been defined has the time integral of the enthalpy of the air based on the inlet temperature measurement. η_{res} is the ratio of the energy restored to the cold air (eq. II - 73) to the energy recovered from the air in the previous phase.

The product of these two efficiencies defines the global restore/recovery energy efficiency η_{global}. Results are shown in Figure 26. The highest global efficiency, two times higher than that of the reference case, is reached for the HESS 1.The HESS 7 shows the lowest efficiency, almost equal to the reference case for the specified time period.

Results also show a decrease of the recovery efficiency from the HESS 1 to the HESS 7 which is related to a coupled effect of the diminution of the mass and of the exchange surface of the HESS. Concerning the restore efficiency, the HESS 2, which has about the same mass as the HESS 1, but has an exchange surface two times less than that of the HESS 1, shows a restore efficiency higher than that of the HESS 1. The HESS 3, with both the mass and the exchange surface inferior to the ones of the HESS 1, shows a recovery efficiency less than that of the HESS 1, but a restore efficiency almost equal to the one of the HESS 1. It is highlighted that for a constant HESS mass, which stands for a same maximum amount of recoverable energy, the crossbars characteristics in terms of distance and thickness have to be conveniently designed. In spite of a recovery efficiency higher than in the reference case, HESS 6 and 7 show a decreased restore efficiency compared to the reference case, nevertheless the global efficiency is always higher than the reference case.

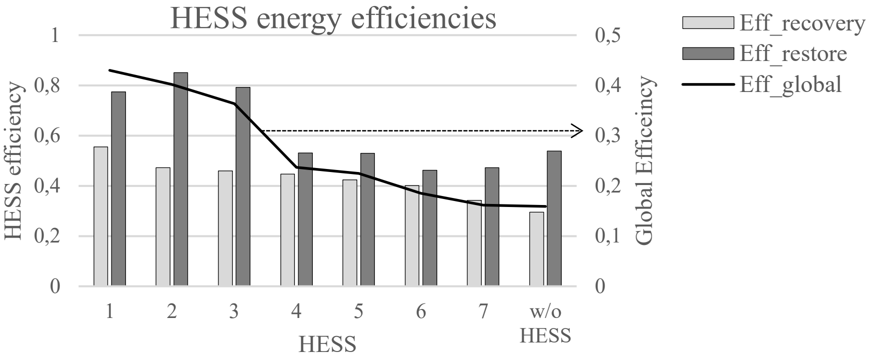

Figure 26: Energy efficiencies of the HESS

- Comparison of the convective heat transfers between experiments and theoretical prediction

This study has also evidenced that the pulsating character of the flow makes the convective heat transfer prediction through the Nusselt correlation based on a steady flow non-adapted.

Starting from the air enthalpy difference in equation II - 68 a global convective heat transfer coefficient has been calculated for the experimental case without HESS. Main purpose was to compare the experimental data to the value calculated from the literature. Convective heat transfer coefficient has been then calculated as:

$$h = \frac{\dot{m}c_p(T_{inlet} - T_{outlet})}{S(T_{c,i} - T_{mean})} \qquad \text{II - 74}$$

Where S is the internal surface of the pipe, $T_{c,i}$ the internal pipe wall temperature and T_{mean} the average temperature of air $(T_{inlet} + T_{outlet})/2$. Since the small thickness of the manifold compared to the manifold length, $T_{c,I}$ has been considered equal to the external wall temperature, experimentally measured as previously presented.

The theoretical convective heat transfer coefficient has been calculated with the Dittus-Boelter correlation of equation II - 42, entrance effects have been accounted for by applying the Bhatti and Shah corrective coefficient [52]. Fluid properties have been computed at the mean temperature T_{mean}.

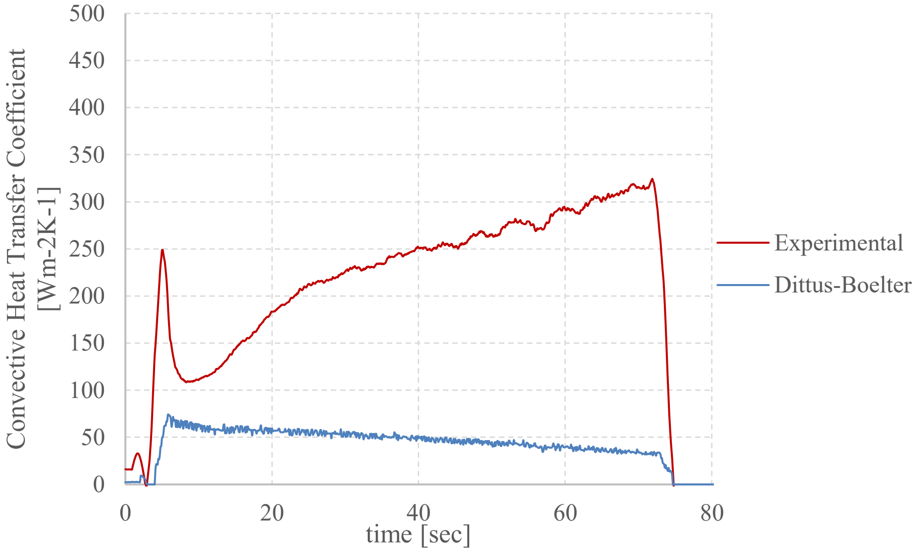

Figure 27: Convective Heat Transfers Comparison between experiments and theoretical prediction

Results in Figure 27 represent the comparison between the convective heat transfer coefficient, during the 'recovery phase', calculated from the experimental data and the theoretical models: it could be observed that the experimental convective heat transfer is up to 6 times higher than the theoretical one. This wide difference could be ascribed to several mistakes made in the application of a stationary Nusselt correlation.

First of all, the theoretical correlation, as previously showed in the paragraph II.2.2, does not account for pulsation frequency effects. It has not possible to test the correlation proposed by Zhai et al. [29] (II - 56) because of none measurement of the air velocity was available.

Furthermore, the entrance effects have been considered using a model for a turbulent stationary flow: as Gundogdu et al. affirmed in their pulsating flow review [19], [20], entrance effect have not been extensively investigated and an universal model has not been still found.

Also compressible effects of the fluid have not been considered: although the pressure oscillate because of the acoustic waves travelling the manifold, during the 'recovery phase' also the time-average component of the air pressure inside the manifold is not constant. It increases from 1 to 10 bar, suggesting that as the pressure increases as the cinematic field modifies.

All these elements make the use of a Nusselt number correlation formulated for a stationary flow non-adapted to this application, as the experimental results show.

II.4 Conclusions, thesis strategy and contribution

In the first part of this chapter, the fundamentals of the convective heat transfer phenomena have been revised, demonstrating that flow pulsations modify the governing equations by adding some terms which cannot be a-priori predicted. For instance, in the phase-average energy balance equation II - 51 for a pulsating turbulent flow, the turbulence influence on the phase-average field of the flow is represented by the phase-averaged cross-product of the turbulent velocity and temperature components. As expressed before, such terms are not theoretically equivalent to the time-average terms for a steady turbulent flow (as in eq. II - 40) and this problem remains nowadays still unsolved.

Furthermore, also in the time-average energy balance equation II - 53, the apparition of the time-averaged cross-product of the oscillating velocity and temperature components makes the Nusselt correlation form for stationary flows non-adapted for a pulsating flows.

It has also reported, by the exhaustive survey of the available previous results, that the variety of the experimental configurations and the variety of the pulsation creation mechanisms have led to some controversies: both enhancement and degradation of the convective heat transfers have been observed, besides, the main physical mechanisms involved have not been fully described. Furthermore, it has been observed that in the specific case of ICE applications a deep understanding of the heat transfers phenomena becomes, nowadays, always an important requirement to face the engine manufacturer needs to respect the stricter emission standards.

Thanks local instantaneous measurements of the flow properties, as well in the study of Dec et al. [24], [25], as well in other studies (Kearney et al. [21], Also Wang et al. [43]) the heat transfers enhancement mechanism according to ejection of fluid during flow reversal increase the heat transversal advection have been observed. In other studies was observed that the ejections usually appearing in a turbulent steady boundary layer (Habib et al. [33], Said et al. [38]) in function of the pulsation frequency could be impacted and then increase heat transfers. However a direct evidence of such impact has not been demonstrated by none measurement.

From a modelling point of view, new Nusselt correlations were proposed to account for pulsation effects: while equation II - 55 was in agreement with the Buckingham Π theorem it was fitted to experimental results with a pulsating flow widely different from the engine exhaust-type pulsating flow. For a pulsating turbulent pipe flow a new correlation (II - 58) was proposed by Hua et al. [32] however it has not been validated in a larger study domain.

Considering all the aforementioned elements, an experimental approach has been chosen to be adopted to fulfill the objective of the thesis: to go further in the comprehension of the convective heat transfer phenomena for engine exhaust-type pulsating.

Because of the difficulty to well manage all the flow properties, a direct study of the heat transfers directly inside an engine manifold has not recommended: an experimental apparatus has been designed and constructed in order to reproduce in a completely managed manner a pulsating pipe hot air flow over a range of $0 \leq f \leq 95$ Hz and $10^4 \leq \mathrm{Re} \leq 5\mathrm{x}10^4$.

To go further on the comprehension of the physical phenomena, a measurement of the instantaneous radial profile of air velocity and temperature has been decided to conduct. Actually such measurement should be useful to compute the different terms in the energy balance equation.

Furthermore, the development of experimental measurements techniques, for pulsating flows, has represented for the Groupe PSA also an important advancement useful to ameliorate the actual diagnostic methodology used in the experimental phase of the ICE calibration. Hot-Wire anemometry and rapid micro-unsheathed thermocouples have been chosen to measure instantaneous radial profiles air velocity and temperature. Such techniques have been validated in the case of pulsating flows, the details are reported in the next chapter.

Data analysis has been split in two different levels of simplification: starting from a time-average 1D analytical approach, the major heat transfer enhancement mechanism has been investigated, and then, the significant terms accounting for pulsation effects has been proposed to be included in a more adapted time-average Nusselt number correlation.

In a second step, experimental data have been analyzed with a 2D phase-average analytical approach: the main purpose is to evidence and demonstrate the presence of a transversal heat advection enhancement which has been found in the previous studies and in different experimental configurations.

Although this 2D approach has been employed to analyse the experimental data, because of the lack of the radial compoenent of the air velocity and because of the lack of spatial detail air temperature, it has not possible to compute all the equations terms deriving by the 2D approach.

In view of this, a CFD phase has been also performed: the main purpose is to study the convective heat transfers for a pulsating turbulent flow in a 2D pipe domain: a particular attention has been paid on the calculation of the axial and radial heat transfer advection to evidence how pulsation impacts such type of heat transport.

The contribution of this thesis should be based on a better comprehension of the mechanisms involving the heat transfer enhancement, as well, in a second step such knowledge should be used to design and optimize the future ICE systems.

In particular, the 1D time-average approach should be useful to account for pulsating effects in the actual time-average Nusselt number correlations, as well the 2D phase-average approach should be advantageous to understand the heat transport mechanisms, and consequently, bend them to fulfill any future thermal requirements.

Chapter / Chapitre III

Material & Methods

Abstract

This chapter focuses on the design and development of the experimental apparatus and the measurement techniques. A test-rig, built with the purpose of study the impact of the pulsation on the convective heat transfer phenomena, it has been designed and presented. For instance, operating conditions are representative of an engine exhaust; in detail pulsation frequency ranges from 10 to 95 Hz and the Reynolds number could be varied between 10^4 and $5x10^4$.

To go further in the comprehension of the heat transfer phenomena a rapid-measurement of air temperature and velocity, within the pulsation cycle, has been applied.

A double parallel hot-wire probe has been used in constant temperature mode to measure the axial component of the air velocity. The unique shape of the probe has permitted to overcome the flow reversal detection limit: a novel methodology to detect flow reversals has been proposed and experimentally validated. Furthermore, also the temperature and pressure impacts on wire voltage have been considerate and compensated after an ad-hoc calibration of the wire.

Type K micro-unsheathed thermocouples have been employed to measure the instantaneous radial profile of the air temperature. A characterization of the time response of the sensor has demonstrated that such sensors require a time-delay compensation due to its first order-type response to a variation in the flow temperature. Although an ‘ex-situ’ characterization of the sensor time-constant has shown its unique dependence on the air velocity, an ‘in-situ’ method has been applied because of the intrinsic limit of the ex-situ methodology of not correctly reproducing the properties of the pulsating flow in controlled conditions. The in-situ technique requires two different thermocouples sensing the same temperature, then, through the Kalman filter mathematics the calculation of the time-constant and the signal compensation could be fulfilled.

The experimental procedure and data reduction have been presented in the case of the pulsating flow, pointing out the impossibility to measure turbulent variations of air velocity and temperature in the case of a hot flow. Contrarily velocity measurements have been conducted for a cold pulsating flow exploiting the advantage of none temperature impact on the wire voltage. Adopting the Reynolds analogy and the hypothesis that the temperature could be considered a passive scalar field, the measurements of the velocity field for the cold flow may be used to have further information on the convective mechanisms. The turbulent temperature fluctuation measurement problem remains still unsolved.

The temperature and velocity radial time-average profiles, for the flow in stationary state, have been analyzed and compared to the available literature models, to be able to affirm that the stationary flow in the test-section could be considered fully developed and the pipe could be considered smooth.

Also an acoustic characterization of the experimental apparatus has been conducted for different pipe lengths, and the results have been presented in this chapter.

III. Material & Methods

III.1 Introduction

As reported by the aforementioned bibliography in paragraph II.3, it has been largely observed that pulsation frequency may have a positive or negative impact on the convective heat transfers, nevertheless, the variety of the experimental configurations and the variety of the pulsation creation mechanisms have led to some controversies. In the majority of the studies both an enhancement and a degradation of the convective heat transfers have been observed, besides the fact that instantaneous temperature and air velocity profiles have not been measured. In this manner authors were not able to evidence the physical mechanisms occurring in the flow.

Main reason of such lack of instantaneous flow property measurement could be likely due to the several inconvenient arising in the case of pulsating flow: a complete overview of pulsating flow measurements has been presented by R. C. Mottram [53].

However, in the recent past years there have been some advancements in the measurement of the flow properties for pulsating flow: a flow facility to instantaneously characterize the flow properties, such as air velocity and temperature, for a pulsating flow was proposed by F. Laurantzon et al. [54]. The pulsating flow was generated by means of a rotating valve and the flow was quantified through a flow measurement module shows in Figure 28:

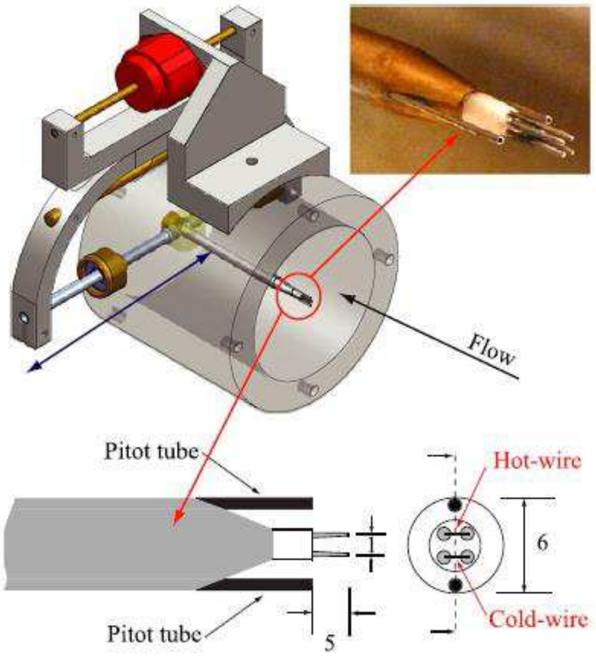

Figure 28: Velocity and temperature measurement module - Laurantzon et al.

Thanks to the measuring probe, which consisted of a hot/cold-wire sensors, the phase-average of the both mass flux and recovery temperature were measured simultaneously. Although, such module has the advantage to measure rapid variations of both air velocity and temperature, it has the disadvantage to be able to be used only for a pulsating flow without flow reversals. Because of the sensor probe is mounted parallel to the flow axis, it can sense the flowing fluid only from one direction, restricting so the available study domain. In particular pulsation frequency reaches the maximum value of 100 Hz for a maximum flow rate of 0.5 kg/s. Anyway, none publication of the results for the heat transfer problem has been found.

A similar test-rig was also proposed by M. O. Carpinlioglu [55], a pulsatile flow was produced by superimposing a purely sinusoidal oscillation on a steady axial flow in a rigid circular pipe. The flow properties were determined via cross-sectional velocity measurements and via wall pressure gradient measurements, a Constant Temperature Anemometer was used to measure air axial velocity. Flow operating conditions, in terms of time-averaged Reynolds number, ranges from 1800 and 60000, and the dimensionless pulsation frequency ω' ranges from 2.72 to 32.21. Anyway, none temperature measurement has been conducted.

In the present chapter, an experimental apparatus able to reproduce a pulsating pipe hot air flow, representative of the behaviour of the engine exhaust, has been designed and tested. Operating conditions cover a wider range than in previous works: the pulsation frequency ranges from 10 to 95 Hz and the Reynolds number, based on the time-average velocity, varies from 10^4 to $5E^4$. In the test-rig a pulsating hot air flow exchanges thermal energy with a water cooled pipe. The novelty of this study consists into the application of specific methodologies to measure instantaneous radial profiles of air temperature and air axial velocity. A hot-wire anemometer and unsheathed type K thermocouples have been adopted to measure respectively phase-detailed air velocity and temperature. The particular shape of the probe has allowed to solve the flow reversal detection problem. Furthermore, a time-delay compensation has been applied to the thermocouple signals through the discrete Kalman filter mathematic to account instantaneous errors in the temperature measurements. The experimental apparatus and the measurements techniques are detailed in the next paragraphs. The experimental procedure and the data reduction, as well as some typical measurement of the flow properties in the case of the pulsating flow are presented without entering the physical details. Also the thermal and acoustic behaviors of the experimental apparatus are investigated and presented in this chapter.

III.2 Experimental apparatus

III.2.1 Test-rig design

A schematic diagram of the pulsatile flow facility is depicted in Figure 29, the test rig can be decomposed in three macro different parts: the first one produces a hot stationary air flow, the second one transforms the stationary flow to a pulsating flow, and, in the last part, in which the flow develops, heat transfers are estimated. In the first part of the test rig, the dry compressed air mass flow rate is measured and regulated by a Brooks SLA5853S {1}, a thermal effect mass flow meter with a maximum flow rate of 2500 Nl/min and with a calibration incertitude of 0.73% of full scale. Then, air is heated by three 'Sylvania inline air heaters' {3} with a total electric power of 12kW, ensuring a maximum air temperature of 400°C at the maximum mass flow rate. Hot flow is finally stored in a steel tank, called 'plenum 1' {4}, with a 30 liters volume designed to withstand a maximum air pressure of 10 bars and to dumper the flow pulsation coming back from the pulse generator.

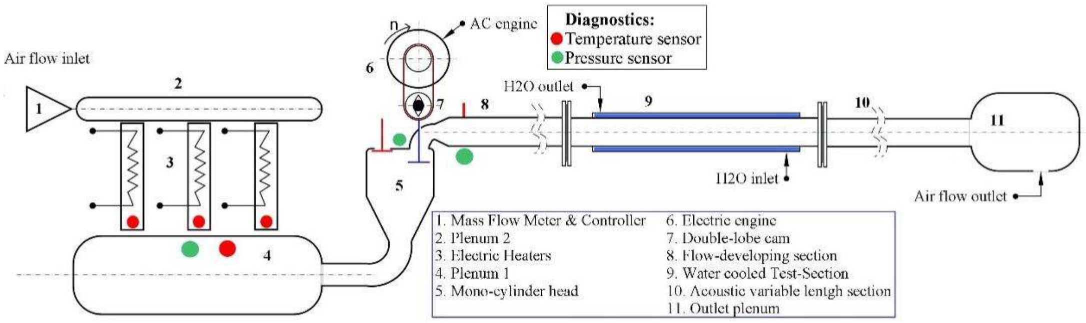

Figure 29: Experimental Apparatus Scheme

Once the hot air flow has been generated it is forced to pass through the pulsating mechanism {5-7}: a mono-cylinder head has been chosen to produce a pulsating flow with a maximum frequency of 95 Hz, equipped with a classical pushrod valve train entrained by an electric engine with a power of 3 kW and a nominal velocity of 3000 rpm. Actually, a siren, a rotating disk with several holes on the periphery as proposed by Hirst [56], was firstly used to create flow pulsations. Such type of pulsation mechanism was used because of the ideal potential to attain up to 200 Hz of pulsation frequencies higher than the cylinder head, anyway, because of air leakage problems it has been abandoned.

Mono-cylinder head has, furthermore, the advantage to be alimented with a high pressure air flow allowing to explore heat transfer mechanisms also for pulsating flow with a time-average pressure widely higher than the ambient pressure. In details, hot air is flowed from the bottom of the cylinder head, and only one intake valve, among the four cylinder valves, is alternately closed and opened to create the pulsating flow. The intake valve has been chosen because of its higher diameter. Air leakages in the cylinder head have been experimentally estimated to be inferior to 0.5 kg/h leading to an error on the mass flow rate measurement inferior to 1%. In order to know the camshaft position and rotation velocity an encoder with a resolution of 0.1° is placed on the camshaft. Once the pulsating flow is generated, it is forced to pass through a steel pipe {8-10} in which it develops and exchanges thermal energy. Finally at the end of the pipe a tank, called 'plenum 2' {11}, with a 6 litres volume it is placed to muffler pressure pulsation, and then, the entire flow facility is linked to the exhaust line of the laboratory.

As shown in Figure 29, the steel pipe is composed of three different sections: the first one, called *developing section* {8}, has a length of 2.65 meters and a pipe length/ internal diameter ratio of 48.4. It has been designed to be length enough to completely develop the cinematic field of the flow if stationary. The pipe is thermally insulated to avoid high heat energy losses. The test section {9} (a particular is showed in Figure 30), with a length of 1 meter, is placed at the outlet of the developing section and is designed to be able to characterize the convective heat transfers. It consists in a double-wall pipe, in which the pulsating air and a cold water flow in opposite directions, respectively in the internal and external part of the pipe. Water cooling has the advantages to be able to manage the wall temperature and to have a homogeneous temperature field in the internal wall of the pipe, moreover, it has the advantage to know from inlet and outlet water temperature measurement the total time-average convective heat transfer 'Q_{conv}' (further details are available in the paragraph IV.2). A 'Kistler Type 2621F conditioning unit', with a maximum cooling power up to 1500 Watt, is used to provide a maximum water flow rate of 6.1 L/min.

As shown in Figure 30, at a distance from the beginning of the test-section of around 10 times the internal pipe diameter, several sensors have been placed to measure the air velocity, temperature, pressure and to measure the water temperature. In particular, in order to calculate the air bulk temperature which corresponds to the section integral of the temperature, in the first section (A – A' in Figure 30) four sheathed type K thermocouples with a 0.5 mm diameter have been placed at different distances from the wall, respectively 1, 0.5, 0.125 , 0.0625 times the pipe radius. Furthermore a 'Kulite' pressure transducer and two 0.5mm sheathed type K thermocouples have been placed to measure the instantaneous static pressure of air and the water temperature. The same arrangement have been used for the outlet section of the test-section. For the remaining sections, except the section B – B', only one 0.5 mm sheathed type K thermocouple has been placed at the centreline of the pipe to measure the air temperature. In the section B – B' one 'Kulite' pressure transducer, a Constant Temperature Anemometer and two unsheathed micro-thermocouples have been placed to measure the instantaneous radial profile of air temperature, velocity and to measure the static air pressure. In particular a Dantec 55P71 double wire probe has been used to measure the air velocity magnitude and to detect flow reversal, moreover, a Kalman Filter method has been applied to the signal of the two micro-thermocouples to calculate in-situ the time constant of the sensor and to account it to correct the measurements and to estimate the real air temperature. An AD595MQ electronic circuit has been used to amplify the thermocouple signals and to compensate the cold junction directly inside the monolithic chip, both the amplifiers have been calibrated to produce a same output voltage for the same temperature measurement. The CTA and the micro-thermocouples have been connected with the pipe with a concentric screw system with a thread pitch of 1 mm. The advantages of such sensors are to analyse the instantaneous variations, within a cycle of pulsation, of the flow properties in order to evidence the momentum and energy transport through the section. As shown in Figure 29, downstream the test-section a pipe with a variable length is used. A modular shape of the pipe has been designed to be able to modify the acoustic behaviour of the pipe.

The total length of the pipe can vary from 3.61 meters to 5.91 meters.

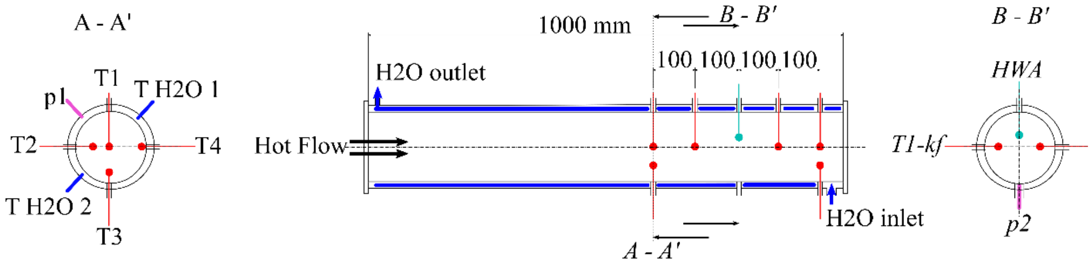

Figure 30: Test-Section

Some photos of the experimental apparatus are reported below:

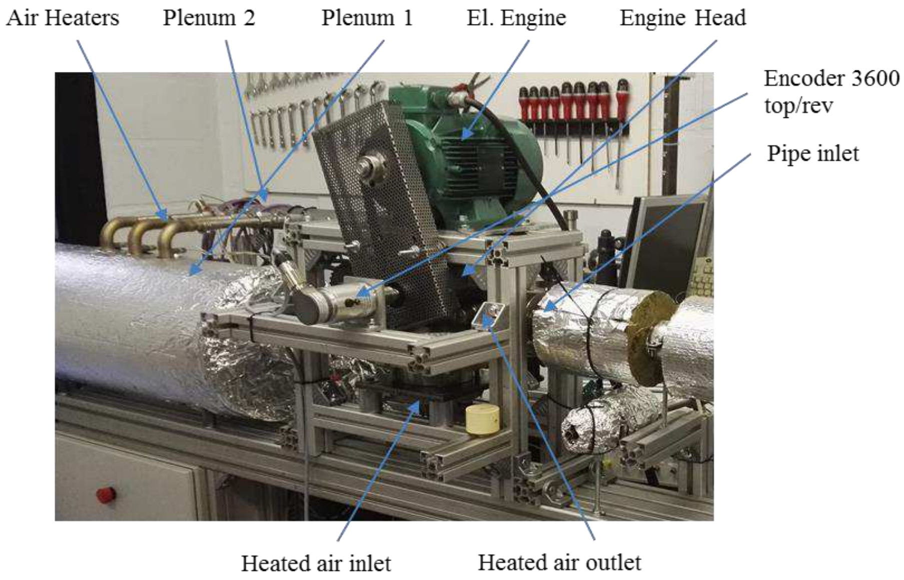

Figure 31: Experimental Apparatus 1

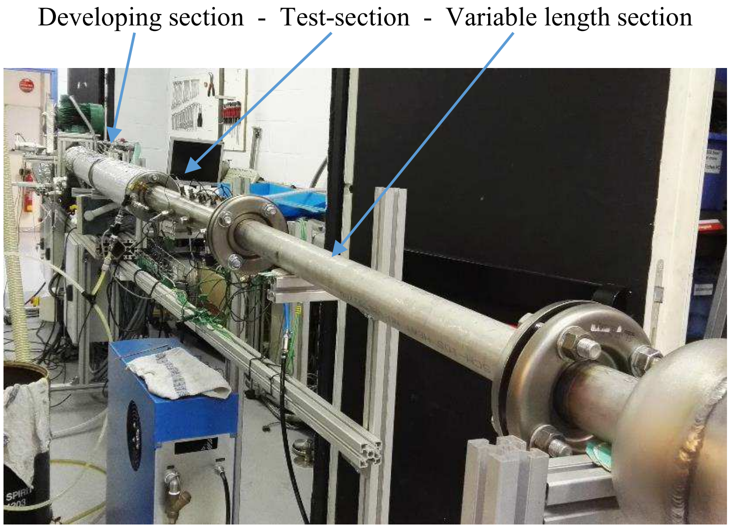

Figure 32: Experimental Apparatus 2

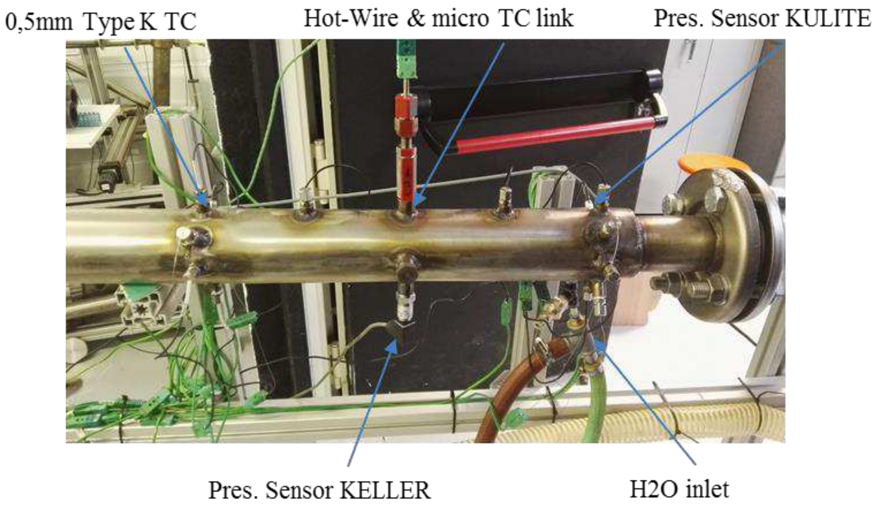

Figure 33: Test-Section detail

III.2.2 Control & Acquisition system and LabView

A NI-9035 cRIO (Figure 34) and the LabView software, are used to control all the devices in the experimental apparatus and to acquire data.

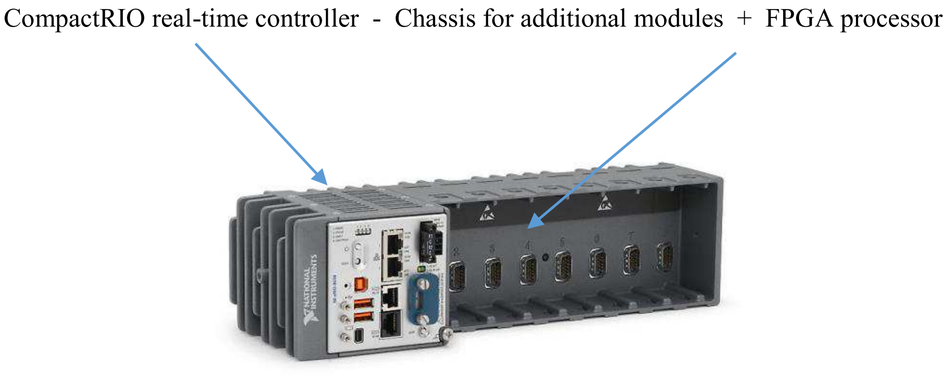

Figure 34: NI-9035 cRIO

CompactRIO (or cRIO) is a real-time embedded industrial controller made by National Instruments for industrial control systems. The CompactRIO system is a combination of a real-time controller chassis, reconfigurable IO Modules (RIO), an FPGA module and an Ethernet expansion chassis. Third-party modules are also available, and are generally compatible with NI-produced chassis controllers. CompactRIO real-time controllers (placed in the left part of the cRIO in Figure 34) include a microprocessor for implementing control algorithms, and support a wide range of clock frequencies. The FPGA Module may be used to implement high-performance data processing on reconfigurable fabric. Such data processing may be performed on data streaming in from connected I/O Modules. The module is powered by a Xilinx Virtex high-performance FPGA. The FPGA can be programmed separately and is connected to the real-time controller using an internal PCI bus. The Ethernet chassis includes an Ethernet port (8P8C), which can connect the CompactRIO controller to a PC. The chassis is available in 4 slot and 8 slot varieties.

The NI-9035 cRIO configuration used in this work is shown in the following figure:

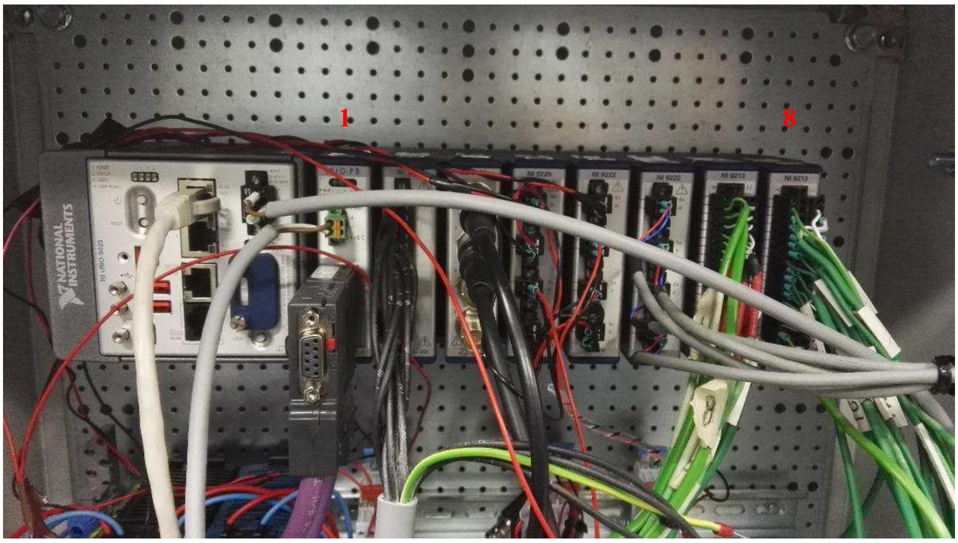

Figure 35: NI-9035 cRIO – final configuration

A chassis with 8 slot has been chosen; the included additional modules are detailed as follows, they are presented in the order starting from the left to the right in Figure 35:

- Profibus Master/Slave Module: used to control the mass flow meter and the electric motor;
- NI 9485 5 is an 8-channel Solid Stare Relay (SSR) sourcing or sinking digital output module. Each channel provides access to an SSR for switching voltages up to 60 VDC, 30 Vrms with switching current of up to 1.2 A per channel for 4 channels and up to 750 mA per channel for all 8 channels. It has been used to control the SSR for the power control of the air heaters. SSRs consist of a sensor which responds to an appropriate input (control signal), a solid-state electronic switching device which switches power to the load circuitry, and a coupling mechanism to enable the control signal to activate this switch without mechanical parts.
- NI 9402, a digital input/output module used to acquire the encoder signals.
- NI 9229, an analog-to-digital input module used to measure mono-cylinder head and the plenum 1 air pressures. Each channel provides a ±60 V measurement range at a 24-bit resolution with a maximum sampling rate of 50 kHz.
- NI 9222 (two modules) is a high-speed simultaneous analog-to-digital module with a sampling rate of 500 kHz, 4 channels are available for each module. In the first module the static air pressures at the outlet of the cylinder head, and at three different axial positions in the test-section have been simultaneously measured. In the second module, the analogic signals of the two parallel wire probe and the output amplified micro-thermocouples from the AD595MQs have been acquired.
- NI 9213 (two modules) is a 16-channel high-density thermocouple module. Each channel passes through a differential filter and then is multiplexed and sampled by a 24- bit analog-to-

digital converter (ADC). The channels share a common ground, COM, that is isolated from other modules in the system (Figure 36). A total of 32 channels for the two modules have been used to measure the thermocouple signals widespread in the test rig. At the High-speed mode a sampling rate of 75Hz per channel is available.

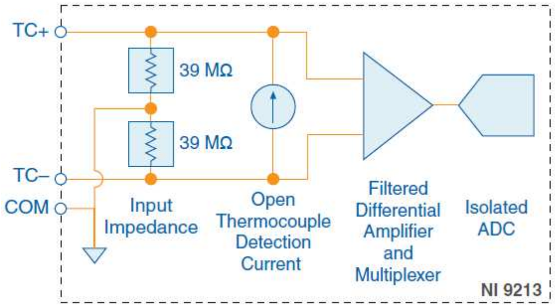

Figure 36: Input Circuitry for One Channel of the NI 9213

The LabView software is a system-design platform and development environment for a visual programming language from National Instruments. The programming language used in LabVIEW, named G, is a dataflow programming language. Execution is determined by the structure of a graphical block diagram (the LabVIEW-source code) on which the programmer connects different function-nodes by drawing wires. These wires propagate variables and any node can execute as soon as all its input data become available. Since this might be the case for multiple nodes simultaneously, G can execute inherently in parallel. Multi-processing and multi-threading hardware is exploited automatically by the built-in scheduler, which multiplexes multiple OS threads over the nodes ready for execution.

It has been used to independently control the real-time and the FPGA processors with two source codes. While in the real-time processor of the cRIO the control of the air heaters and the mass flow meter, and the acquisition of the 0.5 mm thermocouple signals have been performed; in the FPGA processor the digital data from NI 9222, 9229, 9402, 9485 have been acquired.

III.3 Hot-wire anemometry for velocity measurement in a pulsating hot flow

Among the numerous existing several techniques to measure the instantaneous velocity of a flow, in this study the Hot-Wire anemometry has been chosen as the most feasible technique: the main purpose is to measure the radial instantaneous profile of the axial component of the air velocity.

Hot-Wire Anemometers (HWAs) (Figure 37) are devices widely used to measure the variables occurring in turbulent flows [57], such as mean- and fluctuating- velocity components.

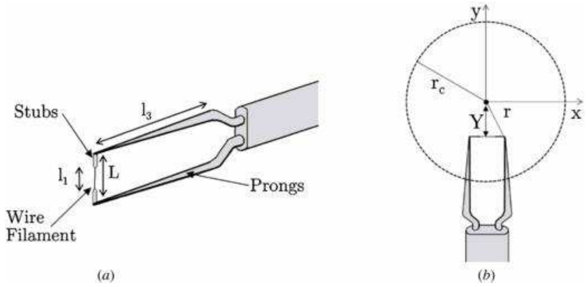

Figure 37: Hot-Wire Anemometer

The sensor is a thin metallic element heated by an electric current, that once it is immerged in a colder incident flow, which acts by virtue of its mass flux and its temperature, the wire exchanges thermal energy with the flow and the voltage or the current traversing the wire change. For flow varying from free-molecular to continuum motion, and speeds from those of natural convection to supersonic, heat transfers around the wire could be characterized by a Nusselt number as follows:

$$Nu = Nu\left(Re, Gr, Ma, Pr, \gamma, \frac{2l}{d_r}, \emptyset, a\right) \qquad \text{III - 75}$$

where the dimensionless parameters involved are respectively:

- Re: Reynolds number based on the wire diameter;
- Gr: Grashof number based on the wire diameter;
- Ma: Mach number of the flow;
- Pr: Prandtl number of the fluid;
- γ: ratio of specific heats of the fluid;
- $\frac{2l}{d}$: aspect ratio of the wire;
- $2l$: length of the wire;
- d_r : diameter of the wire ;
- $\emptyset$: angle between the velocity and the normal to the wire;
- $a = \frac{(\theta_w - \theta_{air})}{\theta_{air}}$: overheat ratio of the wire
- θ_w is the wire temperature and θ_{air} is the flow temperature.

Empirical expressions for III - 75 are available depending on the flow range interest. For forced convection, when compressibility effects are negligible, a frequently used expression is

$$Nu_f = 0.42Pr_f^{0.26} + 0.57Pr_f^{0.33}Re_f^{0.5} \qquad \text{III - 76}$$

as proposed by Kramers (1946). Several restricted to air useful expressions are available at page 213 of [58].

Considering the wire immersed in a fluid flow, and, assuming that the wire is heated by an electrical current input, the energy balance equation follows:

$$mc\frac{\partial\theta_w}{\partial t} = \quad -\lambda\frac{\partial^2\theta_w}{\partial x^2} + h\pi d(\theta_w - \theta_{air}) + \varepsilon\sigma\pi d(\theta_w^4 - \theta_{air}^4) \; + V_w I_w \qquad \text{III - 77}$$

where V_w is the hot-wire voltage and I_w is the input current.

Hot-wire anemometer is also based on the electrical resistance dependence from the wire temperature according the following equation:

$$R_w = R_0(1 + \alpha\Delta T) \qquad \text{III - 78}$$

Where α is the temperature coefficient of the resistance, R_0 the wire resistance at a reference temperature T_0, and $\Delta T = T - T_0$.

Left side term in III - 77 represents the internal energy variation of the wire, while the right side terms represent respectively the heat transfers by conduction, convection and the thermal radiation. The last term in the right side of III - 77 represents the electrical power applied to heat the wire.

Combining eqs. III - 76 and III - 77 a relationship between the flow properties and the wire voltage or current could be found. Two types of thermal (hot-wire) anemometers are commonly used: constant-temperature and constant-current. We used the first one type in which a Wheatstone bridge is used to adjust the current to maintain the wire at constant temperature.

In such operating conditions, neglecting the heat conduction and radiation, the equation III - 77 could be simplified as:

$$h\pi d(\theta_w - \theta_{air}) \; = \frac{V_w^2}{R_w} \qquad \text{III - 79}$$

Where R_w is the resistance of the wire, which for instance is constant during the time.

Several advantages exist in the velocity measurement in low or moderate turbulence intensity flows with a conventional HWA in Constant Temperature Mode (CTA) [57]: a high enough frequency response, it is possible to attain a bandwidth frequency up to 20 - 50 kHz thanks its relatively small size (about 5 μm of diameter and 1 mm of length); a high signal to noise ratio and the potential to apply conventionally conditionally-sampled time-domain and frequency-domain analysis on the wire signal.

Despite its numerous advantages make the HWA suitable for velocity measurements in turbulent stationary cold flows, several problems appear once the hot-wire is subjected to a pulsating turbulent hot flow [59]: both air velocity, temperature and pressure variate within time, making more complex the calibration phase. Velocity, pressure and temperature variations impact the left side term of eq. III - 79.

Furthermore, a high air temperature and velocity require a particular arrangement of the wire due to its mechanical limits. The measurement of the only magnitude of the air velocity makes the flow reversal detection an ulterior inconvenient of the hot-wire anemometry in pulsating flow applications. In the following lines these problems are analyzed and solved.

III.3.1 Choice of the hot-wire material and dimensions

The sensor material has been selected on the basis of the application. Since the wire could be subjected to high air velocity and temperature, to withstand the flow a tradeoff between a high tensile strength and a high maximum operating temperature has to be found.

Although the tungsten is the material widely used in wind tunnel applications because of its highest tensile strength, as could be observed in Figure 38, it presents also a low resistivity and a low maximum operating temperature. Such characteristics imply, respectively, that it should have a low flow sensitivity as well as it should be immerged in a cold flow in order to keep a overheat ratio a of 0.8 giving an over-temperature between 200 and 300°C. Due to its low maximum operating temperature, tungsten wire has not been considered as the right candidate for the hot-wire anemometry.

In Figure 38 it could be also observed that among the pure platinum and platinum alloys which all have an high maximum operating temperature, the Platinum Iridium alloy is the which one with the highest tensile strength as well the highest resistivity, leading so to a high mechanical stress resistance and a high flow sensitivity. For this reason it has been chosen as the best candidate for the hot-wire anemometer.

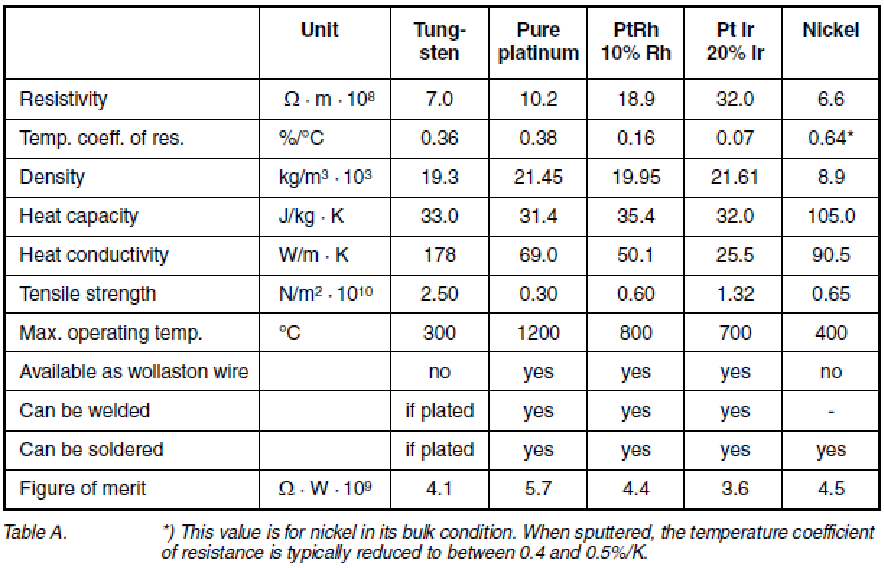

	Unit	Tung-sten	Pure platinum	PtRh 10% Rh	Pt Ir 20% Ir	Nickel
Resistivity	$\Omega \cdot m \cdot 10^8$	7.0	10.2	18.9	32.0	6.6
Temp. coeff. of res.	%/°C	0.36	0.38	0.16	0.07	0.64*
Density	$kg/m^3 \cdot 10^3$	19.3	21.45	19.95	21.61	8.9
Heat capacity	$J/kg \cdot K$	33.0	31.4	35.4	32.0	105.0
Heat conductivity	$W/m \cdot K$	178	69.0	50.1	25.5	90.5
Tensile strength	$N/m^2 \cdot 10^{10}$	2.50	0.30	0.60	1.32	0.65
Max. operating temp.	°C	300	1200	800	700	400
Available as wollaston wire		no	yes	yes	yes	no
Can be welded		if plated	yes	yes	yes	-
Can be soldered		if plated	yes	yes	yes	yes
Figure of merit	$\Omega \cdot W \cdot 10^9$	4.1	5.7	4.4	3.6	4.5

Table A. **) This value is for nickel in its bulk condition. When sputtered, the temperature coefficient of resistance is typically reduced to between 0.4 and 0.5%/K.*

Figure 38: Wire material properties

Once the material has been chosen, several wires of different diameters (10 and 20 µm) and Iridium concentrations (10 and 20%) have been tested in a calibration unit (Figure 39) at different air velocities (0 to 100 m/s), air temperatures (20° to 250°C) and HWA's overheat ratios.

A synoptic scheme of the calibration unit is depicted in the following figure:

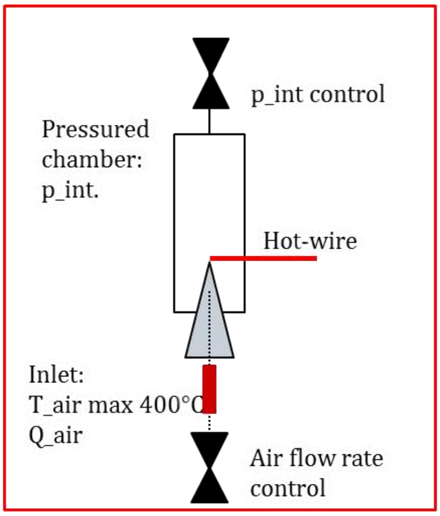

Figure 39: Hot-Wire calibration unit

The hot-wire probe has been placed perpendicular to a jet used to reproduce a flow with a variable velocity and temperature. Both the hot-wire and the jet have been enclosed in a tank. A manual valve has been placed at the outlet port of the tank to be able to control air pressure inside the volume. A thermal mass flow meter Brooks SLA5853S has been used to flow and control the air mass flow rate, and a Sylvania 4kW heaters has been used to warm the air temperature at the jet outlet.

Some photos of the calibration unit are reported in the following figures:

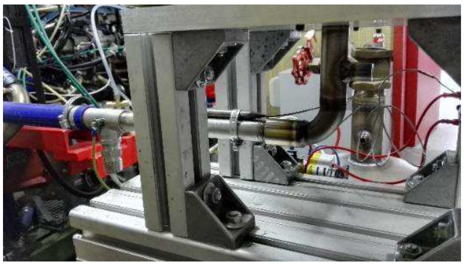

Figure 40: Sylvania air heater

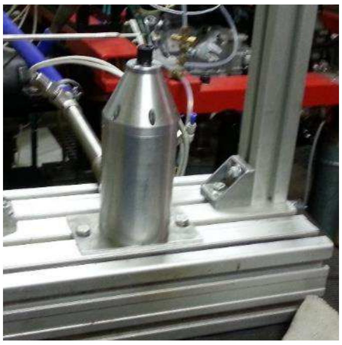

Figure 41: Air jet + Hot-wire probe

Figure 42: Assembly of the calibration unit

The different wires have been respectively welded and tested with a Dantec 55P11 single straight wire probe (Figure 41). The wire of Pt – Ir 20% with a diameter of 10 µm has been finally selected because of the trade-off between its sensitivity to flow temperature variations and its resistance to mechanical stress.

A well-known source of experimental error in hot-wire anemometry measurements of turbulence is the spatial filtering of velocity fluctuations, which occurs when the sensing length of the probe, ‘l’, is larger than the smallest turbulence length scale. Furthermore, increasing the length of the wire has the additional undesired effect of reducing the frequency response of the wire. A standard Dantec 55P11 hot-wire probe has a wire length of 1.25 mm. By reducing the distance between the prongs of the probe, in Figure 37, a wire length of 0.5mm has been tested in the previous hot-wire calibration unit and compared to the 1.25 mm case, in order to investigate the wire length impact on the temporal and spatial filtering. It is important to underline that, a less distance between the prongs may also increase the disturbance of the prongs on the hot-wire measurement.

Both the two wires have been tested under the same flow conditions and with a same overheat ratio. Instantaneous signals have been acquired with a rate of 10 kHz. Results are showed in Figure 43: the Power Spectral Density ‘PSD’ has been computed for both the wires. Results show that, although the shortest wire (blue line in Figure 43) has at high frequency a PSD higher than the second wire, because of a low spatial filtering, the temporal sensitivity of the wire is quite the same, furthermore, in the inertial range of the PSD both the wires show the same behavior. The peaks in both the PSDs at a frequency of around 10^4 Hz has been demonstrated to be caused by electronic noise. A measurement of the hot-wire signal in zero velocity conditions has been used to validate such theory. It has also observed that, a shorter wire is subjected to higher electronic noise due to its lower resistance.

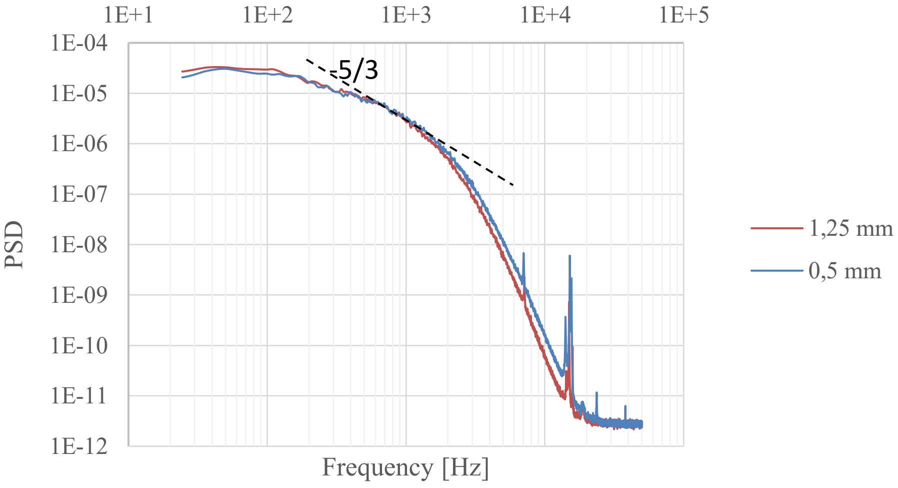

Figure 43: PSD of hot-wire measurement for a steady turbulent jet flow – Wire length investigation

Because of a similar temporal sensitivity and because of the longest wire is less impacted from the electronic noise, in this study the wire with a 1.25 mm of length has been chosen to be used to measure the velocity in the pulsating flow.

III.3.2 Flow properties impact on the Hot-Wire measurement

As previously affirmed, in a pulsating flow both pressure and temperature as well as the pressure variate cyclically. In subsonic incompressible flow, as reported by Stainback et al. [60], the heat transfer from a wire is a function of mass flow, total temperature and wire temperature. In subsonic compressible, transonic and low supersonic flows the effects of compressibility influence the heat transfer from a wire. Evidence exist which indicate that Nu is also a function of a temperature parameter. For these conditions the heat transfer from the wire is a $f(u,\rho,\theta_w,\theta_{air})$, and $Nu(Re,\theta_{air})$.

From the results of P.C. Stainback et al. [60] it has been observed that the density variations due to pressure variations for a subsonic flow could be neglect, implying that the only sensible parameters which impact the heat transfers of the wire are the air temperature and velocity in the case of a constant temperature mode anemometer.

However it has to be considered that the pressure variations due to the acoustic wave could have a considerable influence on the wire voltage, for this reason, and assuming the principle of 'overlapping effects' a sensibility study of the pressure and temperature impact on the wire voltage have been performed in the calibration unit for a wire of Pt – Ir 20% with a diameter of 10 µm.

Pressure has been varied from 1 to 3 bar, results are showed in Figure 44 for a constant air temperature of 22°C: an increase of air pressure implies an increase of the heat transfers between the flow and the wire and then an increase of the wire voltage to keep the wire at constant temperature. A correlation to account for pressure effects and to correct the wire voltage V_{w_corr-p} has been proposed as:

$$V_{w\_corr-p} = V_w \left(\frac{p}{p_{cal}}\right)^n \qquad \text{III - 80}$$

The measured wire voltage V_w is corrected with a coefficient which is an 'n' power of the ratio of the real air pressure and the pressure calibration. An error of 5% has been found between the measure and the corrected wire voltage. Such kind of wire correction needs anyway an ulterior measurement of the air pressure.

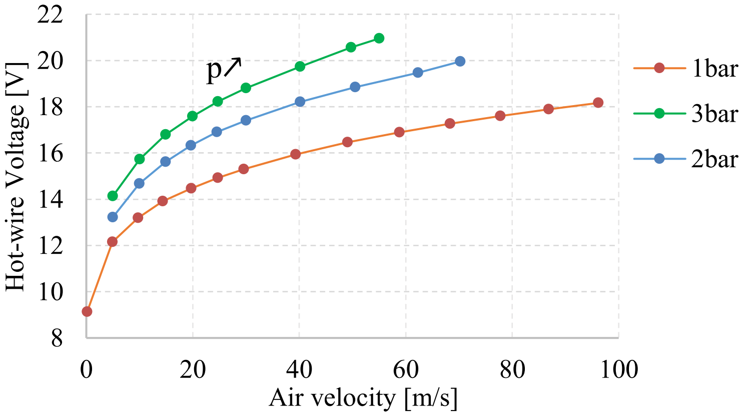

Figure 44: Impact of air pressure on Hot-Wire voltage

Starting from the studies of Collis and Williams [61], Chevray et al. [62] proposed a methodology to measure, with a two hot-wires probe, both air temperature and velocity in the case of a steady turbulent hot flow. Basing on an two hot-wires with different material properties or different overheat ratios, Chevray et al. [62] affirmed that if the two wires sense the same flow, and thus they have the same heat transfer conditions, a two-equation system with two unknowns (u, θ_{air}) is obtained and it can be solved writing the equation III - 79 for both the wires. Such method has been investigated, in this study, but not satisfying results have been found. Figure 45 shows the voltages for a Pt-Ir 10% and Pt-Ir 20% hot-wires with a diameter of 10 μm, in function of the air temperature and velocity. Wires voltage are reported for constant air temperature and constant air velocity: Violet line (in Figure 45) represents the air velocity variation from 5 to 50 m/s for a constant air temperature of 22°C. Green line corresponds to a constant velocity of 30 m/s and a variable temperature from 22 to 120°C; red line corresponds to a constant velocity of 20 m/s and a variable temperature from 22 to 120°C and blue line corresponds to a constant velocity of 10 m/s and a variable temperature from 22 to 100°C.

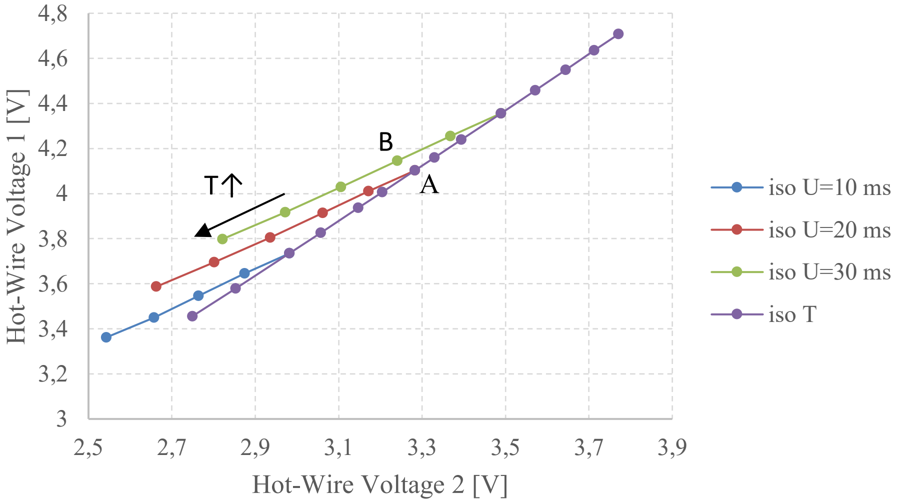

Figure 45: Hot-wires voltage V_1 vs V_2 for a variable air velocity and temperature

Results in Figure 45 show that the slope of the constant temperature and constants velocity curves are not enough different, implying that a diminution of the air velocity produces a decrease of the wire voltages similar to an increase of the air temperature. In this manner, a minimum error in one of the two wire voltages could be interpreted in a quite different couple of air velocity and temperature. For example, in Figure 45 for a wire error inferior to 0.1 V we could measure the point A unlike the B. The flow properties corresponding to these points are quite different and they are respectively 20 m/s - 22°C and 30 m/s – 60°C. In view of all this, such technic has not been used because of the mathematical inversion of the wire voltage measurements to the flow properties was found to be ill-conditioned, leading to temperature errors up to 30% of the real sensed temperature.

A compensation a-posteriori of the temperature effects on the HWA signal has been chosen as a feasible solution, requiring an ulterior rapid temperature measurement, which will be detailed in the next section. Although, in the literature [63]–[66], several correlations for the temperature compensation have been proposed, because of the relatively narrow domain in which air temperature has been varied, an ad-hoc calibration of the hot-wire has been adopted in this work. The wire has been calibrated in a flow with a velocity ranging from 0 to 97 m/s and air temperature varying from the 20 °C to 250 °C (Figure 46).

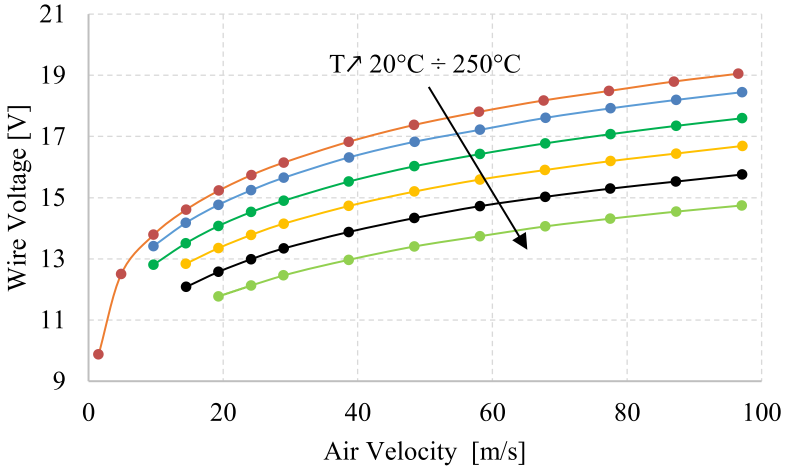

Figure 46: Influence of the air temperature on the Hot-Wire voltage measurement

An increase of air temperature corresponds to a decrease of the wire voltage because of less power in required to keep the wire at constant temperature.

A correction coefficient ‘C_T’ has been defined to compensate the temperature effect on the wire voltage, as shown in following equations:

$$V_{w\_corr-T} = V_w C_T \tag{III - 81}$$

$$C_T = A\left(\frac{\theta_{air}}{\theta_w}\right)^2 + B\left(\frac{\theta_{air}}{\theta_w}\right) + C \tag{III - 82}$$

A, B, C are constants calculated from the hot-wire calibration. C_T has been found to have a second order polynomial form in function of the air/wire temperatures ratio, and it has been found to be valid for each of the air velocity with a temperature maximum error of 1.2%.

Finally, the wire voltage/air velocity transfer function, as showed by the red line in Figure 46, has been interpolated with a 5th order polynomial form. Fitting velocity errors have been found to be inferior to the 1%.

III.3.3 Flow reversal detection

As Berson et al. [59] claimed in a pulsating flow, the inversion of the velocity direction, i.e. flow reversal, could appear. To detect flow reversals several technics were proposed in previous works: an ordinary hot wire anemometer, with two additional fine resistance thermometer wires placed one on either side of the hot wire and at right angles to it, was used to detect flow direction by Downing et al. [67]. The resistance thermometers sense the heated wake of the hot wire and this signal is used to correct the 'rectifying' effect of the hot wire, upon the indicated velocity, under reverse flow conditions. Gupta et al. [68] proposed a reverse flow sensing hot-wire probe based on the principle of detection of the Karman vortex street in the near wake of a circular cylinder was designed and fabricated. In 2004 a shielded hot-wire probe was designed and tested by Benjamin et al. [69] to detect flow reversals in a one-dimensional pulsating flow regime for frequencies of 66 and 100 Hz. The single-sensor hot wire, partially surrounded by a tubular shield with an oblique tip, successfully detected the intermittent flow reversals caused by the flow interruption device in a pulsating air flow rig. Anyway, the time-consuming disadvantage of such technique have made it not suitable in this work. In 2010 a flying hot wire technique was introduced by Fernàndez-Roque et al. [70], and, an ulterior technic was adopted by using a two film probe by Ardekani et al. [71]. Although in the aforementioned works several solutions to the flow reversal detection problem have been proposed, because of the technological complexity, in this study a novel technique based on a double parallel straight hot-wire probe Dantec 55P71 has been investigated. While, placed parallel to the flow direction such probe is widely used to measure the spatial gradient of the flow velocity in the wind tunnel application; in this study it has been placed perpendicular to the flow. In this manner and because of the two wires are parallel and outdistanced of 0.4 mm a variation in the flow direction should likely be detected because of the time delay of the signal minima. Furthermore, a higher phase-average standard deviation of one wire in comparison to the other one, consequence of the perturbations created from the first wire and its prongs to second one, may potentially be used as a second method to validate the detection of the flow direction.

The experimental apparatus, in Figure 29, previously presented has been used to validate such technique, the correct detection of the flow reversal has been validated by the comparison of the calculated time-average axial velocities from the mass flow meter and the hot-wire anemometer. A pulsating cold flow has been generated through the mono-cylinder head. The pulsation frequency has been fixed at 10 Hz, the flow temperature has been keep constant to 25°C and the time-average bulk axial air velocity has been maintained constant to 14.7 m/s (which corresponds to a mean mass flow rate of 110 kg/h flowing in a pipe with an internal diameter of 54.8 mm). A Dantec StreamLine Frame with the 90C10 CTA modules has been adopted to heat the probe in a Constant Temperature Anemometry mode (CTA). In order to apply the phase-average technique hot-wire signals have been triggered with the external encoder signal, which makes possible to define a phase reference angle. The HWA probe has been perpendicularly fixed to the pipe and the wire 1 has been placed upstream the time-average flow direction: in a case in which the particles move coherently to the time-average flow direction, the wire 1 should sense flow velocity before the wire 2, while, when flow reversal occurs the wire 2 becomes the wire upstream to the flow direction. It has been assumed for convention that a positive flow velocity direction corresponds to a flow displacement from the cylinder head to the outlet of the test rig.

Figure 47 shows the phase-average component (solid lines) and the phase-average standard deviation (dot lines) of the both wire signals. The phase-average component has been calculated as showed in (equation II - 44); and, the phase-average standard deviation has been calculated according the following equation:

$$< Z(x,t) >_{SD} = \sqrt{\frac{1}{N}\sum_{n=0}^{N}(Z(x,t+n\tau) - < Z(x,t+n\tau) >)^2} \qquad \text{III - 83}$$

Results show that phase-average standard deviations during the pulsation cycle, they are alternatively inferiors for both the wires: as the Figure 47 shows, in the green zones of the cycle the wire 1 shows a deviation standard inferior to the wire 2, contrarily, to the orange zones. According the results, and knowing the placement of the wires, in the green zones the air should have a positive velocity and in the orange zones the flow reversal should occurs.

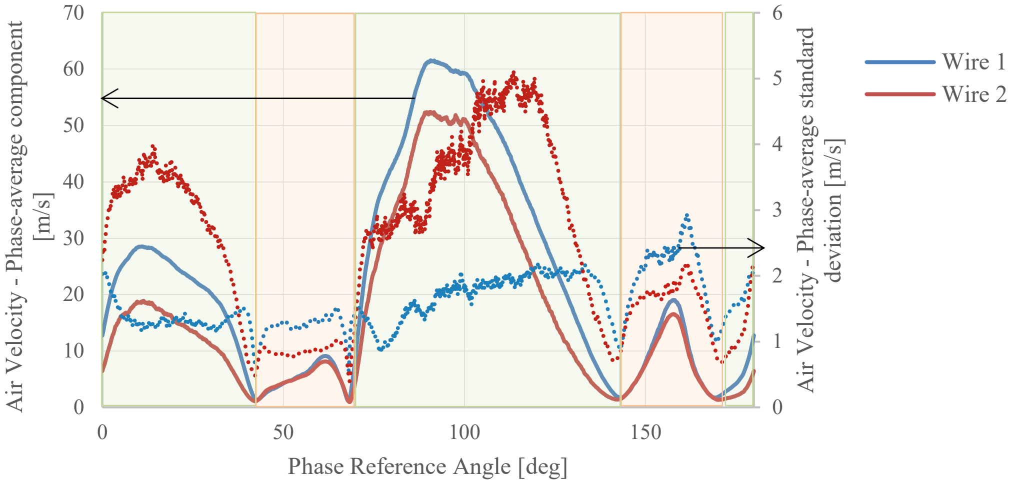

Figure 47: Air velocity components for the double HWA probe

Zooming around the minima of the phase-average component of the velocity, as in Figure 48, it could be also observed that a phase delay between the minima of either the two wire signals exists.

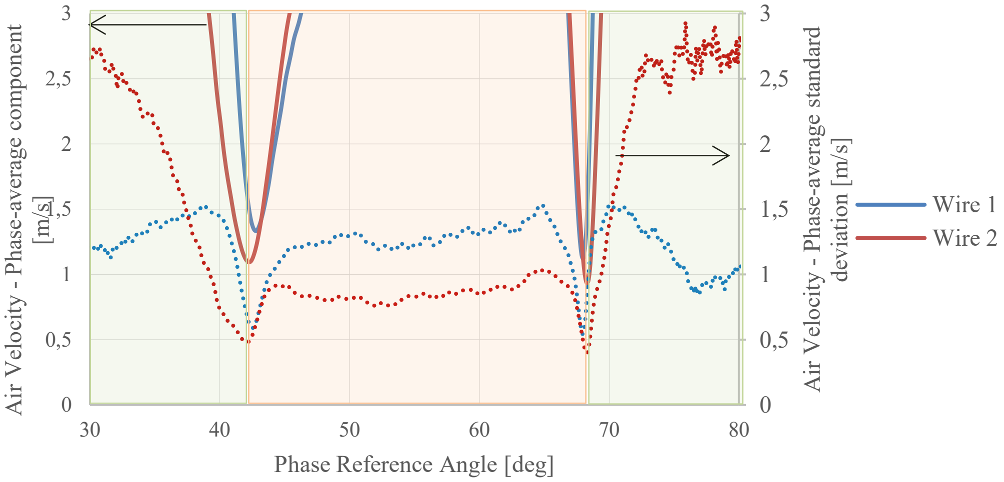

Figure 48: Zoom of the figure 3, time delay of the signal minima

Within the phase angle interval between 40 and 45 camshaft angle degree (CAD), in Figure 48, the wire 2 senses before the wire 1 the deceleration/acceleration of the air velocity, contrarily to which occurs in the interval between 65 and 70 CAD.

Considering that the wire which firstly senses the velocity variation should be the wire upstream the flow instantaneous direction, it could be affirmed that within the phase angle interval between 40 and

45 CAD a flow reversal occurs and the direction of the flow becomes negative, while, in the interval between 65 and 70 CAD another velocity direction change occurs and the direction of the flow should become positive. The phase-average standard deviation and the minimum time-delay analysis show a coherent detection of the flow reversal. Once the flow reversal instants are identified, the real air axial velocity is calculated respectively selecting the velocity measurement from the only wire placed upstream the flow direction.

During the hot-wire measurement analysis it could be noted that some errors at very low velocity exist: a zero velocity is never measured. In such conditions, the hypothesis that the axial velocity component could be considered superior to the others, and the hypothesis that heat is exchanged mainly by the convection process are not anymore valid. As Berson et al. [59] show in their study, near flow reversal, the thermal boundary layer in the oscillating flow is thinner than in the quiescent fluid, resulting in a larger local heat transfer, and it is also slightly asymmetric. It is interesting to note that, near flow reversal, the same absolute Reynolds number corresponds to different Nusselt numbers, so that there is no unique correlation between fluid velocity and heat transfer. In addition, the distortion of the signal near flow reversal becomes more important as the amplitude and the frequency of velocity oscillations increase. Anyway, because of the studied frequencies are widely inferior to the which ones investigated in the works of Berson et al. [59], low velocity errors during flow reversal have not been considered and none correction of the wire signals has been applied in this study.

Finally a straight probe with a double parallel wires has been proposed to measure air velocity magnitude and direction for a pulsating turbulent pipe flow. A method to compensate the HWA signals for air temperature variations and a technic to a-posteriori detect the flow reversals have been presented and discussed, making the HWA a cost-effective method to study fluid-mechanic. An instantaneous temperature measurement is anyway required to calculate the correction coefficient C_T and it will be detailed in the next paragraph.

III.4 Rapid temperature measurement by unsheathed micro-Thermocouples

Thermocouple sensors are widely used to measure the temperature of fluid or solid corps; they are constituted by two different wires which are welded at one end, called ‘hot junction’, and free at the other end, which is called ‘reference end’. Because of the temperature difference between the ‘hot junction’ and the ‘reference end’ a voltage difference, according the Seebeck effect, can be measured between the two thermos-elements. If the thermocouple is immersed in a hot flow heat transfers establish between the flow and the hot junction. The flow temperature ‘T_g’ could be computed by solving the energy balance equation applied to the hot junction ‘T_j’, as stated in the following equation:

$$T_g - T_j = \frac{\rho_c c_j d}{4h_t}\frac{\partial T_j}{\partial t} - \frac{\lambda_j d}{4h_t}\frac{\partial^2 T_j}{\partial x^2} + \frac{\varepsilon_j \sigma}{t}\left(T_j^4 - T_{surr}^4\right) \qquad \text{III - 84}$$

As eq. III - 84 shows the difference between the gas temperature (T_g) and the hot junction temperature (T_j) depends by three effects: a thermocouple temperature delay due to the finite mass of the hot junction and due to the convective heat transfers between the fluid and the hot-junction; a thermal conduction error, a temperature gradient exists between the wire and the support, and heat will conduct from or to the wire; and the radiation error between the junction and the surrounding T_{surr}.

Assuming negligible thermal conduction and radiation, eq. III - 84 may be reduced as following:

$$T_g - T_j = \tau\frac{\partial T_j}{\partial t} \qquad \text{III - 85}$$

Where $\tau = \frac{\rho_c c_j d}{4h}$ represents the time constant of the thermocouples, it is function of the thermocouple properties, mass and the forced convection condition around the hot junction. As could be noted in the eq. III - 85 a thermocouple could be modelled like a first-order system, where τ represents the requested time the sensor needs to reach the gas temperature. For rapid temperature measurements, such time-constant has to be compared to the dynamic of the flow property variations in order to know if a compensation of the time delay has to be applied to the thermocouple signal to compute the real fluid temperature.

III.4.1 ‘Ex-situ’ characterization of the thermocouple response time

In this work, in order to investigate which parameters impact the time constant of a thermocouple sensor, an experimental characterization has been conducted for a type K unsheathed thermocouple with a wire diameter of 25 µm. A special calibration apparatus has been designed for this purpose and it has been showed in Figure 49 and Figure 50.

Figure 49: Thermocouple characterization apparatus – Rotating wheel

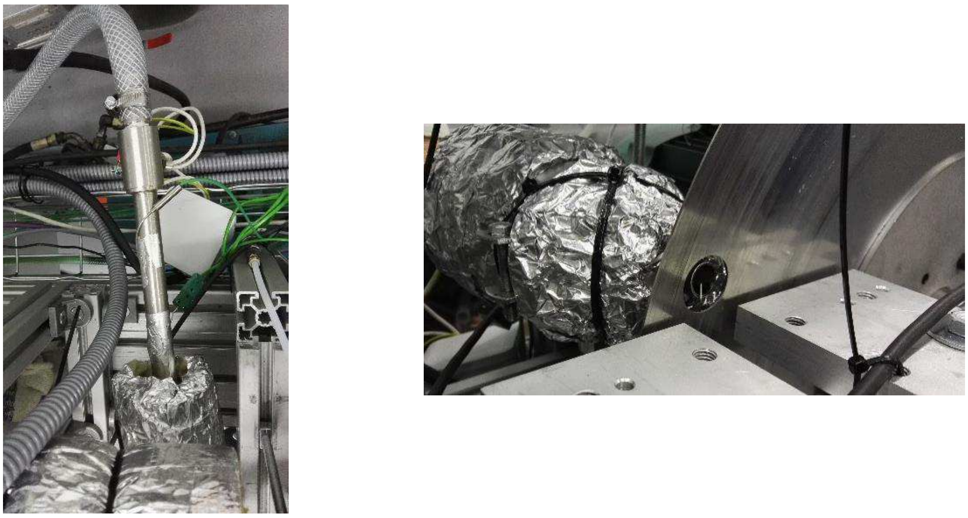

Figure 50: Thermocouple characterization apparatus, a (left) air heater, b (right) air jet

An air flow previously warmed by an electrical heater (Figure 50a) has been forced to flow through a jet (Figure 50b) and then to traverse a rotating wheel (Figure 49) having some holes on the exterior circumference. Such wheel has been used to transform the steady flow in an intermittent hot flow, and then to impose to the sensor a square variation of the flow temperature profile, for a constant flow velocity. The time-average air temperature at the outlet of the jet has been measured with a 0.5 mm sheathed type K thermocouple and the air velocity has been calculated from the time-average mass flow rate and the geometrical dimensions of the jet.

Different flow conditions have been tested: air velocity ranges from 10 to 60 m/s and air temperature varies from 100°C to 200°C.

Figure 51 shows the computed time constant in function of the air velocity for several time-average air temperatures. The time constant has been defined as the time required to the sensor to reach the 66.6% of the flow convergence temperature. Results show that the time constant follows a logarithmic dependency trend in function of the air velocity (green dot line in the Figure 51), while, temperature effects could be neglected. Results also show that a difference of 2% has been observed between the time constant, extrapolated for a velocity of 2 m/s, and the value found in the works of Tagawa et al. [72].

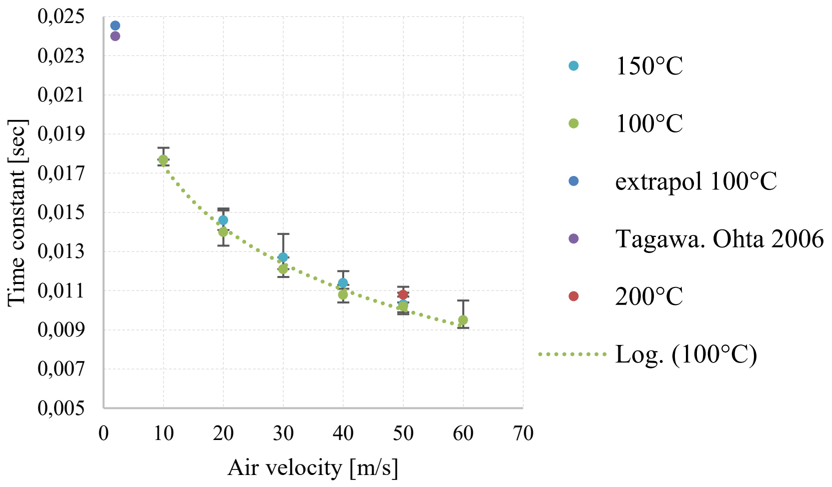

Figure 51: Time constant of a 25µm unsheathed Thermocouple - 'Ex-situ characterization'

From the results, it could be also observed that the dynamic, which the thermocouple of such dimension could follow, has an order of magnitude of around 100 Hz. In this study, such frequency corresponds to the maximum pulsation frequency imposed to the hot flow in the experimental apparatus previously described, suggesting that a time-delay compensation of the thermocouple signal should be applied to know the real fluid temperature.

Although the previous results may be used, by an iterative method, to compensate for the time-delay the thermocouple signals and then to correct the hot-wire signals for the temperature effects, the heat transfer conditions around the hot junction if subjected to a pulsating flow, make the previous characterization useless. Actually, the time constants obtained by the experimental characterization are valid only for a flow which has its operating condition equal to the calibration conditions. Since, it would be next to impossible to perform such dynamic calibration of the thermocouple to cover all experimental conditions, an 'in-situ' characterization of the thermocouple is recommended in this study and it is detailed in the following lines.

III.4.2 'In-situ' characterization of the thermocouple response time

A technique for an 'in-situ' estimation of the sensor time-constant has been proposed in the works of M. Tagawa et al. [72]–[75]: a two-thermocouple probe, which is composed of two fine thermocouples of unequal diameters, has been used in a turbulent steady flow.

According to the authors, once the two-thermocouple probe is immerged in a hot flow, the fluid temperatures sensed by the two thermocouples T_{g1} and T_{g2} can be given by the following first-order lag systems:

$$\begin{cases} T_{g1} = T_1 + \tau_1 \dfrac{dT_1}{dt} \\ T_{g2} = T_2 + \tau_2 \dfrac{dT_2}{dt} \end{cases} \qquad \text{III - 86}$$

where the subscripts 1 and 2 denote the two different thermocouples, T and τ are respectively the hot-junction temperature and its time constant of each thermocouple. Although the time constant is variable in fluctuating velocity and thermal fields, a fixed (mean) time constant is almost always used to compensate the effect of thermal inertia of the thermocouple wire at the cost of measurement accuracy, to some degree.

Although, for the two adjacent thermocouples of the two-thermocouple probe, the relation $T_{g1} \cong T_{g2}$ is hold, while in the reality a difference exists, the system of equation III - 86 could not be solved due to the high number of variables. To overcome such problem Tagawa et al. proposed to minimizing the time-average error $e = \overline{(T_{g2} - T_{g1})^2}$ using the method of least squares or to maximize a time-average correlation coefficient 'R' as in [73]. During the time averaging the time constants are assumed to be kept constant.

In the case of a pulsating flow, in which the flow velocity and thus the time constant widely variate in time, the impossibility to assume that the time constants are time-invariant makes the averaging unfeasible.

An alternative approach could be to consider the time constant time-invariant within a limited interval of the pulsation cycle, in this manner the time averaging of eq. III - 86 could be applied in a moving window of the pulsation cycle.

Although, a first numerical validation of such approach gave satisfying results about the impact of the window size on the method precision, once applied to a real thermocouple measurement such method has been found to be high sensitive to sensor noise as well as to little errors in the thermocouple placement leading thus to different T_{g1} and T_{g2}.

An ulterior method, always based on a two thermocouples measurement, was proposed in 2001 from O'Reilly et al. [76]: a nonlinear extended Kalman filter was used to a-posteriori estimate the time constant from the instantaneous thermocouple signals. The thermocouples model in eq. III - 86 was written as a linear state-space model keeping the assumption of a constant ratio $\frac{\tau_1}{\tau_2}$. The gas temperatures 'T_g' and the time constant 'τ' being the states, are estimated simultaneously and recursively, so there is no time window to be set. Authors claimed that, although, the proposed nonlinear filter technique gave a large increase in bandwidth and an accurate time constant estimation, for a relatively small computational cost, the larger number of parameters; such as the $\frac{\tau_1}{\tau_2}$ ratio, to be set and the dependence on these of the system stability represent a problem.

In a posterior work in 2003 a variation of the Kalman Filter technique, initially introduced by O'Reilly et al., was proposed by K. Kar et al. [77]. The authors claimed that none a-priori assumptions for the time constants ratio has to be made, and, the covariance of observation and state noise could be inferred from the data, thereby eliminating any subjective tuning. Moreover, the two reconstructed temperatures may differ if an error in the placement of the sensor occurs, leading finally to a Kalman filter less susceptible to noise.

In this study, the method proposed by K. Kar et al. [77] has been selected and revised; for the sake of brevity, mathematical details will not be reported in this paper, we leave the reader see the references, while, only the results of a fundamental experiment to validate such technique are reported in the following lines.

Two different thermocouples and a resistance thermometer have been placed at the outlet of the jet previously used to characterize one thermocouple sensor: the resistance thermometer (Dantec 55P31) consists in a platinum wire with a diameter of 1 µm and length of 0.4 mm, its maximum bandwidth frequency reach a value up to 1kHz, as claimed in [78], making it adapted to consider its measurement the reference flow temperature. The cold-wire is subjected to a low constant current of 0.1 mA controlled by the temperature module Dantec 90C20, the applied current warms the wire until a temperature around of 45°C. The wire signal has been filtered by an electronic low-pass filter, with a cut-off frequency of 3 kHz.

The two employed type K thermocouples have been selected with a wire diameter of 25 µm and 50 µm, the hot-junctions are not sheathed and only 2 mm of wire length has been not thermal insulated to reduce the thermal conduction error.

Data have been acquired with the FPGA processor of the NI-cRIO 9035 with an acquisition rate of 10 kHz, and an ulterior encoder is used to have a revolution reference signal to apply the phase-average mathematic.

The air velocity at the outlet of the jet has been varied from 10 m/s to 50 m/s in order to investigate the validity of the method for different sensor time constants. The time-average temperature measured from a 0.5 type K thermocouple has been maintained constant, by a closed-loop control of the heater power, to the value of 100°C. The cycle frequency set to 16.67 Hz, corresponds to a rotating velocity of 100 rpm for a wheel with 10 wholes. Data have been phase-averaged over a period of 100 engine revolutions.

In the Figure 52 the phase-averaged temperatures within one engine revolution have been reported: results show that the thermocouples are not able to follow the rapid temperature variation of the air, measured by the cold-wire, leading to large instantaneous errors in the temperature measurement. Signal compensation for the time-delay should be applied to the thermocouple signals.

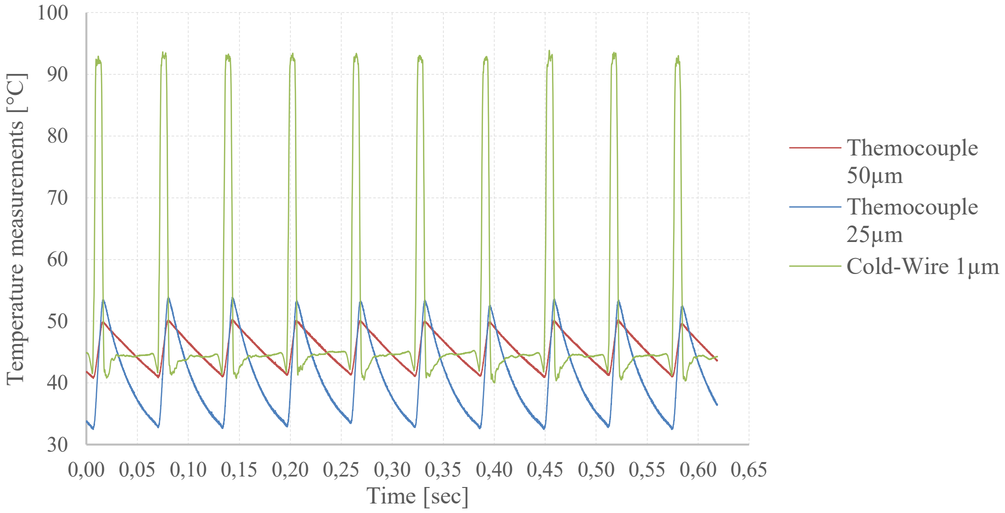

Figure 52: Sensor temperature measurements under an intermittent hot flow

As claimed by K. Kar et al. [77], the Kalman filter for the dynamic linear model of the thermocouple time constants, based on the eq. III - 86, may be written in the following form:

$$\begin{cases} \boldsymbol{\theta}^i = \boldsymbol{\theta}^{i-1} + \boldsymbol{w}^i \\ y^i = \boldsymbol{F}^i \boldsymbol{\theta}^i + v^i \end{cases} \qquad \text{III - 87}$$

Where $\boldsymbol{\theta}$ is the vector of the latent variables which corresponds to the thermocouple time-constants $[\tau_1, \tau_2]$, and $\boldsymbol{w}^i$ is the state noise. The first equation of the system in eq. III - 87 is written by adopting the hypothesis that the time-constants in the present time step are most likely the values in the previous time step. y^i is the univariate observation ($T_{w1} - T_{w2}$) which can be calculated directly from the thermocouple signals, $\boldsymbol{F}$ is a vector containing the time derivative of the sensor signals, and v represents the observation noise which is directly linked to the measurement noise.

In order to apply the recursive estimation of the Kalman filter in eq. III - 87, the calculation of the signal time derivatives as well the definition of the observation and state noises are required. The latter has been calculated by the Jazwinski's method as proposed by the authors. The observation noise has been imposed equal to 1°C, and, it has been calculated by the probability density function of the measured signals.

A 3th order low-pass IIR filter with a passband frequency of 500 Hz and a pass band ripple of 0.1 has been applied to the original signals to reduce the noise. The filter cut-off frequency has been chosen directly from the power spectral density of the signal (in Figure 53) as the point after which the PSD shows a flat behaviour and only the noise high frequency component exists. In Figure 53the PSD for the 25 µm thermocouple signal before and after the filtering operation is reported, results show that only the high frequency noise has been eliminated without modifying the low frequency part of the signal.

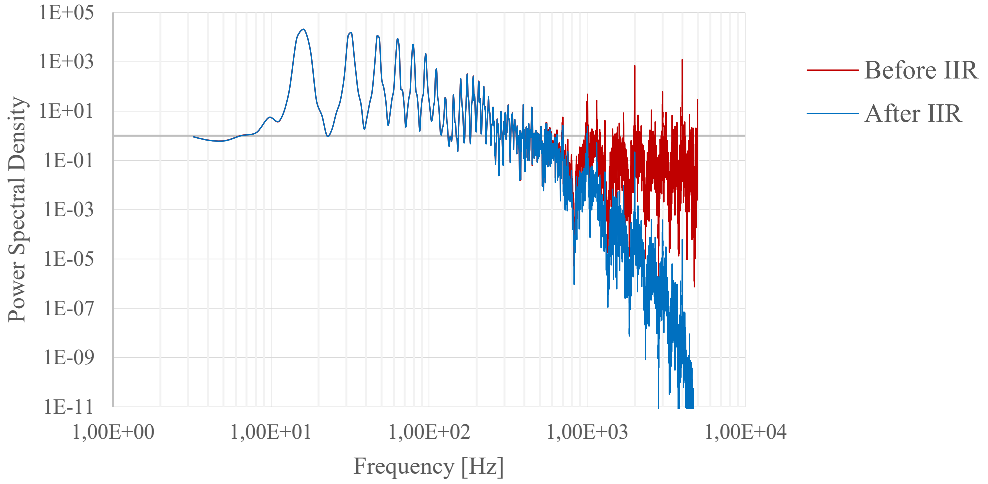

Figure 53: PSD of the 25 µm thermocouple signal

Figure 54 shows the time-constants estimated by the Kalman filter method (red and blue dot-lines), the compensated sensor signals and the cold-wire measurement (black dot line).

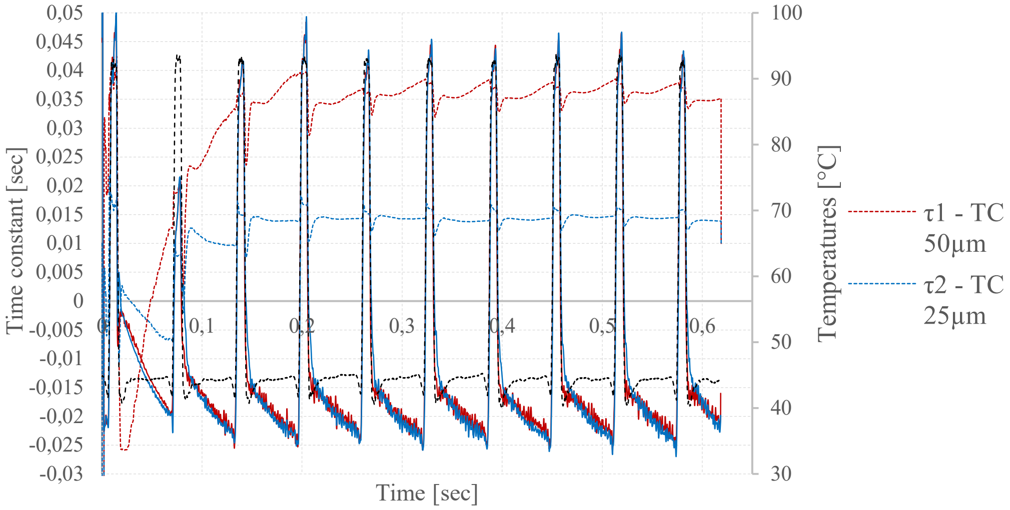

Figure 54: Kalman filter outputs and time-delay compensated sensor temperatures

Results show that because of the time derivative calculation errors at the extremity of the signals and because of the initial imposed value of the covariance matrix, the Kalman filter needs around 3 cycles to converge to the correct value of the time-constants. Results also show that the Kalman filter outputs are coherent with the previous characterization of the thermocouple sensor (Figure 51), for instance, a time-constant of around 17 msec has been calculated from the Kalman filter method for the 25 µm thermocouple.

Once the time constant has been correctly estimated, it has been used to evaluate the real gas temperature according the equation III - 85. A focus of the last cycle of the Figure 54 is showed in Figure 55: results show that the compensated thermocouple signals well follow the dynamic of the cold wire measurement during the first part of the cycle in which the hot-junction is subjected to the forced external convection ('A' – green zone), nevertheless, in the remaining part of the cycle ('B' – orange zone) the behaviour of the compensated signals is quite different from the cold-wire. While the cold-wire temperature measurement shows a value of around 45 °C, thermocouple compensated temperatures show an inferior temperature. Because of the constant electric current of 0.1 mA the wire is slightly warmed to a temperature of around 45°C higher than the ambient temperature, instead of the thermocouples which follow the real air temperature, making the measurements not comparable.

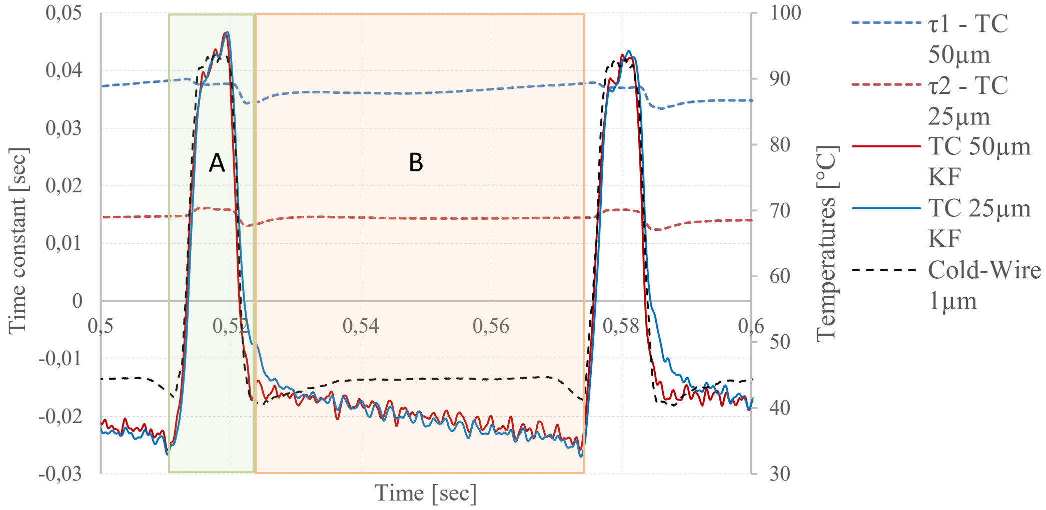

Figure 55: Compensated thermocouple measurements

In the previous lines the application of a discreet and linear Kalman filter technic, as it was originally proposed by K. Kar et al. [77], has been discussed and then validated. Results show the high flexibility of the method which requires two micro-unsheathed thermocouples with a different diameter sensing the same flow temperature and the measurement incertitude. Some attention should be done in the time derivative calculation and in the filtering process as previously discussed.

Anyway, due to the finite mass of the thermocouple hot junction, the Kalman filter method has been validated to work until a pulsation frequency up to 40 Hz. For higher frequencies the inertia of the thermocouples, acting like a physical filter, leads to very slow temperature variations while rapid air temperature variations occur, the founded Kalman filter results were not physical with negative instantaneous time-constant values.

III.5 Experimental procedures, data acquisition & reduction

In the previous paragraphs the technique to measure the air velocity for a pulsating flow and the technique to measure fast temperature variations have been presented and discussed, figuring out their limits and solving the aforementioned problems which arise in the pulsating flow measurement case. In the following lines such techniques will be described in the specific case of the pulsating flow reproduced in the previous depicted experimental apparatus, then, some typical measurement profiles will be presented and discussed. A particular attention is paid in the data reduction while the physical analysis will be detailed in the next chapters.

As previously affirmed, the main purpose of this work is to study the impact of the flow pulsation on the heat transfer phenomena. To accomplish this, in the experimental apparatus a steady hot air flow is excited through a pulsating mechanism with a pulsation frequency ranging from 0 to 95 Hz. The heaters power is controlled by a closed-loop control in order to stabilize the time-average centerline air temperature at the inlet of the test-section to a constant value, imposed for instance for all the experiments, equal to 150°C. The HWA and the micro thermocouples are displaced along the radius with a step of 1 mm to measure the radial profile of the air velocity and temperature. A total of 27 points of measure along the radius have been taken.

HWA, pressure transducers and micro thermocouples signals are acquired with a data rate equivalent to an angular resolution of 0.1 camshaft angle degree 'CAD', constants for all the experiments. Data have been acquired for a period of 200 pulsation cycles, wide enough to apply the statistic and the phase-averaging mathematics.

The data manipulation begins from the estimation of the real gas temperature: once the phase-average component of the thermocouple signals is computed (equation II - 44), the discrete Kalman filter is applied, as discussed before, and the real gas temperature is estimated. It is important to note that the signal compensation has been applied only to the phase-average component of the signals, in order to retire all the cycle-to-cycle temperature perturbations and avoid non-physical Kalman filter outputs. In this manner, only the phase-average air temperature is available as result. Although a phase-average standard deviation of the non-compensated thermocouple signals has been calculated, it has not been possible to attribute this mathematical term to the real turbulent component of the air temperature because of the high thermocouples response time and because of the compensation procedure limit. Such term will be called in the remaining part of this study the phase-average standard deviation, which physically should represent the cycle-to-cycle temperature perturbations having a maximum frequency up to around 100 Hz.

Once the phase-average air temperature has been obtained, the compensation of the HWA signals for the temperature effects has been applied. Because of only the phase-average air temperature is available, the compensation of the HWA signals has been thus applied only to the phase-average term. Once such term has been computed, the signals are analysed to detect the flow direction. The output information of the flow direction detection is the only the phase-average air velocity: as well as for the air temperature, also for air velocity the turbulent component has not been possible to be computed.

While, contrarily to the thermocouple sensor, the hot-wire has a small enough response time to be able to sense the turbulent variations of the air velocity, in this case, the turbulent component of the signal contains also the effect of the turbulent temperature variations on the hot-wire voltage. Such effect has not been possible to be compensated since the turbulent temperature variations have not been measured, as previously affirmed. Figure 56 and Figure 57 show the phase-average bulk properties Z_b of the pulsating hot flow, calculated as the surface integral of the radial profile, for a pulsation frequency case of 10 Hz:

$$Z_b = \frac{1}{S}\int ZdS \qquad \text{III - 88}$$

Where Z is the instantaneous local flow property. The time-average mass flow rate is kept constant at 110 kg/h and the centerline air temperature at the inlet of the test-section is maintained constant at 150°C. Such conditions correspond to a time-average Reynolds number of 30000. The cooling water temperature at the inlet of the test-section is kept constant at 17.4°C for each experiment, with a maximum test-by-test variation of around 0.2°C.

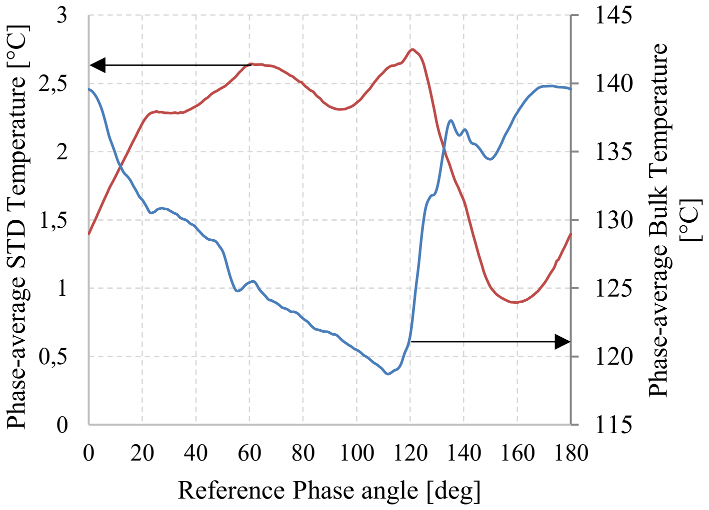

Figure 56: Air bulk Temperatures – Hot Flow, 10 Hz

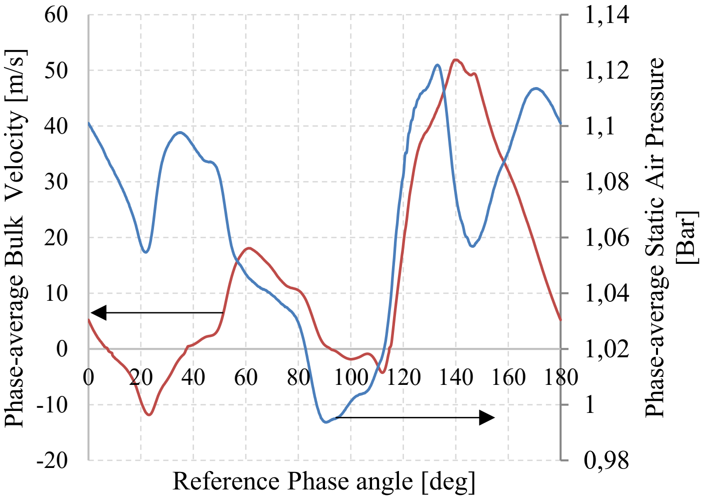

Figure 57: Air Velocity & Pressure – Hot flow, 10 Hz

As discussed before, since the thermocouples have the intrinsic limitations of measuring the turbulent component of the air temperature in the case of a pulsating hot flow, the turbulent component of the air velocity has not thus been possible to be measured.

By conducting the experiments in a cold turbulent pipe flow conditions, such limitation is overcame: the temperature variations, due to flow compression, may be neglected making so the impact of the temperature on the hot-wire signal negligible. Consequently, the instantaneous hot-wire signals could not be compensated for the temperature impact, and hot-wire signals can be directly decomposed in the three component as in eq. II - 43 . Anyway, to measure the turbulent component of the air temperature new measurement techniques should be employed.

Assuming the hypotheses that the temperature is a scalar passive field, then simply transported by advection and not capable to influence the velocity field, makes the study of the velocity field of a cold pulsating flow useful to have some information on the velocity field of a hot flow. In this case two different conditions have been tested: a cold flow with a time-average Reynolds number equal to the hot flow of a cold flow with the same time-average bulk axial air velocity.

Then, adopting the *Reynolds analogy* between the momentum and heat transport, the behavior of the velocity field of a hot flow could be useful to characterize some terms of the energy governing equation.

In the following lines some measurements of the velocity components have been reported for a cold pulsating flow, but none physical discussion have been conducted: a physical analysis of the experimental data will be presented in the following chapters.

To account for the decrease of the sound velocity because of the decrease of the flow temperature, the total pipe length has been reduced to have the same resonance frequencies between the cold pulsating flow and the hot pulsating flow. To keep constant the time-average Reynolds number, 30000 as expressed before, the mass flow rate has been reduced to around 85 kg/h contrarily to the previous 110 kg/h, while, to maintain the time-average axial velocity constant, the mass flow rate has been increase up to 147 kg/h.

In Figure 58 the bulk phase-average air velocity has been reported for the pulsating hot flow (blue line) with a time-average mass flow rate of 110 kg/h, for the cold flow with a constant time-average Reynolds number (green line) and with the same time-average component of the axial velocity (red line).

It could be observed that maintaining constant the time-average axial velocity by increasing the mass flow rate, while the air temperature decreases from 150°C to 25°C, lead to similar velocity oscillation amplitude. Contrarily to which occurs in the case of a constant time-average Reynolds, in which as well as the mass flow rate has been decreased as well the velocity oscillation amplitude decreases.

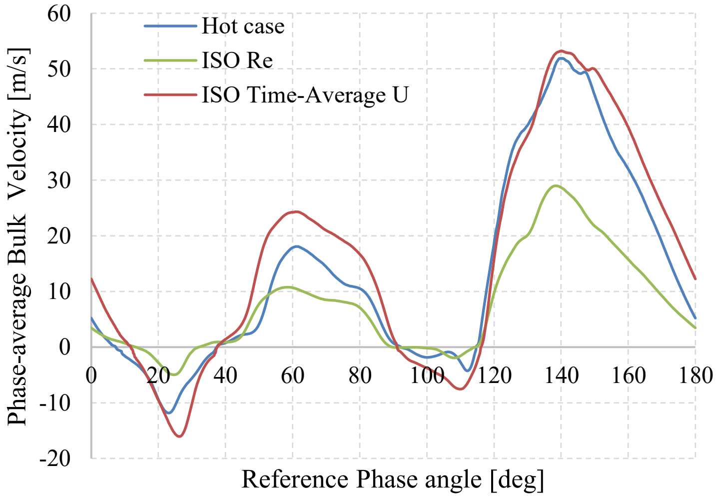

Figure 58: Phase-Average Air Velocity, 10 Hz

In Figure 59 the phase-average static air pressure has been reported for the pulsating hot flow (blue line), for the cold flow with a constant time-average Reynolds number (green line) and with the same time-average component of the axial velocity (red line). As expected the pressure profiles have qualitatively the same profile in terms of timing.

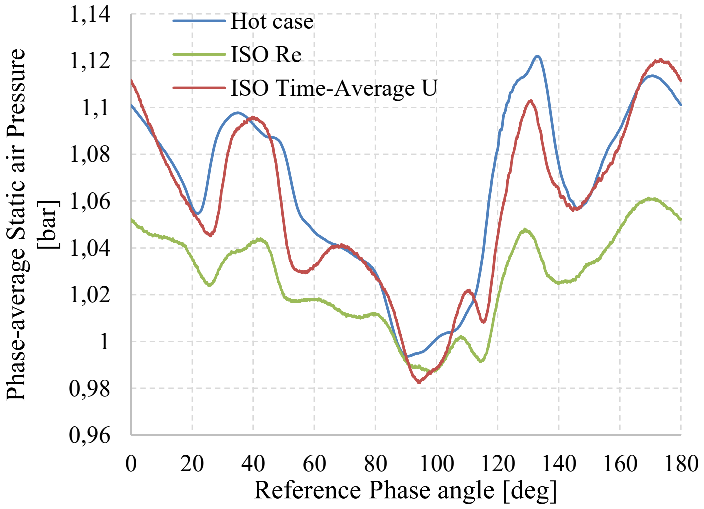

Figure 59: Phase-Average Static Air Pressure, 10 Hz

As previously affirmed, for cold pulsating flow conditions the temperature effects on the HWA measurements could be neglected, allowing in such conditions to affirm that the phase-average standard deviation of the velocity measurement represents the phase-average turbulent component.

In Figure 60 and Figure 61 the phase-average axial velocity turbulent component and the phase-average turbulence intensity have been reported for both the cold pulsating flows with an equal time-average Reynolds number (green line) and time-average axial velocity (red line).

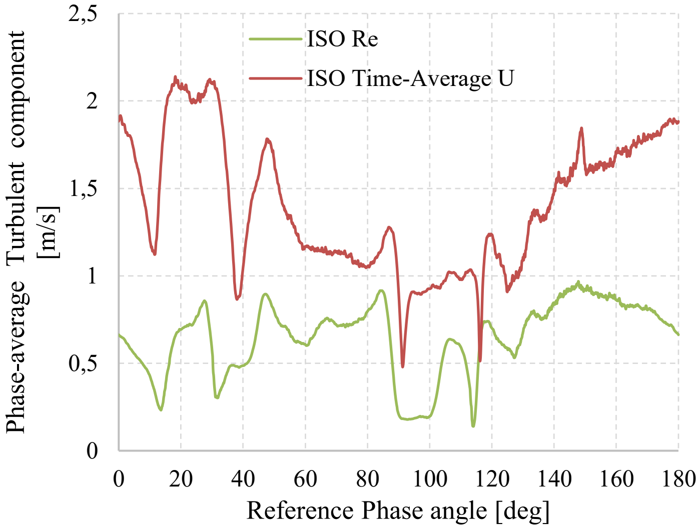

Figure 60: Phase-Average Turbulent component – Cold Flow, 10 Hz

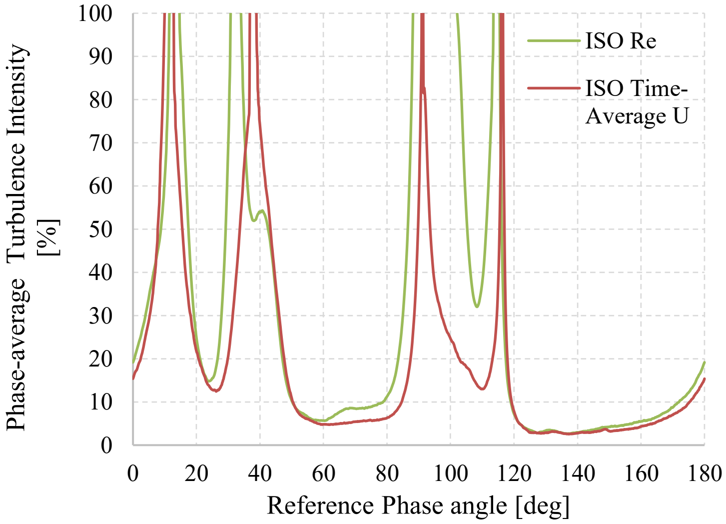

Figure 61: Phase-Average Turbulence Intensity – Cold Flow, 10 Hz

Measurements allow also to compute phase-average radial profile with the purpose to potentially evidence some 2D mechanisms in the velocity and temperature fields. Respectively in Figure 62 and Figure 63 the phase-average velocity and temperature profiles in the cross section are plotted for different instants nearby the flow reversal instant for a 20 Hz pulsating hot flow.

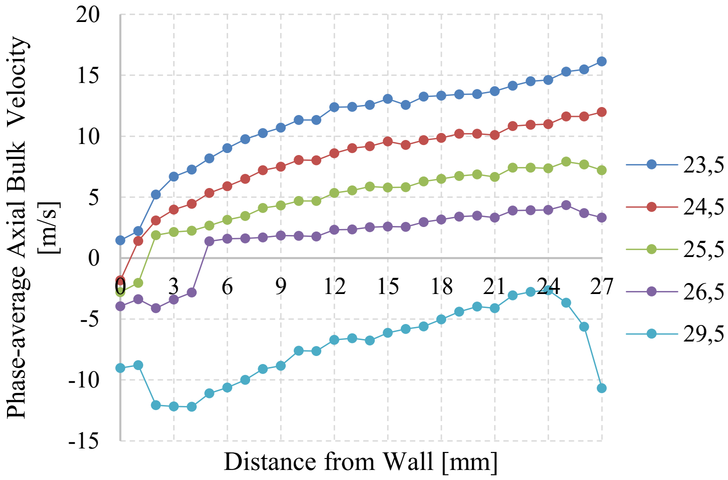

Figure 62: Phase-average velocity, radial profile – Hot flow, 20 Hz

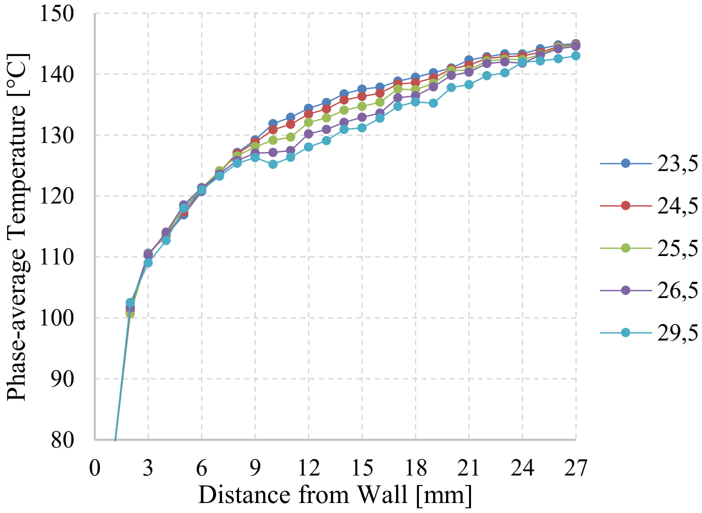

Figure 63: Phase-average Temperature, radial profile – Hot flow, 20 Hz

The measurement of the velocity profile in the case of a cold flow, as previously affirmed, allows to measure the turbulent component of the velocity, useful to evidence the aforementioned transversal advection enhancement. In the Figure 64 and Figure 65 the phase-average velocity and its phase-average standard-deviation have been respectively showed in function of the distance from the wall for the cold pulsating flow having the same time-average axial velocity of the hot pulsating flow.

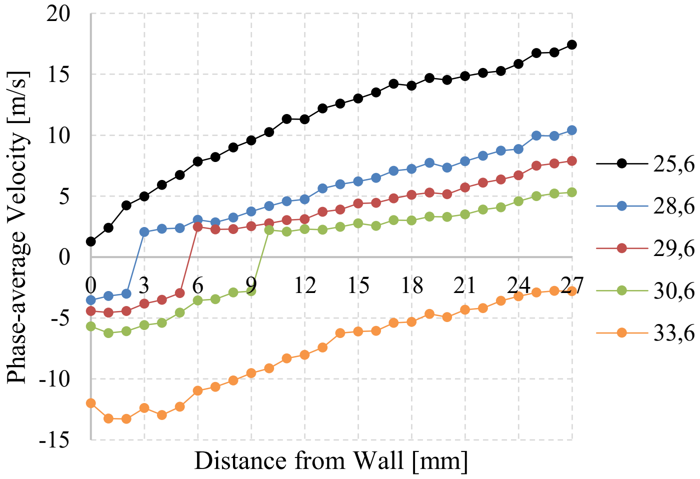

Figure 64: Phase-average axial velocity – Cold flow – ISO U_m, 20 Hz

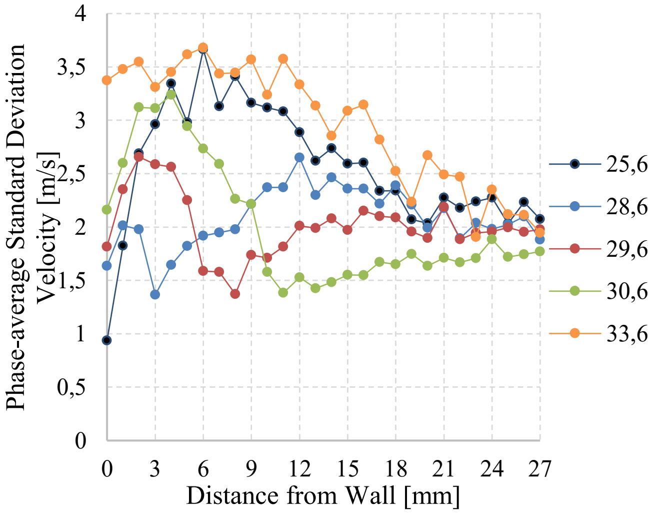

Figure 65: Phase-average STD axial velocity – Cold flow – ISO U_m, 20 Hz

In the previous lines the technique to extract the three components for each of the flow properties has been showed as well some typical measurement has been presented. As recall for the reader, physical analysis will be conducted and presented in the next two chapters.

III.6 Characterization of the flow behavior in stationary conditions

A characterization of the stationary flow has been conducted, and it is presented in the following lines, in order to verify, thorough the flow velocity and temperature profiles if the stationary flow could be considered fully developed in a smoot pipe conditions. Experimental results are compared to the formulas available in literature for a fully developed pipe flow, and are presented in the following lines

For a hot stationary flow with a time-average mass flow rate of 110 kg/h, an internal wall temperature equal to 66°C and an air time-average centerline temperature at the test-section inlet of 150°C, the velocity and the temperature profiles have been measured through the HWAs and the micro-thermocouple. Data have been acquired for a period of 60 sec, the time-average component of the air velocity and temperature are showed in the following figures and compared with literature profiles.

In Figure 66 the dimensionless experimental temperature, calculated as in right side of the following equation, is compared to the formula proposed by Johnk et al. [79].

$$\frac{(\bar{T}_w - \bar{T})}{(\bar{T}_w - T_0)} = (1+s)\left(\frac{y}{R}\right)^{1/m} - s\left(\frac{y}{R}\right)^{(1+s)/sm} \qquad \text{III - 89}$$

Where s = 0.02 for all Reynolds numbers and m is function of the Reynolds number, as in the table 2 of Johnk et al. [79]. For a Reynolds of 30000 m is equal to 5.7.

Historically, the form of eq. III - 89 has been proposed starting from the resolution of the heat transfer problem on walls with uniform temperature. Such boundary conditions are representative of our experimental conditions. In this case temperature distribution in a circular pipe for fully developed laminar flow in the absence of flow work, thermal energy sources, and fluid axial conduction has been solved by Bhatti and presented by Shah and Bhatti [80], as follows

$$\frac{T_w - T}{T_w - T_m} = \sum C_i \left(\frac{y}{R}\right)^{2n} \qquad \text{III - 90}$$

Johnk et al. [79] adapted the power-law form to account the zero slope at the center of the pipe

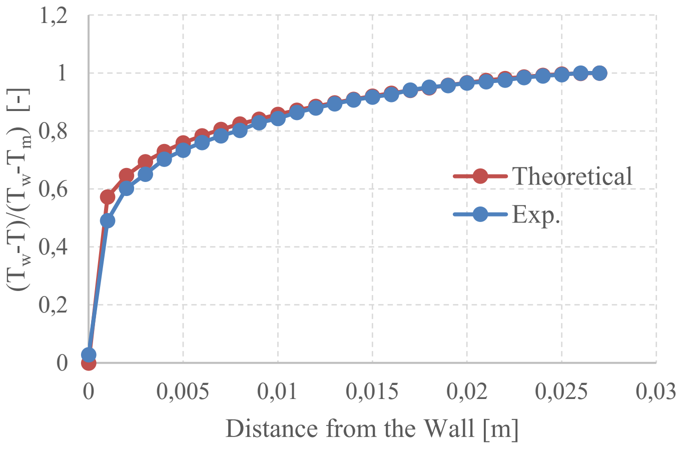

Figure 66: Temperature profile for a stationary turbulent pipe flow – Re = 30000

Results show that this relationship fits the fully developed data quite well for a distance from the wall superior to 10 mm (y/R > 0.04, in agreement with the previous works), while a little difference appears for a distance from the wall inferior to 10 mm. Such behavior could be due to the near wall flow disturbance caused from the cavities in which the sensors, perpendiculars to the pipe, have been placed. In Figure 67 the velocity ratio between the local velocity and the axial velocity is showed and compared to the formula proposed by Nikuradse [81]:

$$\frac{\overline{U}}{U_{axis}} = \left(\frac{y}{R}\right)^{1/n} \qquad \text{III - 91}$$

Where n has been observed to be related to the time-average Reynolds number. From the table 6.5 at pag. 231 of Chassaing [15] n could adopted a value of 6.5.

It is important to note that equation III - 91 has been formulated to predict the velocity only in the core of the pipe flow. Results in Figure 67 shows that the experimental velocity profile is quite similar to the theoretical one in the core region, while a higher velocity has been measured near the wall.

A higher velocity near the wall could justified the lower temperature found in Figure 66 in comparison to the theoretical profile.

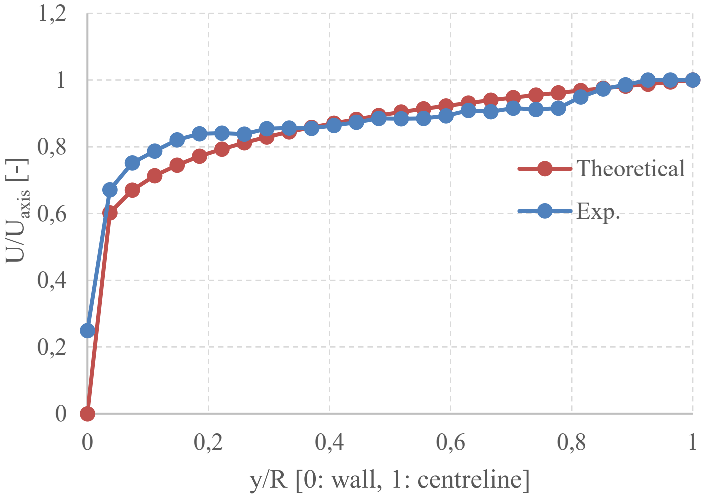

Figure 67: Velocity profile for a stationary hot turbulent pipe flow – Re = 30000

The time-average velocity profile has been measured also for a cold stationary flow with a same Reynolds of 30000. Air mass flow rate has been reduced to 85 kg/h to account for the decrease of the temperature which has been measured to be equal to 22°C. In such conditions, as previously affirmed in the paragraph III.5, it has been possible to measure both the time- and fluctuation- component of the air velocity.

The velocity ratio profile, as in Figure 67, is showed for the stationary cold flow in Figure 68:

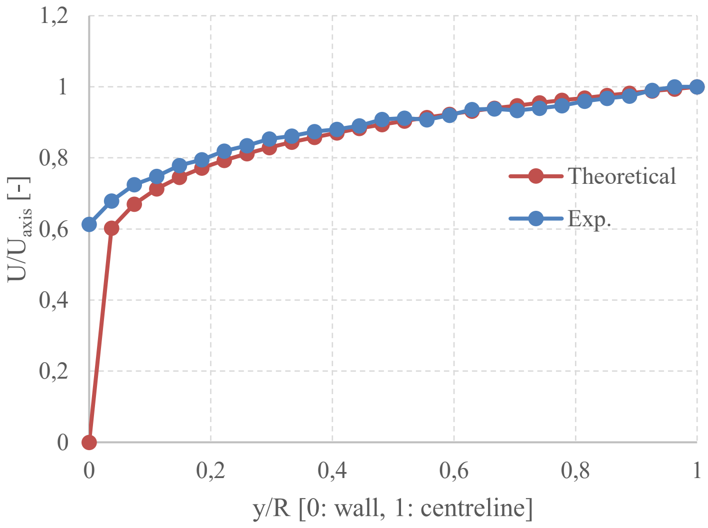

Figure 68: Velocity profile for a stationary cold turbulent pipe flow – Re = 30000

Data shows that in the core region the velocity profiles are quite superposed, suggesting that the stationary flow could be assumed fully developed and the pipe smooth.

Such hypothesis has been furtherly validated from the results in Figure 69, which show that the deficit velocity profile well fit the theoretical profile proposed by Laufer [82], as follows, :

$$\frac{\overline{U}_{axis}-\overline{U}}{u_\tau} = -\frac{1}{\chi}\ln\left(\frac{y}{R}\right)+B' \qquad \text{III - 92}$$

Where u_τ which represents the friction velocity, and it has been calculated according the Blasius formula (table 10.9, pag. 393 of Chassaing [15]); χ and B' are constants respectively equal to 0.41 and 0.45 as proposed by Laufer [82].

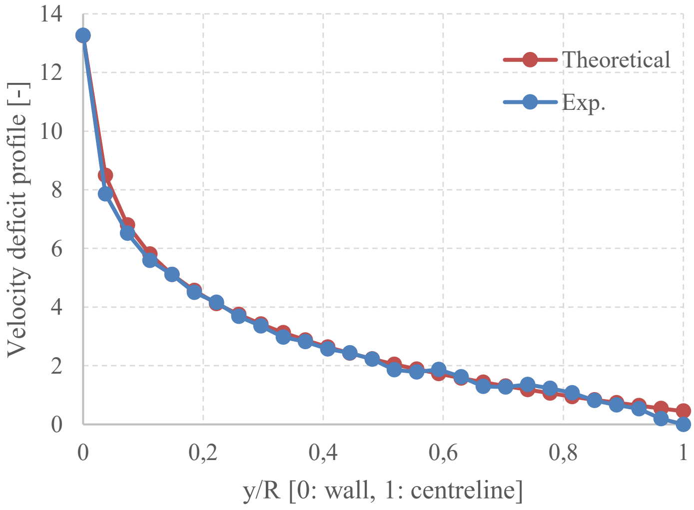

Figure 69: Deficit velocity profile for a stationary cold turbulent pipe flow – Re = 30000

The fluctuating term of the instantaneous velocity measurement has been used to compute the integral length scale Λ. Defining a length or time period that is characteristic of the largest scales in a turbulent flow is of importance both in defining a suitable area or volume for experimental and numerical investigations, and also to understanding the process of energy production and dissipation in the flow. In some cases a suitable scale can be defined by the physical constraints of the flow domain: in the pipe flow the diameter of the pipe should be of the order of the largest eddies in the flow, and the ratio of the pipe diameter to mean velocity along the pipe is a good estimate of the time period required to describe the flow.

The integral length scale of the velocity is defined by:

$$\Lambda = \int_0^\infty R_{ii}(r,t)dr \qquad \text{III - 93}$$

Where R_{ii} indicates the autocorrelation function defined by:

$$R_{ii}(r) = \frac{\|u(x_i,t), u(x_i,t+dt)\|}{\|u(x_i,t)^2\|} \qquad \text{III - 94}$$

The form of the autocorrelation function is such that it generally decreases rapidly to its first zero crossing, after which it may become negative and proceed to oscillate about zero. A typical autocorrelation profile is showed in Figure 71, while, in Figure 71 a detail of the significant part of the autocorrelation is presented:

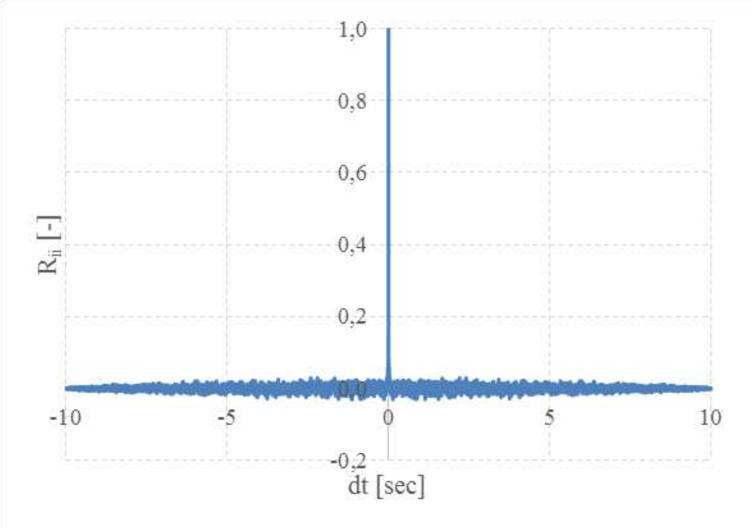

Figure 70: Autocorrelation of the velocity fluctuation component for a stationary flow, Re = 30000

While equation (III - 94) involves the determination of the integral over an infinite domain, the domain of the autocorrelation function from experimental or numerical data is finite as in Figure 71 , and there is some uncertainty on how best to define the integration domain. As observed in Figure 71 the autocorrelation fall rapidly to a low value in a relatively narrow period, outside of it a high disturbance appears in the autocorrelation profile.

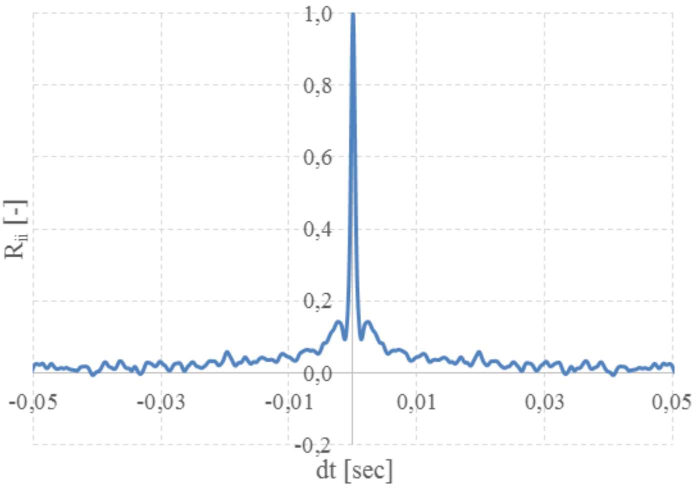

Figure 71: Zoom of the Autocorrelation of the velocity fluctuation component for a stationary flow, Re = 30000

For this reason a particular attention has to be paid in the choice of the integration domain. For the determination of the integral length as a representative length scale of the turbulence it can be specified in a number of ways, as investigated in this study of O'Neill et al. [83]. Authors investigated several integration methods on DNS numerical data:

- integrate over the entire available domain;
- if the autocorrelation function has a negative region, integrate only up to the value where the autocorrelation function is a minimum;
- integrate only up to the first zero-crossing;
- integrate only up to the value where the autocorrelation function falls to 1/e.

In our calculations only the last two methods have been tested, while the remaining have been not considered due to their low precision as O'Neill et al. [83] claimed.

Results are showed in Figure 72, L3 (blue line) represents the scale calculated by integrating up to the value where the autocorrelation function falls to 1/e and L4 (red line) represents the scale calculated by integrating up to the first zero-crossing.

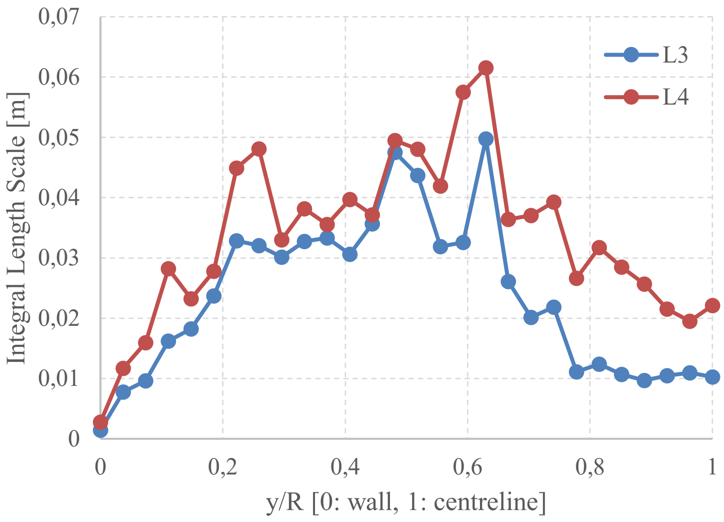

Figure 72: Integra length scales for a turbulent pipe flow – Re = 30000

Knowing that the geometry length scale corresponds to the pipe diameter (D = 54.8 mm), from the results it could be observed that both the scales L4 and L3 are inferior or of the same order of the pipe diameter, confirming that the turbulent structures, created during the flow passage though the mono-cylinder head valve, well dissipate before the flow passes through the test-section. For instance, such criterion has been used to choice the correct length of the developing section of the steel pipe upstream the test-section (paragraph III.2.1).

III.7 Acoustic characterization of the test-rig

A further characterization of the test-rig behavior has been conducted to measure the frequencies of resonance of the acoustic modes of the pipe for three different pipe lengths. After a thermal stabilization of the experimental apparatus, by flowing a steady hot air flow with an air temperature at the inlet of the test section equal to 150°C, the system has been subjected to a pressure impulse and then has been let resonate. Instantaneous pressures were measured at four different axial positions along the pipe.

From the power spectral density 'PSD' of the pressure signals, it is possible to calculate the frequencies of resonance of the system. Such frequencies correspond to the local maxima of the PSD. A second order low-pass filter with a cut-off frequency of 1 kHz was applied to the sensor signals before calculating the PSD. Sensors signals have been acquired at a frequency of 20 kHz, high enough to respect the Nyquist-Shannon sampling theorem. Figure 73 shows the instantaneous pressure, measured at the centre of the test-section, and Figure 74 shows the PSD of the signal. The other measured pressures show the same PSD results and are not reported here. Local maxima of the PSD, identified by the red points on Figure 74, correspond to the resonance frequencies of the system. Table 2 shows the first six calculated resonance frequencies for three different pipe lengths.

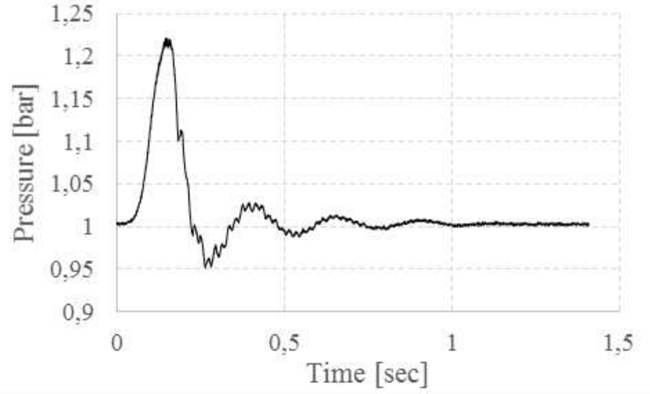

Figure 73: Acoustic characterization - Instantaneous pressure

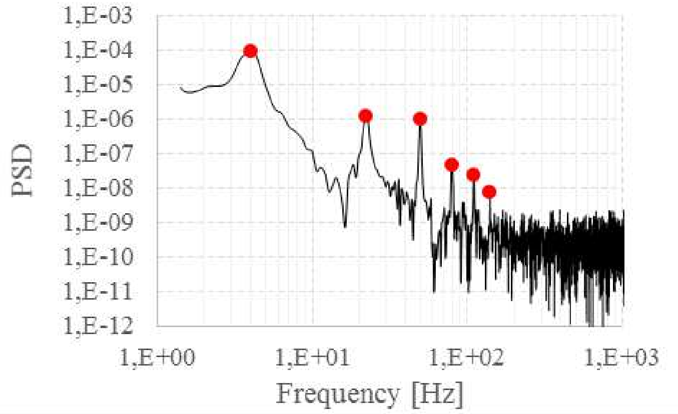

Figure 74: Acoustic characterization – PSD of the instantaneous pressure

Resonance Mode	1	2	3	4	5	6
Resonance Frequency L = 3.69 m [Hz]	6.37	36.1	79.6	126.3	176.2	239.8
Resonance Frequency L = 4.69 m [Hz]	4.7	26.2	63.1	101.3	138.9	175.8
Resonance Frequency L = 5.91 m [Hz]	3.9	22.2	49.5	80.5	110	139.8

Table 2: Resonance frequencies [Hz] of the test-bench for a 3 pipe lengths.

III.8 Conclusions

A versatile test rig has been developed and presented in this chapter. It has been designed to produce a pulsating turbulent flow, with the operating conditions representative of an engine exhaust. Pulsation frequency ranges from 10 to 95 Hz and the Reynolds number could be varied between 10^4 and $5x10^4$. To go further in the comprehension of the heat transfer phenomena a rapid-measurement of air temperature and velocity, within the pulsation cycle, has been applied. Actually, a double parallel hot-wire probe has been used in CTA mode to measure the axial component of the air velocity, furthermore, thanks the unique shape of the probe a novel methodology to detect flow reversals has been proposed and experimentally validated. Temperature impacts on wire voltage have been considerate and compensated after an ad-hoc velocity and temperature calibration of the wire. The instantaneous profile of the air temperature has been measured by type K unsheathed thermocouples. A characterization of the time response of the sensor has demonstrated that such sensors require a time-delay compensation due to its first order-type response to a variation in the flow temperature. Although an ‘ex-situ’ characterization of the sensor time-constant has shown its unique dependence on the air velocity, an ‘in-situ’ method has been applied because of the intrinsic limit of an ex-situ methodology due to impossibility to well reproduce the pulsating flow properties in controlled conditions.

The in-situ technique requires two different thermocouple sensing the same temperature, then, through the Kalman filter mathematics the calculation of the time-constant and the signal compensation could be fulfilled. In this chapter, a validation of such technique has been presented and discussed.

Then, the experimental procedure and data reduction have been presented in the case of the pulsating flow. The encountered limits in the measurement of the turbulent component of the velocity and temperature for a hot pulsating flow have been identified and overcame. Adopting the Reynolds analogy and the hypothesis that the temperature is a passive scalar field velocity measurements have been reported in the cases of a cold pulsating air flows. Such measurements are useful to analyze the turbulent component of the velocity as well as some terms of the energy balance equations.

In a first validation phase of the flow characteristics in stationary conditions, the temperature and velocity radial time-average profiles have been analyzed and compared to the available literature models, to be able to affirm that the stationary flow in the test-section could be considered fully developed and the pipe could be considered smooth.

Also an acoustic characterization of the experimental apparatus has been conducted for different pipe lengths, and the results have been presented in this chapter.

In view of all this, in the following chapters experimental data will be analyzed with a 1D and a 2D assumptions to evidence the heat transfer mechanisms occurring for a turbulent pulsating flow.

Chapter / Chapitre IV

Experimental Investigation and 1D Approach to Convective Heat Transfers analysis

Abstract

With the main purpose to investigate the effect of flow pulsation on the convective heat transfer, in this chapter, a particular development of the energy balance equation has been conducted to correctly calculate the time-average convective heat transfer (Q_{conv} in eq. III - 95): an analytical formulation of the heat transfer problem with a 1D assumption has been made for a pulsating turbulent pipe flow and it follows:

$$\rho c_p \Sigma \left(\underbrace{\bar{u}\bar{T}\big|_0^L}_{A} + \underbrace{\overline{\tilde{u}\tilde{T}}\Big|_0^L}_{B} + \underbrace{\overline{< u'T' >}\Big|_0^L}_{C} \right) = \int_V \overline{< q(x,t) >}\, dV = Q_{conv} \qquad \text{III - 95}$$

The total time-average convective heat transfer Q_{conv} is equal to the sum of three different terms: the term ‘A’ which physically represents the energy variation of the time-mean component of the flow across the pipe, the term ‘B’ which represents the energy variation due to the oscillating component of the flow and the term ‘C’ corresponding to the advective transport of energy by fluctuating motion due to turbulence fluctuations.

An ad-hoc experimental procedure have allowed to evidence that, in the case of a reversed pulsating flow, a contribution to the energy balance equation through the boundaries (consisting in a negative term B), which impacts the total convective heat transfers, may occur.

Results have also shown that the flow pulsation enhances heat transfers in the entire range of the investigated frequencies. In particular, when the flow is excited with a frequency equal to a resonance mode of the system, a strong increase in heat transfers occurs. Instantaneous measurements of air velocity and temperature have demonstrated that the increase of the energy axial advection due to the oscillating component of the velocity is the major cause of the heat transfer enhancement. The relative Nusselt number, defined as the ratio between the Nusselt numbers for the pulsating and counterpart steady flows, has been found to be linearly proportional to the ratio between the velocity oscillation amplitude and the velocity time-average component, suggesting that such parameter, which characterizes the amplitude of the velocity waveform, should be considered in a new Nusselt correlation to account for pulsating effects.

A particular result has been found for the particular frequency of 40 Hz, a local heat transfer enhancement has been observed. Although such phenomenon remains not fully understood due to the lack of more detailed measurements, results allow to suppose that such enhancement is due to local phenomena around the sensor connections. Instantaneous local measurements of air velocity and static pressure in different frequency conditions show that a high oscillating component appears in the signal. Such oscillations have been supposed to be correlated to the *feedback loop* mechanism responsible of an interaction between the kinematic and the acoustic fields. The consequence of such interaction is a high radial velocity component, likely responsible of the heat transfer enhancement. Anyway 2D measurements of the velocity and temperature filed around the sensor connections cavity should be conducted in future to well understand such phenomenon. An interesting aspect of this heat transfer enhancement is that, if fully understood, it could be used as a passive method to increase the convective heat transfers. Anyway, also its impact on the total wall friction should be estimated.

IV. Experimental investigation and data analysis with an analytical 1D approach

IV.1 Introduction

In the present chapter, the experimental investigation of the effect of the flow pulsation on the convective heat transfers is presented. The main purposes are to investigate the impact of the pulsation frequency on heat transfers and to identify the main physical mechanisms which affect convective heat transfers. A particular attention has been paid in the calculation of the time-average convective heat transfer by developing an analytical formulation of the heat transfer problem based on a 1D assumption. For this reason this chapter only focuses on the time- and space-average characterization of the convective heat transfers. Data collection and reduction are presented; results are reported and discussed based on this assumption.

IV.2 Analytical formulation of the problem

The effect of the pulsation on heat transfers, as previously introduced (paragraph II.3.2), may be represented in terms of the relative Nusselt number Nu_{rel} (eq. II - 59) defined as the ratio of the time-average Nusselt number for the pulsating flow to the corresponding one for a steady flow with the same time-average Reynolds number. For a cylindrical control volume, the time-average Nusselt number may be defined as in the following equation:

$$Nu = \frac{hL}{\lambda} = \frac{Q_{conv} D}{S \Delta T_{lm} \lambda} \qquad \text{IV - 96}$$

Where: Q_{conv} is the time-average convective heat transfer, L is the characteristic length of the pipe which corresponds to D, the internal diameter of the pipe. S is the exchange surface, ΔT_{lm} the logarithmic mean temperature difference between the air and the internal wall of the pipe and λ the thermal conductivity of air.

The relative Nusselt number definition has been adopted in several previous studies because of its potentials to bring out the impact of the pulsation frequency on heat transfers and to identify a corrective coefficient for a Nusselt correlation accounting for pulsating effects. The practical difficulty in this approach consists to correctly evaluate the time-average convective heat transfer Q_{conv}. Since in some applications the measurement of the heat flux exchanged with a solid wall is not easily realizable, Q_{conv} is computed starting from the air flow properties by solving the energy balance equation.

The time-average convective heat transfer is generally computed from the variation of the time-average component of the air enthalpy through the inlet and outlet sections of the control volume (as done in previous works revised in the paragraph II.3.2), but it is shown in the following development that this calculation does not take into account characteristic terms related to the pulsating component of the flow. In the present work, Q_{conv} is derived from the time-average and space-integrated form of the instantaneous energy balance equation for a pulsating turbulent pipe flow. The terms related to the heat flux propagated from the advection of the oscillating component of the flow are highlighted.

Assuming negligible viscous dissipation, the 1D instantaneous local energy balance equation for an incompressible pipe flow with constant fluid properties exhibits the following form:

$$\rho c_p \Sigma \left(\frac{\partial T}{\partial t} + \frac{\partial (uT)}{\partial x} \right) = \lambda \Sigma \frac{\partial^2 T}{\partial x^2} + q \qquad \text{IV - 97}$$

Where $u(x,t)$ represents the bulk axial instantaneous air velocity, $T(x,t)$ the bulk temperature of air, ρ the fluid density, c_p the specific heat at constant pressure and q the local specific convective heat transfer exchanged through the perimeter of a pipe length ∂x.

As previously stated in the equation II - 43, Reynolds et al. [18] proposed that in the specific case of a turbulent pulsating flow each of the flow properties may be decomposed in three different terms, as expressed in the following equation:

$$Z(t,x) = \bar{Z}(x) + \tilde{Z}(t,x) + Z'(t,x) \qquad \text{IV - 98}$$

Where $\bar{Z}(x)$ represents the time average component only function of the x-axis, $\tilde{Z}(t,x)$ is the oscillating term of the coherent cycle-stationary pattern and $Z'(t,x)$ corresponds to the turbulent fluctuations term. Time averaging $(\bar{\ })$ determines $\bar{Z}(x)$ and the *phase-average* $(< >)$, i.e. the average over a large ensemble of points having the same phase with respect to a reference oscillator, leads to:

$$< Z(t,x) >= \bar{Z}(x) + \tilde{Z}(t,x) \qquad \text{IV - 99}$$

Phase-averaging process removes the background turbulence and extracts only the organized motions from the total instantaneous profile. For the sake of brevity, some useful mathematical properties that follow from the basic definitions of the time and phase averages are not reported, they are detailed in [18]. Combining eqs. IV - 98 and IV - 99 and then applying phase averaging operator to the obtained equation leads to:

$$\begin{aligned} \rho c_p \Sigma \left(\frac{\partial \bar{T}}{\partial t} + \frac{\partial \tilde{T}}{\partial t} + \frac{\partial (\bar{u}\bar{T})}{\partial x} + \frac{\partial (\tilde{u}\tilde{T})}{\partial x} + \frac{\partial (\bar{u}\tilde{T})}{\partial x} + \frac{\partial (\tilde{u}\bar{T})}{\partial x} +< \frac{\partial (u'T')}{\partial x} > \right) \\ = \lambda \Sigma \left(\frac{\partial^2 \bar{T}}{\partial x^2} + \frac{\partial^2 \tilde{T}}{\partial x^2} \right) +< q > \end{aligned} \qquad \text{IV - 100}$$

In the left-hand side of this equation, the sum of the two first terms represents the rate of change of the air energy inside the control volume ($\frac{\partial \bar{T}}{\partial t}$ is equal to zero because of the time-independency of the component $\bar{T}$); the other terms represent the advective transport of energy by mean flow, oscillating motion and fluctuating motion through the control volume. In the right-hand side of the equation, the sum of the two first terms corresponds to the conduction heat flux through the control volume and the last term represents the phase-average local convective heat transfer between the air and the solid wall.

Time-averaging eq. IV - 100 leads to:

$$\rho c_p \Sigma \left(\frac{\partial(\bar{u}\bar{T})}{\partial x} + \frac{\partial\left(\overline{\tilde{u}\tilde{T}}\right)}{\partial x} + \frac{\partial \overline{<(u'T')>}}{\partial x} \right) = \lambda \Sigma \left(\frac{\partial^2 \bar{T}}{\partial x^2} \right) + \overline{<q>} \qquad \text{IV - 101}$$

By integrating eq. IV - 101 on the volume defined by a cylinder of section 'Σ' and length 'L' (corresponding to control volume, between the inlet and outlet measuring sections, in the following), the energy conservation equation can be written as:

$$\rho c_p \Sigma \left(\underbrace{\bar{u}\bar{T}\big|_0^L}_{A} + \underbrace{\overline{\tilde{u}\tilde{T}}\Big|_0^L}_{B} + \underbrace{\overline{<u'T'>}\Big|_0^L}_{C} \right) = \int_V \overline{<q(x,t)>}\, dV = Q_{conv} \qquad \text{IV - 102}$$

The total time-average convective heat transfer Q_{conv} is equal to the sum of three different terms: the term 'A' which physically represents the energy variation of the time-mean component of the flow across the pipe, the term 'B' which represents the energy variation due to the oscillating component of the flow and the term 'C' corresponding to the advective transport of energy by fluctuating motion due to turbulence fluctuations. The statement of eq. IV - 102 clarifies that, whether a direct measurement of Q_{conv} is not available, instantaneous measurements of the air velocity and temperature are required to correctly compute all the terms in the left-hand side of eq. IV - 102.

In this study, a water flow has been used to cool the external surface of the pipe (paragraph III.2.1), allowing to directly evaluate Q_{conv} from the water temperature measurements.

IV.3 Experimental procedure recall

The study of the impact of the flow pulsation on the convective heat transfers is achieved by exciting a steady hot air flow with a pulsation frequency ranging from 0 to 95 Hz. In practice, a time-average mass flow rate, varying from 70 to 130 kg/h is forced to flow through the mono-cylinder head. The centerline air temperature at the inlet of the test-section is maintained constant at 150°C for all experiments by controlling the air heaters power. Such conditions correspond to a time-average Reynolds number ranging from 19000 to 35000, suggesting that the flow could be considered in a turbulent state. The water mass flow rate is maintained constant as well as the cooling water temperature at the inlet of the test-section, which is kept constant at 17.4°C for each experiment, with a maximum test-by-test variation of around 0.2°C.

IV.4 Calculation of the total time-average convective heat transfer for a pulsating flow

As previously mentioned, given the difficulty of measuring experimentally the three terms in the left-hand side of Eq. IV - 102, the total time-average convective heat transfer Q_{conv} is evaluated from the water temperature measurements. In practice, a constant water volumetric flow rate of 4.74 dm^3/min is forced to pass through an annular section, with an internal diameter of 67.3 mm and a thickness of 7 mm, in order to cool the pipe wall. In these operating conditions, the Reynolds number of the water flow is 788, suggesting a laminar velocity profile under steady state conditions. Consequently, from the energy balance equation for the water, in which the convective heat transfer with the exterior ambient air has been estimated to be less than 10 W and thus has been neglected, Q_{conv} can be solved as the time-average enthalpy difference of the water between the inlet and the outlet of the test-section.

The computed Q_{conv} and the term 'A' of Eq. IV - 102 are plotted in Figure 75 in function of the pulsation frequency. Uncertainties are depicted by error bars in the figure.

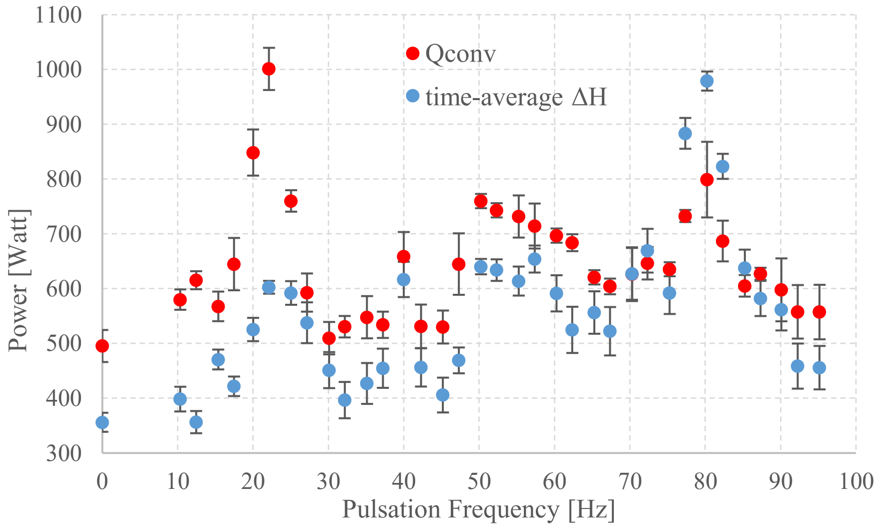

Figure 75: Terms of the air energy balance equation for a turbulent pulsating flow, w/o dry ice

The steady turbulent state (depicted by the markers at the pulsation frequency of 0 Hz) is taken as the reference case. In such particular conditions, the term 'B' in Eq. IV - 102 is null, making possible to compare Q_{conv} computed from experiments to the theoretical predicted one. The Nusselt number has been evaluated using the Colburn (II - 41) and the Dittus-Boelter (II - 42) correlations and applying the Bhatti and Shah corrective coefficient [52] to take into account the entry effects. For a Re of 30000, the space-average Nusselt number has been found equal to 89.4 with the Colburn correlation and equal to 92 with the Dittus-Boelter correlation. The total convective heat transfer linked to the Colburn correlation is 482 W, which corresponds to a difference of 2.7% with the experimental value. With the Nusselt number calculated from the Dittus-Boelter correlation the agreement is even better; with a difference of less than 1%. As a consequence, the small differences between the theoretical predictions and the experiment validate the evaluation of the total convective heat transfer based on water temperature measurements. Comparison between Q_{conv} and term 'A' of Eq. IV - 102, in the case of the steady turbulent flow, shows that the calculation of the variation of the time-average enthalpy of air is not sufficient to correctly compute the total time-average convective heat transfer: not taking into account the turbulent term may lead to an underestimation of the total time-average convective heat transfer of around 22%.

It is observed from Figure 75 that the difference between Q_{conv} and term 'A' shows a significant variation in function of the pulsation frequency: Q_{conv} can take values higher, equal or inferior to the term 'A'. Assuming that the turbulent term in Eq. IV - 102 cannot be negative, which physically would represent a creation of turbulent heat flux inside the test-section, it can be concluded that a negative value of the term $\overline{\tilde{u}\tilde{T}}\Big|_0^L$ may occur. It is of interest to note that a negative value of term 'B' (for instance for a pulsation frequency of 80 Hz) describes an energy contribution to the control volume, through the outlet section, due to the pulsating component of the flow. This mechanism is experimentally made possible by the combination of a warming of the air, once it has left the test-section, followed by a flow reversal.

Downstream the test-section, the steel pipe is not water cooled and the experimental measurements have shown that, after the test-section outlet, the air near the wall has a lower temperature than the external wall of the pipe. Moreover, the calculation of the particle displacement from the instantaneous air velocity profile has shown that, when a flow reversal occurs, the air passes through the boundaries of the test-section several times.

To experimentally demonstrate the importance of this mechanism, the steel pipe downstream the test-section has been cooled by using dry ice in contact with the external wall of the pipe. Dry ice is in solid state at a temperature of -78.5°C and, once subjected to the ambient conditions, it sublimates, absorbing energy from the ambient to ensure the phase change. In this manner, it has been possible to impose an external wall temperature of around -40°C for all the experiments.

In these conditions, the results for Q_{conv} and term 'A' are shown in Figure 76. For each of the investigated pulsation frequencies, it can be observed, on the one hand, that Q_{conv} is always higher than the variation of the time-average air enthalpy and, on the other hand, that Q_{conv} exchanged during the use of dry ice is also always higher than that without dry ice (see Figure 75). As a consequence, these results show that, in the present experimental configuration, an energy contribution coming from the ambient downstream the test-section can occur in the case of reversing pulsating flows.

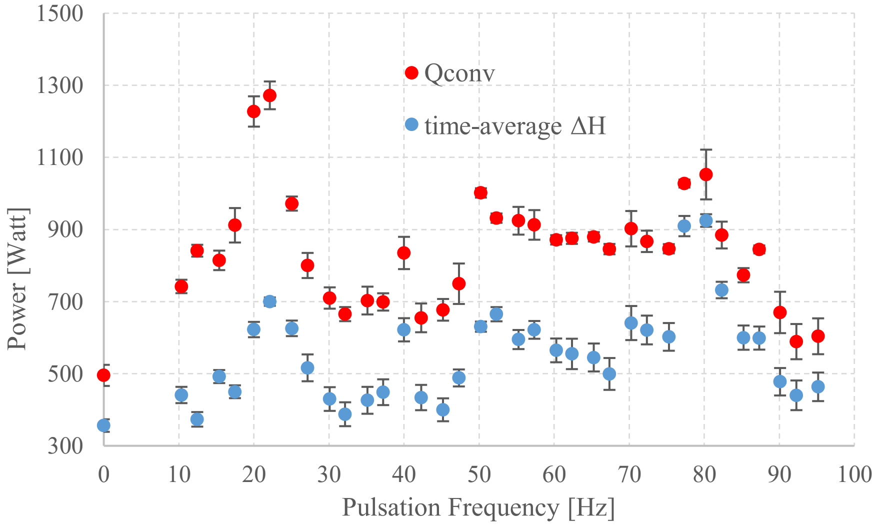

Figure 76: Terms of the air energy balance equation for a turbulent pulsating flow, w/ dry ice

IV.5 Impact of the flow pulsation on the convective heat transfers

The time-average Nusselt number $Nu = \frac{h_{air}D}{\lambda}$ is evaluated by modelling the heat transfer between the hot air and the water with three thermal resistances placed in series to describe the internal forced convection of the air, the radial conduction through the wall and the forced convection of the water.

The air convective heat transfer coefficient h_{air} assumes the following form:

$$h_{air} = \frac{\left(\frac{Q_{conv}}{\Delta T_{lm}} - \frac{\ln\left(\frac{R_{out}}{R_{in}}\right)}{2\pi L \lambda_{wall}} - \frac{1}{h_{water} 2\pi R_{out} L}\right)}{2\pi R_{in} L} \qquad \text{IV - 103}$$

Where R_{out} and R_{in} are the inner and outer diameters of the annular section of the water, L is the length of the test-section, λ_{wall} is the thermal conductivity of the wall, ΔT_{lm} is the logarithmic temperature difference usually used in the case of heat exchangers and h_{water} is the convective heat transfer coefficient of the water. The latter has been calculated according to the work of Dirker et al. [84], and ΔT_{lm} has been calculated according to the following equation:

$$\Delta T_{lm} = \frac{\left(T_{b_{in}} - T_{H2O-in}\right) - \left(T_{b_{out}} - T_{H2O-out}\right)}{\ln\left(\frac{\left(T_{b_{in}} - T_{H2O-in}\right)}{\left(T_{b_{out}} - T_{H2O-out}\right)}\right)} \qquad \text{IV - 104}$$

Where $T_{b_{in}}$ and $T_{b_{out}}$ are respectively the input and output bulk temperatures of the air, calculated as the surface integral of the four measured temperatures. $T_{H2O-out}$ and T_{H2O-in} are the outlet and inlet water temperatures.

The relative time-average Nusselt number Nu_{rel}, corresponding to the experiments with and without the dry ice, is reported on Figure 77. Results show that for the entire frequency range the relative time-average Nusselt number is always superior to 1: flow pulsation has a positive effect on heat transfers so that an enhancement of the internal forced convection, in comparison to the steady flow, is observed. Cooling the pipe downstream the test section has only added a positive offset to the relative time-average Nusselt number on the entire frequency range, without modifying the finding of the heat transfer enhancement. Such offset is due to the increase of Q_{conv} because of the augmentation of the heat energy advection by the oscillating component of the flow.

It can also be observed that, at the frequencies of 22.5, 50 and 80 Hz, a local maximum of the relative time-average Nusselt number appears. Thanks to the previous acoustic characterization of the system, it is possible to identify such frequencies as the 2nd, 3rd and 4th resonance modes of the system (see Table 2 paragraph III.7). A similar result has been found by testing different pipe lengths, in correspondence of the resonance frequency a local maximum in the time-average convective heat transfer has been observed. In this manuscript we paid attention only in the results for the maximum pipe lengths.

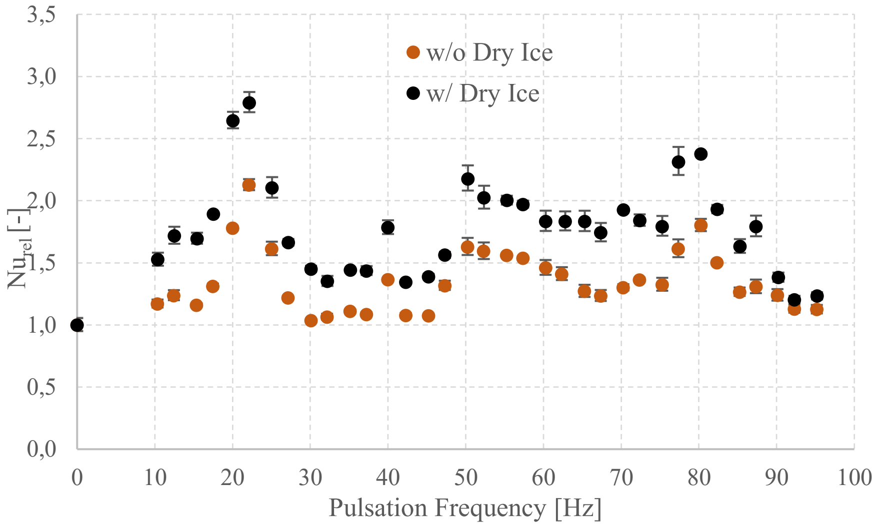

Figure 77: Relative time-average Nusselt number

From the instantaneous radial profile measurements of air velocity and temperature at the middle of the test-section, it is possible to calculate the local terms of the left side of the equation IV - 101. In order to be in agreement with the 1D approach, the physical quantities correspond to the integral of the measured profiles on the cross section.

As reported before, the wall cooling by dry ice does not change the main finding on the heat transfer enhancement, for this reason in the remaining part of the paper only the results for the experimental case conditions, without the pipe cooling by dry ice, have been reported. Furthermore, instantaneous measurements have been conducted only for some pulsation frequencies inferior to 40 Hz, the thermocouple dimensions make the measurements for higher frequencies not exploitable. More in particular, the measurement procedure of the instantaneous profiles of air axial velocity and air temperature, with respectively hot-wire anemometry and micro unsheathed thermocouple, requires a correction of the hot-wire signals to account for the temperature variation of air as well thermocouple signal compensation of the sensor time delay. For frequencies higher 40 Hz the implicit filtering of the real temperature variations, due to the thermal inertia of the sensors, makes the thermocouple signal compensation not feasible, avoiding furthermore, the temperature effect compensation of the hot-wire signals. The pulsation frequencies inferior 40 Hz have been chosen in function of particular heat transfer conditions: 10 Hz and 12.5 Hz have been chosen for the light impact on heat transfers, 20 Hz and 22.5 Hz have been chosen because of they are near the second resonance mode of the pipe and 30 Hz has been chosen due to its smallest relative Nusselt number.

The results of the term $\overline{\tilde{u}\tilde{T}}$ and $\frac{\Delta<u>}{\bar{u}}$ are reported in the following figures in (Figure 78 & Figure 79). Actually the term $\frac{\Delta<u>}{\bar{u}}$, which physically represents the weight of the phase-average velocity oscillation amplitude on the time-average velocity component, it has been choose to be considered in the phenomena analysis because of its potential to evidence the increase of the oscillating component of the flow due to pulsation.

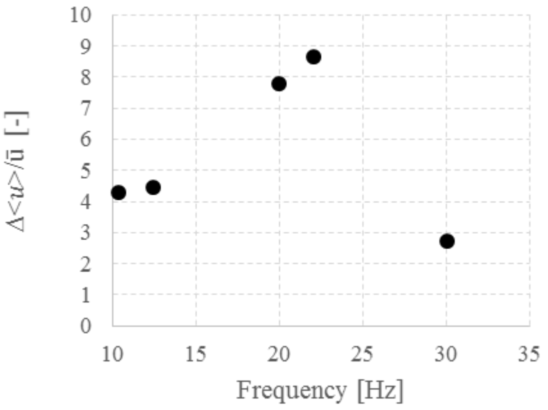

Figure 78: $\frac{\Delta<u>}{\bar{u}}$ *in function of the pulsation frequency*

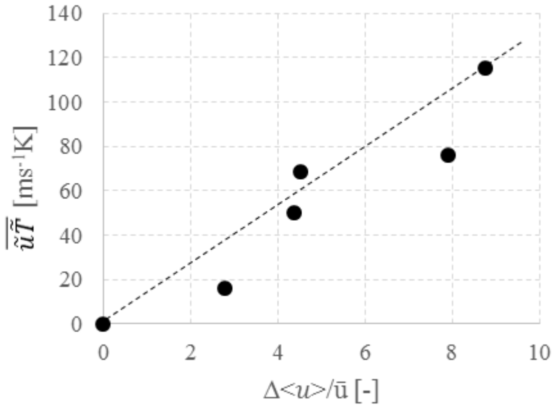

Figure 79: $\overline{\tilde{u}\tilde{T}}$ *in function of* $\frac{\Delta<u>}{\bar{u}}$

Results in Figure 78 show a maximum of the term $\frac{\Delta<u>}{\bar{u}}$ in correspondence of the resonance frequency of the system, suggesting that a flow resonance implies a wide oscillating component of the velocity. Furthermore since the term $\frac{\Delta<u>}{\bar{u}}$ assumes values higher than 1, it could be affirmed that for all the analysed frequencies, flow reversals appear.

Results in Figure 79 show the term $\overline{\tilde{u}\tilde{T}}$ in function of the term $\frac{\Delta<u>}{\bar{u}}$. By linking Figure 78 and Figure 79 it can be observed that large velocity oscillations, which correspond to an high $\frac{\Delta<u>}{\bar{u}}$ value, are favored for pulsation frequencies close to the resonance frequency (the highest values of $\frac{\Delta<u>}{\bar{u}}$ correspond to the frequencies around 22.5 Hz, the second resonance mode of the system) and lead to an almost linear increase of $\overline{\tilde{u}\tilde{T}}$ in function of $\frac{\Delta<u>}{\bar{u}}$. The heat transfer enhancement for these frequencies, observed on Figure 76 and Figure 77, is therefore mainly attributed to a large oscillating component of the fluid velocity which increases the oscillating heat advection.

In order to characterize also the impact of the pulsation frequency on the turbulent energy advection, the term $\overline{< u'T' >}$ in eq. IV - 102 should be evaluated by the instantaneous radial profile measurements of air velocity and temperature. Although hot-wires have a bandwidth frequency up to 10 kHz, high enough to measure the turbulent variation of the air velocity, the thermocouples are not adapted to measure turbulent temperature fluctuations because of their large response time, making so not possible to compute the term $\overline{< u'T' >}$.

Such limitations have been overcome by exploiting the Reynolds analogy between the momentum and heat transport. From the 1D momentum balance equation for an incompressible pulsating turbulent pipe flow, in which the phase and time averaging operators are applied, the following equation is obtained:

$$\rho\left(\underbrace{\frac{\partial(\bar{u}\bar{u})}{\partial x}}_{A}+\underbrace{\frac{\partial(\overline{\tilde{u}\tilde{u}})}{\partial x}}_{B}+\underbrace{\overline{<\frac{\partial(u'\mathrm{u}')}{\partial x}>}}_{C}\right)=\ \mu\left(\underbrace{\frac{\partial^2\bar{u}}{\partial x^2}}_{D}\right)+\underbrace{\overline{<\frac{\partial p}{\partial x}>}}_{E} \qquad \text{IV - 105}$$

It can be observed that the terms A, B and C, which correspond to the different components of the axial momentum of the flow, have the same mathematical form as the 3 terms in the left-hand side of Eq. IV - 101 and differ only from these terms by a multiplicative coefficient which corresponds to the Prandtl number. The terms D and E correspond, respectively, to the viscous dissipation and to the pressure losses due to the viscous effect with the wall of the pipe.

For a turbulent flow with a Prandtl number around 1, which means that the diffusion of momentum and thermal energy is similar, the Reynolds analogy implies that if a given flow field can be determined, the heat transfer characteristics can be found. In the experimental configuration of this work, the Prandtl number is about 0.69 (and is slightly dependent with temperature) so that the Reynolds analogy is commonly adopted in these conditions. Consequently, the terms in the left-hand side of eqs. IV - 101 and IV - 105 must exhibit a similar behavior.

Although the Reynolds analogy makes possible to use momentum transport terms in IV - 105 to identify the behavior of the heat flux transport terms in eq. IV - 102, the limitations of the velocity and temperature measurements don’t allow to compute the terms in eq. IV - 105 from the measurements of the hot pulsating turbulent flow analyzed in the previous part of the paper.

Since the hot-wire signal compensation for the temperature effect is applied only to the phase average signals it is not possible to extract the turbulent component of the air axial velocity from hot-wire signals.

To overcome such measurement limitations, experiments have been conducted for a pulsating cold turbulent pipe flow. Adopting the hypothesis of a scalar passive temperature field, it could be affirmed that a cold pulsating flow, with a same time-average Reynolds number, should have a velocity field behavior similar to the hot pulsating flow case. A same time-average Reynolds number implies that the time-average turbulent contribution to the momentum transport should be likely the same.

Assuming such hypotheses experiments have been conducted for a pulsating turbulent pipe flow with a centerline time-average temperature of 25°C: none air heating has been applied. In such experimental conditions the temperature variations, due to the flow compression, may be neglected making so the impact of the temperature on the hot-wire signal negligible. Consequently, the instantaneous hot-wire signals have not been compensated for the temperature impact, and they have been directly decomposed in the three component as in eq. IV - 98 ensuring the calculation of the turbulent component of the air axial velocity.

To account for the decrease of the sound velocity because of the decrease of the flow temperature, the total pipe length has been reduced to have the same resonance frequencies for the cold pulsating flow and the hot pulsating flow.

The computed terms A, B and C of Eq. IV - 105 are reported in Table 3. Results show that in the case of resonant flow state the time-average product of the oscillating component of the air axial velocity $\overline{\tilde{u}\tilde{u}}$ increases. This behavior is in agreement with the variation of the term $\overline{\tilde{u}\tilde{T}}$, as previous shown. The turbulent term $\overline{< u'u' >}$ also shows a local maximum in correspondence with the fluid resonant state, suggesting that pulsation frequency impacts the turbulent properties of the flow. Nevertheless, because of its lower order of magnitude than the term $\overline{\tilde{u}\tilde{u}}$, its contribution to the momentum transport could be neglected in comparison to the which one of the term $\overline{\tilde{u}\tilde{u}}$. Such results may be similarly applied to the heat flux transport: the effect of the turbulent heat flux advection on the convective heat transfer has not the major role on the convective heat transfer enhancement in comparison with the oscillating heat flux advection.

Frequency [Hz]	$\bar{u}\bar{u}$ [m²/s²]	$\overline{\tilde{u}\tilde{u}}$ [m²/s²]	$\overline{< u'u' >}$ [m²/s²]
10.4	245.7	375.8	6.4
12.4	242.3	293.4	3.6
20.0	211.3	1291.8	22.1
22.1	231.3	1893.5	40.3
30.0	214.6	210.2	2.6

Table 3: Terms A, B, C of equation IV - 105

A particular feature could be observed in the Figure 75, Figure 76 and Figure 77: for the specific frequency of 40.2 Hz a local maximum in the time-average convective heat transfer appears, besides, such frequency correspond to none resonance mode of the pipe.

To try to figure out the physical mechanism responsible of this heat transfer enhancement the centerline time-average air temperature in function of the test-section axial position has been reported in Figure 80. The temperature for the axial position equal to zero corresponds to the test-section inlet temperature which has been kept constant to 150°C for all the experiments, and, the temperature at 0.4 m of axial position corresponds to the outlet of the test-section. As noted in the figure, for the axial position of 0.2 m none measurement is reported. In correspondence of such section, as showed in the Figure 30, the hot-wire and the micro-thermocouples have been placed, however, temperature measurements have not been exploited for the particular case of 40.2 Hz, further details are reported in the following lines.

Results show that for the 40.2 Hz, while the temperatures at 0 and 0.1 m are quite constants for the three pulsation frequencies suggesting that the same amount of energy has been exchanged by convection, the air temperature at 0.3 m shows that in the case of 40.2 Hz an increase of the axial temperature gradient appears. Higher convective heat transfers occur in the central part of the test-section contributing to the heat transfer enhancement.

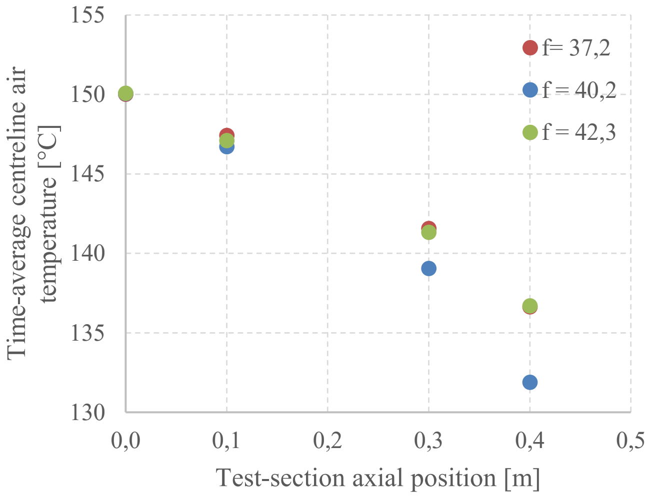

Figure 80: Centerline time-average air temperature in function of the test-section length, for a pulsating flow for three different pulsation frequency with a time-average Reynolds number of 30000

Analyzing in detail the test-section geometry it could be observed that, differently from the remaining part of the test-section, in correspondence of the placements of the hot-wire and the micro-thermocouples some cavities are present perpendicularly to the pipe wall. In the remaining part of the test-section the sheathed thermocouples cross the pipe wall through a hole of 0.5 mm, and the pressure sensors are placed directly on the internal surface of the pipe. Therefore, the sensor cavities are the only element which could be supposed to cause this local heat transfer enhancement by perturbing the velocity and temperature field of the flow.

To better figure out why the cavities could perturb the flow an excursus on the design of the test-section, focusing on the geometry of such cavities placed at the axial position B-B’ in Figure 30, must done. The design of the connections of each sensor in the section B-B’ is depicted in the following figure.

A cylinder with a length of 20 mm of length and an external diameter of 19 mm has been welded to the external wall of the inner pipe of the test-section. This cylinder is used to screw the support of the sensors. To avoid a wide cavity, perpendicular to the air pipe, the hole, which the thermocouples or the hot-wire probe traverse, has a diameter ‘d1’ of 7 mm, designed to let the most thick probe to be introduced in the pipe (the support of the hot-wire probe is a Dantec 55H25, which has an external diameter ‘d2’ of 6 mm, while the thermocouple has a diameter of 5 mm). The thickness of the inner pipe wall is of 2.77 mm.

Once the support of each sensor is screwed, as showed in Figure 81, the volume of the cavity between the sensor probe and the external wall of the inner pipe has been filled with several disks of Teflon, designed with a thickness of 1 mm and internal diameter ‘d2’ related to each of the used sensor probe. Although in this manner the volume of the connection has been widely reduced, a cylindrical cavity is still present in the pipe wall, characterized by a diameter of 7 mm and a deepness ‘L’ of minimum 2.77

mm in the case of the thermocouples and hot-wire connections and by a deepness of 10 mm in the case of the pressure sensor cavity.

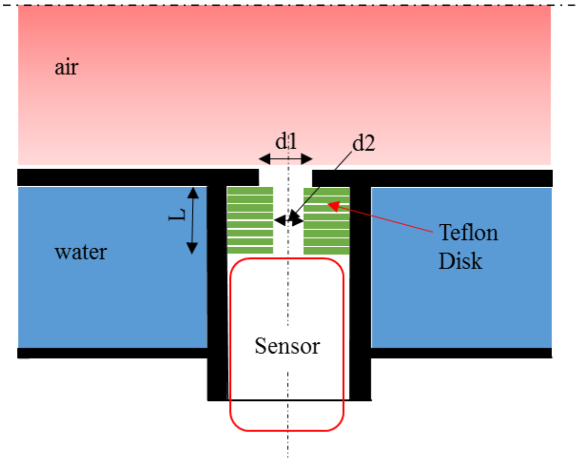

Figure 81: Detail of the connection, inside the test-section, in which the hot-wire probe, the micro thermocouple and the pressure transducer are placed

Theoretically these cavities could affect the velocity field of the flow and consequently also the convective heat transfers. Although air temperature and velocity radial profiles have been measured for this particular frequency, it has not been possible to compute the reals air velocity and temperature because of the data reduction, previously presented, gave unsatisfactory results. The thermocouple time-constants computed with the Kalman filter has shown negative non-physical values. In particular, though the thermocouple sensors have been placed at the same distance from the wall, it has been observed that a different time-average air temperature has been measured, suggesting that the flow was not anymore axial-symmetric. Furthermore, due to the lack of the air temperature measurement it has not been possible to compensate the hot-wire measurements and then to calculate the air velocity. Each of the sensor cavities has probably perturbed the flow in a different manner, leading to the loss of an axial-symmetric field. The only available instantaneous measurements were static air pressures for three different axial pipe locations (as showed in Figure 30 in the paragraph III.2.1), they are showed in the image below:

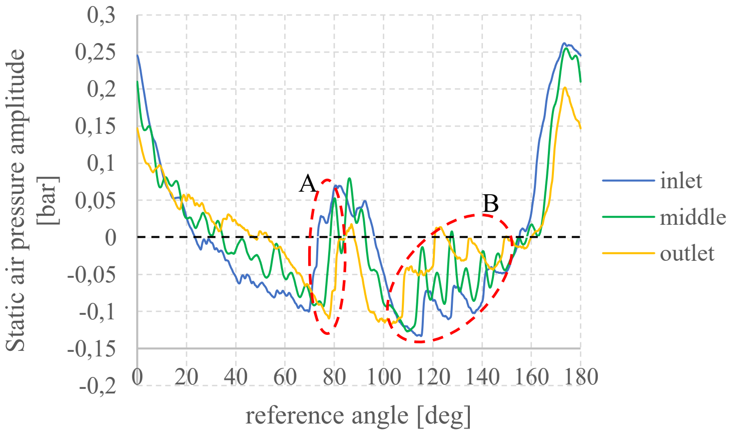

Figure 82: Static air pressure oscillating components for three different axial positions in the test-section, pulsating hot flow with f = 40 Hz

In Figure 82 two different features could be observed: firstly, as highlighted by zone A & B, instantaneous step-type variations of the air pressure occur during the cycle. Focusing on the axial order in which such variations appears, it could be noted that in the zone A the pressure variation occurs firstly in the inlet section, then in the middle and finally in the outlet section. Contrarily, in the zone B, the instantaneous pressure variations appear respectively in the order from the outlet to the inlet section.

The cause of such pressure variation has not been fully understood. In a first moment it has been supposed that for the particular frequency of 40 Hz, the cylinder head valve beating occurs. Valve beating is caused by the resonance of the mass-spring-dumper system, such phenomena is thus related to the rotational velocity of the camshaft and the mechanical properties of the valve/push-road/spring system. Starting from the hypothesis that the valve beating is independent from the pipe length, to verify such theory, pressure measurements are analyzed for a pulsation frequency of 40 Hz and for three different pipe lengths. Rapid air pressure variations, characterized by a step-shape profile, have not been observed for the shorter tested different pipe lengths, suggesting thus, that the valve beating should not be supposed to be the cause of this rapid pressure variation.

In the following lines a brief development of the acoustic theory is reported to evidence which should be the cause responsible of these rapid pressure variations.

Assuming that the waves propagating at a frequency lower than a critical frequency f_c called the cut-off frequency in a hard-walled pipe, equal to c/2D, and neglecting friction, then below the cut-off frequency, the (propagating part of the) acoustic field in a pipe consists only of plane waves. The conservation laws of mass and momentum are for a one dimensional flow given by:

$$\frac{\partial \rho}{\partial t}+u\frac{\partial \rho}{\partial x}+\rho\frac{\partial u}{\partial x}=\frac{\partial(\rho\beta)}{\partial t} \quad \text{IV - 106}$$

$$\rho\left(\frac{\partial u}{\partial t}+u\frac{\partial u}{\partial x}\right)+\frac{\partial p}{\partial x}=f_X \quad \text{IV - 107}$$

Where $\rho\beta$ corresponds to an external mass injection in the flow and f_X is an external force per unit of volume.

We assume now that the field consists of a uniform state (ρ_0, p_0, u_0), plus a perturbation (ρ', p', u') small enough to allow linearization:

$$\rho=\rho_0+\rho' \quad \text{IV - 108}$$

$$u=u_0+u' \quad \text{IV - 109}$$

$$p=p_0+p' \quad \text{IV - 110}$$

Introducing eqs. IV - 108 ÷V - 126 in eqs. IV - 106 and IV - 107

$$\frac{\partial \rho'}{\partial t}+u_0\frac{\partial \rho'}{\partial x}+\rho_0\frac{\partial u'}{\partial x}=\rho_0\frac{\partial \beta}{\partial t} \quad \text{IV - 111}$$

$$\rho_0\left(\frac{\partial u'}{\partial t}+u_0\frac{\partial u'}{\partial x}\right)+\frac{\partial p'}{\partial x}=f_X \quad \text{IV - 112}$$

We can eliminate ρ' by using the constitutive equation $p'=c^2\rho'$ which implies that we assume a homentropic flow.

A one-dimensional wave equation is obtained by subtracting the divergence of the momentum conservation law (IV - 107) from the convected time derivative ($\frac{\partial}{\partial t} + u_0 \frac{\partial}{\partial x}$) of mass conservation law (IV - 106) (to eliminate u'):

$$\left(\frac{\partial}{\partial t} + u_0 \frac{\partial}{\partial x}\right)^2 p' - c_0^2 \frac{\partial^2 p'}{\partial x^2} = c_0^2 \left(\rho_0 \frac{\partial' \beta}{\partial t} - \frac{\partial f_x}{\partial x}\right) \qquad \text{IV - 113}$$

A widely used alternative method to analyze the acoustic waves is to write the wave equation (IV - 113) in characteristic form. This allows a simple geometrical interpretation of the solution of initial condition and boundary condition problems with the help of a so-called (x,t) diagram.

In the absence of the source term in eq. IV - 113 this simply states that along the characteristics $c^{\mp}$ the Riemann invariant $\Gamma^{\mp}$ is conserved:

$$\Gamma^{+} = u' + \int \frac{dp}{\rho c} \text{ constant along } c^{+} = \left\{(x,t) \middle| \frac{dx}{dt} = u + c\right\} \qquad \text{IV - 114}$$

$$\Gamma^{+} = u' - \int \frac{dp}{\rho c} \text{ constant along } c^{-} = \left\{(x,t) \middle| \frac{dx}{dt} = u - c\right\} \qquad \text{IV - 115}$$

Addition and subtraction of the two previous equations yields, along the c+, the result:

$$u = \frac{1}{2}\left(\Gamma^{+} + \Gamma_0^{-}\right) \qquad \text{IV - 116}$$

$$\int \frac{dp}{\rho c} = \frac{1}{2}\left(\Gamma^{+} + \Gamma_0^{-}\right) \qquad \text{IV - 117}$$

Hence, the velocity u is constant along the c+ considered. As in addition to the thermodynamic quantity ($\frac{dp}{\rho c}$) also the entropy s is constant along the c+ (because the flow is homentropic), we conclude that all thermodynamic variables are constant along the c+.

In particular the speed of sound c is constant along a c+ in the simple wave. Therefore, the slope (u + c) of the c+ characteristic is constant, and the characteristic is a straight line in an (x,t)-diagram.

As an example of an application we consider the simple wave generated for x > 0 by a given boundary condition $p(0,t)$ at x = 0, assuming a uniform quiescent fluid ($u_0 = 0$) with a speed of sound $c = c_0$ for t < 0. The sound speed $c(0,t)$ at x = 0 is calculated by using the equation of state:

$$\frac{p}{p_0} = \left(\frac{\rho}{\rho_0}\right)^{\gamma} \qquad \text{IV - 118}$$

Which implies:

$$\frac{c}{c_0} = \left(\frac{p}{p_0}\right)^{\frac{(\gamma-1)}{2\gamma}} \qquad \text{IV - 119}$$

The message from the c^--characteristics implies:

$$u = \frac{2c_0}{\gamma - 1}\left(\frac{c}{c_0} - 1\right) \qquad \text{IV - 120}$$

Introducing eq. IV - 119 in IV - 120 leads to:

$$u = \frac{2c_0}{\gamma - 1}\left(\left(\frac{p}{p_0}\right)^{\frac{(\gamma-1)}{2\gamma}} - 1\right) \qquad \text{IV - 121}$$

We can now easily construct the simple wave by drawing at each time t the c^+-characteristic emanating from x = 0. We see from these equations that a compression $\frac{\partial}{\partial t}p(0,t) > 0$ implies an increase of both c(0,t) and u(0,t), and of course the opposite for a decompression or expansion. As a result, characteristics at the peak of a compression wave have a higher speed (u + c) than those just in front of it. This results into a gradual steepening of the compression wave. This non-linear deformation of the wave will in the end result into a breakdown of the theory because neighboring c^+-characteristics in a compression intersect for travelling times larger than t_s or distances larger than x_s.

The approximation on which the equations are based will already fail before this occurs because the wave steepening involves large gradients so that heat conduction and friction cannot be ignored anymore. This limits the process of wave deformation. For large pressure differences across the wave the final gradients are so large that the wave thickness is only a few times the molecular mean free path, so that a continuum theory fails. The wave structure is in the continuum approximation a discontinuity with jump conditions determined by integral conservation laws. We call this a shock wave. Apart from discontinuous, the solution is also dissipative, as there is production of entropy in the shock wave.

The aforementioned development justifies that the rapid pressure variations should be likely caused by the superposition of the travelling acoustic waves, which induces local shocks. Nevertheless, ulterior measurements of the air pressure at different pipe axial positions as well as in the outlet plenum 2 should be performed to perform calculation of the acoustic characteristics and to validate such theory.

The second phenomena, which could be also observed in Figure 82, is that in addition to the observed steepening compression waves, rapid oscillations appear only for the pressure at the middle of the test-section (see Figure 30). Inlet and outlet air pressure don't show this behavior.

These rapid pressure oscillations should be the cause of the consequence of a perturbation of the velocity field. Although, as previously claimed, hot-wire and thermocouple measurements have not been exploited to compute the real air velocity and temperature profiles, to have further information on the velocity field near the sensor cavity air velocity has been measured for the pulsating flow in cold conditions. As previously done to study the pulsation impact on the turbulence field, assuming that the temperature field be a passive scalar filed allows to affirm that the velocity filed of a cold flow could be considered representative of the velocity field of a hot flow. In particular, a pulsating cold flow with the same time-average component of the axial bulk velocity has been produced and tested.

Air pressure and velocity have been measured, the procedure to detect flow reversal has been applied and both the phase-average and the turbulent component of the signal have been extracted from the signals.

Through the phase-average component of the static air pressure at three axial positions in the test-section, showed in the following figure, it has been possible to observe if rapid pressure oscillations appear also for a cold pulsating flow.

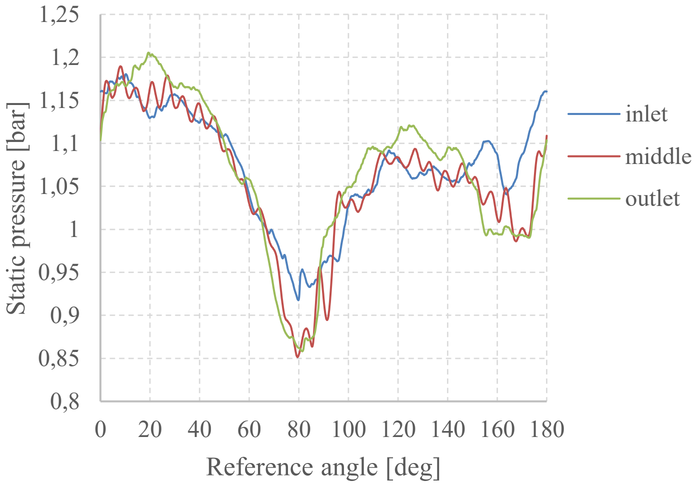

Figure 83: Static air pressures in the test-section, f = 40 Hz, cold flow, constant $\overline{U}_b$

Results in Figure 83 show two important features: firstly, contrarily to the hot pulsating case, steepening flow compressions don’t exist in the cold pulsating case. Such evidence is another experimental ascertainment that enriches the hypothesis that the valve beating cannot be considered as a cause. Lower flow temperatures imply lower sound speed as well as the fluid properties, suggesting, as the results show, that the acoustic characteristics, previously introduced, interact differently between each other don’ leading to the steeping flow compressions observed for the hot pulsating flow.

Though the rapid pressure variations, already observed only for the pressure at the middle of the test-section, have been observed also for the cold flow. The advantage of having these pressure variations also in a cold flow has been that in such conditions it has been possible to also measure the air axial velocity.

Pressure and axial air velocity profiles in correspondence of the middle axial position of the test-section are reported in Figure 84. The phase-average component of the axial air velocity has been reported for three different distances from the wall corresponding to a y/R ratio of 0, 0.4 and 1 respectively.

Results show that as well as for the pressure profile also the velocity near the wall (y/R = 0, blue line Figure 84) exhibit a rapid variations which have a dynamic equal to the pressure variations.

A second interesting feature evidenced from the results is that as the distance from the wall increases, the velocity oscillations have a decreasing amplitude, as well as it could be observed that the local maxima of such variations starting from the wall to the core have a positive phase-delay. In view of all this it could be supposed that a perturbation is produced near the wall and it diffuses away from the wall to the core of the fluid.

The supposed perturbations could be the responsible of an enhancement of the convective heat transfer between the wall and the fluid, for instance, they contribute to the energy advection over the section; however furthers 2D air velocity and temperature measurements should be conducted to evidence this phenomenon.

The comprehension of this phenomenon represents actually the main challenge: itis the acoustic field, near the wall cavity, oscillates and consequently impacts the velocity field and then the energy convection; or is the velocity field which is affected from the wall cavity and then it creates local pressure waves and it increases the local energy convection. It can be anyway affirmed that these perturbations are likely due to the interaction between the flow and the wall cavity.

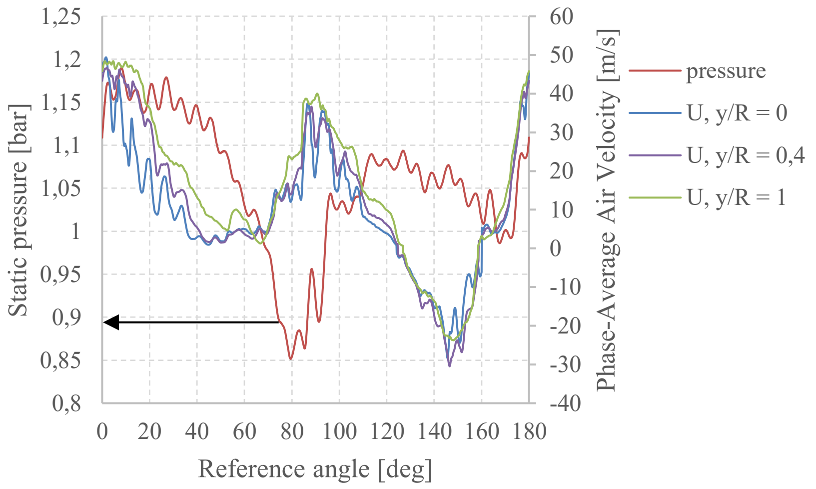

Figure 84: Static air pressure & air velocity in the test-section, f = 40 Hz, cold flow, constant $\overline{U}_b$

The noise radiated by a flow past a cavity has been widely studied during the last fifty years because of its practical interest and because of the variety of theoretical questions that it raises. A complex feedback process sustains coherent oscillations in the shear layer developing above the cavity, leading to important radiated noise. This noise consists of intense discrete and broadband components. In the following lines the fundamentals of the cavity flow noise are presented and discussed.

The first to shed light on the inherent mechanism has been Lord Rayleigh from his observations of a high-pitched whistle called a bird call because it was used by hunters to lure birds. He suggested quite correctly we know now that "when a symmetrical excrescence of the jet reaches the second plate, it is unable to pass the hole with freedom, and the disturbance is thrown back, probably with the velocity of sound, to the first plate, where it gives rise to a further disturbance, to grow in turn during the process of the jet". The fact that the self-sustained oscillations are present both in the flow and acoustic field suggest that a stable phase relationship occurs between the upstream and downstream solid surfaces: such phenomenon is called *feedback loop* (cavity flow sketch in Figure 85).

The very organized oscillations in cavities are self-sustained by the following chain of events:

- The feedback consists in the upstream propagation of pressure perturbations generated in the impingement region toward the region of maximum receptivity of the shear layer, as it separates from the upstream edge.
- Flow instabilities are then shed near the upstream edge.
- The amplification of the instabilities rapidly induces non-linear vortices, which continue to grow due to fluid entrainment and viscous effects.
- During the impingement, new pressure perturbations are generated, which propagate toward the upstream direction, closing the loop.

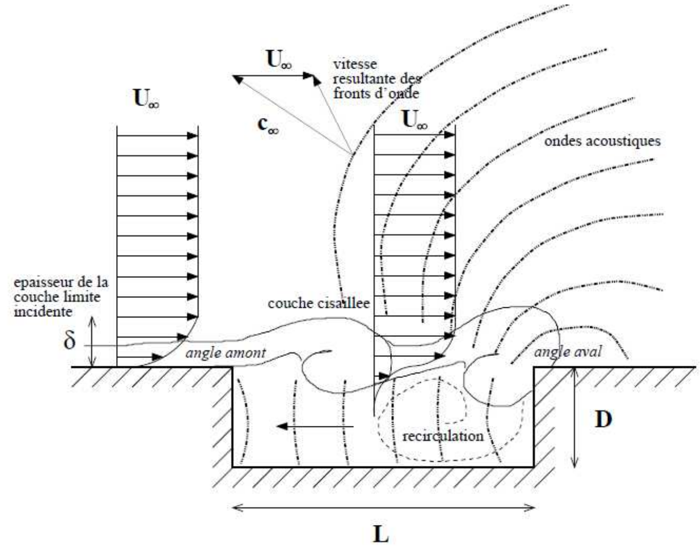

Figure 85: Sketch of cavity flow

Although the intimate details of the feedback mechanism are still not completely known, the experimental works for various conditions have shown that the pressure perturbations, that influence the upstream flow development, have either an acoustic or an aero/hydrodynamic nature.

As Powell [85] observed in his studies, for low-speed flows in a gas when the ratio between the length between the birth of the shear layer and the obstacle and the acoustic wave length λ is widely inferior to one, the feedback phenomenon arises in the near-field, and is essentially aerodynamic in nature. The conversion of pressure fluctuations, which arrive in the separation region, into vortical fluctuations has been studied by Morkovin and Paranjape [85]. They show how the pressure gradient plays an essential role in the conversion process. Moreover, they suggested that the back-and-forth motion near the separation point helps to convert irrotational pressure fluctuations into rotational vorticity perturbations.

We generally talk about *Rossiter modes* when the self-sustained selection results from an aero-acoustic feedback loop, as described in the previous section. Kelvin-Helmholtz-type instabilities, shed periodically in the shear layer near the upstream separation corner, grow during convection toward the downstream edge. A sound pulse is generated when these vortical structures reaches the downstream edge, then propagates upstream and excites the shear layer formation.

At low Mach numbers, the acoustic response of the cavity can superimpose on the aeroacoustics feedback. For frequencies close to that of the acoustic resonances, the acoustic forcing by the cavity resonance can overwhelm that provided by the impingement pulse. The turbulent shear layer spanning the cavity open can act as a broadband noise source which can drive longitudinal or depth resonance modes of the cavity box closed by the shear layer or the Helmholtz resonance depending on the cavity opening and volume. The influence of the freestream flow velocity has been investigated in the majority of the experimental studies, however, experimental configurations ere focused on a stationary flow grazing the cavity contrarily to our case. The effect that the velocity variates modify the boundary layer structures within the pulsation cycle, none experimental evidence in such operating conditions is available in literature. Further measurement of the 2D flow velocity field, near the cavity, should be conducted to better understand the nature of such phenomena. Anyway, the theory that the cavity noise has an acoustic nature, i.e. the cavity acoustically resonates and then superimposes to the hydrodynamic field seems to be inappropriate: in this case the cavity is widely called ‘Helmholtz resonator’. A Helmholtz resonator (Figure 86) is a large volume ended by a neck (contraction), like for instance the neck of a bottle. When the bottle is small compared to the acoustic wavelength, the body of the bottle acts as an acoustic spring while the neck of the bottle is an acoustic mass.

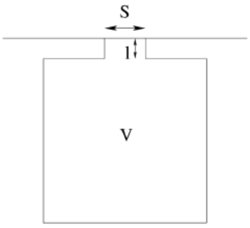

Figure 86: Helmholtz resonator

The Helmholtz frequency is $\omega = \sqrt{\frac{c^2 S}{Vl}}$, and as the expression states it is dependent only of the geometry characteristics of the cavity, a unique fundamental frequency of resonance exists. As results show in Figure 87, rapid pressure oscillations occurs also for different flow pulsation frequencies: while at 45.24 Hz pressure oscillations don’t exist, at 57.38 Hz (black line in Figure 87) pressure oscillations have been observed, suggesting so that acoustic resonance of the cavity should not likely be mechanism responsible of the generation of the flow cavity noise.

Figure 87: Static air pressures at the middle of the test-section for different pulsation frequencies

Although the physical mechanisms causing the heat transfer enhancement have not been understood, previous results bring an important claim: an attention should be always paid to well design the sensor connections to avoid that the interaction between the cavity and the flow have a non-negligible influence on the flow behavior.

IV.6 Influence of the Reynolds number and pulsation variations on the convective heat transfers

The impact of the flow pulsation on the convective heat transfer has been investigated also for four different Reynolds numbers varying from 18900 to 35000. Experimental conditions, such as the air temperature at the inlet of the test-section as well as the water mass flow rate and inlet temperature have been main constants. The pipe downstream the test-section has not been cooled with dry-ice. Results are shown in the figure below:

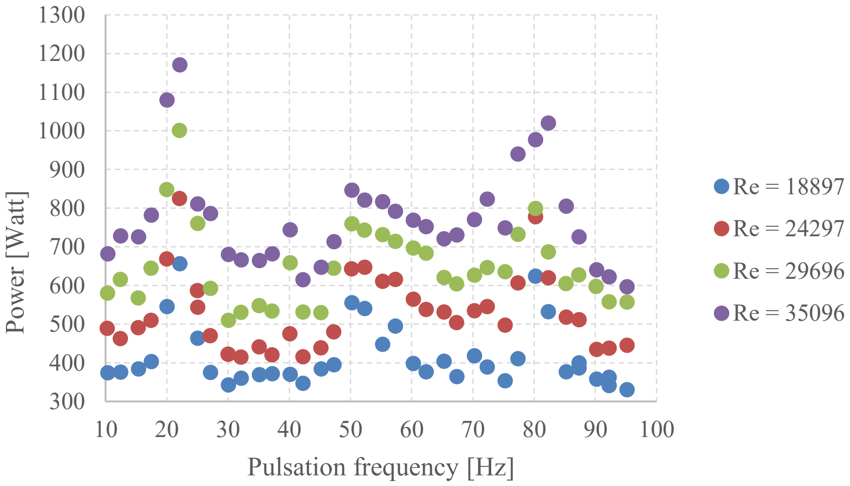

Figure 88: Convective heat transfer power in function of Re & f, w/o dry ice

Results show that flow pulsation has the same impact for all the test time-average Reynolds number: a heat transfer enhancement exists at the resonance frequencies of the pipe.

It could be also observed that for a low Reynolds number of 24297 the heat transfer enhancement at 40 Hz of pulsation frequency is less important that the higher Reynolds number, while for a Re = 18897 it doesn't exist anymore. With a constant air temperature at the inlet of the test-section, a decrease of the Reynolds number implies a decrease of the time-average mass flow rate. Consequently, lower instantaneous velocities are reached inside the test-section, suggesting that the feedback loop, the possible cause of the particular heat transfer enhancement at this pulsation frequency as discussed before, it is likely not anymore activated by the interaction of the kinematic and acoustic fields.

IV.7 A quasi-steady approach for the convective heat transfers prediction

Most attempts to solve the heat transfer problem for a pulsating flow analytically or numerically resort to using steady or quasi-steady assumptions. Quasi-steady, as applied to oscillating flows, means that at any point in the cycle the flow is assumed to behave as if it were steady at the instantaneous velocity. This assumption should only be valid for flows with low frequencies or small oscillation amplitudes, since it requires that the flow come to fully developed equilibrium within a time much less than the cycle time.

The first known use of this approach was by Martinelli et al. in 1943 [23], equation IV - 122 shows the quasi-steady adaptation of the Colburn correlation for turbulent heat transfer assuming a sinusoidal profile of the axial air velocity.

$$\overline{Nu} = 0.023\overline{Re}^{0.8}Pr^{1/3}\int_0^1 (|1 + Bcos(2\pi t)|)^{0.8} \, dt \qquad \text{IV - 122}$$

B corresponds to the ratio $\frac{\Delta<u>}{\bar{u}}$ and t corresponds to the dimensionless cycle time.

In the right side of equation IV - 122 could be noted that the term outside the integral operator corresponds to the Nusselt number calculated for a stationary flow, it is based to a the time-average value of the bulk axial velocity. The remaining term, inside the time integral, corresponds thus to the relative Nusselt number previously introduced.

A second manner to predict the relative Nusselt number, assuming a quasi-steady hypothesis, consists into the calculation of a phase-average Nusselt number, defined with the Colburn correlation based on the Reynolds number computed from the phase-average component of the bulk axial velocity.

Then, integrating it over the pulsation period leads to the time-average Nusselt number.

In the following figure the results of the previously cited two methods are presented and compared to the Nusselt number experimentally calculated. In this case calculation are made only for the experiments with a time-average Reynolds number of 30000.

Bblack circle markers correspond to the relative Nusselt number calculated with the equation IV - 122, the term B has been computed from the experimental data. The green square markers correspond to the relative Nusselt number obtained by computing the Colburn correlation introducing the experimental phase-average bulk axial velocity profile, and, by integrating it through the entire cycle. The red triangle markers represent the relative Nusselt number calculated from the time-average variations of the water enthalpy from the experiments.

Results in Figure 89 show that the equation IV - 122 widely overestimates the convective heat transfers up two times the experiments for the 22.5 Hz case, while the application of the Colburn correlation on the experimental phase-average bulk axial velocity profile overestimates the experiments up to 50%.

It could be claimed that predicting the convective heat transfers with a quasi-steady assumption largely overestimates the experimental results.

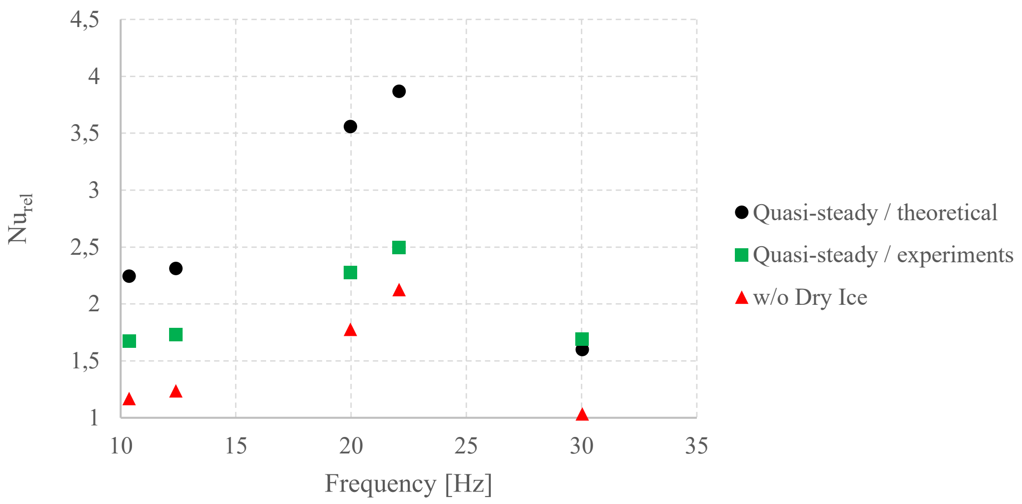

Figure 89: Nu_{rel} prediction with a quasi-steady assumption

A comparison between the results of a quasi-steady approach and the experimental results should be conducted for higher pulsation frequencies motivated by the fact that as the pulsation frequency increases as the hydrodynamic and temperature field have not enough time to become in equilibrium, and finally the quasi-steady assumption losses its applicability.

IV.8 Towards a Nusselt correlation for pulsating turbulent pipe flows

As cited in the previous paragraph II.2.3, whereas for a stationary turbulent pipe flow it has been widely demonstrated that the Nusselt number is function of the Gz_T, Re and Pr numbers, for an unsteady convection process, the Vaschy-Buckingham Π analysis, for a low-speed laminar flow in a pipe, shows that the time-average Nusselt number may depend on as many as seven dimensionless groups [21] (as expressed in eq. II - 54):

$$\overline{Nu} = f\left(\frac{\Delta < u >}{\bar{u}}, \frac{U_0}{\omega D}, \frac{c}{\omega D}, Wo, Gz_T, Re, Pr\right) \qquad \text{IV - 123}$$

Additional parameters arise because of the flow pulsation:

- the Womersley number $Wo = \sqrt{\frac{\rho \omega D^2}{\mu}}$, which is a ratio of the channel height to the Stokes boundary-layer thickness. It is a dimensionless expression of the pulsatile flow frequency in relation to viscous effects.
- the amplitude ratio $\frac{\Delta<u>}{\bar{u}}$, which is a measure of the amplitude of the velocity waveform, as mentioned earlier in this study,
- the parameter $\frac{U_0}{\omega D}$, which represents the relative magnitudes of the Lagrangian and convective accelerations and dictates the importance of ''acoustic streaming''. This term has been investigated in the works of Jackson et al. [22]: U_0 represents the Lagrangian velocity generated from the acoustic streaming which is generally calculated from the acoustic theory for a plane wave propagation.
- the grouping $\frac{c}{\omega D}$ which is a measure of the wavelength of the applied pressure oscillation to the relevant streamwise length scale (c is the velocity of sound).

The time-average Reynolds and the Prandtl number could be considered constants for all the experiments. The $Gz_T = D/L_d RePr$ which represents the thermally developing flow entrance length $'L_d'$ for a laminar flow, it has not been experimentally measured. As affirmed in the paragraph II.2.3, exhaustive experimental evidences on the impact of the flow pulsation on the entrance length are not available.

The specific flow conditions in our study allow, furthermore, to neglect the term $\frac{U_0}{\omega D}$ representative of the the acoustic streaming effect on heat transfers. Acoustic streaming, as observed from Jackson et al. [22], is a phenomenon which appears in the resonant pulsating flows, according to a flow oscillation that varies in amplitude with axial position, generates a secondary time-averaged velocity component. The flow generated by acoustic streaming have the form of large longitudinal recirculation cells that are one quarter the length of the acoustic wavelength and occur at half-wavelength intervals. In the quarter wavelength between these cells, acoustic streaming causes a velocity component towards the wall of the pipe, increasing the velocity near the wall. In our experimental conditions acoustic streaming effects have been neglected because of the different nature of excitation of the flow: the pulsating mechanism adds a pulsation on the mean component of the flow, nevertheless, the flow is not always in resonant state.

In the following figures (Figure 90, Figure 91 and Figure 92), the relative Nusselt number is shown in function of the remaining relevant parameters $\frac{c}{\omega D}$, Wo and $\frac{\Delta<u>}{\bar{u}}$ for all the investigated pulsation frequencies inferior to 30 Hz. As previously the following results have been computed for the experiments without the pipe cooling by dry ice.

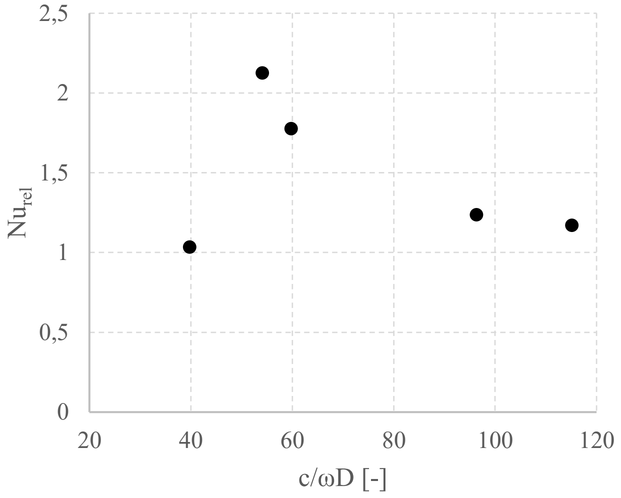

Figure 90: Nu$_{rel}$ vs c/ωD

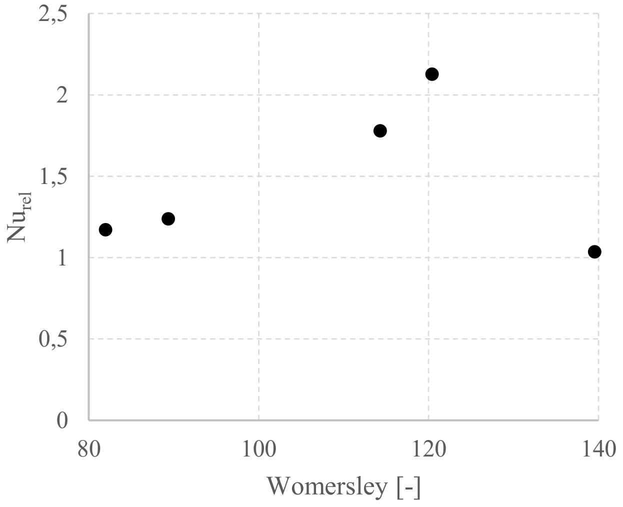

Figure 91: Nu$_{rel}$ vs Womersley number

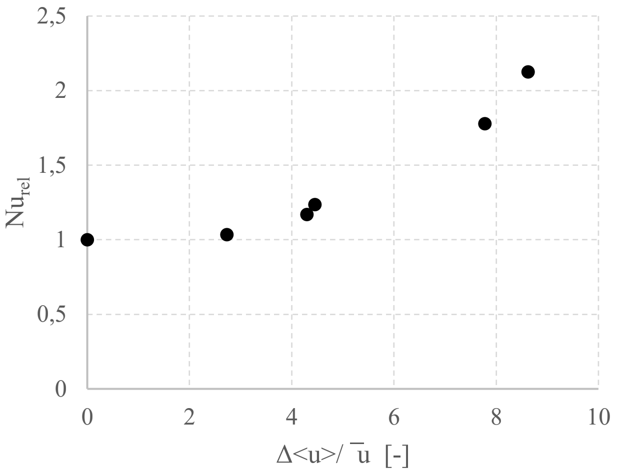

Figure 92: Nu$_{rel}$ vs $\frac{\Delta<u>}{\bar{u}}$

Results in the Figure 90 show that by increasing the pulsation frequency the term $\frac{c}{\omega D}$ decreases, as well as the relative Nusselt number increases till a local maximum which corresponds to the second resonance mode of the system. Then for a higher frequency the relative Nusselt number decreases. It could be then affirmed that the relative Nusselt number dependence from the term $\frac{c}{\omega D}$ does not show a monotonic trend, suggesting that such parameters should not be considered in a new Nusselt correlation to account for pulsating effects. A similar non monotonic finding could be observed in Figure 91: an augmentation of the Womersley number, which represents an augmentation of the inertial force weight, due to pulsation, on the viscous effects, corresponds to an increase of the relative Nusselt number until a local maximum at the second resonance mode frequency. A similar behavior was found by Hua et al. [32], a local maximum in the heat transfers was found for a particular Wo corresponding to a frequency of 90 Hz, for all the tested Reynolds number.

The relative Nusselt number dependence from the term $\frac{\Delta<u>}{\bar{u}}$, in Figure 92, shows a monotonic behavior: as well the amplitude of the axial velocity increases, for a constant time-average bulk axial air velocity, as the relative Nusselt number increases.

A similar result has been found in the works of Wang et al. [43], it is reported in Figure 93 for a fixed pulsation frequency corresponding to a Womersley number of 40, the relative Nusselt number has been found to increase monotonic in function of the velocity amplitude scale.

In their work authors numerically studied the convective heat transfers in pulsating turbulent flow with large velocity oscillating amplitudes in a pipe at constant wall temperature is numerically studied. A low-Reynolds-number (LRN) k–e turbulent model has been used in the turbulence modeling. The model analysis indicates that Womersley number is a very important parameter in the study of pulsating flow and heat transfer. Flow and heat transfer in a wide range of process parameters are investigated to reveal the velocity and temperature characteristics of the flow. Both larger amplitude of velocity oscillation and flow reversal in the pulsating turbulent flow also greatly promote the heat transfer enhancement.

It has to be noted that the pulsation frequencies in our experiments range from 80 to 200 higher than the works of Wang et al.

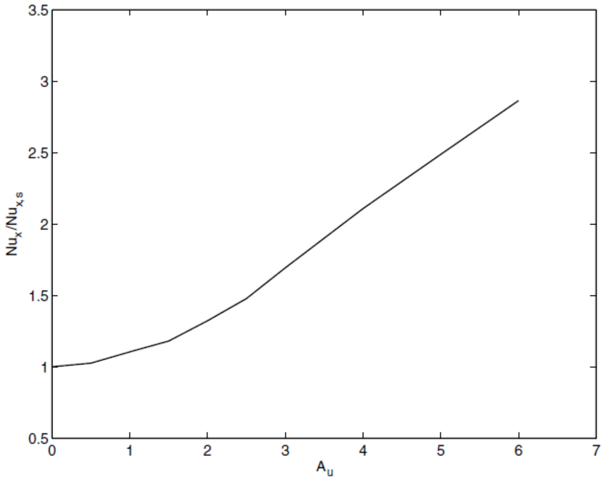

Figure 93: The effect of velocity oscillating amplitude on heat transfer enhancement for Re = 25000, Wo = 40.

Experimental results also agree with the finding previously presented: the increase of the oscillating velocity component represents the mechanism which has the major role in the heat transfer enhancement, suggesting that the velocity ratio $\frac{\Delta<u>}{\bar{u}}$ should be considered in a new Nusselt correlation to account for pulsating effects.

IV.9 Conclusions

In this study the heat transfer problem for a pulsating turbulent pipe flow has been investigated. A test-rig, designed to generate a pulsating hot air flow representative of the intake and exhaust of an internal combustion engine, has been presented in the previous chapter. In such experimental apparatus a pulsating turbulent hot air flow exchanges energy with a water cooled pipe; pulsation frequency ranges between 10 and 95 Hz and the Reynolds number based on the time-average velocity may range between $1.8 \times 10^4 < Re < 3.6 \times 10^4$.

In this chapter, a particular attention has been paid in the calculation of the time-average convective heat transfer by developing an analytical formulation of the heat transfer problem for a 1D pulsating turbulent pipe flow.

An ad-hoc experimental procedure have allowed to evidence that, in the case of a reversed pulsating flow, a contribution to the energy balance equation through the boundaries, which impacts the total convective heat transfers, may occur. Such boundary energy contribution is mainly due the simultaneous apparition of two different phenomena: in a first moment the air which flows out the test-section receives thermal energy from the wall, then due to flow reversal such energy is reintroduced in the test-section.

Results have also shown that the flow pulsation enhances heat transfers in the entire range of the investigated frequencies up to around three times the stationary case. In particular results have showed that when the flow is excited with a frequency equal to a resonance mode of the system (previously acoustically characterized), a strong increase in convective heat transfers occurs. Punctual instantaneous measurements of air velocity and temperature for a fixed pipe section have demonstrated that the increase of the energy axial advection due to the oscillating component of the velocity represents the major cause of the heat transfer enhancement.

The relative Nusselt number, defined as the ratio between the Nusselt numbers for the pulsating and counterpart steady flows, has been found to be monotonic proportional to the ratio between the velocity oscillation amplitude and the velocity time-average component, suggesting that such parameter, which characterizes the amplitude of the velocity waveform, should be considered in a new Nusselt correlation to account for pulsating effects.

A fully don’t understood phenomenon has been found to enhance convective heat transfers for the particular frequency of 40 Hz. Such enhancement has been found to appear locally in the central part of the test-section, where hot-wire, pressure and micro-unsheathed thermocouples sensor connections are placed. Instantaneous measurements of air velocity and static pressure for different frequency conditions show that a high oscillating component appears. Because the sensor connections behavior like a cavity, the *feedback loop* mechanism characteristic of the cavity flows, it has been supposed to be the cause of an interaction between the kinematic and the acoustic fields. The direct consequence is a high radial velocity component due to local flow recirculation, which in a second moment increases convective heat transfers. It is worth to affirm that if such phenomenon should be fully understood, it may be used in future, like a passive method, for the heat transfer enhancement.

Although, as previously affirmed, the increase of the energy axial advection due to the oscillating component represents the major cause of the heat transfer enhancement, secondary phenomena of radial convection enhancement during flow reversal, in accordance with the previous results of Dec et al. [26], [27], have been observed from the temperature and velocity profile measurements. They will be presented and discussed in the following chapter. In particular to evidence and demonstrate the importance of such mechanisms and its impact on the convective heat transfer to the wall the heat transfer problem will be analytically developed with a 2D assumption.

Chapter / Chapitre V

Characterization of the radial transport of thermal energy by a 2D analytical approach

Abstract

The data analysis with a 1D assumption, presented in the chapter IV, has evidenced that an increase of the axial energy advection due to large velocity oscillations represent the major mechanism of the heat transfer enhancement. However, the analysis of the phase-average profiles of the air axial velocity and air temperature, in this chapter, have suggested that secondary mechanisms exist, such as the increase of the radial heat advection during flow reversal.

In this chapter a 2D analytic development of the energy governing equation has been presented to evidence the terms in the equation which are representative of the radial energy advection, as well as it has been demonstrated that the impact of such phenomenon on the convective heat transfer at the wall could not be directly estimated.

In view of this, the temperature and velocity profiles for a 10 Hz pulsating flow have been reported and discussed: results suggest that during the flow reversal an enhanced temperature mixing over a pipe section occurs, as well as from the velocity profile for a cold pulsating flow it has been possible to affirm that a perturbation of the velocity field diffuses from the wall to the core during flow reversal.

These two element contribute to the hypothesis of an enhanced radial energy aviation during flow reversal. However, due to the lack of the measurement of the radial component of the flow velocity it has not been possible to compute all the terms of the 2D energy governing equation, and it has not possible to numerically demonstrate the existence of such radial advective phenomenon.

Such inconvenient has been overcome through a 2D modelling phase of the heat transfer problem with the Fluent-Ansys CFD software. The main purpose has been to reproduce a flow reversal similar to which one experimentally observed, then, to calculate the terms of the energy equations and evidence its correlation with the convective heat transfer to the wall. The Fluent modelling of the governing equations, as well as its limitations have been revised in the previous paragraphs.

CFD results have showed that as experimentally observed, during flow reversal an enhancement of the radial energy advection occurs, and thanks to the computation of the energy equation terms it has possible to evidence that such mechanism assumes a weight more important than the axial advection.

It has been also observed that such phenomena locally increase the heat transfer coefficient during flow reversal.

In the last part of the chapter the time-average component of the radial advection term has been computed for different pulsation frequencies and it has been compared to the steady case, with the main purpose to evidence the impact of the pulsation frequency on the radial advection mechanism. Results have shown that the maximum of such profile moves from the core to the wall of the pipe as the pulsation frequency increases suggesting that the radial advection remains enhanced in a narrower layer near the pipe wall.

V. Characterization of the Radial Transport of Thermal Energy by a 2D Analytical Approach

V.1 Introduction

In the previous chapter the impact of the flow pulsation and the Reynolds number, based on the time-average bulk axial air velocity, on the time-average convective heat transfers have been experimentally investigated. Results show that in the entire frequency range (ranging between 10 to 95 Hz), and Reynolds number range (from 19000 to 35000), an enhancement of the time-average convective heat transfer, in comparison with the counterpart stationary flow, has been found. A 1D analytical approach has allowed to evidence that the increase of the energy axial advection due to a large axial velocity oscillating component represents the major cause of the heat transfer enhancement.

In this chapter a particular attention is paid in the investigation of the radial transport of the thermal energy in the case of a pulsating flow. In particular, an instantaneous and local enhancement of the radial heat advection is supposed to exist during flow reversals, as explanation for the particular velocity and temperature radial measured profiles.

As recall of what has been previously presented, a radial advection increase during flow reversal was previously observed by Dec et al. [24]–[27] for a turbulent pulse combustor tail pipe and by Kearney et al. [21] in the boundary layer of a pulsating channel. A combination of increased shear-layer generated turbulence, and, strong convection at the zero-velocity crossings by transverse flows were the best explanation for the mechanisms causing the observed heat transfer enhancement. Results showed that the cycle-resolved impact of flow reversal was a dramatic thickening of the thermal boundary layer, which appeared to be caused by a vertical ejection of fluid from the near-wall region and by a limited degree of turbulent transition.

Since, as will be demonstrated in the following paragraph, the 1D analytical approach previously adopted is not suitable to evidence the impact of the radial transport of the thermal energy on the convective heat transfers, in this chapter a particular development of the local instantaneous energy governing equation, with a 2D assumption, is conducted.

Starting from this analytical development, results have been analysed to evidence the presence of such transversal heat transfer advection enhancement appearing during flow reversals, and to evidence its dependency from the pulsation frequency. Due to the limited experimental measurements, in the second part of the chapter, a 2D – CFD modelling through the Fluent-Ansys software is performed and presented with the main purpose of furnishing further elements useful for the phenomenon comprehension.

V.2 Analytical formulation of the problem

Assuming negligible viscous energy dissipation, the 2D instantaneous local energy balance equation in cylindrical coordinates, for an incompressible pipe flow with constant fluid properties exhibits the following form (as eq. II - 48):

$$\rho c_p\left(\frac{\partial T}{\partial t}+\frac{\partial(uT)}{\partial x}+\frac{\partial(vT)}{\partial r}\right)=\lambda\left(\frac{1}{r}\frac{\partial}{\partial r}\left(r\frac{\partial T}{\partial r}\right)+\frac{\partial^2 T}{\partial x^2}\right) \qquad \text{V - 124}$$

Where $u(x,r,t)$ and $v(x,r,t)$ represent the radial and the axial instantaneous air velocity component, $T(x,r,t)$ the bulk temperature of air, ρ the fluid density, c_p the specific heat at constant pressure.

Combining Eq. V - 124 with the triple-decomposition in eq. II - 43, proposed by Reynolds et al. [18], and then applying phase averaging operator (eq. II - 44) to the obtained equation leads to (for the simplicity of the writing the phase-average quantity is indicated as following $<Z(x,r,t)>= Z(x,r,t)$):

$$\begin{aligned}\rho c_p\left(\frac{\partial T}{\partial t}+\frac{\partial(vT)}{\partial r}+\frac{\partial(u\,T)}{\partial x}+<\frac{\partial(v'T')}{\partial r}>+<\frac{\partial(u'T')}{\partial x}>\right)\\ =\lambda\left(\frac{1}{r}\frac{\partial}{\partial r}\left(r\frac{\partial T}{\partial r}\right)+\frac{\partial^2 T}{\partial x^2}\right)\end{aligned} \qquad \text{V - 125}$$

In the left-hand side of the previous equation, the first term represents the rate of change of the air energy inside the control volume, while, the other terms represent the advective transport of energy by the phase-average component of the flow and by the fluctuating motion through the control surface. In the right-hand side of the equation the sum of the two terms corresponds to the conduction heat flux through the control surface.

The enhancement of the radial energy advection during the flow reversal should correspond to an increase of the term $\frac{\partial(v_rT)}{\partial r}$ in equation V - 125, while, the impact of the pulsation on the turbulent motion corresponds to an increase of the terms $<\frac{\partial(v_r{}'T')}{\partial r}>,<\frac{\partial(v_z{}'T')}{\partial z}>$ in eq. V - 125.

The instantaneous convective heat transfer $Q(x,t)$ per unit of length, exchanged with the wall of the pipe, with a 2D assumption doesn't directly appear in eq. V - 125, and it should be theoretically computed from the temperature profile near the wall according the following equation:

$$Q(x,r,t)=-\frac{\lambda\left.\frac{\partial T}{\partial r}\right|_{r=0}}{T_b-T_w}L\Delta T=-\lambda\left.\frac{\partial T}{\partial r}\right|_{r=0}L \qquad [W/m] \qquad \text{V - 126}$$

To demonstrate that a 1D assumption doesn't allow to evidence the supposed energy radial advection contrarily to a 2D assumption, and, to demonstrate that the weight of such energy advection on the convective heat transfers at the wall cannot be estimated, an analytical development of the 2D local phase-average energy balance equation has been proposed in the following lines.

Such development is based on the assumption that the flow properties could be decomposed as follows:

$$Z(x,r,t)=Z_b(x,t)+Z_r(x,r,t) \qquad \text{V - 127}$$

Where $Z(x,r,t)$ represents the instantaneous local flow property, $Z_b(x,t)$, defined as the mean integral of the flow property across the pipe section, is called bulk property, which is constant over the pipe section and $Z_r(x,r,t)$ represents the component of the flow property which is function of the distance from the pipe centerline.

$$Z_b(x,t) = \frac{1}{\Sigma}\int_{\Sigma} Z(x,r,t)dS \qquad \text{V - 128}$$

Where $\Sigma = \pi R^2$ is the section of the pipe.

Thanks to the definition of the bulk property, introducing eq. V - 128 in eq. V - 127 and integrating the latter over the pipe cross section leads to the following statement:

$$\int_{\Sigma} Z_r(x,r,t)dS = 0 \qquad \text{V - 129}$$

The integral over the pipe cross section of the radial-dependent component of each flow property is equal to zero.

The development of the 2D energy balance equation begins by integrating it over the pipe section 'Σ':

$$\begin{aligned}\rho c_p\Bigg(\int_{\Sigma} \frac{\partial T}{\partial t}dS + \int_{\Sigma} \frac{\partial (vT)}{\partial r}dS + \int_{\Sigma} \frac{\partial (u\,T)}{\partial x}dS + \int_{\Sigma} < \frac{\partial (v'T')}{\partial r} > dS \\ + \int_{\Sigma} < \frac{\partial (u'T')}{\partial x} > dS\Bigg) + \qquad \text{V - 130} \\ = \lambda\left(\int_{\Sigma}\left(\frac{1}{r}\frac{\partial}{\partial r}\left(r\frac{\partial T}{\partial r}\right)\right)dS + \int_{\Sigma} \frac{\partial^2 T}{\partial x^2}dS\right)\end{aligned}$$

Thanks to the decomposition of eq. V - 127 could be easily demonstrated that:

$$\int_{\Sigma} \frac{\partial T}{\partial t}dS = \Sigma\frac{\partial T_b}{\partial t} \qquad \text{V - 131}$$

$$\int_{\Sigma} \frac{\partial^2 T}{\partial x^2}dS = \Sigma\,\frac{\partial^2 T_b}{\partial x^2} \qquad \text{V - 132}$$

For the axial gradient of the crossing product between the axial velocity and the air temperature in eq. V - 130, as well as for the axial gradient of phase-average crossing product between the axial velocity and the air temperature turbulent components, by introducing the decomposition of eq. V - 127 it could be demonstrated that:

$$\begin{aligned}\int_{\Sigma} \frac{\partial (u\,T)}{\partial x}dS &= \int_{\Sigma} \frac{\partial[(u_b + u_r)(T_b + T_r)]}{\partial x}dS \\ &= \int_{\Sigma} \frac{\partial (u_bT_b + u_bT_r + u_rT_b + u_rT_r)}{\partial x}dS\end{aligned} \qquad \text{V - 133}$$

Thanks to the definitions of eqs. V - 128 and V - 129:

$$\int_{\Sigma} \frac{\partial (u_bT_r)}{\partial x}dS = \int_{\Sigma} \frac{\partial (u_rT_b)}{\partial x}dS = 0 \qquad \text{V - 134}$$

To lead finally to:

$$\int_{\Sigma} \frac{\partial(u\,T)}{\partial x} dS = \Sigma \frac{\partial(u_b T_b)}{\partial x} + \int_{\Sigma} \frac{\partial(u_r T_r)}{\partial x} dS \qquad \text{V - 135}$$

With the same mathematic steps, also the axial gradient of phase-average crossing product between the axial velocity and the air temperature turbulent components could be simplified as follows:

$$\int_{\Sigma} < \frac{\partial(u'T')}{\partial x} > dS = \Sigma \frac{\partial(u_b' T_b{}')}{\partial x} > + \int_{\Sigma} < \frac{\partial(u_r' T_r{}')}{\partial x} > dS \qquad \text{V - 136}$$

Introducing eqs. V - 131, V - 132, V - 134, V - 135 and V - 136 in equation V - 130 leads to the 2D energy balance equation integrated over the pipe section Σ:

$$\begin{aligned} &\rho c_p \Sigma \left(\frac{\partial T_b}{\partial t} + \frac{\partial(u_b T_b)}{\partial x} + \frac{1}{\Sigma} \int_{\Sigma} \frac{\partial(u_r T_r)}{\partial x} dS \right) + \\ &+ \rho c_p \Sigma \left(\frac{\partial(u_b' T_b{}')}{\partial x} > + \frac{1}{\Sigma} \int_{\Sigma} < \frac{\partial(u_r' T_r{}')}{\partial x} > dS \right) + \cdots \\ &\ldots = \lambda \Sigma \frac{\partial^2 T_b}{\partial x^2} + \left[\lambda \int_{\Sigma} \left(\frac{1}{r} \frac{\partial}{\partial r} \left(r \frac{\partial T}{\partial r} \right) \right) dS + \right. \\ &\left. - \rho c_p \left(\int_{\Sigma} \frac{\partial(vT)}{\partial r} dS + \int_{\Sigma} < \frac{\partial(v'T')}{\partial r} > dS \right) \right] \end{aligned} \qquad \text{V - 137}$$

Previous equation, it could be noted that corresponds to a 1D energy balance equation since the bulk properties don't depends anymore from the pipe radius, while, the impact of the Z_r terms is accounted from the integral over the pipe section. Such equation could be compared to the eq. IV - 100, which has been directly formulated assuming that the flow properties are constant over the pipe section. Eq. IV - 100 is following reminded:

$$\begin{aligned} \rho c_p \Sigma \left(\frac{\partial \bar{T}}{\partial t} + \frac{\partial \tilde{T}}{\partial t} + \frac{\partial(\bar{u}\bar{T})}{\partial x} + \frac{\partial(\tilde{u}\tilde{T})}{\partial x} + \frac{\partial(\bar{u}\tilde{T})}{\partial x} + \frac{\partial(\tilde{u}\bar{T})}{\partial x} + < \frac{\partial(u'T')}{\partial x} > \right) \\ = \lambda \Sigma \left(\frac{\partial^2 \bar{T}}{\partial x^2} + \frac{\partial^2 \tilde{T}}{\partial x^2} \right) + < q > \end{aligned} \qquad \text{V - 138}$$

As specified previously in eq. V - 137 for a simplification of the notation it has been supposed that

$$< Z(x,r,t) >= Z(x,r,t) \qquad \text{V - 139}$$

According V - 139, and recalling that the flow properties with a 1D assumption are supposed to be constant over the pipe section, so they corresponds to the first component (the bulk property) in the decomposition V - 127 the 1D energy balance equation could be rewritten as:

$$\rho c_p \Sigma \left(\frac{\partial T_b}{\partial t} + \frac{\partial(u_b T_b)}{\partial x} + < \frac{\partial(u_b' T_b{}')}{\partial x} > \right) = \lambda \Sigma \left(\frac{\partial^2 T_b}{\partial x^2} \right) + < q > \qquad \text{V - 140}$$

Comparing eqs. V - 137 and V - 140 it could be observed that in the left hand side the terms $\frac{\partial T_b}{\partial t}, \frac{\partial (u_b T_b)}{\partial x}, < \frac{\partial (u_b' T_b')}{\partial x} >$ are equal for both the formula, while, ulterior terms such as $\frac{1}{\Sigma}\int_\Sigma \frac{\partial (u_r T_r)}{\partial x} dS$ and $\frac{1}{\Sigma}\int_\Sigma < \frac{\partial (u_r' T_r')}{\partial x} > dS$ appear only in the 1D formulation of V - 137. They represents the contribution of the radial dependent component of the air velocity and temperature on the energy balance, that, with a 1D assumption, because of the hypothesis of constant air velocity and temperature profiles over the section disappear.

Comparing eqs. V - 137 and V - 140, it could be also observed that in the right hand side of each equation, while the axial conduction heat is the same term for both the equations, the specific convective heat transfer term $< q >$ in eq. V - 140 corresponds to the sum of three different terms as follows:

$$
\begin{aligned}
< q(x,t) >= \lambda \int_\Sigma \left(\frac{1}{r}\frac{\partial}{\partial r}\left(r \frac{\partial T}{\partial r} \right) \right) dS + \\
- \rho c_p \left(\int_\Sigma \frac{\partial (vT)}{\partial r} dS + \int_\Sigma < \frac{\partial (v'T')}{\partial r} > dS \right)
\end{aligned}
\qquad \text{V - 141}
$$

The first term in the right hand side corresponds to the radial heat conduction, while the remaining ones correspond to the heat energy radially transported by the coherent and the turbulent fields of the flow. By applying the following transformation of the surface integral for an axial-symmetric flow, it could be stated that the integrals in the second part of right hand side of the eq. V - 141 can be considered equal to zero.

$$
\int_\Sigma dS = \int_{r=0}^{r=R} d(\pi r^2) = 2\pi \int_{r=0}^{r=R} r dr \qquad \text{V - 142}
$$

Introducing eq. V - 142 in the second term of eq. V - 141:

$$
\begin{aligned}
\int_\Sigma \frac{\partial (vT)}{\partial r} dS &= 2\pi \int_{r=0}^{r=R} r \frac{\partial (vT)}{\partial r} dr = 2\pi r v T|_{r=0}^{r=R} = 0 \\
\int_\Sigma < \frac{\partial (v'T')}{\partial r} > dS &= 2\pi \int_{r=0}^{r=R} r < \frac{\partial (v'T')}{\partial r} > dr = 2\pi r < vT >|_{r=0}^{r=R} = 0
\end{aligned}
\qquad \text{V - 143}
$$

Because of the axial-symmetric boundary condition on the pipe axis, both the phase-average and the turbulent components of the radial velocity may considered equal to zero. A condition of null scalar flux perpendicular to the axis is imposed, as well as also at the wall, where the no-permeability and no slip conditions are considered. Consequently, eq. V - 141 is simplified as follows:

$$
< q(x,t) >= \lambda \int_\Sigma \left(\frac{1}{r}\frac{\partial}{\partial r}\left(r \frac{\partial T}{\partial r} \right) \right) dS = 2\pi\lambda \int_{r=0}^{r=R} \left(\frac{1}{r}\frac{\partial}{\partial r}\left(r \frac{\partial T}{\partial r} \right) \right) r dr \qquad \text{V - 144}
$$

If the integral in eq. V - 144 is developed, we lead:

$$
< q(x,t) >= 2\pi\lambda \left(r \frac{\partial T}{\partial r} \right)\Big|_{r=0}^{r=R} \qquad \text{V - 145}
$$

At r = 0, which represents the pipe centreline $\frac{\partial T}{\partial r} = 0$ for an axial-symmetric flow, and it remains only the term evaluated at the wall:

$$< q(x,t) >= 2\pi R\lambda \left(\frac{\partial T}{\partial r}\right)\Big|_{wall} \qquad \text{V - 146}$$

Eq. V - 146 corresponds to the eq. V - 126 integrated over the pipe section.

As presented in the previous lines, the 1D assumption is not suitable to be used to evidence the radial energy advection as well as also its impact on the convective heat transfer, because of the hypothesis of property independence from the radial direction. Furthermore, it has also demonstrated that the impact of the radial energy advection on the convective heat transfers at the wall could not be directly quantified. It has been analytically demonstrated that by integrating the 2D local energy equation over the pipe section doesn't allow anymore to highlight the total impact of the radial energy advection on the convective heat transfers. Actually, the physical meaning of such advection consists only in spreading the thermal energy over the entire section.

It could be finally claimed that only a 2D assumption could be applied to the data analysis to evidence such phenomena: in view of all this, in the next paragraph some experimental results are presented and discussed to furnish some elements contributing to theory that an energy radial advection increase appears during flow reversals, as previously observed by Dec et al. [24]–[27] and Kearney et al. [21].

V.3 Experimental Results

Temperature and velocity instantaneous radial profiles have been measured for several different frequencies. A particular attention has been paid in the moment of flow reversal. Since among all the tested frequencies the flow behaviour are similar, in this chapter the data to be presented correspond to a pulsating hot flow having a pulsation frequency of 10 Hz and a time-average mass flow rate of 110 kg/h. The electrical power of the air heaters has been controlled to keep, for all the experiments, the time-average component of the air temperature at the centreline of the test-section inlet constant to a value of 150°C. Such operating conditions correspond to a time-average Reynolds number of around 30000. Instantaneous measurements of the air velocity and temperature profiles have been taken for a fixed axial position in the test-section, and for different radial distances from the wall (see Figure 30). In detail, 28 points of measurements have been taken to define the radial profile with a constant step of 1 mm.

The phase-average bulk flow properties of the pulsating hot flow, calculated according eq. III - 88, are reported in the following figures:

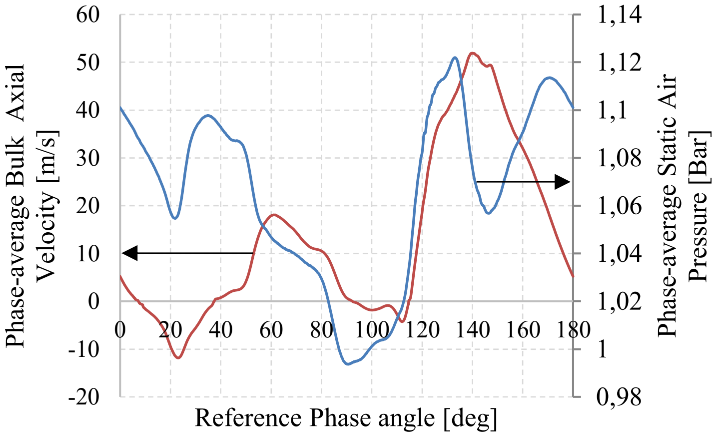

Figure 94: Phase-average bulk Velocity & Static pressure for a hot pulsating flow, Re = 30000, f = 10 Hz

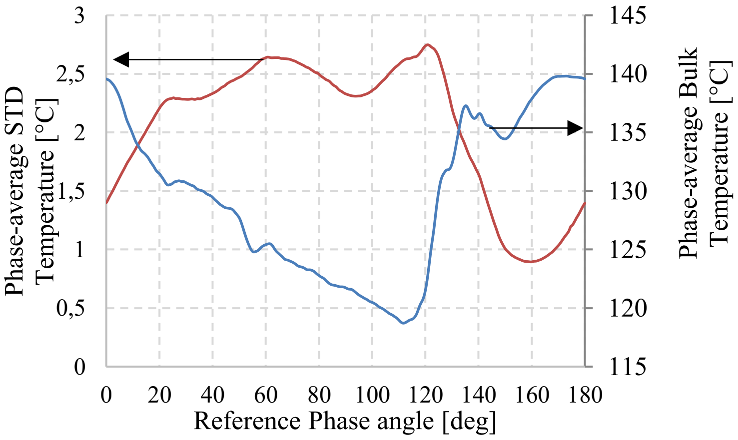

Figure 95: Phase-average bulk Temperature & STD component for a hot pulsating flow, Re= 3x10^4, f= 10 Hz

Figure 94 reports the phase-average bulk axial velocity and the phase-average static pressure profiles, while, Figure 95 shows the phase-average bulk air temperature and its standard deviation term.

Results show that the flow reversal appears two times within the pulsation cycle, and that the velocity and pressure maxima are quite in phase (10 CA of phase delay have been found).

Two interesting features are present in the temperature field, although the detailed structure varies with operating condition. The results of a Fourier series decomposition of the temperature profile is plotted in Figure 96: the red line is the first harmonic or fundamental oscillation and the blue line represents the second harmonic. Such decomposition makes simpler to visualize these two features: first, there is a fundamental oscillation at the pulsation frequency, which is around 30 degrees out-of-phase with the velocity and 40 degrees out-of-phase with the pressure. Second, superimposed on this oscillation there are two dips and one peak (phase locations of 20, 60 and 130 deg) in the temperature which slightly phase-lag the zero-velocity crossings. Furthermore, it could be also observed that, slightly phased lag to such points, a local maximum of the phase-average standard deviation temperature exists in Figure 95, suggesting an increase of the turbulent component of the temperature variations.

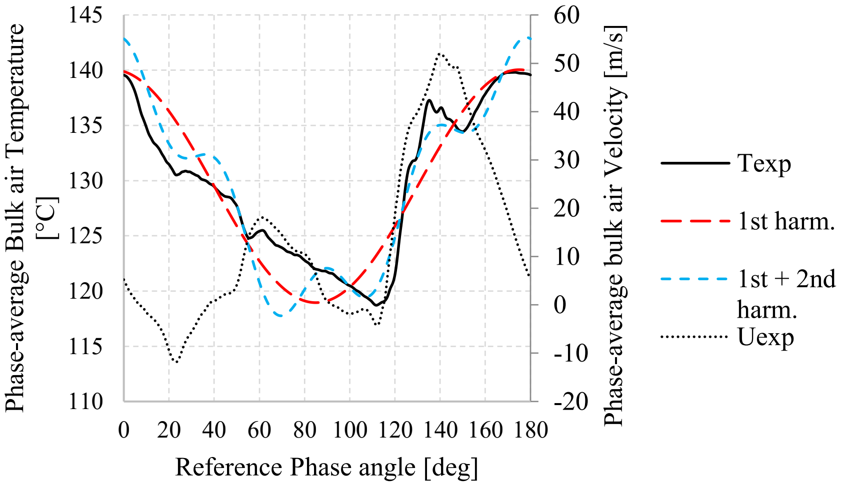

Figure 96: First and Second Fourier decomposition harmonics of the phase-average air bulk temperature profile for a hot pulsating flow, Re = 30000, f = 10 Hz

The cause of these temperature dips is not certain; however, a possible mechanism has been supposed to consist into an enhanced radial transportation rate of energy to the wall, temporally correlated with the zero-velocity crossing. As remind for the reader, such phenomenon has been already experimentally observed in the works of Dec et al. [24]–[27] for a pulsating turbulent combustor tail pipe and, Kearney et al. [21] for a laminar reversing pulsating channel flow.

Such hypothesis is corroborated by the following phase-average radial profiles of air temperature and velocity: Figure 97 shows the phase-average air axial velocity around the first flow reversal in Figure 94, while, the Figure 100 and Figure 101 report the phase-average and phase-average STD components of the air temperature. The different lines in the figures correspond to different phase during the pulsting cycle.

From the velocity profile it could be observed that the flow revers before near the wall while the bulk velocity remains still positive. Furthermore, in the first moment of the negative bulk velocity the velocity maximum still remains near the wall implying an inflection point in the velocity profile. Such phenomena has been experimentally observed also in the works of Dec et al. [26] and it was analytically discovered in the 1953 from Uchida [86].

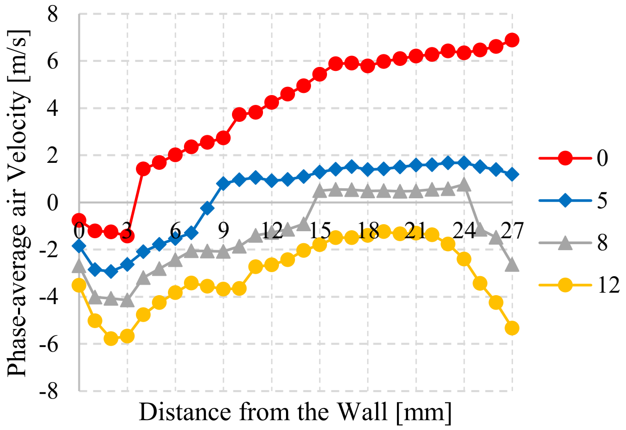

Figure 97: Phase-average air velocity profile for a hot pulsating flow during a flow reversal, Re = 30000, f = 10 Hz

Uchida [86] proposed an exact solution of pulsating laminar flow superposed on the steady motion in a circular pipe, under the assumption of parallel flow to the axis of pipe. Total mass of flow on time average is found to be identified with that given by Hagen-Poiseuille's law calculated on the steady component of pressure gradient. It founded that the periodical part of velocity distribution is characterized by the parameter $ka = \sqrt{\frac{2\pi\omega}{\nu}}D$.

When high viscous liquid pulsate slowly in a narrow pipe, the parameter $ka \ll 1$ becomes sufficiently small that approximately the velocity distribution is given by a parabola as in the case of steady Poiseuille flow, while the magnitude of velocity varies periodically in the same phase with that of pressure gradient. When low viscous liquid pulsates rapidly in a large pipe, if parameter $ka > 10$ becomes very high, it will be found that maximums of velocity distribution exist in the neighbourhood of wall in the rapid vibration as in Figure 98. For instance, in our experiment conditions $ka = 89.4$.

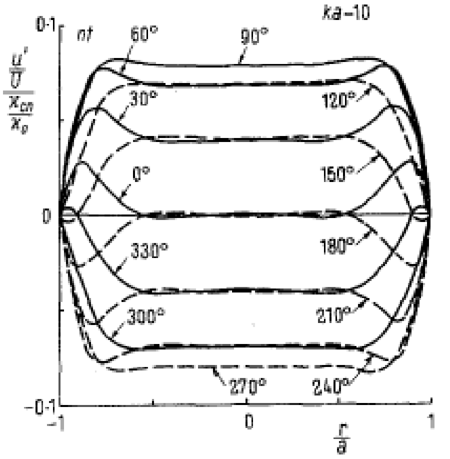

Figure 98: Velocity profile for a pulsating laminar flow, analytical calculation from Uchida, $\sqrt{\frac{2\pi f}{\nu}}D = 10$

An ejection event during periodic flow reversal can be explained in terms of continuity due to such particular velocity radial profiles. Considering streamwise fluid motion at a fixed distance from the wall, the downstream flow will respond more quickly to temporal changes in the pressure gradient as a consequence of its lower momentum. A localized flow reversal will then initiate near the downstream end of the channel, as shown schematically in Figure 99. As reversed fluid begins to move upstream, it will immediately encounter stationary or forward-moving fluid, and a secondary, transverse and/or spanwise flow must be established to preserve continuity. If we consider a two-dimensional model and neglect the changes in gas density owed to temperature, then the simplified continuity relation applies:

$$\frac{\partial u}{\partial x} + \frac{\partial v}{\partial y} = 0 \qquad \text{V - 147}$$

For a positive-to-negative, zero-velocity crossing, $\frac{\partial u}{\partial x} < 0$ so that $\frac{\partial v}{\partial y} > 0$. An ejection event must then occur almost simultaneously with a local flow reversal to satisfy both continuity and the no-slip condition. Such ejection should enhance the radial transport of the thermal energy from the wall to the core.

This description and the necessary inflectional velocity profiles are similar in concept to steady separation, with the exception that the inviscid core flow still conforms to the shape of the wall.

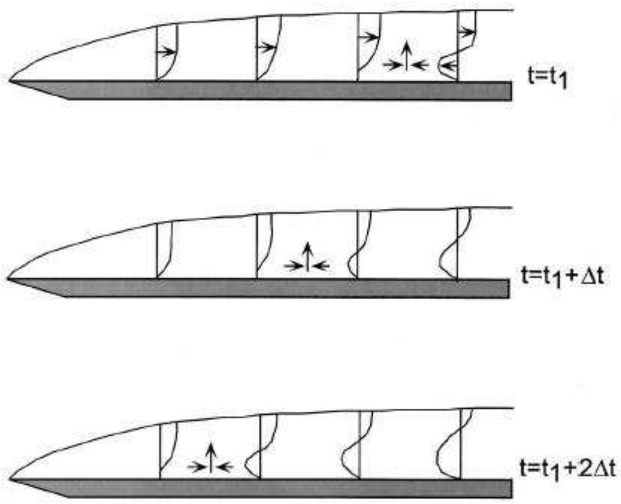

Figure 99: Schematic of streamwise boundary-layer profiles during periodic flow reversal

Due to high temperature differences, buoyancy may induce secondary flows in the form of thermal plumes could also be a source of vertical fluid motion at cycle times near flow reversal when the fluid velocity is nearly stagnant across the pipe section, anyway our measurements are not able to evidence such phenomena.

Phase-average radial air temperature profiles, in Figure 100, show that during the flow reversal a temperature increase near the wall appears, while, starting from 3 mm of distance from the wall the temperature decreases. Such phenomena is likely due to a radial mixing enhancement of the thermal energy.

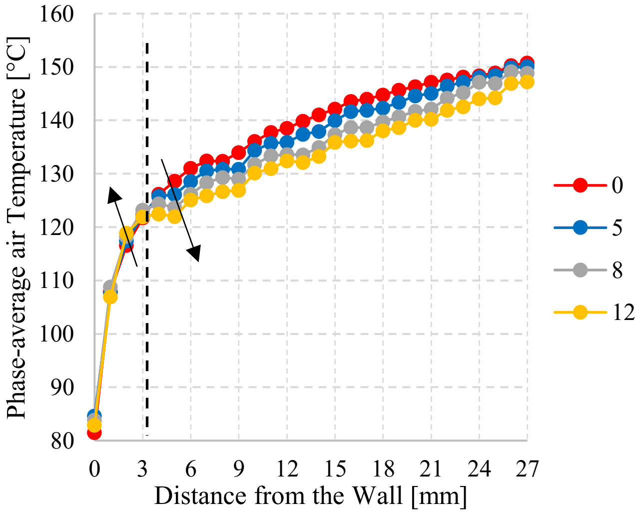

Figure 100: Phase-average air temperature profile for a pulsating hot flow during periodic flow reversal, Re = 30000, f = 10 Hz

This hypothesis is furtherly corroborated by the following phase-average STD air temperature radial profiles (Figure 101). It is important to note that the phase-average STD of the air temperature doesn't properly represent the turbulent component, because, as previously affirmed, thermocouple sensors are not able to sense turbulent variations of the air temperature. The Phase-average STD represents the cycle-by-cycle variations of the temperature which can have a dynamic up to around 100 Hz (such frequency has been demonstrated to represent the sensor bandwidth frequency, if the hot junction is subjected to a flow with a velocity superior to 50 m/s, paragraph III.4.1)

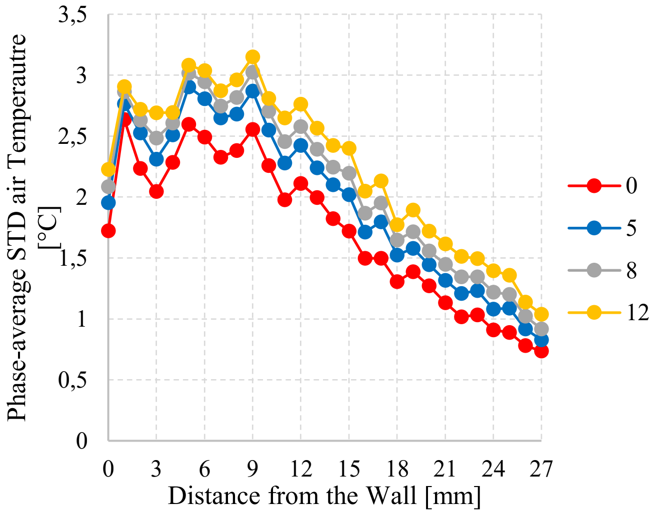

Figure 101: Phase-average air STD temperature profile for a pulsating hot flow during periodic flow reversal, Re = 30000, f = 10 Hz

All the temperature standard deviation profiles in the above figure show a monotonic growing behaviour starting from the core of the flow, until a maximum point after that the STD decreases till the wall. Such trend is similar to the which one found in the works of M. Ferro [87] reported in the following figure:

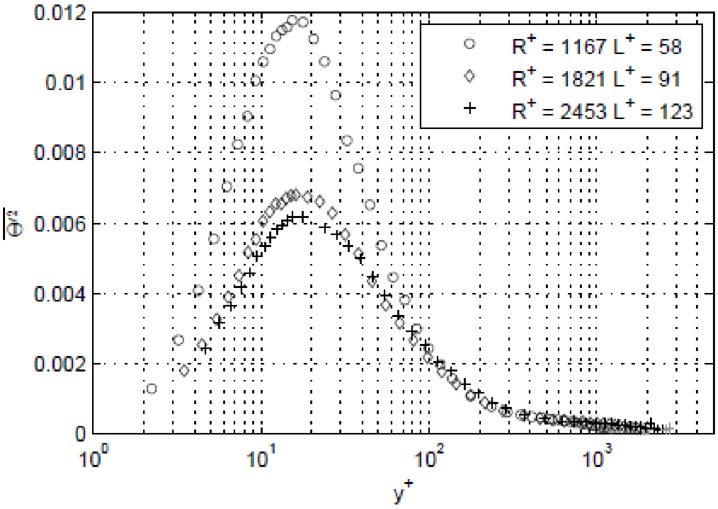

Figure 102: Dimensionless temperature variance vs y^+ for a steady turbulent pipe flow

Figure 102 shows the dimensionless temperature variance defined as follows, in function of the dimensionless distance from the wall y which has been scaled with the inner variable of the boundary layer theory $y^+ = \frac{yu_*}{\nu}$, where $u_* = \sqrt{\tau_w/\rho}$ represents the friction velocity.

$$\overline{\theta'^2} = \frac{\overline{T'^2}}{(\bar{T}_{cl} - T_{min})^2} \qquad \text{V - 148}$$

Where T_{min} is the lowest temperature measured with the cold-wire probe (approximately equal to the wall temperature), $\bar{T}_{cl}$ is the time-average centerline temperature and $\bar{T'}$ is the temperature standard deviation.

It is worth to note that the profile in Figure 102 has been computed for a steady turbulent pipe flow, while, in the case of Figure 101 the STD air temperature corresponds to the phase-average STD, which is dependent from the cycle phase angle. Furthermore in Figure 101 the STD profile has not been reported in function of y^+ because of the impossibility to compute the friction velocity from velocity measurement: due to the lack of precision near the wall, τ_w the wall friction as in eq. II - 3 cannot be calculated.

Anyway, the fact that the phase-average STD has a similar trend of the STD in the steady case, suggests that as for the stationary flow, a lively turbulent activity of the temperature field exists near the wall, while it decreases in the direction of the pipe centreline.

Results, in Figure 101, also show that contemporarily to the flow reversal, the maximum of the STD profile moves away from the wall, implying that the turbulent activity is transported from the wall to the core of the fluid due to flow pulsation.

Despite such interesting results, the lack of the radial velocity component measurement doesn’t allow to compute the convective terms in equation V - 125, as well the phase-average convective heat transfer coefficient cannot be calculated from the temperature profile has in the eq. V - 126, because of the low quality of the measurements near the wall.

As consequence the influence of such transversal advection enhancement on the convective heat transfers has not possible to be experimentally estimated.

Furthers elements supplying such theory have been anyway deduced from the flow properties measurements for a cold pulsating flow. Assuming the same hypotheses used in the paragraph IV.4; air velocity measurements have been conducted for a cold pulsating flow having the same time-average component of the air velocity. In such conditions the velocity field has been considered to have the same behaviour of the hot pulsating flow (for details see paragraph IV.4). Furthermore assuming the Reynolds analogy it could be affirmed that the momentum and the energy are similarly transported by the flow.

Figure 103 reports the phase-average bulk axial velocity profile comparison between the hot pulsating case (blue line) and the cold pulsating flow (orange line) with the same time-average velocity component: the curves show the same global behaviour, the flow reversal occurs two time for both the experiments.

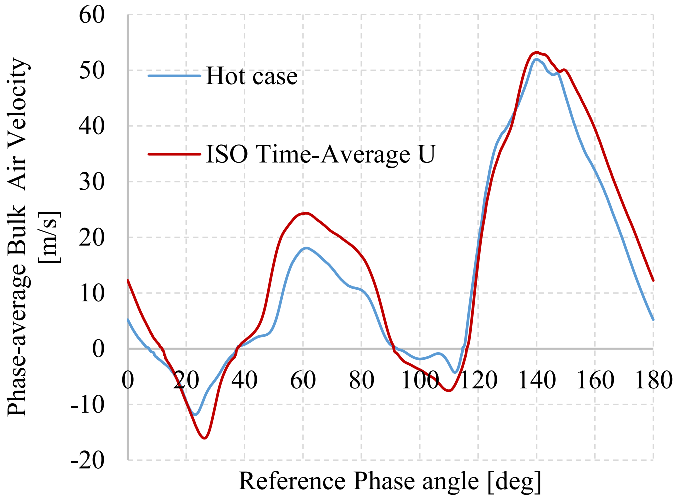

Figure 103: Phase-average bulk air velocity for a pulsating cold & hot flows

Figure 104 reports the static pressure profile comparison between the hot pulsating case (blue line) and the cold pulsating flow (orange line) with the same time-average velocity component.

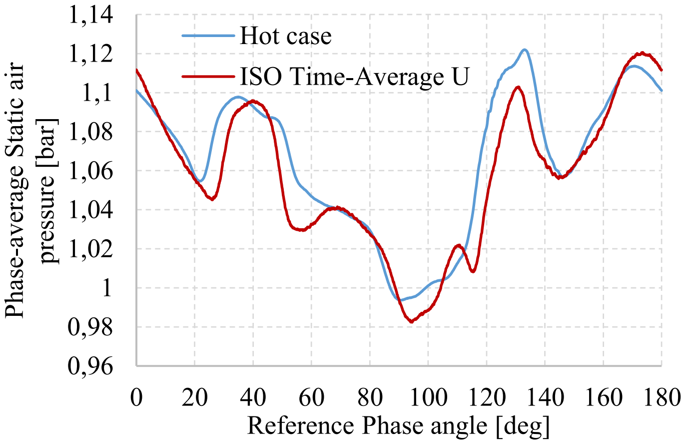

Figure 104: Phase-average static air pressure for a pulsating cold & hot flows

It could be observed that fundamental pressure pulsations show a same behaviour; while, likely because of the variation of the sound velocity, a different composition of the travelling pressure wave appears, implying some little magnitude and phase-lag variations between the higher harmonics of the signals.

It is the case of pressure within the cycle period from 20 to 60 deg, both curves show a bell shape with a maximum near 1.1 bar, however, in the cold pulsating flow case the pressure increase/decrease occurs in a shorter period. A similar behaviour has been observed for the air velocity profile in the same cycle phase in Figure 103: flow reverses, in the cold pulsating case, within a shorter period than the hot case.

In the Figure 105 the phase-average radial profiles of axial air velocity are reported for the cold pulsating flow, during the first flow reversal: as well as for the hot pulsating case, also in such conditions it has been observed that the velocity inverses before in the neighbourhood of the wall. Contrarily once the flow totally reverses, the velocity profile in the core of the flow looks flatter than the hot case.

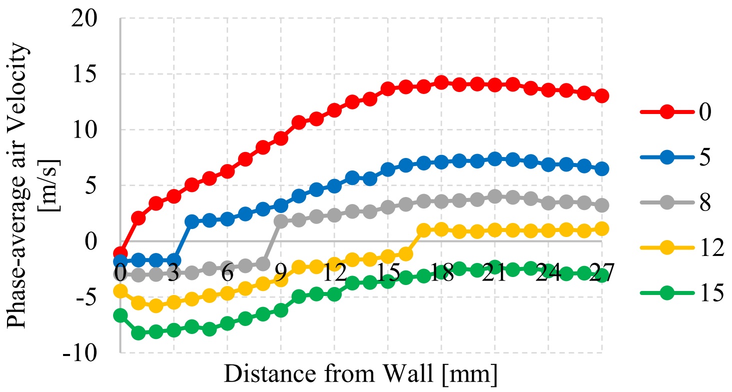

Figure 105: Phase-average air velocity profile for a pulsating cold flow during periodic flow reversal, Re = 40000, f = 10 Hz

The advantage of a cold pulsating operating conditions, consists, as affirmed in the paragraph III.5, into the possibility to extract the turbulent component of the air velocity from the hot-wire measurements, which has been reported in the Figure 106.

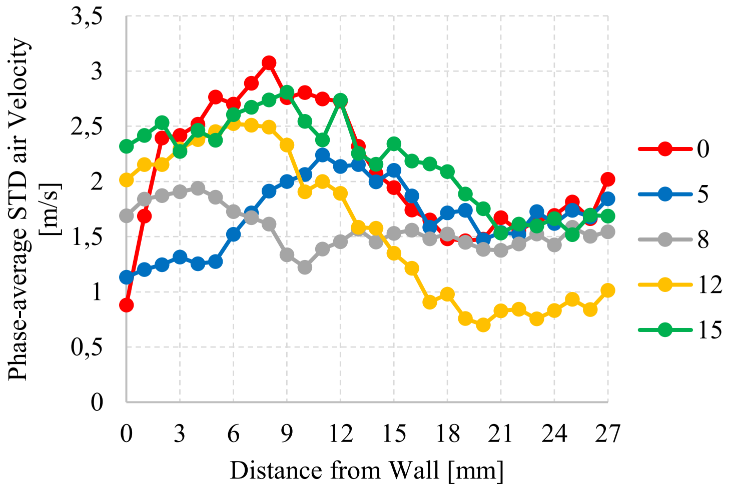

Figure 106: Phase-averaged turbulent component of the air velocity for a pulsating cold flow during periodic flow reversal, Re = 40000, f = 10 Hz

It could be observed that, contemporarily to the flow reversal, a wave of the phase-average STD component of the air velocity propagates from the wall to the core of the flow. The presence of such wave suggests that a flow coherent structure propagates from the wall to the core, such structure should likely correspond to the ejection previously presented. Considering that the temperature is simply advected from the velocity field, such evidence furnishes an important ulterior element which contributes to the hypothesis of a heat transversal advection enhancement mechanism exists during flow reversals.

To summary, in this first part of the data analysis experimental results have showed that a flow structure propagates from the wall to the core during flow reversal, such structure should transport cold air from the wall to the core, increasing so the radial heat advection, as the phase-average temperature profiles have shown. However, a direct impact of such radial advection enhancement on the instantaneous convective heat transfer coefficient has not been possible to be observed.

Although a convective heat transfer energy has been calculated in the paragraph IV.4, it represents the space- and time- integral of the convective heat transfers through all the test-section: so it cannot be correlated to the observed 2D phenomena.

Further elements which supply the theory according to it is impossible to correlate the time- and space-average results to the local observed phenomena can be furnished by the results of Jackson et al. [22] in the 1965, Andre et al. [88] in the 1981, or by a recent study of Liu et al. [89]. By these works it could be affirmed that for a pulsating pipe flow the time-average Nusselt number is not constant in function of the axial position across the pipe, its behaviour shows an oscillating wave form: a local heat transfer peaks occur at approximately half wavelengths of the flow pulsation and multiples thereof if vortex cells are formed, as reported in the Figure 107.

Such results suggest that the structure observed in one local section of the pipe, may locally enhance the convective heat transfers but cannot be transposed for all the pipe length, consequently, what has been locally observed cannot be used to justify the convective heat transfer enhancement discussed in the previous chapter. A measurement of the local instantaneous convective heat transfer coefficient, as well as also a measurement of the convective heat transfer coefficient for different axial positions should be conducted in future.

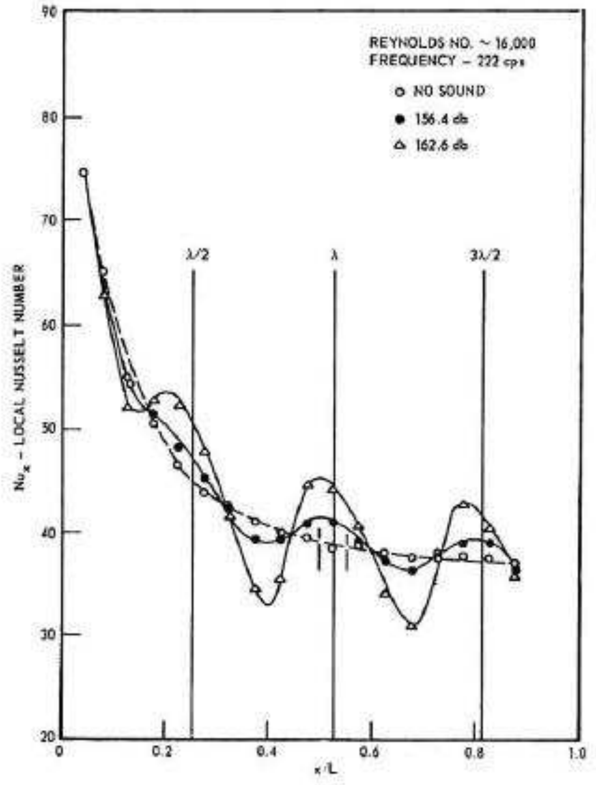

Fig. 3 Local Nusselt number versus x/L

Figure 107: Local Nusselt numbers versus x/L for various sound pressure levels, Jackson et al.

To go further on the study of the impact of this radial energy advection enhancement on heat transfer, the heat transfers problem has been analysed with a 2D modelling approach with the Ansys-Fluent CFD software. From the numerical results all the terms in eq. V - 125 could be computed in order to evidence the importance of the radial advection in comparison with the others terms in the equation, as well as its impact on the instantaneous local convective heat transfer to the wall.

In the following paragraph the Fluent model, the solved equations and the results are presented and discussed. A particular attention is paid in the simplification level of the governing equations adopted on Fluent in order to highlight its potential.

V.4 Fluent modelling of a turbulent pulsating flow in a pipe with a 2D assumption

As previously showed, the analysis of the phase-average radial profiles of the axial air velocity has showed that contemporarily to the flow reversal, a wave of the phase-average STD component of the air velocity propagates from the wall to the core of the flow. The presence of such wave suggests that a flow coherent structure propagates from the wall to the core. Considering that the temperature in our experimental conditions could be considered as a passive scalar field, thus simply advected from the velocity field, such evidence furnishes an important ulterior element which contributes to the hypothesis of a heat transversal advection enhancement mechanism, as the analysis of the phase-average temperature profile has shown.

Although an analytical development of the 2D local energy governing equation has permitted to identify which are the equation terms representative of the radial energy advection, due to the lack of the measurement of the radial component of the air velocity, these terms have not been possible to be computed and the presence of such phenomena has not been directly demonstrated. At the same time a particular development of the 2D phase-average energy governing equation has showed that the impact of this convective mechanism on the thermal energy exchanged between the fluid and the wall could not be directly evidenced.

This inconvenient have been overcome by performing 2D simulations of the heat transfer problem for a turbulent pulsating flow in a pipe, with the Ansys-Fluent CFD software. The main purposes are to reproduce a flow reversal similar to which one encountered in the experiments, and, to demonstrate, by computing all the terms of the 2D energy balance equation, the presence and the role of the radial transport mechanism of the thermal energy, previously supposed from the experimental result analysis.

In the following lines the governing equations solved by Fluent are revised and discussed in the application case of a pulsating turbulent pipe flow in order to evidence the limit of such approach. Then, the turbulent model is detailed as well as the flow model, the mesh and the boundary conditions definition; to finally lead to the results and the discussions.

V.4.1 Governing equations

Governing equations contain many levels of complexity; the most significant being the following:

- They form a system of five (in three-dimensional space) fully coupled time-dependent partial differential equations for the five unknowns, velocity vector (three unknowns), and two thermodynamic quantities, such as for instance pressure and density, or pressure and temperature. The coupling occurs through the velocity and density fields, possibly also through the temperature field, when thermal effects are significant.
- Each of these equations is nonlinear. The nonlinearity of the flow equations is not just a mathematical observation, as it has major consequences on the whole of fluid mechanics: The dominant nonlinearity is provided by the momentum convection term. This term is also

> responsible for the appearance of turbulence, which is a spontaneous instability of the flow, whereby all quantities take up a statistical (chaotic) behaviour. For compressible flows, the products of density and velocity represent another nonlinearity, leading to the existence of shock waves in supersonic flows. Through a shock, velocities, pressure, temperature, undergo a discontinuous jump and, as we will see later on, these discontinuities are indeed exact solutions of the nonlinear inviscid Euler equations. With non-uniform temperature fields, flow-thermal nonlinearities appear. Nonlinearities lead to non-unique solutions. This has also major consequences, under the form of the existence of multiple flow configurations for the same initial and boundary conditions, resulting from bifurcations from one flow state to another.

These complexities in fluid dynamics pose considerable challenges for CFD, in particular for turbulent flows.

The issue of the time and length scales of the description of the physical flow features is also critical to the world of simulation. The same flow will appear very different when we reduce the scale at which we look at it.

The applications of CFD to real life flow systems, in nature or in technology, require the ability to handle turbulent flows, as these are the most widely encountered situation. Hence we need to take into account the effects of turbulence on the mean flow and this requires approximate models, as DNS is not a short-term option. A direct numerical simulation (DNS) is a simulation in computational fluid dynamics in which the Navier–Stokes equations are numerically solved without any turbulence model. This means that the whole range of spatial and temporal scales of the turbulence must be resolved. All the spatial scales of the turbulence must be resolved in the computational mesh, from the smallest dissipative scales, up to the integral scale, associated with the motions containing most of the kinetic energy.

Two families of models are presently available: one family, called Large Eddy Simulation (LES) is of the same category as DNS, in that it computes directly the turbulent fluctuations in space and time, but only above a certain length scale. Below that scale, called the subgrid scale, the turbulence is modeled by semi-empirical laws. The other family, called the Reynolds Averaged Navier–Stokes (RANS) model, ignores the turbulent fluctuations and aims at calculating only the turbulent-averaged flow. This is currently the most widely applied approximation in the CFD practice, as well as the software Fluent employs. A scheme of the approximation levels and the range of application of the models used to solve the governing equation is showed in Figure 108.

We concentrate our attention to the RANS models which are solved from the Fluent software. As introduced in the paragraph II.2.1, the turbulent averaging process is introduced in order to obtain the laws of motion for the 'mean', time-averaged, turbulent quantities. This time averaging is to be defined in such a way as to remove the influence of the turbulent fluctuations, while not destroying the time dependence connected with other time-dependent phenomena with time scales distinct from those of turbulence.

In the case of a pulsating flow, as previously introduced, a triple-decomposition is used for the flow properties, and by the phase-averaging mathematic the turbulent component is erased.

The phase-averaged mass, momentum and energy balance equations, as in the paragraph II.2.3, are reported as follows (they are usually called Unsteady Reynolds Average Navies-Stokes equations).

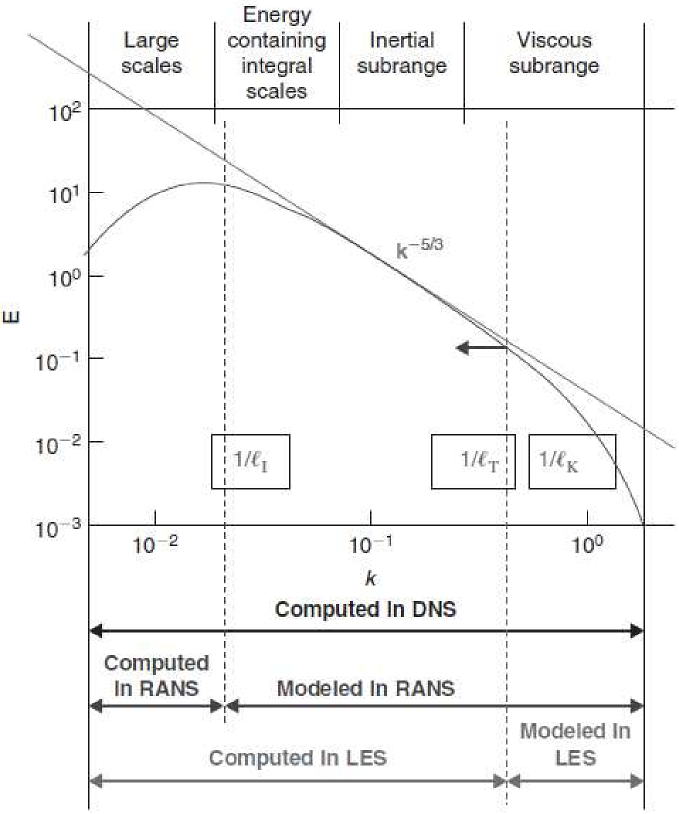

Figure 108: Energy spectrum of turbulence in function of wave number k, with indication of the range of application of the DNS, LES and RANS models.

Commonly, a U-RANS simulation is employed, when long-term periodical oscillations in a turbulent flow should be investigated. Turbulent fluctuations of flow quantities are not resolved in the U-RANS approach.

$$\frac{\partial u}{\partial x}+\frac{1}{r}\frac{\partial (rv)}{\partial r}=0 \qquad \text{V - 149}$$

$$\rho\left(\frac{\partial v}{\partial t}+u\frac{\partial v}{\partial x}+v\frac{\partial v}{\partial r}+\frac{\partial <u'v'>}{\partial x}+\frac{\partial <v'v'>}{\partial r}\right)=-\frac{\partial p}{\partial r}+\mu\left(\frac{\partial^2 v}{\partial r^2}+\frac{1}{r}\frac{\partial v}{\partial r}-\frac{v}{r^2}+\frac{\partial^2 v}{\partial x^2}\right) \qquad \text{V - 150}$$

$$\left(\frac{\partial u}{\partial t}+u\frac{\partial u}{\partial x}+v\frac{\partial u}{\partial r}+\frac{\partial <u'u'>}{\partial x}+\frac{\partial <u'v'>}{\partial r}\right)=-\frac{\partial p}{\partial x}+\mu\left(\frac{\partial^2 u}{\partial r^2}+\frac{1}{r}\frac{\partial u}{\partial r}+\frac{\partial^2 u}{\partial x^2}\right) \qquad \text{V - 151}$$

$$\rho c_p\left(\frac{\partial T}{\partial t}+u\frac{\partial T}{\partial x}+v\frac{\partial T}{\partial r}+\frac{\partial <u'T'>}{\partial x}+\frac{\partial <v'T'>}{\partial r}\right)=\lambda\left(\frac{1}{r}\frac{\partial}{\partial r}\left(r\frac{\partial T}{\partial r}\right)+\frac{\partial^2 T}{\partial x^2}\right) \qquad \text{V - 152}$$

Where u, v, T, p are the solved flow properties which are function of the axial 'x', radial 'r' direction and the time t; while,ρ, c_p, λ are the fluid properties considered constants in function of the temperature. As previously presented the above governing equations are the result of a phase-averaging of the local instantaneous governing equations. In this manner the turbulent component of the flow is not solved, while, it is modeled through a turbulence model. In practice its impact on the phase-average cycle is accounted for from the terms in the parenthesis <…> in eqs. V - 150, V - 151 and V - 152.

Such terms represent respectively the Reynolds stresses and the turbulent heat flux.

The first imprecision of such approach consists into assuming that the literature turbulence models be valid for a pulsating flow, actually, they have been created for stationary turbulent flow.

For a pulsating flow the main difference consists into a different writing of the Reynolds stresses and the turbulent heat flux, as follows:

$$Reynolds\ stresses = \begin{cases} steady\ flow - \rho\overline{u_i' u_j{}'} \\ pulsating\ flow \quad - \rho < u_i' u'_j > \end{cases} \qquad \text{V - 153}$$

For a steady flow Reynolds stresses correspond to the time-average product of the velocity turbulent components, while for a pulsating flow the time-averaging is replaced from the phase-averaging. The still unanswered question resides in the doubt if stationary turbulent model may be directly transposed to a pulsating flow or not. In practice using the turbulent models, derived from a steady flow, in a pulsating flow conditions is equivalent to affirm that the flow pulsation are so slowly that don't impact the turbulence field. The validity of such hypothesis is not still confirmed.

It has to be considered, however, that the main purpose of this thesis is not to study the turbulence for a pulsating flow, but to study the impact of the flow pulsation on the convective heat transfer phenomena.

For this reason, the attention has been paid only on the heat transfer problem; furthermore, two different turbulence models have been tested and compared to see their impact on the phase-average velocity and temperature field.

Nevertheless, it is worth to affirm that the convective mechanism, which we are trying to evidence through the CFD modelling phase, as the experimental results show, belongs to the phase-average flow field. It occurs in the larger flow scales than the turbulent ones, as well as it should also transport the major part of the thermal energy. In view of all this, the U-RANS equations solved by the Fluent software should be able to evidence, if existent, the presence of such phenomenon.

In the following lines, for the sake of brevity, the main difference between the turbulence models is discussed from a general point of view, while, only the turbulence model used to solve the governing equations has been revised (details are available in [90]).

The first tested turbulence model it the $k - \varepsilon$ model, it employs the Boussinesq hypothesis to relate the Reynolds stresses to the mean velocity gradients, as follows:

$$-\rho\overline{u_i' u_j'} = \mu_t \left(\frac{\partial u_i}{\partial x_j} + \frac{\partial u_j}{\partial x_i}\right) - \frac{2}{3}\left(\rho k + \mu_t \frac{\partial u_k}{\partial x_k}\right)\delta_{ij} \qquad \text{V - 154}$$

Where μ_t is the dynamic turbulent viscosity, $\delta_{ij}$is the delta of Kronecker, k is the turbulent kinetic energy while $\frac{2}{3}\rho k$ in the analog of a dynamic pressure due to the turbulent agitation.

The Boussinesq hypothesis is used in the Spalart-Allmaras model, the models $k - \varepsilon$, and the models $k - \omega$. The advantage of this approach is the relatively low computational cost associated with the computation of the turbulent viscosity μ_t. Then in function of the turbulent model the turbulent viscosity is solved by one or two additional transport equations.

The disadvantage of the Boussinesq hypothesis as presented is that it assumes μ_t is an isotropic scalar quantity, which is not strictly true. However the assumption of an isotropic turbulent viscosity typically works well for shear flows dominated by only one of the turbulent shear stresses. This covers many technical flows, such as wall boundary layers, mixing layers, jets, etc.

The alternative approach, embodied in the RSM and tested for one pulsation frequency as the second turbulence model, is to solve transport equations for each of the terms in the Reynolds stress tensor. An additional scale-determining equation is also required. This means that five additional transport equations are required in 2D flows and seven additional transport equations must be solved in 3D. In many cases, models based on the Boussinesq hypothesis perform very well, and the additional computational expense of the Reynolds stress model is not justified. However, the RSM is clearly superior in situations where the anisotropy of turbulence has a dominant effect on the mean flow. Such cases include highly swirling flows and stress-driven secondary flows.

The $k - \varepsilon$ and the RMS models have been tested for only the 10 Hz case, results show equal instantaneous profiles of velocity and temperature suggesting so that the turbulent effects on the phase-average cycle have been equally accounted for. For this reason, and considering the low computational coasts of the $k - \varepsilon$ model, it has been finally employed for all the simulations. Moreover, as demonstrated by the works of Elshafei et al. [41], [42] such model was able to well predict the experimental results in their study.

The turbulent viscosity in the standard $k - \varepsilon$ model is computed as follows:

$$\mu_t = \rho C_\mu \frac{k^2}{\varepsilon} \qquad \text{V - 155}$$

Where C_μ is a constant; k and the dissipation rate ε are obtained from the following transport equations at page 47 of [91]. In the Fluent turbulence library three different $k - \varepsilon$ models are available: the standard, RNG, and the realizable $k - \varepsilon$ model. All three models have similar forms, with transport equations for k and ε. The major differences in the models are as follows: the method of calculating turbulent viscosity, the turbulent Prandtl numbers governing the turbulent diffusion of k and ε; and the generation and destruction terms in the ε equation. The features that are essentially common to all models follow, including turbulent generation due to shear buoyancy, accounting for the effects of compressibility, and modeling heat and mass transfer.

The realizable $k - \varepsilon$ has been chosen for our application: it contains a new formulation for the turbulent viscosity and a new transport equation for the dissipation rate, ε that is derived from an exact equation for the transport of the mean-square vorticity fluctuation. The term "realizable" means that the model satisfies certain mathematical constraints on the Reynolds stresses, consistent with the physics of turbulent flows. Neither the standard k-ε model nor the RNG k-ε model is realizable. It introduces a variable C_μ instead of constant. An immediate benefit of the realizable k-ε model is that it provides improved predictions for the spreading rate of both planar and round jets. It also exhibits superior performance for flows involving rotation, boundary layers under strong adverse pressure gradients, separation, and recirculation. In virtually every measure of comparison, Realizable k-ε demonstrates a superior ability to capture the mean flow of the complex structures. Details of such model are available at page 51 of [91].

A particular attention has been also paid in the modelling of the turbulent heat flux in the energy balance equation: the terms $\frac{\partial<u\prime T\prime>}{\partial x}+\frac{\partial<v\prime T\prime>}{\partial r}$ in eq. V - 152 are generally modeled as follows:

$$\rho c_p < u'T' > = \rho c_p \epsilon_H \frac{\partial T}{\partial x} \qquad \text{V - 156}$$

$$\rho c_p < v'T' > = \rho c_p \epsilon_H \frac{\partial T}{\partial r} \qquad \text{V - 157}$$

Where ϵ_H is the eddy thermal diffusivity $\epsilon_H = \frac{\lambda_{turb}}{\rho c_p}$.

In the particular case of the Fluent models, for a 2D axial-symmetric flow and neglected viscosity and diffusivity effect energy governing equations shows the following form:

$$\rho c_p\left(\frac{\partial T}{\partial t}+\frac{\partial(vT)}{\partial r}+\frac{\partial(u\,T)}{\partial x}\right) = \lambda_{eff}\left(\frac{1}{r}\frac{\partial}{\partial r}\left(r\frac{\partial T}{\partial r}\right)+\frac{\partial^2 T}{\partial x^2}\right) \qquad \text{V - 158}$$

Where $\lambda_{eff} = \lambda + \lambda_t$ is the effective conductivity which account both the fluid property λ and the flow property due to turbulence λ_t, which is solved from the turbulence model, as follows:

$$\lambda_t = \frac{c_p \mu_t}{Pr_t} \qquad \text{V - 159}$$

Where $Pr_t$the turbulent Prandtl number is kept constant to 0.85.

In practice the turbulent model is used to compute the turbulent kinetic energy and the dissipation rate, then the turbulent viscosity is calculated, and considering a constant turbulent Prandtl number the turbulent thermal conductivity (in eq. V - 159) is finally calculated.

The solver adopted in the Fluent for the previous governing equations is called ‘pressure-based’ (page 626 [91]): the velocity field is obtained from the momentum equations, while the pressure field is extracted by solving a pressure or pressure correction equation which is obtained by manipulating continuity and momentum equations and then the energy equation is solved. A control-volume-based technique is used that consists of division of the domain into discrete control volumes using a computational grid. Integration of the governing equations on the individual control volumes to construct algebraic equations for the discrete dependent variables (“unknowns”) such as velocities, pressure, temperature, and conserved scalars. Linearization of the discretized equations and solution of the resultant linear equation system to yield updated values of the dependent variables.

An overview of the pressure-based solution method is depicted in the following figure:

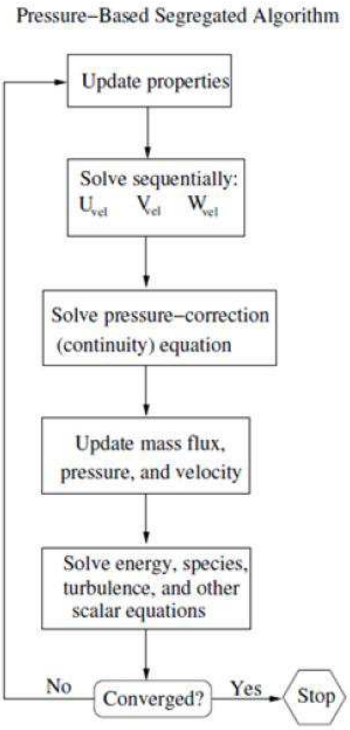

Figure 109: Overview of the Pressure-Based Solution method of Fluent

The fluid properties except the density have been maintained constant for all the simulations, in this way the energy equation has been decoupled from the momentum and continuity equations. Such assumption is coherent with the previous hypotheses applied in the 1D analytical approach in the paragraph IV.4. The density has been considered pressure dependent as for an ideal gas.

The discretization of the governing differential equations is performed using the finite volume method applied to a staggered orthogonal grid system. A power-law scheme is employed for convection fluxes. The SIMPLEC algorithm which is a powerful algorithm to solve fluid flow and heat transfer problems, is used and the discretized equations are solved with the line-by-line ADI (Alternating-Direction Implicit) iterative method. The solution of each point at each grid line is directly obtained through the TDMA (TriDiagonal Matrix Algorithm). To accelerate convergence, a recommended value 1.85 of the relaxation parameter is introduced in the TDMA solver. The convergence criteria with Euclidean norm of the residuals are used in solving the governing equations in each cycle of iteration. Meanwhile, under-relaxation is applied for the momentum equations, k-equation, and e-equation.

V.4.2 Geometry, Mesh & Boundary conditions

The model geometry is depicted in the following figure:

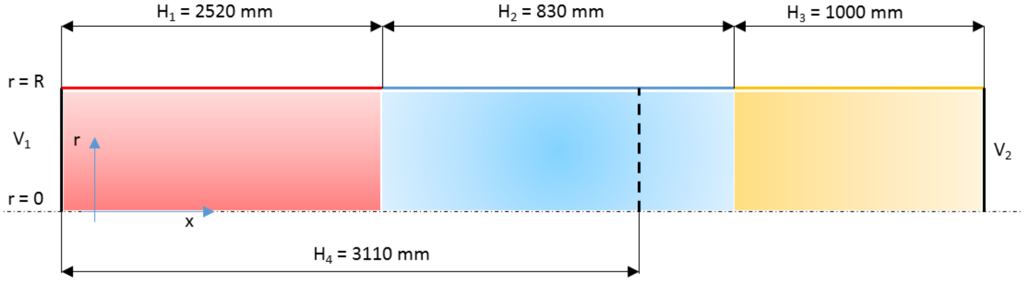

Figure 110: Geometry of the pulsating pipe flow with a 2D assumption modelled in Fluent

While the experimental apparatus is composed of a complex pulsating mechanism and of a steel pipe with a length up to around 6 m, in the modelling phase only a limited part of the test-rig has been simulated. The pulsating mechanism has not been considered, its contribution to the creation of a pulsating flow has been account for in the inlet boundary condition. Furthermore as the experiments has demonstrated in the paragraph III.6, the calculation of the integral length scale has revealed that the perturbation created from the valve are well dissipated in the first part of the pipe (called developing section), making useless and time-consuming to model it in Fluent.

The pipe has been simplified, to respect the 2D assumption, in a rectangular geometry composed of three different parts:

- V_1-H_1 represents the developing section, as in Figure 29, from the beginning of the straight pipe until the inlet of the test-section.
- V_1-H_2 represents the part of the test-section which is water cooled;
- V_2-H_3 represents only one partial part of the variable length section. Because modelling all the entire length was considered time-consuming from a computational point of view, the last part of the pipe has been designed with a length (H_3) of 1 m. It has been considered to be long enough in order that the outlet boundary conditions don't influence the heat transfers inside the test-section. In the previous chapter (IV.4) has been furthermore demonstrated that only the 500 mm of length of the pipe placed downstream the test-section may impact the convective heat transfer inside the test-section if both flow reversal and air warming appear.

Adopting the hypothesis of axial-symmetric flow only half of the pipe diameter has been modelled (R = 0.02775 mm). For instance, the section in which the hot-wire probe and the thermocouple sensors are placed corresponds to an axial distance from the inlet of the pipe 'H_4' of 3110 mm (it corresponds to the black dot line in Figure 110).

A structured mesh, composed of only rectangular element, has been applied to the geometry: the developing section length has been decomposed in 140 axial element with a non-uniform division which increase at the boundary of the section, the test-section has been decomposed in uniform 110 element (which corresponds to an element length of 7.55 mm) and the last section has been decomposed in 50 element refined at the beginning of the length. Totally 290 subdivisions are available in the axial direction, while in the radial direction 40 element have been used with a refinement near the wall.

Finally 11600 elements have been used to discretize the geometry, a particular of the mesh is shown in the following figure:

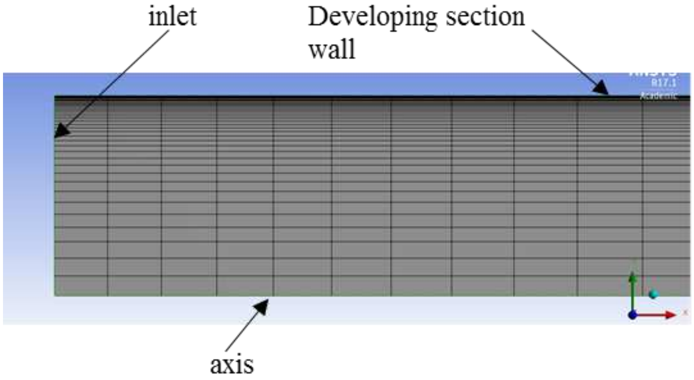

Figure 111: Mesh radial refinement

A particular attention has been paid in the boundary conditions definition: for the wall segments H1, H2, H3 no slip and fixed constant temperature conditions have been applied. The temperature have been extracted from the experiments results: for the segment H1 a temperature of 165°C has been fixed, for the test-section a temperature of 17,4 °C has been computed from the water temperature measurement, adopting the hypothesis of homogeneous temperature field; while for the last section a temperature of 100°C has been fixed and experimentally measured.

For the outlet section a pressure constant condition has been imposed with a relative pressure of 0 bar, while a constant temperature of 100 °C has been imposed for the energy balance equation.

Regarding the inlet section, different boundary conditions have been considered, the main challenge consists into imposing a time-dependent boundary conditions useful to reproduce the pulsating flow. The only way to impose a time-variant boundary conditions is to use a User-Defined Function.

A user-defined function, or UDF, is a function that can be dynamically loaded with the FLUENT solver to enhance the standard features of the code. UDFs are written in the C programming language. They are defined using DEFINE macros that are supplied by Fluent Inc. They access data from the FLUENT solver using predefined macros and functions also supplied by Fluent Inc. Every UDF contains the udf.h file inclusion directive (#include "udf.h") at the beginning of the source code file, which allows definitions for DEFINE macros and other Fluent-provided macros and functions to be included during the compilation process. UDFs are executed as either interpreted or compiled functions in FLUENT. Values that are passed to the solver by a UDF or returned by the solver to a UDF must be specified in SI units.

The UDF has been constructed to be able to impose at each time-step, and not at each iteration, of the simulation an inlet boundary conditions: among all the different possibilities of Fluent, the imposed inlet velocity or pressure profiles have not however been considered. If the air temperature and density are not well predicted, it is likely possible to not converge to the same time-average mass flow rate of the experiments. Only an imposed mass flow rate or specific mass flow rate can be used. Since the first one cannot be imposed through a UDF, the latter one has been finally selected as the inlet boundary condition, in this way the condition of equal time-average mass flow rate between the simulation and the experiments will be always respected. Once the specific mass flow rate is passed to the solver from the UDF, knowing the air density and section dimension, the instantaneous velocity is computed.

The inlet temperature has been fixed to the constant value of 165 °C which has been valuated from the experiments.

The instantaneous mass flow rate, since not experimentally measured at the inlet of the pipe, has been extracted from the results of a 1D modelling of the entire test-bench performed with the GT-Suite software. This software has allowed to model the cylinder head and the valve system of our test-rig (for the sake of brevity only some details are reported in this manuscript). A Gt-Suite scheme of the experimental apparatus in Figure 29 is showed in the following figure:

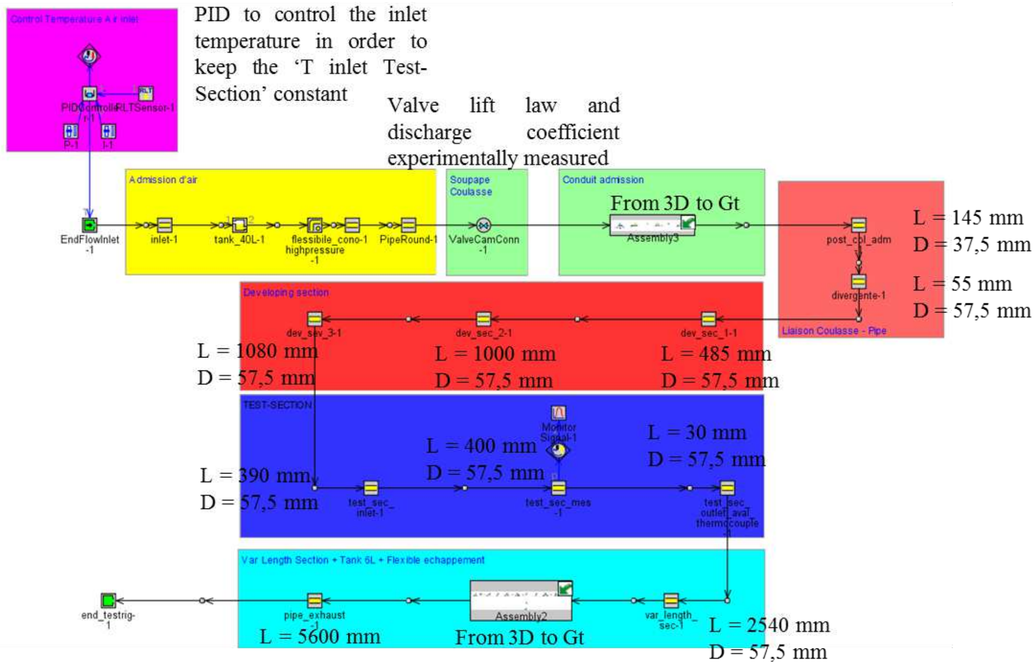

Figure 112: Experimental apparatus model on Gt-Suite

The test-rig has been modelled starting from the outlet of the air heaters, an inlet condition (the violet square at the top-left of the Figure 112) has been applied to impose a time-average constant mass flow rate and an inlet flow temperature. Then the volume between the air heaters and the cylinder head has been modelled with some bend pipes, a tank and straight pipes. The cylinder valve has been experimentally characterized in term of the flow coefficient, and valve lift law. Several mass flow rates have been flowed through the cylinder head, the pressure lost across the valve have been measured and then the valve flow coefficient has been computed in function of the valve lift.

The steel pipe at the outlet of the cylinder head has been modelled in three different blocks as in Figure 112: the red block represents the developing section, the blue block represents the test-section, while the latter one represents the variable length section more the outlet 6L plenum and the pipe used to connect the experimental apparatus to the exhaust line of the laboratory.

Since the pressure losses are not well predicted from the 1D modelling, the length of the last pipe section has been increased of 800 mm more than its real pipe length, with the main purpose to find the same resonance frequencies which have been experimentally measured in the paragraph III.7.

To be coherent with the 2D model, the inlet boundary condition should be extracted from the first pipe element of the developing section in Figure 112. Gt-Suite allows to select among all the output the mass flow rate profile for different axial positions over the pipe, nevertheless, due to flow reversal it has not been possible to use the Gt-Suite output into the 2D model as boundary condition.

As observed, in correspondence of such section a flow reversal appears, implying negative values of the specific mass flow rate. Once the Fluent solver uses a negative inlet mass flow rate it was not able to converge to the solution for the momentum and continuity equations.

To overcome such inconvenient, from the results of the 1D simulation the specific mass flow rate has been extracted for the cylinder head valve and used for the inlet boundary condition in the UDF.

The specific mass flow rate calculated, for a time-average mass flow rate of 110 kg/h, from the Gt-Suite results is showed in the following figure, it has been observed to be independent of the pulsation frequency:

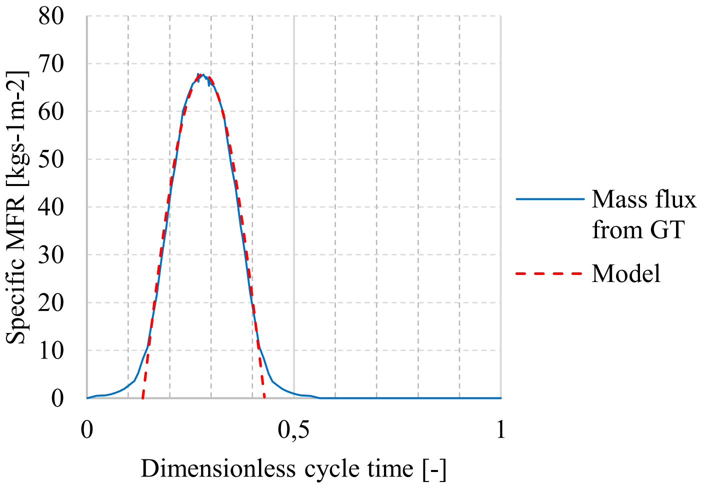

Figure 113: Specific MFR from Gt-Suite

In order to be implemented in the User-Defined Function such profile has been simplified with a sinusoidal equation existent between 0 and π (dot red line in Figure 113) defined as follows:

$$\dot{m}_s = A sin(2\pi f t_{dim} f_{dim}) \quad \text{V - 160}$$

Where A represents the maximum value of the specific mass flow rate extracted from Gt-Suite, f is the pulsation frequency of the flow, t_{dim} the dimensionless cycle time, and $f_{dim} = 1.7$ is a dimensionless frequency that has been chosen in order to have the same time-average specific mass flow rate in comparison with the Gt-Suite profile.

The correct timing of the valve opening has been determined from the experimental pressure measurements inside the cylinder head.

The dimensionless time t_{dim} follows the equation below:

$$t_{dim} = current - \big((k+1)T - RT\big) \quad \text{V - 161}$$

Where $current$ is the real flow time, T is the pulsation period, k the number of the simulated pulsation cycle and R represents a constant corresponding to the ratio between the open valve cycle period over the totality of the cycle period, for instance $R = 0.2943$.

Initial flow conditions have been deduced from the inlet conditions for a t = 0, and they have been applied to all the entire geometry assuming a hypothesis of quite homogeneous velocity and temperature fields.

Once the simulation is started, a high enough number of pulsation cycle is solved till the time-average value of the temperature and velocity in correspondence of the Hot-Wire section (dot black line in Figure 110) remains constant.

V.4.3 Results

The results presented in the following lines correspond to a pulsation frequency of 10 Hz, a time-average Reynolds number of around 30000. Phase-average flow properties have been extracted from the Fluent results for the section at the axial position corresponding to the hot-wire measurements in the experiments, in order to be directly compared with the experimental results previously presented.

Figure 114 shows the Fluent solved bulk air velocity and temperature, it could be observed that as in the experimental conditions (Figure 94) velocity reverses two times within the cycle, while a zero phase lag exist between the maxima of the velocity and temperature profiles. Such maxima correspond to the part of the cycle during which the cylinder exhaust valve is open.

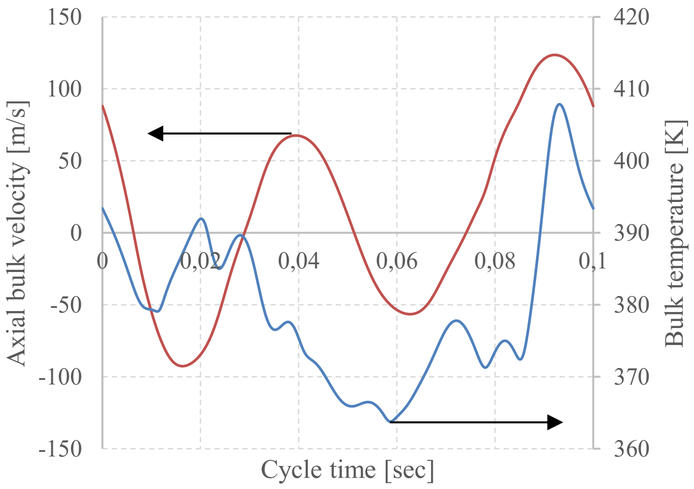

Figure 114: Phase-average Bulk Air temperature and velocity from Fluent

In the following figure the local phase-average convective heat transfer to the wall is showed and compared to the temperature difference between the wall and the pipe centreline.

Since the temperature difference between the gas and the wall should drive the heat transfer, the heat flux would be expected to oscillate with the gas temperature, if the rate of convection were constant.

It can be seen that the heat flux has a fundamental oscillation that is almost in phase with the fundamental oscillation of the temperature. We focus on the characteristic point A in the Figure 115: it could be observed that the minimum points between the heat flux and the temperature difference are phase-delayed, furthermore they occurs near a flow reversal instant.

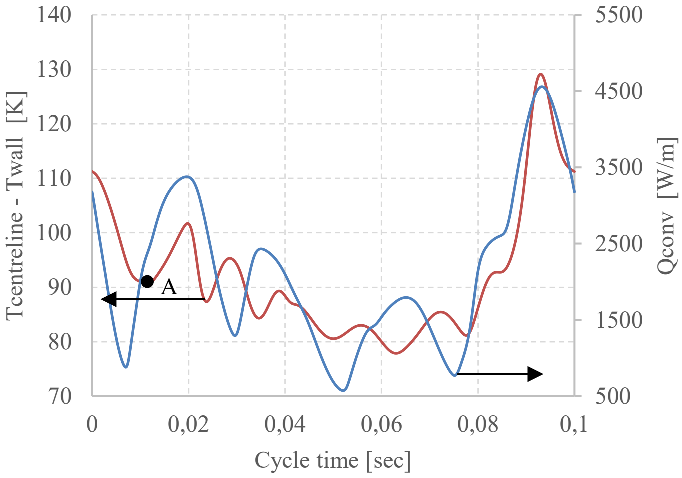

Figure 115: Phase-average convective heat transfer and wall/centreline temperature difference

In particular, during the flow reversal it could be observed that while the temperature difference continues to decrease, suggesting that also the heat flux to the wall should decrease (since temperature difference should drive the heat flux), nevertheless heat flux starts to increase. In the following lines, phase-average radial profile of air temperature and axial and radial velocities are reported to understand the reasons of such behaviour.

In Figure 116 the radial profile of the phase-average component of the air axial velocity is reported for different cycle instants around the flow reversal: it could be observed that as predicted from Uchida [86] and as experimentally observed, the flow reverses before near the pipe wall and then in the core of the flow, as well as during the flow reversal, the maximum of the radial profile remains near the wall implying an inflection point in the velocity profile.

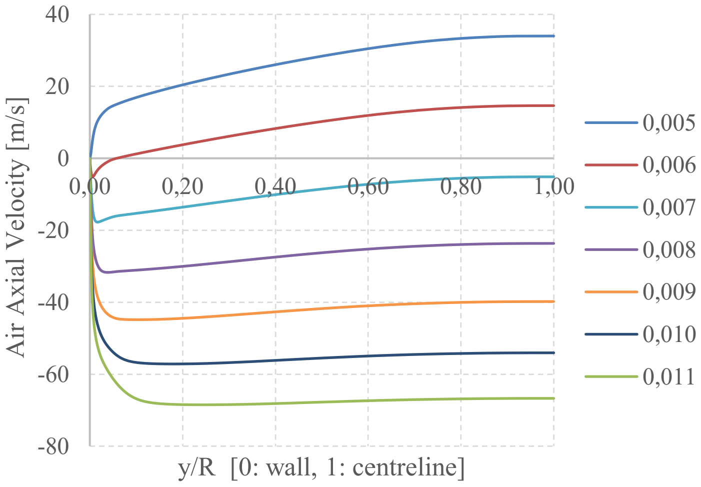

Figure 116: Phase-average air axial velocity profile during flow reversal

Figure 117 shows the radial air velocity, inaccessible from experimental measurements, during flow reversal as in Figure 116. Results show that similarly to the axial component, the radial component reverses before near the wall, furthermore, a velocity wave diffuse from the wall to the core. It has to be claimed that the radial velocity magnitude is widely inferior to the axial one, suggesting that the flow remains quite parallel to the wall.

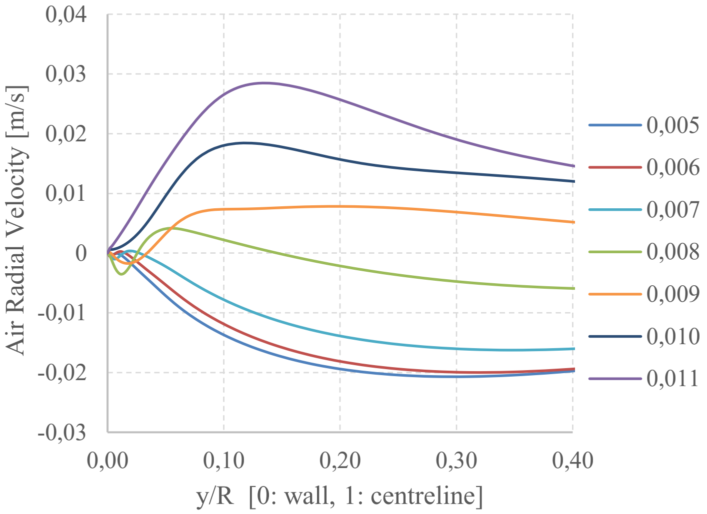

Figure 117: Air radial velocity profile during flow reversal

The temperature radial profiles, during flow reversal, are showed in Figure 118: a decrease of the air temperature near the wall is observed as well as a thickening of the thermal boundary layer.

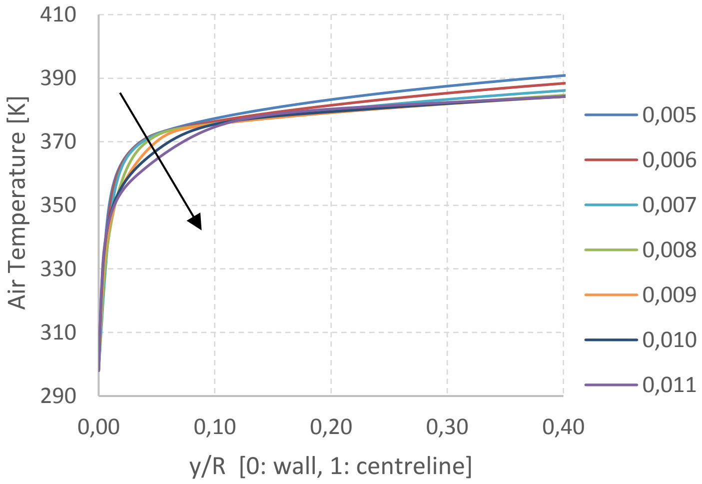

Figure 118: Air temperature profile during flow reversal

To be able to understand which is the major mechanism transporting the heat energy, the terms in eq. V - 158 (following reminded) are respectively computed in correspondence of the hot-wire section (dot black line in Figure 110):

$$\rho c_p \left(\frac{\partial T}{\partial t} + \frac{\partial (vT)}{\partial r} + \frac{\partial (u\,T)}{\partial x} \right) = \lambda_{eff} \left(\frac{1}{r}\frac{\partial}{\partial r}\left(r \frac{\partial T}{\partial r} \right) + \frac{\partial^2 T}{\partial x^2} \right) \qquad \text{V - 162}$$

In the following lines the discretization of the partial derivative is reported. Time-variation term has been discretized with a forward finite difference, the first derivative of the axial and radial advections have been discretized with respectively a centred and a forward finite differences. While the second derivative of the axial and radial conduction and turbulence terms have been discretized with a second order Taylor polynomial approximation.

$$\rho_{i,x,r} c_p \frac{\partial T_{i,x,r}}{\partial t} = \rho_{i,x,r} c_p \left. \frac{T_{i+1} - T_i}{dt} \right|_{x,r} \qquad \text{V - 163}$$

$$\rho_{i,x,r} c_p \frac{\partial (u\, T)_{i,x,r}}{\partial x} = \rho_{i,x,r} c_p \left. \frac{(u\, T)|_{x+\Delta x_1} - (u\, T)|_{x-\Delta x_2}}{\Delta x_1 + \Delta x_2} \right|_{i,r} \qquad \text{V - 164}$$

$$\rho_{i,x,r} c_p \frac{\partial (v\, T)_{i,x,r}}{\partial r} = \rho_{i,x,r} c_p \left. \frac{(v\, T)|_{r+\Delta r} - (v\, T)|_{r}}{\Delta r} \right|_{i,x} \qquad \text{V - 165}$$

$$\lambda_{eff_{i,x,r}} \frac{\partial^2 T_{i,x,r}}{\partial x^2} = \lambda_{eff_{i,x,r}} \left. \frac{T|_{x+\Delta x} - 2T|_x + T|_{x-\Delta x}}{\Delta x^2} \right|_{i,r} \qquad \text{V - 166}$$

$$\lambda_{eff_{i,x,r}} \frac{1}{r} \frac{\partial}{\partial r}\left(r \frac{\partial T_{i,x,r}}{\partial r} \right) = \lambda_{eff_{i,x,r}} \left. \left(\frac{1}{r_r} \frac{T|_{r+\Delta r} - T|_r}{\Delta r} + \frac{T|_{r+\Delta r} - 2T|_r + T|_{r-\Delta r}}{\Delta r^2} \right) \right|_{i,x} \qquad \text{V - 167}$$

The terms of the eqs. V - 163 ÷ V - 167 are plotted in Figure 119 during the first flow reversal in function of the distance from the wall, as in Figure 118.

The energy accumulation rate inside the fluid element, showed in Figure 119a, shows that when the flow revers a negative rate occurs near the wall and propagates away from it. In such conditions the penetration length of such wave is around 0.1R. A negative rate implies a decrease of the temperature, similarly it has been observed in Figure 118 according to during the flow reversal a temperature decrease appears near the wall.

The analysis of the remaining terms of the energy balance equations should be useful to evidence which mechanism among the axial advection of energy (term in eq. V - 164), the radial advection of energy (term in eq. V - 165), the axial or radial conduction and the radial or axial turbulent advection, is the major and the responsible of the temperature decrease.

The latter, as stated in eq. V - 162, is accounted for directly in the conduction terms by the effective conductivity.

By the figures Figure 119d and Figure 119e it could be observed that the impact of the conductive and turbulent flux on the energy accumulation rate could be neglected in comparison to the axial and radial advection flux because of their lower order of magnitude. It could be anyway observed that during the flow reversal a local peak, in the radial profile of the effective conductive radial term, appears near the wall and it is transported away from it. By separating the fluid and the turbulent conductivity terms, it has been observed that this local peak was mainly due to the turbulent radial energy flux. Such result is in coherence with the hypothesis of an increase of turbulent kinetic energy due to the particular profile of the axial velocity during the flow reversal. For instance, as previously observed in figure V - 131, an inflection point exists near the wall, during flow reversal, with the direct consequence of a high radial gradient. Analysing the turbulent kinetic energy equation of the $k-\varepsilon$ turbulent model, followed reported (details at pag. 52 of [91]), it could be noted that the production term G_b, which physically represents the energy transferred from the phase-average filed of the flow to the turbulent one, is proportional to both the Reynolds stress ($\rho\overline{u_i' u_j'}$) and the spatial gradient of the phase-average component of the velocity ($\frac{\partial u_j}{\partial x_i}$) as stated in eq. V - 169.

$$\frac{\partial(\rho k)}{\partial t}+\frac{\partial\left(\rho k u_j\right)}{\partial x_j}=\frac{\partial}{\partial x_j}\left[\left(\mu+\frac{\mu_t}{\sigma_k}\right)\frac{\partial k}{\partial x_j}\right]+G_k+G_b-\rho\varepsilon-Y_M+S_K \qquad \text{V - 168}$$

$$G_k = -\rho\overline{u_i' u_j'}\frac{\partial u_j}{\partial x_i} \qquad \text{V - 169}$$

According the Boussinesq hypothesis production term is modelled as follows:

$$G_k = \mu_t S^2 \qquad \text{V - 170}$$

Where S is the modules of the mean rate-of-strain tensor, defined as

$$S = \sqrt{2S_{ij}S_{ij}} \qquad \text{V - 171}$$

Thus, it could be affirmed that an increase of the velocity spatial gradients may enhance the mean rate-of-strain sensor and then increase the production of the turbulent kinetic energy, which consequently increases the Reynolds stress and the turbulent heat flux, as the results show.

Focusing on the axial and radial advection terms (eqs. V - 164 & V - 165) showed in Figure 119b and Figure 119c which play the major roles in the energy transport, it could be observed that besides the fact that the axial advection is always higher than the radial advection in the core of the flow, during the flow reversal the radial advection magnitude overcomes the axial magnitude in a zone near the wall. It could be finally affirmed that in such conditions the major mechanism responsible of the energy transport is represented by the radial advection, as the experimental results suggested.

To evidence the impact of such mechanism on the heat transfers the convective heat transfers at the wall extracted from the Fluent results have been reported in Figure 120 through a red-line. Furthermore, also the phase-average bulk axial velocity, and the convective heat flux calculated from the Dittus-Boelter correlation of eq. II - 42 (green line) are reported and compared to the Fluent calculation. The Dittus-Boelter correlation has been applied to calculate the phase-average Nusselt number and then the heat flux exchanged at the wall has been computed. The Nusselt number has been calculated from the Reynolds number based on the phase-average bulk axial velocity extracted from the Ansys results. It is important to claim that the convective heat flux calculated from the theoretical correlation contains some errors: at very low air velocities the Dittus-Boelter correlation, found for a turbulent steady flow is not anymore adapted. The flow may became laminar or the heat exchanged could be dominated from thermal conduction. Convective heat transfer should be thus corrected to account for such phenomena. Although the calculation has not been corrected to account such phenomena, the important feature to be noted remain unchanged: the minimum of the convective heat transfer profile is phase-delayed in comparison with the velocity reversal as well as in comparison with convective heat flux theoretically computed.

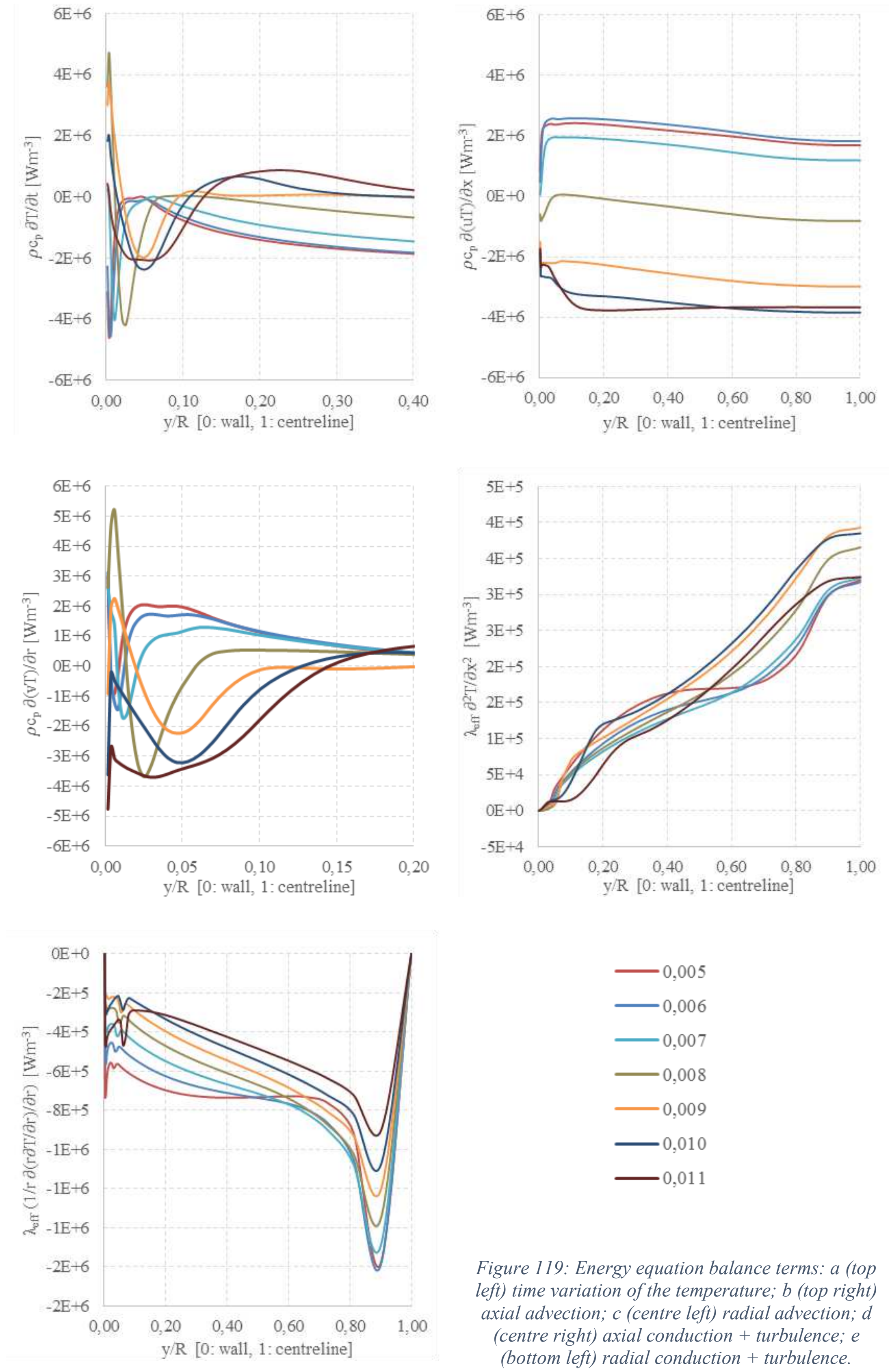

Figure 119: Energy equation balance terms: a (top left) time variation of the temperature; b (top right) axial advection; c (centre left) radial advection; d (centre right) axial conduction + turbulence; e (bottom left) radial conduction + turbulence.

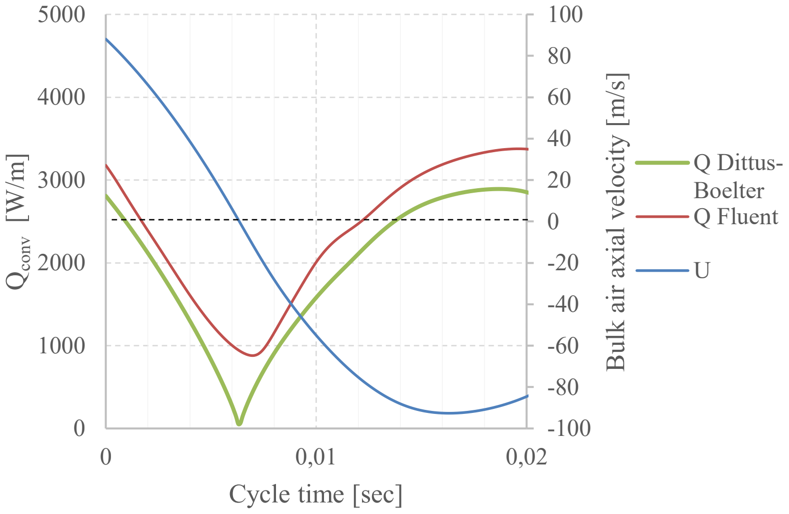

Figure 120: Focus on the convective heat transfer during the flow reversal

In view of all this it could be argued that the high radial advection, during the flow reversal, delays the diminution of the convective heat transfer, and it spreads the thermal energy over the pipe cross section decreasing the centreline pipe temperature as the previous results show. Also the turbulent heat flux is influenced by the pulsation during the flow reversal, anyway, its role on the convective heat transfer to the wall could be neglected.

The terms of the equation V - 162 are compared during all the pulsation cycle. Figure 121 shows, through a colour code, the major in absolue value term of eq. V - 162 in function of the cycle time and the distance from the wall for a constant axial position over the geometry (section H_4 in the Figure 110). The colour-bar represents the colour code which corresponds to each term in the energy balance equation.

Results show that while away from the wall the axial advection (light blue) widely represents the major mechanism of energy transport during the pulsation cycle, near the wall there are some moments in which radial advection overcomes the axial advection (as previously demonstrated in correspondence of the first flow reversal). Comparing Figure 114 and Figure 121 it is noted that high radial advection coherently occurs during flow reversal.

Results in Figure 121 also show that in function of the local flow conditions, the radial advection is more or less spread away from the wall, implying a higher penetration length of the radial advection wave as previously observed in Figure 119c.

A similar behaviour has been found in previous studies regarding the shear waves of the cinematic field: the condition of no-slip at the wall necessitates that for a pulsating flow, in order to accommodate the imposed variation of flow rate additional vorticity must be generated in the boundary layer in a manner which varies with time. Thus coherent shear waves are excited, which propagate from the wall into the fluid and are attenuated as they do so.

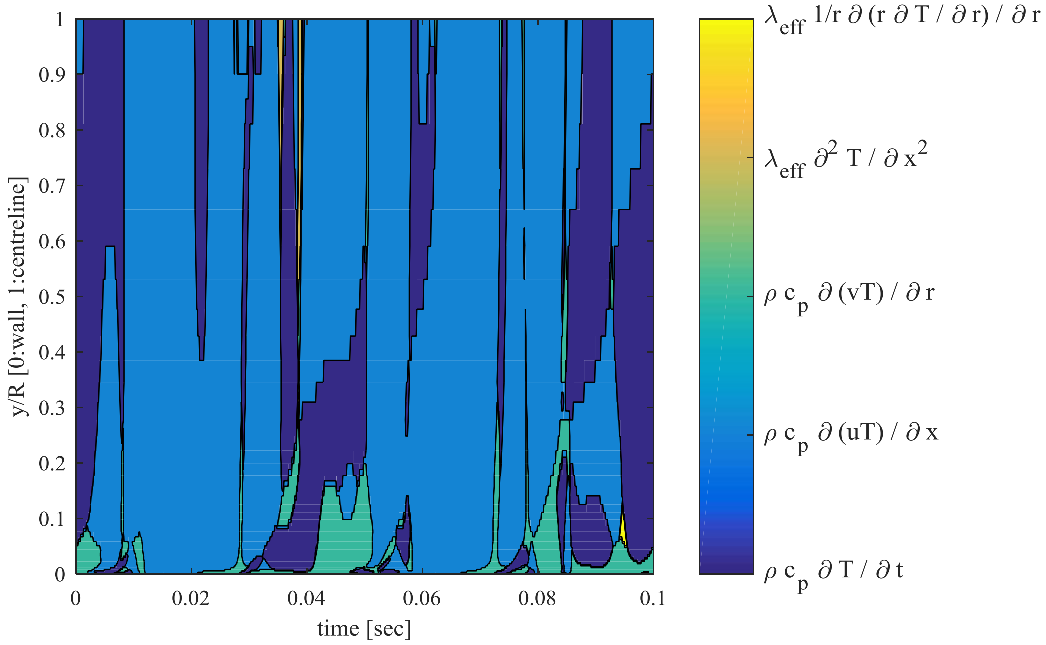

Figure 121: Major mechanism of energy variation over the HW section

Being able to modify the penetration length of such radial advection wave may represent a potential method to increase convective heat transfers. For instance, if the penetration length should be correlated with the pulsation frequency and the pipe diameter, the latter could be particularly chosen to enhance such convective mechanism and its effects on the heat transfers. Such potential should motivate future studies of this mechanisms.

In order to see the impact of the frequency on the penetration length of the wave of the radial transport of the thermal energy four different frequencies have been simulated, which are 10 – 20 – 30 and 40 Hz.

Because of the phase-average bulk axial velocity profiles for the four tested frequencies are not similar, in particular, flow reverses different times in function of the pulsation frequency and the term $\frac{\Delta<u>}{\bar{u}}$ is different for each frequency, the velocity amplitude and variations are not the same.

Comparing, among all the frequencies, the instantaneous profiles of the energy axial advection term is thus not useful, since the local velocity and temperature conditions are not the same.

For this reason only the time-average component of the radial advection term, in eq. V - 165, has been compared among all the tested frequencies, such term contains the average impact of the oscillating component on the time-average one.

It has been reported in function of the distance from the wall for four simulated frequencies and it has been compared to the turbulent stationary casein the Figure 122.

The first difference which could be observed between the pulsating and the steady cases is that contrarily to the pulsating cases the radial advection term is always positive for a stationary turbulent flow. A positive term implies that the energy is transported from the core to the wall, according the reference axis convention used in Figure 110, over the entire pipe section.

Contrarily, for the pulsating cases the advection term assumes both a positive and a negative value, suggesting the existence of two difference layers in which the energy is radially advected in opposite directions. This implies also the existence of an inflection point far from the wall in which the advection from the wall and from the core meet together in the same fluid volume.

Being able to predict the thicknesses of such layers should be advantageous for an optimized choice of the pipe diameter, furthermore, as previously affirmed the prediction of such phenomenon could be exploited as a technique to increase convective heat transfers.

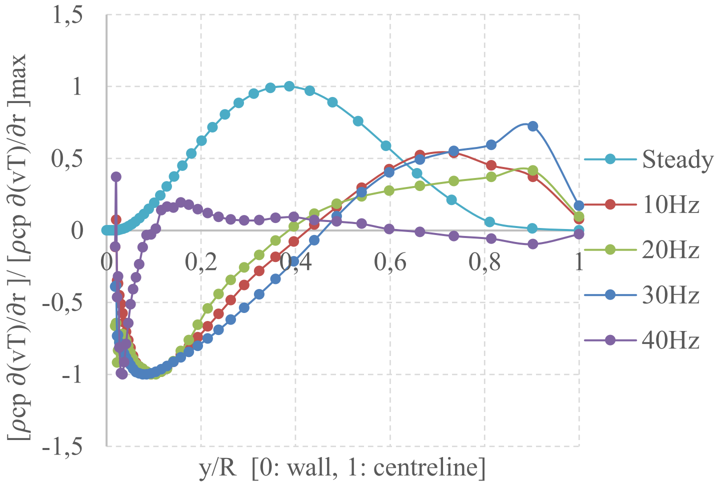

Figure 122: Time-average dimensionless radial energy advection term

Figure 122 shows an ulterior interesting feature: the negative peak in the radial advection term profile, which represents the maximum of the radial advection, moves from the core to the wall as well as the pulsation frequency increases.

As previously cited, a similar behaviour has been found in previous studies for the shear waves of the cinematic field: the condition of no-slip at the wall necessitates that for a pulsating flow, in order to accommodate the imposed variation of flow rate additional vorticity must be generated in the boundary layer in a manner which varies with time. Thus coherent shear waves are excited which propagate from the wall into the fluid and are attenuated as they do so.

In the case of laminar pulsating flow, as claimed from Uchida [86], the wave attenuation is characterised by a length scale $l_s = \sqrt{\frac{2\nu}{\omega D}}$ (in which ν is the kinematic viscosity of the fluid and ω is the radian frequency of the pulsation). This length scale is usually referred to as the Stokes layer thickness in recognition of the pioneering contribution which Stokes made to the theory of unsteady flow. Thus, the higher the frequency of the pulsation the thinner is the Stokes layer and the greater is the attenuation. This decay in shear wave amplitude is accompanied by a variation of the modulation of the local temporal mean velocity field in response to the imposed pulsation. Beyond the location where the shear wave is effectively fully-attenuated, the modulation becomes uniform and the flow can be thought of as oscillating in a ‘plug flow’ manner about a temporal mean distribution of velocity.

Turning next to turbulent pulsating flow, taking a time mean view of a turbulent wall shear flow leads to the concept of turbulent shear stresses being present in addition to viscous stresses and enables such a flow to be considered as being steady and made up of different regions defined according to the relative magnitude of these two kinds of stress. In the case of a turbulent flow the length scale has been called turbulent Stokes layer thickness l_t, several works have been made to attempt to characterize such scale for turbulent flow [20], [92]–[97], we cite the relatively recently work of Scotti and Poimelli [98] in which a particularly valuable contribution to the understanding of pulsating turbulent channel flow has been made using Direct Numerical Simulation and Large Eddy Simulation. In comparison with physical experiments, where the number and scope of measurements are usually rather limited, their 'numerical experiments' produced detailed turbulence statistics as well as information on the topology of the coherent structures. Their results were generally consistent with experimental data reported earlier in literature and enabled them to develop a detailed picture of turbulent pulsating flow in terms of the categories based on the concept of a turbulent penetration depth suggested by Ramaprian and Tu [36], [37]. Below, we present a summary of that picture and of the relationship between the various dimensionless scaling parameters which can be used for correlating data on turbulent pulsating flow.

If a pulsation of sufficiently high frequency is imposed on a steady turbulent flow, the shear waves propagating into the fluid from the wall will be strongly attenuated and mainly confined to the viscous sub-layer region. For this to be so, the thickness of the Stokes layer must be significantly less than that of the viscous sub-layer. Thus $l_s^+ = \frac{l_s u_\tau}{\nu}$ should be less than about 1. Noting that the inner scale Strouhal number, used to give a dimensionless frequency scale, $\omega^+ = \frac{\omega \nu}{u_\tau^2}$ is related to l_s^+ by the expression $\omega^+ = \frac{2}{l_s^{+2}}$, we see that for this condition to apply ω^+ must have a value greater than about 2.

For the very high frequency condition under consideration, the inner and outer layers are completely decoupled and the turbulence in the outer region is not affected by the imposed pulsation of flow rate.

The velocity field in the outer region is made up of the corresponding steady state velocity field with a uniform modulation applied to it. Such a flow can be viewed as one in which the turbulence is 'frozen' and is simply being advected in a 'plug flow'.

Some reduction of the frequency of the imposed pulsation below that for which the velocity and turbulence fields are just described, but still keeping within a relatively high frequency range will lead to a situation where the shear waves propagate into the region beyond the viscous sub-layer where turbulent stresses are significant compared with those due to viscous action. In doing so the shear waves will interact with the steady turbulence field generated by the temporal mean flow, producing an oscillating response in the turbulence quantities.

In such case the turbulent stokes layer thickness scale has been found to assume the following form:

$$l_t = l_s \left[\frac{k l_s^+}{2} + \sqrt{\left(\frac{k l_s^+}{2}\right)^2 + 1} \right] \qquad \text{V - 172}$$

The formula to have a dimensionless length scale by the inner variable, in the case of the turbulent Stokes layer thickness, is

$$l_t^+ = \frac{l_t u_\tau}{\nu}. \qquad \text{V - 173}$$

Further reduction of the frequency of the pulsation into a range which might be described as being of intermediate frequency leads to a stronger coupling of the inner and outer layers and a significant response of the turbulence field to the imposed pulsation.

If the frequency of the imposed pulsation is reduced to a value such that the time for a shear wave to travel across the flow from the near wall region to the centre is very small compared with the time period of the imposed oscillation, the turbulence will have time to relax to local (in time) equilibrium. The phases of each of the turbulence quantities then become independent of position and the velocity and turbulence distributions will be similar to those of a steady flow through the pipe or channel at a flow rate equal to the instantaneous value. Such a pulsating flow can be described as being quasi-steady.

The dimensionless penetration length corresponding to the radial advection wave in Figure 122 is compared to the turbulent and laminar stoke layer scale in the following figure.

Since the friction velocity has not been possible to be computed from the experiments, it has been calculated with the correlation available in literature for the counterpart steady flow with a same time-average Reynolds number. The Blasius correlation, valid for a smooth pipe with a Re between 10^4 and 10^5, is followed reported:

$$C_f = 0.3164\left(\frac{\overline{U}D}{\nu}\right)^{-1/4} \qquad \text{V - 174}$$

Where the fluid properties has been evaluated at the time-average bulk temperature at the middle of the test-section length.

The friction velocity has been so computed:

$$u_\tau = U_{ref}\sqrt{C_f/8} \qquad \text{V - 175}$$

Where U_{ref} corresponds to the axial velocity calculated from the time-average mass flow rate.

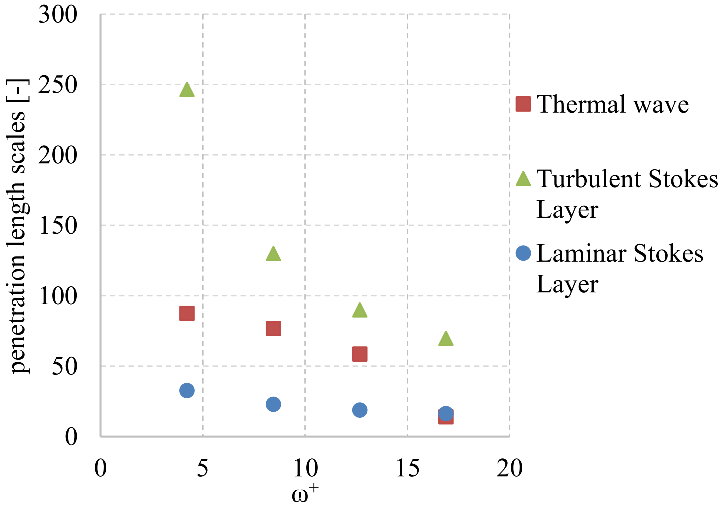

Figure 123: Penetration lengths of the time-average radial energy advection waves

Results show that the penetration length of the radial advection wave is placed between the turbulent and laminar stokes layers. While, increasing the frequency leads to a penetration length for the radial convective energy flux wave equal to the laminar stokes layer.

Such result shows that by pulsating a turbulent flow the radial advection is perturbed in a pipe layer smaller than the shear wave, and, that increasing the pulsation frequency leads to a narrower enhanced radial convection layer. Instantaneous 2D measurement of the flow temperature and velocity should be conducted in future in order to have further evidence of such phenomena.

V.5 Conclusions

The data analysis with a 1D assumption, presented in the chapter IV, has evidenced that an increase of the axial energy advection due to large velocity oscillations represent the major mechanism of the heat transfer enhancement. However, the analysis of the phase-average profiles of the air axial velocity and air temperature, in this chapter, has suggested that secondary mechanisms exist, such as the increase of the radial heat advection during flow reversal.

As preamble in this chapter a 2D analytic development of the energy governing equation has been presented to evidence the terms in the equation which are representative of the radial energy advection, as well as it has been demonstrated that the impact of such phenomenon on the convective heat transfer at the wall could not be directly estimated.

In view of this, the temperature and velocity profiles for a 10 Hz pulsating flow have been reported and discussed: results suggest that during the flow reversal an enhanced temperature mixing over a pipe section occurs, as well as from the velocity profile for a cold pulsating flow it has been possible to affirm that a perturbation of the velocity field diffuses from the wall to the core during flow reversal.

These two element contribute to the hypothesis of an enhanced radial energy aviation during flow reversal. However, due to the lack of the measurement of the radial component of the flow velocity it has not been possible to compute all the terms of the 2D energy governing equation, and it has not possible to numerically demonstrate the existence of such radial convective phenomenon.

Such inconvenient has been overcome through a 2D modelling phase of the heat transfer problem with the Fluent-Ansys CFD software. The main purpose has been to reproduce a flow reversal similar to which one experimentally observed, then, to calculate the terms of the energy equations and evidence its correlation with the convective heat transfer to the wall. The Fluent modelling of the governing equations, as well as its limitations have been revised in the previous paragraphs.

CFD results have showed that as experimentally observed, during flow reversal an enhancement of the radial energy advection occurs, and thanks to the computing of energy equation terms it has possible to evidence that such mechanism assumes a weight more important than the axial advection. It has been also observed that such phenomena locally increase the heat transfer coefficient during flow reversal.

In the last part of the chapter the time-average component of the radial advection term has been computed for different pulsation frequencies and it has been compared to the steady case, with the main purpose to evidence the impact of the pulsation frequency on the radial advection mechanism. Results have shown that the maximum of such profile moves from the core to the wall of the pipe as the pulsation frequency increases suggesting that the radial advection remains enhanced in a narrow layer near the pipe wall. Phase-detailed measurement of the 2D temperature and velocity fields should be conducted in future to study in detail such phenomenon.

Chapter / Chapitre 6

Thesis Conclusions and Perspectives

VI. Thesis Conclusions and Perspectives

Legislation on vehicle emissions continues to become more stringent in an effort to minimize the impact of Internal Combustion Engines 'ICEs' on the environment, forcing engine manufacturers companies to face always more the challenge of increasing engine efficiency and decreasing pollutant emissions.

ICE efficiency is still improving but it is today limited at best to around 40%, a large part of energy contained in the fuel is lost in coolant, oil, exhaust gas and air around the engine.

To fulfill these objectives in the recent years a particular attention is being paid to the Waste Energy Recovery technologies as well as in the design optimization of the exhaust line of ICEs accounting for thermal flux loss constraints. This is the reason of a higher interest in the comprehension of the heat transfer phenomena appearing in the engine manifolds.

Heat transfers in the engine exhaust, as well for the engine intake, occur under pulsating conditions. The term 'pulsating' is used for the class of cycle-stationary flow in which the oscillations occur around a time-average value different from zero. It means that coherent phenomena in heat transfers occur and may be deduced and then used in our advantage to face the stricter emission standards.

Although for a stationary flow the Reynolds number characterizes the laminar or turbulent behavior of the bulk flow, the amplitude and the frequency of the superimposed oscillations play a dominant role in the structures of the pulsating flow. Over the past decades, widespread studies have been dedicated to pulsating flows, and their associated heat transfer process, in a wide range of experimental configurations. However, some available results are contradictory and the main questions are still open: *does pulsation enhance or else degrade heat transfers compared to a steady flow? Which are the main heat transfer mechanisms?*

In the first part of the second chapter, the fundamentals of the convective heat transfer phenomena have been revised, demonstrating that flow pulsation modifies the governing equations by adding some terms which cannot be a-priori predicted. It has also reported, in the exhaustive survey of the available previous results, that the variety of the experimental configurations and the variety of the pulsation creation mechanisms have led to some controversies: both enhancement and degradation of the convective heat transfers have been observed, besides, the main physical mechanisms involved have not been fully described. Furthermore, it has been observed that in the specific case of ICE applications a deep understanding of the heat transfers phenomena becomes, always more, an important requirement to face the engine manufacturer needs to respect the stricter emission standards.

For all these reasons, the objective of this thesis has been to progress in the comprehension of the heat transfer phenomena for engine exhaust-type pulsating flows by an experimental approach.

Because of the difficulty to well manage all the flow properties in a direct study of the heat transfers directly inside an engine manifold, a versatile test rig has been developed and presented in the third chapter. It has been designed to produce a pulsating turbulent pipe flow, with the operating conditions representative of an engine exhaust. Pulsation frequency ranges from 10 to 95 Hz and the Reynolds number could be varied between 10^4 and $5x10^4$. To go further in the comprehension of the heat transfer phenomena a rapid-measurement of air temperature and velocity, within the pulsation cycle, has been applied. Actually, a double parallel hot-wire probe has been used in CTA mode to measure the axial component of the air velocity, furthermore, thanks the unique shape of the probe a novel methodology to detect flow reversals has been proposed and experimentally validated. Temperature impacts on wire voltage have been considerate and compensated after an ad-hoc velocity and temperature calibration of the wire. The instantaneous profile of the air temperature has been measured by type K unsheathed thermocouples. A characterization of the time response of the sensor has demonstrated that such sensors require a time-delay compensation due to its first order-type response to a variation in the flow temperature. Although an 'ex-situ' characterization of the sensor time-constant has shown its unique dependence on the air velocity, an 'in-situ' method has been applied because of the impossibility to well reproduce the pulsating flow properties in controlled conditions. The in-situ technique requires two different thermocouple sensing the same temperature, then, through the Kalman filter mathematics the calculation of the time-constant and the signal compensation could be fulfilled.

These measurement techniques could be in future employed by the Groupe PSA to ameliorate its metrology procedures. Today, for example, during the testing phase of the ICE prototypes, exhaust temperatures are widely measured with sheathed type K thermocouples, because of their highest mechanical resistance. However, the thermocouple's sheathing increases the response time of the sensor because of the heat transfer conditions are degraded while the ulterior sheathing mass increases the thermal inertia of the system. The response times resulting from a characterization of several sheathed type K thermocouple, with the test-rig used in the paragraph III.4.1, are showed in the following figure:

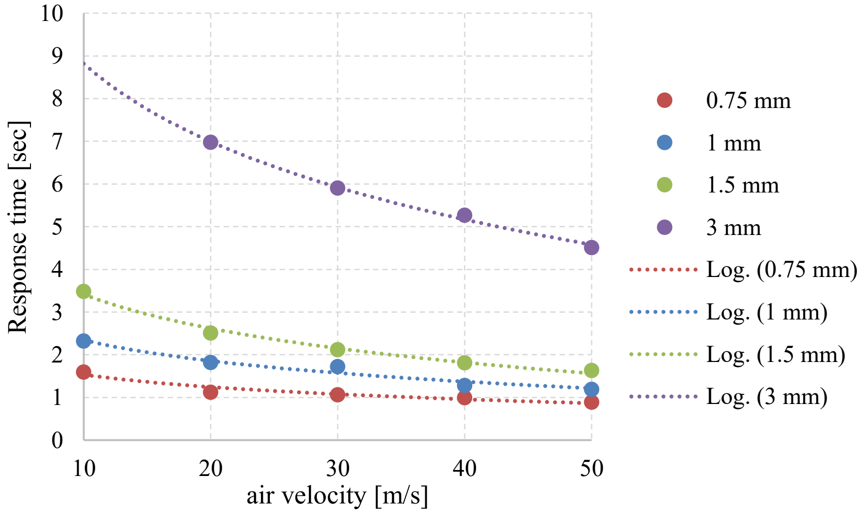

Figure 124: Response time for several sheathed type K thermocouples

It could be observed that for a thermocouple of 3 mm the time response is superior to 4 sec: if such thermocouple is used to measure the gas temperature under transitory engine operating conditions, a large errors in the temperature measurements will be effected. Assuming the hypothesis that the exhaust gases properties are similar to the air properties, by knowing the instantaneous exhaust mass flow rate of the engine, with an iterative method the air velocity could be computed, the time response could be estimated from our characterization and then the temperature measurements could be corrected.

With the same purpose, also the air velocity measurement technique could be adapted to measure instantaneous mass flow rate in the EGR lines of ICEs. Nowadays due to the high temperature conditions none type of mass flow meter is employed in the EGR lines. For this reason, a particular attention should be paid in the choice of the wire material and dimension, as well in the correction of the wire voltage to account temperature effects. As demonstrated in this work a Pt-Ir 20% wire could be heated till a temperature of 700°C enough elevated to measure the velocity of the EGR gasses, however, the wire diameter should be increased to stand the elevated gas velocity. The constraint which could limit the wire dimension is its bandwidth frequency, which could be higher than the frequency of the pulsating flow in the EGR line. An experimental characterization of the hot-wire time response should be primarily effectuated.

In the same chapter the temperature and velocity radial time-average profile of the flow in stationary state have been analyzed and compared to the available literature models, to be able to affirm that the stationary flow in the test-section could be considered fully developed and the pipe could be considered smooth. Also an acoustic characterization of the experimental apparatus has been conducted for different pipe lengths, and the results have been presented in such chapter.

In the fourth chapter, with the purpose to investigate the effect of pulsation on the convective heat transfers, a particular attention has been paid in the calculation of the time-average convective heat transfer by developing an analytical formulation of the heat transfer problem for a 1D pulsating turbulent pipe flow. An ad-hoc experimental procedure have allowed to evidence that, in the case of a reversed pulsating flow, a contribution to the energy balance equation through the boundaries, which impacts the total convective heat transfers, may occur.

Results have also shown that the flow pulsation enhances heat transfers in the entire range of the investigated frequencies. In particular, when the flow is excited with a frequency equal to a resonance mode of the system, a strong increase in heat transfers occurs. Instantaneous measurements of air velocity and temperature have demonstrated that the increase of the energy axial advection due to the oscillating component of the velocity is the major cause of the heat transfer enhancement.

This result should be applied to ICE applications: with the main purpose to decrease the thermal lost into the exhaust manifold and consequently rapidly warm the catalytic converter, the exhaust system should be designed in order that its resonance frequencies be in a range different from the ICE operating condition range. In this manner high flow oscillations should be avoided, decreasing the heat loss.

Experimental results have also shown that the relative Nusselt number is monotonically proportional to the ratio between the velocity oscillation amplitude and the velocity time-average component, suggesting that such parameter, which characterizes the amplitude of the velocity waveform, should be considered in a new Nusselt correlation to account for pulsating effects.

A fully don't understood phenomenon, anyway, has been found to enhance heat transfers for the particular frequency of 40 Hz for a Reynolds number based on the time-average component of the axial bulk velocity equal to 30000. Such enhancement has been found to appear locally in the central part of the test-section where cavities at the wall are used to screw the several used sensors. Instantaneous measurements of air velocity and static pressure in different conditions have shown that a high oscillating component appears, a theory has been proposed to explain such evidences: the *feedback loop* characteristic for flow grazing cavities has been suggested to be the mechanism responsible of an interaction between the kinematic and the acoustic filed. A direct consequence should likely be the creation of a high radial velocity component which transport thermal energy across the pipe section and increases the convective heat transfers as observed.

Although the fundamentals of this mechanism have not been understood, such kind of result represents an important advancement: such acoustic/hydrodynamic phenomenon may act like a heat transfer enhancement mechanism, if fully understood. Cavities could be placed at the wall of a pipe in order to intentionally create an increase of the energy radial advection. However; a particular attention should be paid in the calculation of the wall shear stress to evaluate the weight of a possible pressure lost in comparison with an enhancement of the convective heat transfers

In the chapter V, the analysis of the phase-average profiles of the air axial velocity and air temperature, have suggested that a secondary mechanisms exists, such as the increase of the radial heat advection during flow reversals.

As preamble in this chapter a 2D analytic development of the energy governing equation has been presented to evidence the terms in the equation which are representative of the radial energy advection, as well as it has been demonstrated that the impact of such phenomenon on the convective heat transfer at the wall could not be directly estimated.

In view of this, the temperature and velocity profiles for a 10 Hz pulsating flow have been reported and discussed: results suggest that during the flow reversal an enhanced temperature mixing over a pipe section occurs, as well as from the velocity profile for a cold pulsating flow it has been possible to affirm that a perturbation of the velocity field diffuses from the wall to the core during flow reversal.

These two element have contributed to the formulation of the hypothesis of an enhanced radial energy aviation during flow reversal.

However, due to the lack of the measurement of the radial component of the flow velocity it has not been possible to compute all the terms of the 2D energy governing equation, and it has not possible to numerically demonstrate the existence of such radial transport phenomenon.

Such inconvenient has been overcome through a 2D modelling phase of the heat transfer problem with the Fluent-Ansys CFD software. The main purpose has been to reproduce in a first phase a flow reversal similar to the which one experimentally observed, and then, calculate all the terms of the energy governing equation and analytically demonstrate the presence of such phenomenon.

CFD results have showed that as experimentally observed, during flow reversal an enhancement of the radial energy advection occurs, and thanks to the computing of energy equation terms it has possible to evidence that such mechanism assumes a weight more important than the axial advection. It has been also observed that such phenomena locally increase the heat transfer coefficient during flow reversal. In the last part of the fifth chapter the time-average component of the radial advection term has been computed for different pulsation frequencies and it has been compared to the steady case, with the main purpose to evidence the impact of the pulsation frequency on the radial advection mechanism.

Results have shown that the maximum of such profile moves from the core to the wall of the pipe as the pulsation frequency increases suggesting that the radial advection remains enhanced in a narrow layer near the pipe wall. A similar behaviour has been observed for the shear wave transport in the velocity field from ancient experimental studies. More precise measurement of the 2D temperature and velocity field should be conducted in future to study in detail such phenomenon.

To conclude on this thesis we can affirm that several elements which contribute to the comprehension of the heat transfer phenomena for pulsating turbulent pipe flows have been discovered: finally adding a pulsation on the flow field acts like a heat transfer enhancement techniques; however, as perspectives several action could be proposed.

First of all, to face the requirement of an always more rapid measurement of the air temperature variations, a smaller sensor should be adopted according the idea that the thermal inertia of the sensing elements acts like a filter to the rapid temperature variations. In order to measure turbulent temperature variations such sensors should have a response frequency bandwidth of up to 3-5 kHz, which is comparable to which one of a hot-wire anemometer. As experimentally demonstrated, a cold-wire with a diameter of 1μm doesn’t represent a possible solution due to its mechanic resistance which is insufficient to stand rapid and high air velocity oscillations. Thin-film thermocouple could be a possible solutions: as observed in the works of Dec et al. [27], more than an optic TLAF temperature measurement technique, thermocouples were used in their test-rig. TLAF technique, which utilizes two continuous-wave dye lasers tuned to pump two electronic transitions of atomic indium seed atoms was enough rapid to allow a data acquisition rate of 2 kHz, suggesting that it represents an optimum methodology to have planar measurements of the air temperature. Authors also claimed that for a thin-film thermocouples of 10 nm of thick a response time less of 100 μsec was obtained. In their study, such thin-film thermocouples were vacuum deposited on the wall of the tail pipe, in our case it should be deposited on a thin ceramic tube to avoid high thermal conduction. A particular attention should be paid also in the magnetic isolation of the electronic circuit which should be used to amplify the thermocouple signals and to compensate the cold junction. As observed during the experimental design of the test-bench, such circuit was noted to be high sensible to electronic noise coming from the exterior ambient. The very low electric currents, which were estimated to be inferior to 1 mA, were high sensible to the induced electromagnetic current.

Once the temperature velocity measurements will be increased it could be possible to measure air velocity and temperature turbulent components. In our study temperature measurements were limited for a pulsation frequency up to 40 Hz.

With the main purpose of increase the frequency investigation domain the pulsating mechanism could be modified: as previously affirmed the choice of a cylinder head has been the consequence to the air leakages problems of the siren system previously tested. By enclosing the siren wheel in a sealed plenum chamber, as in the Figure 125, the driving air supply could be used as the mean flow rate for the heat transfer measurements. The siren design proposal in the Figure 125 consists in a siren (green rotating disk) which is enclosed in volume, plus a second disk (light blue disk) which should be used to variate the flow section and thus modify the pulsation amplitude variations, while, the pulsation frequency is directly correlated to rotating velocity of the siren and the number of holes. The technology challenge of such system consists into consideration of the thermal deformations due to high temperatures for a correct choice of the backlashes between the static and the rotating parts.

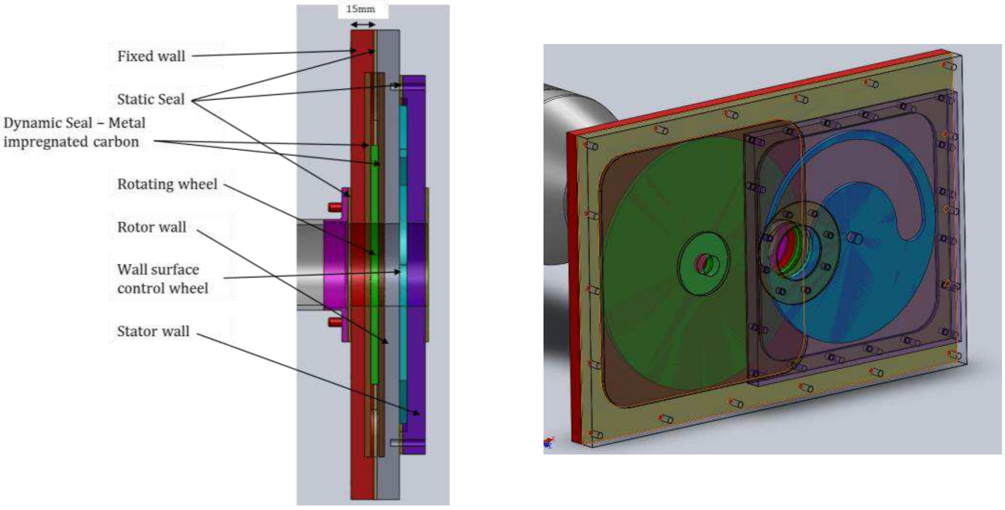

Figure 125: New siren design proposal

Such system will be useful also to study very low pulsating flow, with a frequency inferior to 10 Hz. Actually, the cylinder head system used in this study was not able to pulsate the system at very low frequencies because of the electric motor was not capable to control the high dynamic instantaneous couple to keep the velocity constant. The lower resistance couple of the siren should avoid such inconvenient.

Also a siren by-pass manifold should be added to the pulsating mechanism. According to the results showed in the chapter IV, it has been observed that term $\beta = \frac{\Delta<u>}{\bar{u}}$ is able to be representative of the major mechanism of the heat transfer enhancement: with a valve in such by-pass the mass flow rate traversing such part could be controlled in order to avoid flow reversal in the test-section. With such kind of system the term β should be independently controlled from the pulsation frequency and the mass flow rate allowing to perform a parametric study of the impact of such term on the relative Nusselt number.

In order to avoid any energy contribution from the boundaries, the water cooled part of the test-section should be also enlarged. Furthermore, air temperature measurements should be conducted over all the test-section length to study the axial variation of the Nusselt number as previously affirmed. The minimum and maximum thermocouple distance should be chosen in function of the minimum and maximum length scales of the velocity pulsations. A particular attention should be also paid to the design of the sensor connection to avoid any cavity in the pipe wall; furthermore the radial displacement of the sensor should be automatically controlled in order to ensure a higher precision near the wall to better describe the boundary layer flow behaviour.

As affirmed in the chapter V the lack of an instantaneous measurement of the heat flux at the wall has represented a limitation in the heat transfers study. Only a time- and a space- average convective heat transfer has been computed in the chapter IV. To go further in the convective heat transfer prediction for pulsating flows an instantaneous convective heat transfer flux should be analyzed in order to revise the validity of the actual Nusselt correlations used to predict heat transfers. Actually if the heat flux to the wall could be measured, all the terms in the 1D local governing energy equation (eq. IV - 97) could be computed.

Thin Film Gauge 'TFG' heat flux sensors are widely used in internal engine applications to measure wall heat flux. This sensor consists of a platinum RTD (Resistance Temperature Detector) on an insulating substrate which is typically a ceramic. An example of a TFG sensor is proposed by De Cuyper et al. [99], their homemade sensor consists of a platinum RTD (Resistance Temperature Detector) on an insulating Macor® (ceramic) substrate. Authors claimed that the sensor has a high frequency response (up to 100 kHz) and is small and robust. These properties make the TFG sensor adequate for measurements in turbulent pipe flow. The TFG sensor measures the temperature of the wall and thus first of all requires a steady state temperature calibration, to determine the temperature sensitivity coefficient. Signal processing is necessary to derive the heat flux perpendicular to the wall from the measured wall temperature. This temperature is then used as a boundary condition to solve the one dimensional heat conduction:

$$\frac{\partial^2 T(x,t)}{\partial x^2} = \frac{\rho c}{\lambda}\frac{\partial^2 T(x,t)}{\partial t^2} \qquad \text{VI - 176}$$

Where $T(x,t)$ is the temperature of the substrate at a given depth x.

A widely used signal processing method is the Fourier-method. The measured wall temperature trace is transformed into an analytic expression using a Fourier analysis, the resulting expression is given in the following equation:

$$T_w = B + \sum_{n=1}^{\infty} K_n \cos(n\omega t) + \sum_{n=1}^{\infty} G_n \sin(n\omega t) \qquad \text{VI - 177}$$

And the heat flux is as follows

$$Q = -\lambda \frac{dT(x,t)}{dx} \qquad \text{VI - 178}$$

Introduction eqs. VI - 176 and VI - 177 in eq. VI - 178 we lead to:

$$q = \sqrt{\rho c \lambda}\sqrt{\frac{n\omega}{2}}\sum_{n=1}^{\infty}[(K_n + G_n)\cos(n\omega t) + (-K_n + G_n)\sin(n\omega t)] \qquad \text{VI - 179}$$

The term $\sqrt{\rho c \lambda}$ is the thermal product of the TFG sensor and it needs to be experimentally calibrated. To correctly use such kind of the sensor in a pulsating pipe flow, the thermal product should be equal to the thermal product of the pipe wall. Furthermore, also the temperature sensitivity of the RTD wire should be calibrated. Actually a rapid 'Vatell Heat Flux Microsensor' is proposed by company 'Vatell Corporation' [100], manufacturer claims à response time up to 17 µsec. A particular attention in the utilization of such sensor should be paid to account the fact that the sensor material should be different from the wall material, implying different thermal inertia and thus different heat transfer conditions.

VII. Reference

[1] G. Bourhis and P. Leduc, “Energy and Exergy Balances for Modern Diesel and Gasoline Engines,” *Oil Gas Sci. Technol. – Rev. l’Institut Français du Pétrole*, vol. 65, no. 1, pp. 39–46, 2010.

[2] H. Aghaali and H.-E. Ångström, “A review of turbocompounding as a waste heat recovery system for internal combustion engines,” *Renew. Sustain. Energy Rev.*, vol. 49, pp. 813–824, 2015.

[3] X. Zhang and K. T. Chau, “An automotive thermoelectric-photovoltaic hybrid energy system using maximum power point tracking,” *Energy Convers. Manag.*, vol. 52, no. 1, pp. 641–647, 2011.

[4] S. RK, W. A, and A. C, “The potential for thermo-electric devices in passenger vehicle applications,” in *SAE 2010 World Congress & Exhibition - nso. 2010-01-0833*, 2010.

[5] D. T. Crane and G. S. Jackson, “Optimization of cross flow heat exchangers for thermoelectric waste heat recovery,” *Energy Convers. Manag.*, vol. 45, no. 9–10, pp. 1565–1582, 2004.

[6] W. Aladayleh and A. Alahmer, “Recovery of Exhaust Waste Heat for ICE Using the Beta Type Stirling Engine,” *J. Energy*, vol. 2015, 2015.

[7] U. Ramesh and T. Kalyani, “Improving the efficiency of marine power plant using Stirling engine in waste heat recovery systems,” *Int. J. Innov. Res.*, vol. 1, no. 10, pp. 449–466, 2012.

[8] Caleb C. Lloyd, “A low temperature differential Stirling engine for power generation,” 2009.

[9] Joaquin G. Ruiz, *Waste heat recovery in automobile engines : potential solutions and benefits*. 2006.

[10] C. Sprouse and C. Depcik, “Review of organic Rankine cycles for internal combustion engine exhaust waste heat recovery,” *Appl. Therm. Eng.*, vol. 51, no. 1–2, pp. 711–722, 2013.

[11] Snežana D. Petkovic, Radivoje B. Pesic, and Jovanka K. Likic, “Heat Transfer in Exhaust System of a Cold Start,” *Therm. Sci.*, vol. 14, pp. 209–221, 2010.

[12] R. Host, P. Moilanen, M. Fried, and B. Bogi, “Exhaust System Thermal Management : A Process to Optimize Exhaust Enthalpy for Cold Start Emissions Reduction,” *SAE Tech. Pap.*, no. 2017-01–0141, 2017.

[13] A. Bejan, *Convection Heat Transfer*, Fourth Edi. Wiley, 2013.

[14] W. M. Rohsenow, J. R. Hartnett, and Young I. Cho, *Handbook of Heat Transfers*, Third Edit. McGraw-Hill, 1998.

[15] P. Chassaing, *Turbulence en mécanique des fluides: analyse du phénoméne en vue de sa modélisation à l’usage de l’ingénieur*. Cépaduès-Editions, 2000.

[16] O. Reynolds, “On the Dynamical Theory of Incompressible Viscous Fluids and the Determination of the Criterion,” *Philosiphical Trans. R. Soc. London*, 1894.

[17] A. P. Colburn, “A method of correlating forced convection heat-transfer data and a comparison with fluid friction,” *Int. J. Heat Mass Transf.*, vol. 7, no. 12, pp. 1359–1384, 1964.

[18] W. C. Reynolds and A. K. M. F. Hussain, “The mechanics of an organized wave in turbulent shear flow. Part 3. Theoretical models and comparisons with experiments,” *J. Fluid Mech.*, vol. 54, no. 2, pp. 263–288, 1972.

[19] M. Y. Gundogdu and M. O. Carpinlioglu, “Present State of Art on Pulsatile Flow Theory : Part 1: Laminar and Transitional Flow Regimes,” *JSME Int. J. Ser. B Fluids Therm. Eng.*, vol. 42, no. 3, pp. 384–397, 1999.

[20] M. Y. Gundogdu and M. O. Carpinlioglu, “Present State of Art on Pulsatile Flow Therory (Part 2: Turbulent Flow Regime),” *JSME Int. J.*, vol. 42, no. 3, pp. 398–410, 1999.

[21] S. P. Kearney, A. M. Jacobi, and R. P. Lucht, “Time-Resolved Thermal Boundary-Layer Structure in a Pulsatile Reversing Channel Flow,” *J. Heat Transfer*, vol. 123, pp. 655–664, 2001.

[22] T. W. Jackson and K. R. Purdy, “Resonant Pulsating Flow and Convective Heat Transfer,” *J. Heat Transfer*, pp. 507–512, 1965.

[23] R. C. Martinelli, L. M. K. Boelter, E. B. Weinberg, and S. Yakahi, “Heat transfer to a fluid flowing peridiocally at low frequecies in a vertical tube.,” *Trans. ASME*, vol. 65, pp. 789–798, 1943.

[24] J. E. Dec, J. O. Keller, and V. S. Arpaci, “Heat transfer enhancement in the oscillating turbulent flow of a pulse combustor tail pipe,” *Int. J. Heat Mass Transf.*, vol. 35, no. 9, pp. 2311–2325, 1992.

[25] J. E. Dec and J. O. Keller, “Pulse combustor tail-pipe heat-transfer dependence on frequency, amplitude, and mean flow rate,” *Combust. Flame*, vol. 77, no. 3–4, pp. 359–374, 1989.

[26] J. E. Dec, J. O. Keller, and I. Hongo, “Time-Resolved Velocities and Turbulence in the Oscillating Flow of a Pulse Combustor Tail Pipe,” *Combust. Flame*, vol. 83, pp. 271–292, 1991.

[27] J. E. Dec and J. O. Keller, “Time-resolved Gas Temperatures in the Oscillating Turbulent Flow of a Pulse Combustor Tail Pipe,” *Combust. Flame*, vol. 80, pp. 358–370, 1990.

[28] Y. Xu, M. Zhai, L. Guo, P. Dong, J. Chen, and Z. Wang, “Characteristics of the pulsating flow and heat transfer in an elbow tailpipe of a self-excited Helmholtz pulse combustor,” *Appl. Therm. Eng.*, vol. 108, pp. 567–580, 2016.

[29] M. Zhai *et al.*, “Heat transfer in valveless Helmholtz pulse combustor straight and elbow tailpipes,” *Int. J. Heat Mass Transf.*, vol. 91, pp. 1018–1025, 2015.

[30] J. T. Patel and M. H. Attal, “An Experimental Investigation of Heat Transfer Characteristics of Pulsating Flow in Pipe,” *Int. J. Curr. Eng. Technol.*, vol. 6, no. 5, pp. 1515–1521, 2016.

[31] A. E. Zohir, “Heat Transfer Characteristics in a Heat Exchanger for Turbulent Pulsating Water Flow with Different Amplitudes,” *J. Am. Sci.*, vol. 8, no. 2, pp. 241–250, 2012.

[32] L. Hua, Z. Yingjie, Z. Xuemei, D. Kai, L. Haihao, and C. Luyin, “Experimental Study of Convective Heat Transfer in Pulsating Air Flow inside Circular Pipe,” in *International Conference on Power Engineering*, 2007, pp. 880–885.

[33] M. A. Habib, A. M. Attya, A. I. Eid, and A. Z. Aly, “Convective heat transfer characteristics of laminar pulsating pipe air flow,” *Heat Mass Transf.*, vol. 38, no. 3, pp. 221–232, 2002.

[34] M. A. Habib, S. A. M. Said, A. A. Al-Farayedhi, S. A. Al-Dini, A. Asghar, and S. A. Gbadebo, "Heat transfer characteristics of pulsated turbulent pipe flow," *Heat Mass Transf.*, vol. 34, no. 5, pp. 413–421, 1999.

[35] S. Tardu, *Transport and Coherent Structures in Wall Turbulence*. .

[36] B. R. Ramaprian and S. W. Tu, "Fully developed periodic turbulent pipe flow. Part 2. The detailed structure of the flow," *J. Fluid Mech.*, vol. 137, no. 1, p. 59, 1983.

[37] S. W. Tu and B. R. Ramaprian, "Fully developed periodic turbulent pipe flow. Part 1. Main experimental results and comparison with predictions," *J. Fluid Mech.*, vol. 137, p. 31, 1983.

[38] S. A. M. Said, Al-Farayedhi A., M. Habib, S. A. Gbadebo, A. Asghar, and S. Al-Dini, "Experimental Investigation of Heat Transfer in Pulsating Turbulent Pipe Flow," *J. Heat Fluid Flow*, p. 54, 2005.

[39] S. V Nishandar and R. H. Yadav, "Experimental investigation of heat transfer characteristics of pulsating turbulent flow in a pipe," *Int. Res. J. Eng. Technol.*, vol. 2, no. 4, pp. 487–492, 2015.

[40] T. Moschandreou and M. Zamir, "Heat transfer in a tube with pulsating flow and constant heat flux," *Int. J. Heat Mass Transf.*, vol. 40, no. 10, pp. 2461–2466, 1997.

[41] E. A. M. Elshafei, Safwat Mohamed, H. Mansour, and M. Sakr, "Numerical study of heat transfer in pulsating turbulent air flow," *J. Eng. Technol. Res.*, vol. 4, no. October, pp. 89–97, 2012.

[42] E. A. M. Elshafei, M. Safwat Mohamed, H. Mansour, and M. Sakr, "Experimental study of heat transfer in pulsating turbulent flow in a pipe," *Int. J. Heat Fluid Flow*, vol. 29, no. 4, pp. 1029–1038, 2008.

[43] X. Wang and N. Zhang, "Numerical analysis of heat transfer in pulsating turbulent flow in a pipe," *Int. J. Heat Mass Transf.*, vol. 48, no. 19–20, pp. 3957–3970, 2005.

[44] A. R. A. Khaled, M. Siddique, N. I. Abdulhafiz, and A. Y. Boukhary, "Recent advances in heat transfer enhancements: A review report," *Int. J. Chem. Eng.*, vol. 2010, no. 1, 2010.

[45] H. R. Kharvani, F. I. Doshmanziari, A. E. Zohir, and D. Jalali-Vahid, "An experimental investigation of heat transfer in a spiral-coil tube with pulsating turbulent water flow," *Heat Mass Transf.*, 2015.

[46] H. Ghaedamini, P. S. Lee, and C. J. Teo, "Enhanced transport phenomenon in small scales using chaotic advection near resonance," *Int. J. Heat Mass Transf.*, vol. 77, pp. 802–808, 2014.

[47] C. Wantha, "Effect and heat transfer correlations of finned tube heat exchanger under unsteady pulsating flows," *Int. J. Heat Mass Transf.*, vol. 99, pp. 141–148, 2016.

[48] I. P. Kandylas and A. M. Stamatelos, "Engine exhaust system design based on heat transfer computation," *Energy Convers. Manag.*, vol. 40, no. 10, pp. 1057–1072, 1999.

[49] H. Fu, X. Chen, I. Shilling, and S. Richardson, "A One-Dimensional Model for Heat Transfer in Engine Exhaust Systems." SAE International , 2005.

[50] C. H. G. Brito, C. B. Maia, and J. R. Sodré, "A Mathematical Model for the Exhaust Gas Temperature Profile of a Diesel Engine," *J. Phys. Conf. Ser.*, vol. 633, p. 12075, 2015.

[51] Gamma Technologies, *GT-SUITE 7.4 - Flow Theory Manual*. 2014.

[52] John H. Lienhard, “A heat transfer Textbook,” p. 356, 2008.

[53] R. C. Mottram, “Introduction An overview of pulsating flow measurement,” *Flow Meas. Instrum.*, vol. 3, no. 3, pp. 114–117, 1992.

[54] F. Laurantzon, N. Tillmark, R. Orlu, and H. H. Alfredsson, “A flow facility for the characterization of pulsatile flows,” *Flow Meas. Instrum.*, vol. 26, pp. 10–17, 2012.

[55] M. Ö. Çarpinlioğlu and E. Özahi, “An experimental test system for the generation, control and analysis of sinusoidal pulsatile pipe flows (An application case for time dependent flow measurements),” *Flow Meas. Instrum.*, vol. 32, pp. 27–34, 2013.

[56] S. L. Hirst, “Heat transfer to a resonant pulsating air stream in a pipe,” Durham, 1974.

[57] H. H. Bruun, *Hot-wire Anemometry: Principles and Signal Analysis*. 1995.

[58] G. Comte-Bellot, “Hot-Wire Anemometry,” *Annu. Rev. Fluid Mech.*, vol. 8, no. 1, pp. 209–231, 1976.

[59] A. Berson, P. Blanc-Benon, and G. Comte-Bellot, “On the use of hot-wire anemometry in pulsating flows. A comment on ‘A critical review on advanced velocity measurement techniques in pulsating flows,’” *Meas. Sci. Technol.*, vol. 21, no. 12, p. 128001, 2010.

[60] P. C. Stainback and K. A. Nagabushana, “Review of Hot-Wire Anemometry Techniques and the Range of their Applicability for Various Flows,” *Electron. J. Fluids Eng. Trans. ASME*, vol. 167, pp. 1–54, 1993.

[61] D. C. Collis and M. J. Williams, “Two-Dimensional Convection from Heating Wires at Low Reynolds Numbers,” *J. Fluid Mechnics*, vol. 6, no. Goldstein 1938, pp. 357–389, 1959.

[62] R. Chevray and K. T. Narinder, “Simultaneous measurements of temperature and velocity in heated flows,” *Rev. Sci. Instrum.*, vol. 43, no. 10, pp. 1417–1421, 1972.

[63] S. F. Benjamin and C. A. Roberts, “Measuring flow velocity at elevated temperature with a hot wire anemometer calibrated in cold flow,” *Int. J. Heat Mass Transf.*, vol. 45, no. 4, pp. 703–706, 2001.

[64] L. Meyer, “Calibration of a three-wire probe for measurements in nonisothermal flow,” *Exp. Therm. Fluid Sci.*, vol. 5, no. 3, pp. 260–267, 1992.

[65] W. K. George, P. D. Beuther, and A. Shabbir, “Polynomial calibration for how wire in thermally varying flows,” *Symp. Therm. anemometry*, pp. 230–235, 1987.

[66] A. Abdel-Rahman, C. Tropea, P. Slawson, and A. Strong, “On temperature compensation in hot-wire anemometry,” *J. Phys. E.*, vol. 20, no. 3, p. 315, 1987.

[67] P. M. Downing, “Reverse flow sensing hot wire anemometer,” *J. Phys. E.*, vol. 5, no. 9, pp. 849–851, 1972.

[68] A. K. Gupta and A. Srivastava, “Feasibility study of a reverse flow sensing probe,” *J. Phys. E.*, vol. 12, pp. 1029–1030, 1979.

[69] S. F. Benjamin, Z. Liu, and C. a. Roberts, “A shielded hot-wire probe to detect flow reversals with one-dimensional pulsating flow,” *Proc. Inst. Mech. Eng. Part C J. Mech. Eng. Sci.*, vol.

218, no. 7, pp. 797–801, 2004.

[70] T. Fernández-Roque, M. Toledo-Velázquez, and J. F. Vázquez-Flores, “Detection and measurement of the inverse axial flow by means of the flying hot wire technique,” *Meas. J. Int. Meas. Confed.*, vol. 43, no. 1, pp. 1–8, 2010.

[71] M. A. Ardekani, M. Aminy, and A. Khoshnevis, “Investigation on the determination of flow direction using two parallel cylindrical hot film sensors,” *Meas. J. Int. Meas. Confed.*, vol. 43, no. 4, pp. 527–537, 2010.

[72] M. Tagawa, K. Kato, and Y. Ohta, “Response compensation of fine-wire temperature sensors,” *Rev. Sci. Instrum.*, vol. 76, no. 9, 2005.

[73] M. Tagawa, T. Shimoji, and Y. Ohta, “A two-thermocouple probe technique for estimating thermocouple time constants in flows with combustion: in situ parameter identification of a first-order lag system,” *Rev. Sci. Instrum.*, vol. 69, no. 9, pp. 3370–3378, 1998.

[74] M. Tagawa and Y. Ohta, “Two-thermocouple probe for fluctuating temperature measurement in combustion - Rational estimation of mean and fluctuating time constants,” *Combust. Flame*, vol. 109, no. 4, pp. 549–560, 1997.

[75] M. Tagawa, K. Kato, and Y. Ohta, “Response compensation of temperature sensors: Frequency-domain estimation of thermal time constants,” *Rev. Sci. Instrum.*, vol. 74, no. 6, pp. 3171–3174, 2003.

[76] P. G. O. Reilly, R. J. Kee, R. Fleck, P. T. Mcentee, and P. G. O. Reilly, “Two-wire thermocouples : A nonlinear state estimation approach to temperature reconstruction,” *Rev. Sci. Instrum.*, vol. 72, no. 8, 2001.

[77] K. Kar, S. Roberts, R. Stone, M. Oldfield, and B. French, “Instantaneous exhaust temperature measurements using thermocouple compensation techniques,” *SAE Tech. Pap.*, pp. 169–190, 2004.

[78] A. Berson, G. Poignand, P. Blanc-benon, and G. Comte-Bellot, “Capture of instantaneous temperature in oscillating flows : Use of constant-voltage anemometry to correct the thermal lag of cold wires operated by constant-current anemometry,” *Rev. Sci. Instrum.*, vol. 81, pp. 1–8, 2010.

[79] R. E. Johnk and T. J. Hanratty, “Temperature profiles for turbulent flow of air in a pipe: I, The fully developed heat-transfer region,” *Chem. Eng. Sci.*, vol. 17, pp. 867–879, 1962.

[80] R. K. Shah and M. S. Bhatti, “Laminar Convection Heat Transfer in Ducts,” *Handb. Single-Phase Convect. Heat Transf.*, 1987.

[81] J. Nikuradse, “Stromungsgesetze in rauhen rohren,” *Forrsch. Arb. Ing. Wes.*, vol. 361, 1933.

[82] Laufer J., “The Structure of turbulence in fully developed pipe flow,” *NASA Tech Br.*, vol. 2954, no. June, 1953.

[83] D. Nicolaides, D. Honnery, and J. Soria, “Autocorrelation Functions and the Determination of Integral Length with Reference to Experimental and Numerical Data,” in *15th Australasian Fluid Mechanics Conference*, 2004.

[84] J. Dirker and J. P. Meyer, “Convective Heat Transfer Coefficients in Concentric Annuli,” *Heat*

Transf. Eng., vol. 26, no. 2, pp. 38–44, 2005.

[85] M. V. Morkovin and S. V. Paranjape, “On acoustic excitation of shear layers,” *Z. Flugwiss*, vol. 8/9(2), pp. 328–335, 1971.

[86] Uchida S., “The Pulsating Viscous Flow Superposed on the Steady Laminar Motion of Incompressible Fluid in a Circular Pipe,” *J. Phys. Soc. Japan*, vol. VII, pp. 403–422, 1956.

[87] M. Ferro, “Experimental study on turbulent pipe flow,” 2012.

[88] P. Andre, R. Creff, and J. Crabol, “Etude des conditions particulieres de frequence favorisant les transferts thermiques en ecoulements pulses en canalisation cylindrique,” *Int. J. Heat Mass Transf.*, vol. 24, no. 7, pp. 1211–1219, 1981.

[89] C. L. Liu, J. Von Wolfersdorf, and Y. N. Zhai, “Time-resolved heat transfer characteristics for periodically pulsating turbulent flows with time varying flow temperatures,” *Int. J. Therm. Sci.*, vol. 89, pp. 222–233, 2015.

[90] David C; Wilcox, *Turbulence modeling for CFD*. 1994.

[91] *ANSYS Fluent Theory Guide*, vol. 15317, no. November. 2013.

[92] M. Manna and A. Vacca, “Spectral dynamic of pulsating turbulent pipe flow,” *Comput. Fluids*, vol. 37, no. 7, pp. 825–835, 2008.

[93] P. K. Papadopoulos and A. P. Vouros, “Pulsating turbulent pipe flow in the current dominated regime at high and very-high frequencies,” *Int. J. Heat Fluid Flow*, vol. 58, pp. 54–67, 2016.

[94] M. Manna, A. Vacca, and R. Verzicco, “Pulsating pipe flow with large-amplitude oscillations in the very high frequency regime. Part 1. Time-averaged analysis,” *J. Fluid Mech.*, vol. 700, pp. 246–282, 2012.

[95] M. Manna, A. Vacca, and R. Verzicco, “Pulsating pipe flow with large-amplitude oscillations in the very high frequency regime . Part 2 . Phase-averaged analysis,” *J. Fluid Mech.*, vol. 766, pp. 272–296, 2015.

[96] S. He and J. D. Jackson, “An experimental study of pulsating turbulent flow in a pipe,” *Eur. J. Mech. B-Fluids*, vol. 28, no. 2, pp. 309–320, 2009.

[97] G. Binder, S. Tardu, and P. Vezin, “Cyclic Modulation of Reynolds Stresses and Length Scales in Pulsed Turbulent Channel Flow,” *Proc. R. Soc. A Math. Phys. Eng. Sci.*, vol. 451, no. 1941, pp. 121–139, 1995.

[98] A. Scotti and U. Piomelli, “Numerical simulation of pulsating turbulent channel flow,” *Phys. Fluids*, vol. 13, no. 5, pp. 1367–1384, 2001.

[99] T. De Cuyper *et al.*, “Calibration of a TFG Sensor for Heat Flux Measurements in a S.I. Engine,” *SAE Tech. Pap.*, vol. 8, pp. 1692–1700, 2015.

[100] V. Corporation, “HFM Operator’s Manual,” no. 540. pp. 1–18, 2015.

Marco SIMONETTI

Etude du transfert thermique convectif dès écoulements turbulents pulsés dans un conduit cylindrique

Résumé :

Dans le but de réduire la consommation en carburant et les émissions de CO_2 des moteurs à combustion interne, un des leviers, qui a intéressé diffèrent acteurs dans le secteur automobile, est la récupération de l'énergie thermique disponible dans les gaz d'échappement. Malgré différents technologie ont été investigués dans le passé; les transferts de chaleur qui apparient dans les gaz d'échappement n'ont pas encore étés suffisamment étudiés. Le fait que les échanges de la chaleur apparent dans des conditions pulsatives, notamment due aux conditions de fonctionnement moteur, rende les connaissances acquis jusqu'à présent limités et ne pas exploitables. A l'état actuel on n'est pas capable de pouvoir prédire le transfert thermique convectif des écoulements pulsé. Les travaux de cette thèse s'instaurent dans la continuité de ce besoin, l'objectif principal est donc l'étude expérimentale du transfert thermique convectif des écoulements turbulent pulsés dans un conduit cylindrique. La première partie de ce travail a été consacrée à le dimensionnement d'un moyen d'essais permettant la création d'un écoulement pulsé type moteur; en suite différents méthodes de mesures ont étés développes afin de connaitre les variations instantanés de vitesse et température de l'écoulement. Plusieurs essais ont été reproduits afin de caractériser l'impact de la pulsation sur le transfert de la chaleur. Les résultats expérimentaux ont été analysés avec deux approches différentes: dans un premier temps une approche analytique 1D a permis de mettre en évidence le mécanisme principal responsable de l'amélioration du transfert thermique convectif, ainsi, il a fourni des éléments supplémentaires pour le futur développement de modèles mathématiques plus adaptés à la prédiction des transferts d'énergie. En suite une approche 2D, supporté d'une phase de modélisation numérique, a permis de caractériser le mécanisme de transport radial d'énergie thermique.

Mots clés : moteurs à combustion interne, récupération thermique, amélioration du transfert thermique convectif, écoulement turbulent pulsé dans un conduit cylindrique.

Study of convective heat transfer phenomena for turbulent pulsating flows in pipes

Summary:

Waste Energy Recovery represents a promising way to go further in fuel saving and greenhouse emissions control for Internal Combustion Engine applications. Although several technologies have been investigated in the past few years, the convective heat transfers, playing an important role in the energy exchanges at the engine exhaust, has not receive enough attention. Heat transfers, in such applications, occur in pulsating conditions because of the engine operating conditions, making thus the actual knowledge of the heat transfer phenomena limited and not exploitable. Nowadays there is not any model capable to predict convective heat transfers for pulsating flows. In this context, the present thesis addresses the purpose to study the convective heat transfer phenomena, by an experimental approach, occurring for turbulent pulsating flows in pipes. In the first part of this work, an experimental apparatus has been designed to reproduce an exhaust-type pulsating flow in fully managed conditions, as well as, several measurement techniques have been developed to know the instantaneous profiles of air temperature and velocity. Many experiments have been performed in order to characterize the impact of the flow pulsation on the convective heat transfers. In the second part of this work, the experimental results have been analyzed with two different approaches: firstly, with a 1D assumption the time-average convective heat transfers has been computed, and the major mechanism responsible of the heat transfer enhancement has been pointed out. Furthermore, it has been possible to highlight the mathematical term representative of such mechanism, which should be accounted in future to define a more adapted numerical model for the heat transfer prediction. In a second phase with a 2D assumption, and, with an energy and a fluid-mechanic computational phase, the radial transport of thermal energy has been characterized for a pulsating flow.

Keywords: Internal combustion engines, waste energy recovery, convective heat transfer enhancement, turbulent pulsating flows in pipes

Laboratoire PRISME
8 Rue Léonard de Vinci
45072 Orléans, FRANCE